SLAC – 334
UC – 28
(A/E)

LINEAR COLLIDER WORKING GROUP REPORTS FROM SNOWMASS '88*

Edited by
Ronald D. Ruth

Stanford Linear Accelerator Center
Stanford University
Stanford, California 94309

March 1989

Prepared for the Department of Energy
under contract number DE–AC03–76SF00515

Printed in the United States of America. Available from the National Technical Information Service, U.S. Department of Commerce, 5285 Port Royal Road, Springfield, Virginia 22161. Price: Printed Copy A05, Microfiche A01.

* Papers Extracted from the DPF Summer Study: SNOWMASS '88, High Energy Physics in the 1990s. Snowmass, Colorado, June 27–July 15, 1988

TABLE OF CONTENTS

SUMMARY OF THE LINEAR COLLIDER WORKING GROUP*

RONALD D. RUTH

INTRODUCTION

The focus of the Linear Collider Working Group was on a next generation linear collider with the general parameters shown in Table 1. The energy range is dictated by physics with a mass reach well beyond LEP, although somewhat short of SSC. The luminosity is that required to obtain $10^3 - 10^4$ units of R_0 per year. The length is consistent with a site on Stanford land with collisions occurring on the SLAC site. The power was determined by economic considerations. Finally, the technology was limited by the desire to have a next generation linear collider before the next century.

Table 1. General parameters.

Energy	0.5 - 1.0 TeV in center-of-mass.
Luminosity	$10^{33} - 10^{34}$ cm^{-2} sec^{-1}.
Length	Each Linac $\lesssim$ 3 Km.
Power	$\lesssim$ 100 MW per Linac.
Technology	Must be realizable by 1990–92.

The basic configuration of such a linear collider is shown in Fig. 1. The beam is accelerated by an injector linac and then injected into a damping ring which damps the emittance of the beam and provides the beam with appropriate intensity and repetition rate. After extraction, the bunch must be compressed in length twice in order to achieve the short bunches suitable for the linac and final focus. The linac is used to accelerate the beams to high energy while maintaining the emittance. Finally, the final focus is used to focus the beams to a small spot for collision. This must yield a luminosity with tolerable beam-beam effects (disruption and beamstrahlung) and must also provide a reasonably background-free environment for the detector.

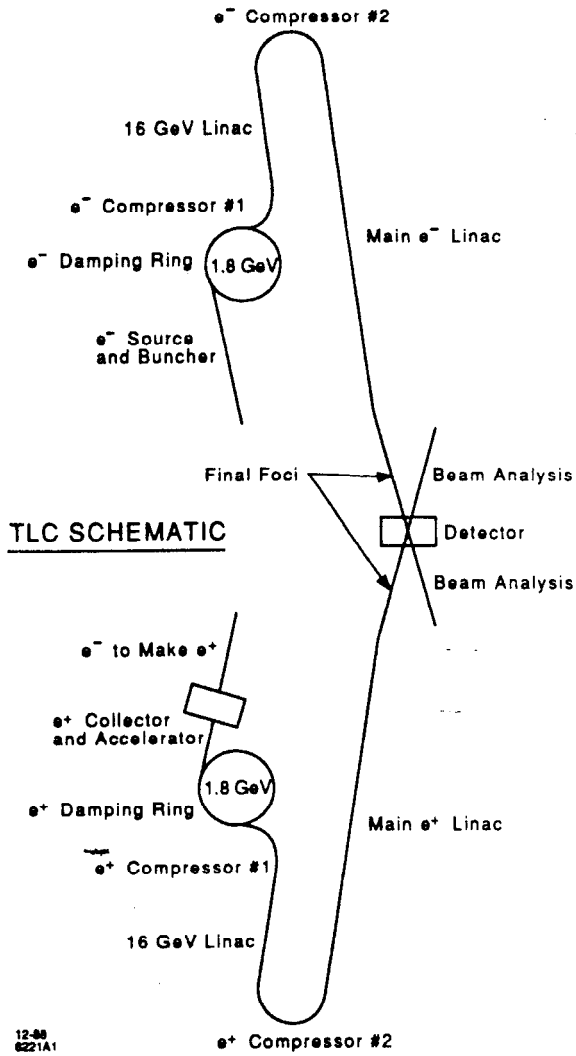

Fig. 1. Schematic layout of the TLC. The angles shown are exaggerated.

* Work supported by the Department of Energy, contract DE-AC03-76SF00515.

Before launching into a rather detailed discussion of the contributions to the Linear Collider section of the Snowmass Proceedings, it is useful to discuss generally the overall results of the workshop and the months following. Perhaps one of the most important developments is the increased interest in an Intermediate Linear Collider (ILC) with an energy of 0.5 TeV in the center-of-mass. This is a factor of two below the TeV Linear Collider (TLC) and thus would require a factor of four less peak power provided that the machines were the same length. One can imagine designing an ILC which would be upgradable in energy by the addition of RF power and minor modifications to the final focus system.

If we begin the discussion of an ILC or TLC at the lower energy end, the damping ring and bunch compressor designs seem relatively straightforward with, however, somewhat tighter tolerances than usual. The main linac will probably have a structure similar to SLAC, except at 4–6 times the frequency. The irises will have slots coupled to radial waveguides to damp the transverse and longitudinal higher order modes. This makes possible the use of multiple bunches per RF fill, which increases the luminosity by a factor of 10 for "free."

There is no definite power source as yet. The recent demonstration of binary pulse compression at SLAC has focused attention on more conventional approaches to long-pulse power production. Low power, low loss tests of RF pulse compression are continuing at SLAC and initial results look very promising. There are plans to build a high power klystron at SLAC to feed the RF pulse compressor, and there are many new ideas for power sources which would drive RF pulse compressors. The relativistic klystron results have been somewhat discouraging, but much as been learned about the problems associated with these high current, high energy beams.

Once the power source problem is solved, we are still left with the luminosity problem. These two aspects are only partially decoupled due to the use of many bunches (a batch) per RF fill. To obtain the luminosity, we must preserve the emittance of the beam throughout the linac. This means tighter tolerances on vertical magnet alignment than are presently achieved. The final focus demagnifies the beam to obtain a very flat beam at the final focus. The chromatic correction for this is quite delicate, and tolerances are tight. Finally, we must measure the beam size at the interaction point in order to tune the final focus. Many of these problems can be addressed via a model final focus at a lower energy. Towards this end, there is presently work ongoing at SLAC to create a Final Focus Test Beam in order to test flat beam final focus optics, measurement techniques, alignment techniques, etc. This would use the 50 GeV SLC beam straight ahead into the old C-line at SLAC.

During the SLAC Workshop in December 1988, following Snowmass, there was one important discovery which should be mentioned here. Beamstrahlung photons create e^+e^- pairs upon interacting with the opposing bunch. One particle of the pair is deflected strongly by the field of the bunch. This, in turn, can cause serious background problems. P. Chen and B. Palmer discuss this in their papers.

Table 2. Linear collider working group participants.

B. Ash—SLAC	R. Miller—SLAC
R. Blankenbecler—SLAC	A. Odian—SLAC
F. Bulos—SLAC	K. Oide—KEK/SLAC
D. Burke—SLAC	R. Palmer—BNL/SLAC
P. Chen—SLAC	E. Paterson—SLAC
Y. Chin—LBL	T. Raubenheimer—SLAC
B. Gabella—U. of Colo.	R. Ruth—SLAC
T. Himel—SLAC	K. Thompson—SLAC
S. Kheifets—SLAC	W. Vernon—UCSD
W. Kozanecki—SLAC	J. Wang—SLAC
N. Kroll—UCSD	B. Warnock—SLAC
G. Loew—SLAC	P. Wilson—SLAC
P. McIntyre—Texas A&M	

The list of working group participants is given in Table 2, while the Table of Contents gives a list of the contributions to the Proceedings. The purpose of the remainder of this paper is to provide guidance to the reader for the papers shown in the Table of Contents. To do this, I first discuss parameters briefly and then discuss damping rings. After discussing the basic concepts of bunch compression, I move to the contributions on linac structures and linac power sources. Since there is no specific paper on beam dynamics issues, in the next section I discuss emittance preservation in the linac in some detail. Next, the final focus papers are discussed and last, but not least, I introduce some of the issues for multibunch effects.

PARAMETERS

In this section, R. Palmer contributed a paper on linear collider energy scaling. Linear colliders are being considered for accelerators ranging from B-factories to Z-factories, up to a TeV Linear Collider. The purpose of this paper is to explore the change in the design of linear colliders as a function of energy given that one is always trying to maximize luminosity, but always respecting the limit on wall plug power shown in Table 1. A very wide range of energies is considered, and this leads to widely differing designs. In particular, one sees that the optimized RF frequency tends to decrease at lower energy while the repetition rate increases.

Table 3. Parameters for ILC and TLC.

		Low grad ILC	High grad ILC	TLC
General				
CM energy	TeV	.5	.5	1
luminosity 10^{33}	cm^{-2} sec^{-1}	1.5	2.9	6.2
RF wavelength	cm	1.75	1.75	1.75
repetition rate	kHz	.36	.36	.36
accel gradient	MV/m	93	186	186
number bunches		10	10	10
particles/bunch	10^{10}	.7	1.4	1.4
wall power	MW	52	103	210
length	Km	7.3	3.7	7.3
Damping				
emittance ϵ_x/ϵ_y		100	100	100
emittance $\gamma\epsilon_x$	μm	3.5	6.0	7.0
emittance $\gamma\epsilon_z$	m	.04	.04	.04
bunch spacing	m	.2	.2	.2
damping time	msec	2.1	2.3	2.3
RF				
pulse length	ns	60	60	60
peak power/length	MW/m	146	580	580
total RF energy	KJ	51	103	210
Linac				
loading η	%	2.5	2.5	2.5
iris radius a	mm	3.5	3.5	3.5
section length	m	1.6	1.6	1.6
Linac tolerances				
alignment	μm	20	35	30
vibration	μm	.009	.017	.012
Final focus				
β_y^*	mm	.1	.12	.11
crossing angle	mrad	4.2	6.1	3.8
disruption angle	mrad	.23	.31	.25
free length	m	.36	.43	.7
Intersection				
σ_y	nm	2.7	3.9	2.8
Oide min σ_y	nm	1.3	1.9	1.9
σ_x/σ_y		132	132	132
σ_z	μm	70	70	70
disruption D		5	5	5
lum enhance H		1.6	1.6	1.6
beamstrahlung δ	%	2	4	11
Δp/p physics	%	.7	1.1	3.2

In addition, due to the interest in the ILC, Palmer considers two possible options for an ILC, both of which would be upgradable to a TLC with additional length/power sources. Perhaps the most attractive option is the low gradient ILC which has a physical layout identical to TLC but has one-half the acceleration gradient. The parameters for ILC and TLC are compared in Table 3.

There is also an addendum to Palmer's paper which discusses the problem of e^+e^- pair creation at the interaction point by beamstrahlung photons interacting with the oncoming bunch. He finds that by using his idea of 'crab crossing' it is possible to collide beams with a very large crossing angle. In this way, with the help of solenoidal guide fields, the deflected e^+ or e^- can exit through a large aperture hole adjacent to the incoming quadrupole. This means that the parameter sets which have been presented will have to be modified to include various changes, but the basic parameters still will be rather similar to those given in Table 2.

DAMPING RINGS

The paper by T. Raubenheimer, L. Rivkin and R. Ruth discusses many of the basic design considerations for the damping ring. The basic parameters of the TLC damping ring are shown in Table 4 where they are compared to those of the SLC. The key differences are the decrease of the horizontal emittance by an order of magnitude, the increase of the repetition rate and the requirement of $\epsilon_x/\epsilon_y = 100$. Although asymetrical emittances have been measured in the SLC damping ring, they are not required for SLC operation.

The desired repetition rate is obtained by having many batches of bunches in the ring. Each batch of 10 bunches is extracted on one kicker pulse and accelerated on one RF fill in the linac. The remaining batches are left in the ring to continue damping while an additional batch is injected to replace the extracted one. The threshold current refers to the threshold for the "microwave instability" or "turbulent bunch lengthening."

The basic layout of a possible damping ring is shown in Fig. 2. Notice that there are several insertions which contain wigglers. In order to obtain the high repetition rate, it is necessary to decrease the damping time by the addition of wigglers in straight sections.

Table 4. Basic parameters of the SLC and TLC damping rings.

	TLC	SLC
Energy	$1 \sim 2$ GeV	1.15 Gev
Emittance, $\gamma\epsilon_x$	3.0 μmrad	36 μmrad
Emittance, $\gamma\epsilon_y$	30 nmrad	500 nmrad
Repetition rate	360 Hz	180 Hz
Bunch length	4 mm	5 mm[11]
Threshold Current	batches of 10 bunches of 2×10^{10}	1.5×10^{10}[11]

In Tables 5 and 6, you see the basic parameters for the ring. The lattice is combined function which allows the

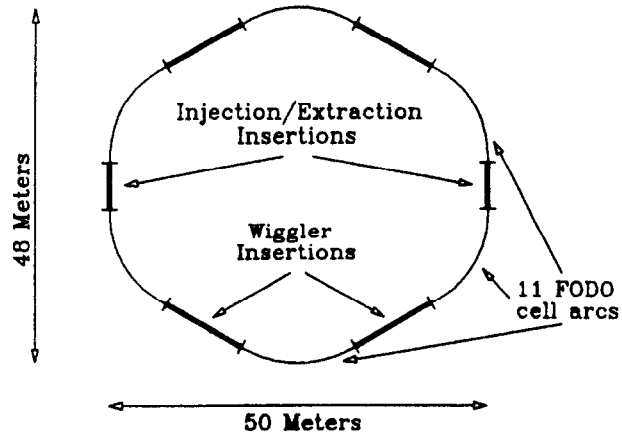

Fig. 2. Schematic of the TLC damping ring.

partition of the damping times to trade horizontal damping time for longitudinal. The RF frequency for this example is necessarily 1.4 GHz since the bunch spacing in this example is about 20 cm. The threshold impedance $(Z/n)_t$ is that for the microwave instability. It is quite small due to the small momentum compaction factor, but is only about a factor of three below that obtained in the SLC damping rings.

Table 5. TLC damping ring parameters.

Energy	$E_0 = 1.8$ GeV
Length	$L = 155.1$ meters
Momentum compaction	$\alpha = 0.00120$
Tunes	$\nu_x = 24.37, \quad \nu_y = 11.27$
RF frequency	$f_{RF} = 1.4$ GHz
Current	10 batches of 10 bunches of $2 \times 10^{10} e^+/e^-$

Table 6. TLC damping ring parameters.

	Wigglers Off	Wigglers On
Natural $\gamma\epsilon_x$	2.46 μmrad	2.00 μmrad
$\gamma\epsilon_x$ w/ intrabeam	3.33 μmrad	2.74 μmrad
Damping, τ_x	3.88 ms	2.50 ms
Damping, τ_y	9.19 ms	3.98 ms
Rep. rate, $f_{\rm rep}$	155 Hz	360 Hz
Damp. partition, J_x	2.37	1.59
Energy spread, σ_ϵ	0.00128	0.00104
Radiation/turn, U_0	203 KeV	468 KeV
Bunch length, σ_z	5.6 mm	5.2 mm
Synch. tune, ν_s	0.0068	0.0058
$(Z/n)_t$	$\mathcal{F} \times 0.32\Omega$	$\mathcal{F} \times 0.20\Omega$
Natural chrom., ξ_x	-28.35	-28.07
Natural chrom., ξ_y	-25.10	-22.27

Another key aspect of the TLC design is the small vertical emittance. The design calls for an emittance ratio $\epsilon_x/\epsilon_y = 100$. This size emittance ratio is quite common in $e^\pm$ storage rings. However, the tolerances for obtaining such a small vertical beam size are proportional to this size. In the damping ring paper, those tolerances which are related to maintaining the emittance ratio are calculated. The tolerances presented in Sec. 5 of the paper are in the 100 μm range and could be improved by adding correction skew quadrupoles in the ring.

BUNCH COMPRESSION AND PRE-ACCELERATION

Designs for bunch compression are presented in a paper by S. Kheifets *et al.* In order to obtain the very short bunches necessary for the linac, it is necessary to perform at least two bunch compressions. A bunch length of about 50 μm in the linac puts a tight constraint on the longitudinal emittance of the damping ring. In addition, during the bunch compressions, it is necessary to keep the energy spread small to avoid the dilution of the transverse emittance. If we assume that we can transport 1% energy spread without diluting either transverse emittance, then at least two bunch compressions are needed. For example, if we consider a 1.8 GeV damping ring with energy spread $\Delta E/E = 10^{-3}$ and a bunch length of 5 mm, the two compressions are shown in Table 7. The first one decreases the bunch length by an order of magnitude. This is followed by a pre-acceleration section to decrease the relative energy spread in the beam by an order of magnitude. One must avoid an increase of energy spread due to the cosine of the RF wave (and also due to beam loading). If this pre-acceleration is done at the present SLAC frequency and if the bunch current is as shown in Table 3, then the additional energy spread induced is about 5×10^{-4}. Neglecting this small increase, the next bunch compression happens at 18 GeV and serves to reduce the bunch length to about 50 μm. This is suitable for injection into the high frequency, high gradient structure.

Table 7. Bunch compression.

E	$\Delta E/E$	σ_z	Compress →	$\Delta E/E$	σ_z
1.8 GeV	10^{-3}	5 mm	Compress →	10^{-2}	0.5 mm
[pre-acceleration at long wavelength, $\lambda = 10.5$ cm]					
18 GeV	10^{-3}	0.5 mm	Compress →	10^{-2}	50 μm

The two designs shown in the paper by S. Kheifets *et al.* are for bunch compressors which have small bending angles. However, 180° bends which do the same job have also been designed.

LINAC

The linac is envisioned to be similar to the SLAC disk-loaded structure with a frequency at least four times the present SLAC frequency. The example shown in Table 3 is for six times the present SLAC frequency. The irises in the design are relatively larger to reduce transverse wakefields. The structure may have other modifications to damp long-range transverse wakefields. This would be driven by a power source capable of about 600 MW/m for the TLC or about 150 MW/m in the case of the ILC. In the case of the low gradient ILC, one can imagine an upgrade consisting of the addition of power sources.

Structures

The first paper on structures by G. Loew and J. Wang treats the question of RF breakdown. There have been many experiments done at various frequencies. If the scaling laws thus obtained are extrapolated to 11.4 and 17.1 GHz, the breakdown limited surface fields obtained are 660 and 807 MV/m, respectively. To convert this to effective accelerating gradient, a reduction factor of 2.5 is typically used.

In both cases, the accelerating gradient is above the 200 MeV/m used for the TLC design in Table 3. However, the measurements also indicated significant "dark currents" generated by captured field-emitted electrons. The question of the effects of dark current on loading and beam dynamics is not yet resolved and needs further study.

The next paper in the structures section is written by R. Palmer on Damped Accelerator Structures. As mentioned in the Introduction, in order to make efficient use of the RF power and to achieve high luminosity, it seems essential to accelerate a train of bunches with each fill of the RF structure. This leads to two problems: (1) the energy of the bunches in the train must be controlled and (2) the transverse stability of the bunch train must be ensured. Both of these problems are helped greatly by damping higher modes (both transverse and longitudinal) in the RF structure. This paper describes a technique of using slotted irises coupled to radial waveguides to damp these modes: Q's as low as 10–20 have been measured in model structures. This encouraging evidence has led to a development program at SLAC to do more detailed studies of slotted structures. The beam dynamics consequences of damping the higher modes is explored in the section on multibunch effects.

RF Power Sources

There are several papers contributed on the subject of RF power sources. The first and second paper are on the relativistic klystron and RF pulse compression, respectively. It is useful to contrast these approaches.

RF Pulse Compression

In Fig. 3(a), you see illustrated the basic principle of RF pulse compression. A long modulator pulse is converted by a high power, 'semi-conventional' klystron or some other power source into RF power with the same pulse width. This RF pulse is then compressed by cleverly slicing the pulse using phase shifts and 3 db hybrids and re-routing the portions through delay lines so that they add up at the end to a high peak power but for a small pulse width. This scheme was suggested by D. Farkas at SLAC and is presently under experimental investigation.[2] With a factor of 16 in pulse compression, the TLC would require a 50 MW klystron with a 1 μsec pulse length for each meter of the accelerator while the ILC would require a 50 MW klystron for each 4 meters of structure.

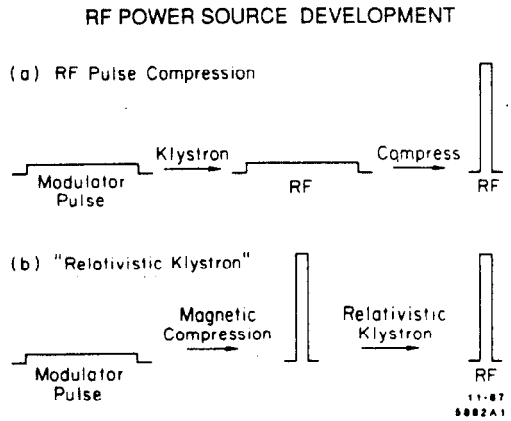

Fig. 3a. Illustration of RF pulse compression. 3b. Illustration of the relativistic klystron with magnetic compression.

The Relativistic Klystron

In Fig. 3(b), you see the principle of the relativistic klystron illustrated. In this case, the pulse compression happens *before* the creation of RF. This technique makes use of the pulsed power work done at LLNL in which magnetic compressors are used to drive induction linacs to produce multi-MeV e^- beams with kiloampere currents for pulses of about 50 nsec. These e^- beams contain gigawatts of power. The object, then, is to bunch the beam at the RF frequency to extract a significant fraction of this power. This can be done either by velocity modulation or by dispersive magnetic "chicanes." After bunching, the beam is passed by an RF extraction cavity which extracts RF power from the beam.

In the relativistic klystron paper by M. Allen *et al.*, four experiments are described. These are the result of a SLAC-LLNL-LBL collaboration which makes use of the

ARC facility (e^- beams 1.2 MeV and $\lesssim$ 1 KA) at LLNL. Thus far the record peak power for any of the devices tested is 200 MW; however, in this case, the RF envelope was noticeably shortened. The highest power obtained with a wide RF pulse was about 80 MW. The most serious problem encountered in the experiment is the pulse shortening phenomenon; however, recent experiments suggest that this is caused by loading due to anomalous charged particle currents. A second serious problem is poor beam transmission. Finally, this RF power has been used to drive a 26-cm travelling wave structure at 11.4 GHz. The peak power of 200 MW corresponds to a local acceleration gradient of 140 MV/m. Work is continuing on this experiment.

In the second paper on RF pulse compression and alternative RF sources, P. Wilson describes RF pulse compression in some detail including estimates of efficiencies. There is an experimental test ongoing at SLAC which seeks to test a low loss, low power system. Initial results of this test have been very encouraging. A 100 MW, 11.4 GHz, "semi-conventional" klystron is presently being constructed at SLAC to perform high power tests of pulse compression. In the second section, the paper discusses other alternative RF sources for input to RF pulse compression.

The next paper on RF power, by W. Vernon, discusses another RF compression technique which uses RF energy storage combined with a high power switch to obtain very large compression of RF. This idea has been tested experimentally but needs much more work on high power switches to be feasible.

The next contribution on the cluster klystron, by R. Palmer and R. Miller, describes a multiple beam array of "klystrinos" which when coupled together can give impressive results. By dividing a single beam into many beams shielded from each other, the problems of space charge are effectively eliminated. This source could be used as a driver for RF pulse compression. Alternatively, with the addition of a grid and an oil-filled transmission line for energy storage, the device could directly produce short RF pulses. Thus far, there has been no experimentation; but calculations and cost estimates are encouraging.

The final paper in this section on RF power is on the Gigatron by H. Bizek *et al.* This device makes use of the lasertron concept to produce a bunched beam directly at the cathode. Field emitting arrays are used for the cathode while a ribbon beam geometry is envisioned to control space charge effects. This device is another candidate for RF pulse compression and has an impressive efficiency on paper. Experimental tests are presently being prepared.

Emittance Preservation

There was no specific contribution to the Snowmass Proceedings on emittance preservation in the linac. The purpose of this section is to fill in that gap. The effects discussed are treated in more detail in Ref. 3.

Chromatic Effects

The filamentation of the central trajectory in a linac can cause dilution of the effective emittance of the beam. If we first consider a coherent betatron oscillation down the linac, then to be absolutely safe, we must require that it be small compared to the beam size. If the spread in betatron phase advance is not too large, then this tolerance is increased to perhaps twice the beam size for the cases shown in Table 3.

The chromatic effect of a corrected trajectory is rather different. In this case, it is the distance between an error and a corrector which matters, and the effects partially cancel yielding a growth $\propto \sqrt{N_{quad}}$. This yields a tolerance on magnet misalignment the order of 20 to 30 times the beam size in the linac (about 30 μm) for the cases shown in Table 3. This is also the tolerance on BPM measurements. If the phase advance of the linac or some subsection is not too large, then this yields a linear correlation of position with momentum (dispersion) which can, in principle, be corrected since it does not vary in time. Therefore, it may be possible to have looser tolerances if such correction is provided.

Transverse Wakefields and BNS Damping

The wakefield left by the head of a bunch of particles, if it is offset in the structure, deflects the tail. If the transverse oscillations of the head and tail have the same wave number, the tail is driven on resonance. This leads to growth of the tail of the bunch.[4] This effect can be controlled by a technique called BNS damping.[5] The bunch is given a head-to-tail energy correlation so that the tail is at lower energy. The offset of the head by an amount $\hat{x}$ induces a deflecting force on the tail away from the axis. The tail, however, feels an additional force $\Delta K\hat{x}$, where ΔK is the difference in focusing strength. These two forces can be arranged to cancel, thereby keeping the coherence of the bunch as a whole. For the designs shown in Table 3, the spread in energy for BNS damping is $\sim \pm .3\%$. This correlation can be accomplished by moving the bunch slightly on the RF wave to obtain a linear variation across the bunch.

Recently, BNS damping has been tested at the SLAC linac with great success. It is now part of normal operating procedure.

Jitter

In order to maintain collisions at the interaction point, the bunch must not move very much from pulse to pulse. Since the optics of the final focus also demagnify this jitter, the tolerance is always set by the local beam divergence compared to the variation of some angular kick. The jitter

tolerance on the damping ring kicker is thus related to the divergence of the beam at that point. This is discussed in the paper on damping rings. At the injection point to the linac, the offset caused by this jitter must be small compared to the local beam size.

If all the quadrupoles in the linac are offset by random amounts, the effects accumulate down the linac and the orbit offset grows $\propto \sqrt{N_{quad}}$. This sets the tolerance on the random motion of quadrupoles to be much smaller than the beam size. In the examples in Table 3, the random jitter tolerances are $\simeq 0.01$ μm. On the other hand, tolerances for correlated effects are much less severe. In either case, this size motion from pulse-to-pulse is unlikely due to the large repetition rate of the collider. More gradual motion, which is larger, can be corrected with feedback.

Jitter in RF kicks can cause similar effects. These effects can be reduced by reducing the DC component of the RF kick. This is done by eliminating asymmetries in couplers and by careful alignment of structures.

Coupling

Finally, we discuss coupling of the horizontal and vertical emittance. The beam size ratio in the linac is 10:1. The tolerance on random rotations is given by

$$\Theta_{rms} << \frac{\sigma_y}{\sigma_x} \frac{1}{\sqrt{2N_q}} \quad .$$

For the examples shown in Table 3, the right-hand side is about 3 mrad. This seems quite straight forward. If the errors are not random, larger rotations can indeed result; however, because the beam size is so small, the effects are very linear. This means that skew quadrupoles can be used effectively as correction elements. Certainly in the final focus, skew quads will be an integral part of the tuning procedure to obtain flat beams.

FINAL FOCUS

The final focus, as described in the parameters in Table 3, is a flat beam final focus with a crossing angle. The purpose of the flat beam is to increase the luminosity while controlling beamstrahlung and disruption. The crossing angle is to allow different size apertures for the incoming and outgoing beam. Another invention, "crab-wise crossing," discussed in R. Palmer's paper, allows a much larger crossing angle than the diagonal angle of the bunch. As discussed in Palmer's contribution and in P. Chen's paper in this section, this type of geometry may now be essential due to the production of e^+e^- pairs by beamstrahlung photons in the field of the bunches.

The first paper in this section by K. Oide treats the design of a flat-beam final focus. The vertical size is limited by the synchrotron radiation in the final quadrupole doublet coupled with the chromatic effect of a quad. He also shows how the system can be made much shorter and how the aperture of the final doublet can be increased. Finally, Oide discusses the pulse-to-pulse jitter tolerances on elements in the final focus. The most restrictive requirement is on the final doublet which must be stable pulse-to-pulse to about 1 nm.

Since vibration of the final doublet is the most serious problem, it is considered in some detail in the next paper by W. Ash. In this paper, it is shown that passive vibration isolation seems to be more than adequate to handle the vibrations above ~ 10 Hz at the high frequency end. For low frequencies, Ash suggests an interferometric feedback system to control motion to about 1 μm. Beam steering feedback can then be used to control slow variations in the 1 nm to 1 μm region.

A summary of beam-beam effects is presented by P. Chen. He begins by covering beamstrahlung and disruption for flat beams. The next subject is the kink instability induced if the beams are slightly offset vertically from each other. This effect actually causes the luminosity to be less sensitive to offsets because the beams attract each other and collide anyway. There is also a multibunch kink instability which is more serious since it can cause the trailing bunches to miss each other entirely. The effect of this is to place restrictions on the product of the vertical and horizontal disruption per bunch. This effect is shielded somewhat if the quadrupoles are close to the interaction point. Chen concludes the main body of the paper with a discussion of energy spectrum and maximum disruption; issues which are important for final quad design and backgrounds.

The final section of Chen's paper is an addendum added after the SLAC Workshop in December 1988. As mentioned earlier in the Introduction, it was discovered that the beamstrahlung photons pair-produce in the coherent field of the bunch. The corresponding incoherent process has been known for some time, but its importance has only just been realized. The problem is that low energy e^+e^- pairs are produced in an extremely strong field which then deflects the charge of the appropriate sign while confining the other. This leads to large angular kicks, as mentioned earlier in Palmer's paper on parameters. These stray particles can lead to more background problems, which must be addressed by further interaction point design. Some initial ideas were presented in Palmer's paper, but the problem needs much more study.

The discussion of beam-beam effects continues in a paper by R. Blankenbecler and S. Drell. They show how beamstrahlung photons can be used to create a photon-photon collider. They show an increase in luminosity for real photons *vs* virtual photons. At the time of Snowmass, the problem of pair creation had not been realized. This will probably not effect the luminosity results but would cause difficult background problems.

There is one final paper in the final focus section by T. Himel which deals with some of the background issues. He discusses background from synchrotron radiation in the final quad and also discusses the maximum disruption angle of an electron which has radiated most of its energy.

Clearly, with all this new information on the swarm of e^+e^- pairs produced, there needs to be much more study of the background problems, as well as interaction point geometry.

The measurement of the final spot size was not studied at the Snowmass workshop. This is an extremely important, but as yet unsolved, problem. From SLC experience, it is probably possible to use beam-beam effects to minimize spot sizes. However, for the initial tune-up of the final focus, a single-beam method is almost essential. There was some initial work done at the workshop in June 1988 in Capri, Italy which was also reported at the SLAC workshop.[6] In addition, preliminary results were presented at the SLAC workshop on the use of beamstrahlung from an ionized gas jet.[7] Although this looks promising, there is still much work to be done.

MULTIBUNCH EFFECTS

As mentioned earlier, in order to efficiently extract energy from the RF to obtain high luminosity, it is essential to have many bunches per RF fill. This, however, leads to transverse beam breakup. K. Thompson and R. Ruth have written a paper for this section which traces the problem of multibunches all the way through the linear collider, subsystem by subsystem. Damped accelerating cavities are required for the main linac and the damping rings. Other systems can get by with very strong focusing. Thus, from the transverse point of view, stability seems possible.

In addition, it is necessary to control the energy spread from bunch to bunch very precisely ($\Delta E/E \lesssim 10^{-3}$). This can be accomplished by injecting the bunches before the RF structure is full to match the extraction of energy by the bunches to the incoming energy as the structure fills. This leads to tight tolerances on phase and amplitude of the RF, as well as tight control of the pulse-to-pulse number of particles in a batch of bunches.[8] However, the benefits of multibunching seem to far outweigh any difficulties they impose due to the order of magnitude increase in luminosity.

OUTLOOK

A key result of the Snowmass Workshop is the increased interest in an ILC, that is, a linear collider with 0.5 TeV in the CM which might be upgradable to 1.0 TeV with additional power sources. Since there is a factor of four difference in peak power for the ILC and TLC (for a fixed length), the power source looks much easier to do. Designs of damping rings, bunch compressors and final focus systems are continuing. Perhaps the most important point was realized only after theSnowmass Workshop — beamstrahlung pair creation at the interaction point. The control of backgrounds in the face of pair creation needs much more work. However, with a sufficiently intensive R&D program towards power sources, final focus systems, etc. during the next few years, we may see a proposal for a next generation Linear Collider in the early 1990's.

ACKNOWLEDGEMENTS

I would like to thank Fred Gilman, Mel Month, and the entire organizing committee for a stimulating and well-organized workshop. Also, I would like to thank all the members of the working group for their stimulating discussions and for their excellent contributions to the Proceedings.

REFERENCES

1. L. Z. Rivkin *et al.*, "Bunch Lengthening in the SLC Damping Ring," SLAC–PUB–4645 (1988).
2. Z. D. Farkas, *IEEE Transcripts on Microwave Theory and Techniques*, **MTT–34**, No. 10 (1986) 1036, and also SLAC/AP–59.
3. R. D. Ruth, *Emittance Preservation in Linear Colliders*, in Lecture Notes in Physics, **296**, Frontiers of Particle Beams, Eds. M. Month, S. Turner, South Padre Island, Texas, 1986, and in SLAC–PUB–4436.
4. A. Chao, B. Richter and C. Yao, *Nucl. Instr. Meth.* **178**, 1 (1980).
5. V. Balakin, A. Novokhatsky and V. Smirnov, *Proceedings of the 12th International Conference on High Energy Accelerators*, Fermilab, (1983) p. 119.
6. J. Norem, presented at the *International Workshop on Next Generation Linear Colliders*, in preparation.
7. D. Burke, P. Chen, M. Hildreth and R. Ruth, work in progress.
8. R. D. Ruth, *Multi-Bunch Energy Compensation*, in proceedings of workshop on "Physics of Linear Colliders," Capri, Italy, 1988; and in SLAC–PUB–4541.

ENERGY SCALING, CRAB CROSSING AND THE PAIR PROBLEM*

R. B. PALMER

Stanford Linear Accelerator Center, Stanford University, Stanford, California 94309
and
Brookhaven National Laboratory, Upton, New York 11973

ABSTRACT

Making reasonable assumptions, the luminosities of linear colliders are calculated for center-of-mass energies of 10 GeV, 100 GeV and 1 TeV. A calculation is also mode for a 1/2 TeV collider that could be upgraded to 1 TeV later. The improvements possible using "crab-like" crossing are also given.

1. INTRODUCTION

The design of linear colliders is a complex problem because of the interdependence of the critical parameters.[1] Changing the number of particles per bunch effects the damping ring design and thus the emittance; it effects the wakefields in the linac and thus the momentum spread; the momentum spread effects the final focus design and thus the final β^*; but the emittance change also effects the final focus design; and all these come together to determine the luminosity, disruption and beamstrahlung at the intersection. Changing the bunch length, or almost any other parameter, has a similar chain reaction. Dealing with this problem by simple scaling laws is very difficult because one does not know which parameter is going to be critical and thus which should be held constant. In the face of this problem, I have written a PC program that—given various assumptions—simultaneously calculates:

- Emittances, damping rate and impedance requirements in the damping ring.
- RF properties of the accelerating structure.
- Longitudinal wakes in the linac.
- Transverse wakes in the linac.
- Focusing requirements for BNS damping and tolerances in the linac.
- Required final focus chromatic correction.
- Required pole tip fields in the final focus quadrupoles.
- Disruption and beamstrahlung at the intersection.
- Multibunch instabilities at the crossing.

Most of the calculations are done using analytic expressions. Inevitably, many approximations have been used. It is not the intent of the program to actually design a machine. It is the object to explore the parameter space and get a feeling for what is and is not possible.

*Work supported by DOE contract numbers DE-AC02-76CH00016 and DE-AC03-76SF00515.

In an earlier paper,[1] I used the program to select reasonable parameters for a .5 on .5 TeV Collider. In this paper, the emphasis is on discovering the scaling to lower energies. There are, however, a number of changes in the assumptions and calculations since Ref. 1:

1. It is assumed that damped acceleration cavities[2] can be used, and thus multiple bunches can be accelerated without buildup of transverse wakes.
2. The longitudinal wakes are correctly integrated, assuming a Gaussian bunch profile (a four-bunch approximation had been used in Ref. 1).
3. Dilutions are introduced: (a) between damping ring and linac, (b) in the linac and (c) in the final focus. Dilutions are specified for emittances in all three directions and for β.
4. The Oide limit on spot size from synchrotron radiation in the final quads is calculated and applied.

2. ASSUMPTIONS

2.1 Ratio of Horizontal to Vertical Emittances

Assume the ratio of horizontal to vertical emittances in the damping ring to be less than or equal to 100:1. An asymmetric emittance is natural in a damping ring and comes with essentially no price. It allows the generation of a flat beam profile. The original motive for using such a flat beam was to minimize the beamstrahlung without loss of luminosity. It also allows the use of a finite angle crossing, so that the disrupted beam does not have to pass through the opposite quadrupole. I find that the best luminosity always requires the maximum ratio of emittances.

2.2 Ratio of Horizontal to Vertical Betas

With conventional crossing, I assume the undiluted ratio of horizontal to vertical betas at the intersection to be 3.24 times the ratio of emittances. When this condition is satisfied, the beam size in the final quads is approximately the same horizontally and vertically, and maximum luminosity is achieved. With 100:1 emittance ratio and this assumption, the beam will have an aspect ratio of 180:1.

With crab crossing (see Sec. 3.3), greater luminosity is obtained with smaller ratios of the betas; but the beamstrahlung rises, and has been limited to a value of $\delta \leq .3$

in this study. The maximum luminosity is reached for a β ratio of 3.2.

2.3 Crossing Angle

In order to avoid excessive luminosity loss, a finite crossing angle is selected that is 0.7 times the bunch diagonal angle (*i.e.*, $0.7 \times \sigma x/\sigma z$). The bunch length is then selected to give a crossing angle sufficiently large, compared with the maximum disruption angle, to avoid collisions of the disrupted beam with the poles of the quadrupole. A larger factor is required at the higher energies because of assumed quantum fluctuations in the disrupted beam (this is yet to be calculated). The required ratios were: crossing/disruption = 24 (1 TeV), = 19 (.1 TeV) and = 14 (10 GeV).

2.4 Damping Ring

A wiggler damping ring is assumed. The energy is chosen to make the contributions from intrabeam scattering and quantum fluctuations the same. The ring diameter is then chosen to give a longitudinal impedance requirement of Z/n = 0.5 Ω. The wiggler fields are 2 T, the quadrupole apertures 12 mm radius and pole tip fields 1.4 T, the partition functions were normal, $\beta y/\beta x = 4$, and phase advance per cell 65°.

2.5 Quadrupole Doublet Final Focus

A conventional, chromatically-corrected quadrupole-doublet final focus is assumed. The ratio of the assumed corrected β to a calculated uncorrected value is taken to be $S = .04 \times dp/p$ (scaling law from K. Brown). The maximum pole tip field is assumed to be 1.4 T. The aperture is taken to be ten times the rms beam size.

2.6 Accelerating Structure

A conventional iris loaded accelerating structure is assumed. The iris radius is taken to be 0.2 times the wavelength. This gives a relatively high group velocity (0.08) and lower wakefields than for a SLAC–like structure (radius 0.1 times the wavelength). The fill time for the structure is usually taken to be 0.3 times the attenuation time. But in the case when the wavelength is 17 mm (1 TeV example), then the fill time is taken to be 0.6 times the attenuation length to avoid using pulses of less than 45 ns.

2.7 BNS Damping

Transverse wakes are assumed to be controlled by BNS damping. Focusing in the linac is taken to give a β that rises with the square root of the energy. Five percent of the linac length is assumed taken up with quadrupoles whose apertures are 1.26 times the structure irises and whose pole tip fields are 1.4 T.

2.8 Number of Bunches

It is assumed that transversely damped accelerating structures are used and that multiple bunches can be used without beam breakup. A limit is set on the number of bunches such that not more than 25% of the total stored energy is extracted. This limit is consistent with considerations of energy constancy.

2.9 Repetition Rate

The repetition rate is set to keep the wall power to 200 MW. A klystron efficiency of 36% is assumed.

2.10 Dilution

The following dilutions are assumed:

Emittance z in buncher:	1.4
Emittance x from kicker:	1.4
Particle transmission through buncher:	1/1.2
Emittance y in linac:	1.4
Particle transmission through final focus:	1/1.2
Emittance x y in final focus:	1.2
β^* x y in final focus:	1.2

2.11 Longitudinal Emittance

At high energies the contribution of the longitudinal emittance in the damping ring to the momentum spread at the intersection is negligible. In this case the longitudinal emittance is constrained by considerations of the bunch length in the damping ring to be less than 0.04 m $\times dp/p$ at $\gamma = 1$.

At low energies the longitudinal emittance is constrained only by considerations of momentum spread in the linac and for physics.

2.12 Bunch Length

The bunch length is selected to maximize the final luminosity. In general, a longer bunch length will allow a larger longitudinal emittance and thus, from the damping ring, smaller transverse emittances and higher luminosity. The primary constraint on the bunch length is the loss of luminosity that arises when the diagonal angle becomes less than the finite crossing angle. Another constraint arises when luminosity is lost because the bunch length has become much longer than the β^* at the intersection.

2.13 Accelerating Fields

From the machine physics point of view there seems no disadvantage in high accelerating fields. The optimized luminosity is little effected, the tolerances are easier and of course the length is less. The field used should thus be the highest possible consistent with breakdown and dark current considerations. I have assumed that these limits are wavelength dependent and used: G = 46.5 MV/m for f = 2 GHz, G = 93 MV/m for f = 6 GHz and G = 186 MV/m for f = 17 GHz.

2.14 Wavelength

The wavelength, like the acceleration gradient, has little effect on the optimized luminosity (for the same loading and average power consumption, the larger wavelength collider will have more luminosity per cycle, but a lower repetition rate). At higher energies a lower wavelength is preferred because it will have the lower stored RF energy, lower peak power requirements and thus a cheaper power source; and lower wavelength solutions are also found to have lower beamstrahlung. However, as the wavelength falls the power source becomes harder to build and the linac tolerances become tighter (both alignment and jitter). I selected 17 GHz as the maximum RF frequency.

At lower energies, if the wavelength is reduced, the repetition rate (for fixed wall power and luminosity) becomes excessive, and it would be very hard to design a damping ring (or rings) to provide the low emittance positrons. But, at lower energies beamstrahlung is less of a consideration; also, the accelerator is shorter so the cost of the power supply is less of a consideration. It is then reasonable to use a larger wavelength. Rather arbitrarily I used for:

10 GeV c.m.: f(rep) = 1.7 kHz at P(wall) = 200 MW,
giving f(rf) = 2 GHz ;

100 GeV (rep) = 1.0 kHz at P(wall) = 200 MW,
giving f(rf) = 6 GHz ;

1 TeV f(rep) = 0.4 kHz at P(wall) = 200 MW,
giving f(rf) = 17 GHz .

2.15 Loading (η)

At high energies, when the longitudinal emittance is held to a constant maximum practical value, the loading has a negligible effect on the momentum spread at the final focus. In this case, the luminosity per bunch is found to be nearly independent of the loading. (A higher loading, and thus higher N, would naturally increase the luminosity, but this is offset by the higher emittance from the damping ring and by the higher β^* because of the greater difficulty in correcting the higher momentum spread from higher wakes.) With multibunching, however, the number of bunches is inversely proportional to the loading, and thus the total luminosity turns out to be inverse with the loading. There are various limits to this: when the momentum spread gets too low, the chromatic correction scaling will break down, or the tolerances will get too tight. I limit the chromatic correction factor to 30, which results in the luminosity reaching its maximum for a loading of about 2.5%.

At lower energies the longitudinal emittance dominates the momentum spread at the final focus, and in this case the luminosity per bunch increases with loading. With multibunching the luminosity now becomes independent of the loading. The choice of loading is now rather arbitrary, providing it is not so large as to give an excessive momentum spread. When in doubt, I have used 2.5%.

3. RESULTS

3.1 Conventional Finite Angle Crossing

With these assumptions I have generated the parameter lists for machines at center-of-mass energies of 10 GeV, 100 GeV and 1 TeV [see Table 1 and Fig. 1 (dots)]. For the 10 GeV case, the momentum spread was restricted to less than 0.2% in order to be not larger than the width of the $\Upsilon(4s)$ state.

Note that far more thought has been given to the 1 TeV case than the lower energy examples, so it is not clear that these lower energy examples are fully optimized. In addition, some of the parameters for the B factory case are unreasonable or unphysical (they are indicated by ***). The damping ring design is unphysical and unreasonably small, but the performance indicated is not unreasonable and can, almost certainly, be obtained in a real design. The accelerator section lengths are also too long, but these could be lowered by adding some magnetic coupling between cells.

The exact performances given should not be taken too seriously. Nevertheless we note that the luminosity seems to fall from a value close to 10^{34} at 1 TeV, to only a little above 10^{33} at 10 GeV: falling about as the root of the energy. This conclusion is reached assuming constant wall power (200 MW). In practice it is hard to believe one would consider a collider at 10 GeV using so much power, so the realistic luminosity of such a B-factory would be even lower.

Table 1. Parameters of optimized colliders at three energies.

		B factory	Z factory	TLC
General				
c.m. energy	TeV	.01	.1	1
RF wavelength	cm	15	5	1.7
repetition rate	kHz	1.7	1.0	.36
accel gradient	MV/m	46	93	186
number bunches		10	10	10
particles/bunch	10^{10}	37	6	1.4
wall power	MW	200	200	200
Damping				
emittance x/y		100	100	100
emittance y (ϵ_n)	μm	4.2	.4	.06
emittance z	m dp/p γ	.005	.014	.04
bunch spacing	m	2.4	.5	.2
ring Energy	GeV	.6	.8	1
ring radius	m	.7***	4	15
(avg B)/(peak B)		3***	.7	.24
damping time	msec	3.8	2.8	2.3
RF				
pulse length	ns	680	150	60
peak power/length	MW/m	260	380	580
total RF energy	KJ	40	67	210
Linac				
loading η	%	2.5	2.5	2.5
iris radius a	mm	44	10	3.5
section length	m	57***	4	1.6
dp/p for BNS	%	.04	.17	.4
dp/p from wakes	%	.09	.11	.12
dp/p incl emit	%	.18	.16	.08
RF phase for BNS	deg	20	22	15
Linac tolerances				
alignment	μm	—	300	30
vibration	μm	1.9	.12	.012
Final focus				
β_y^*	mm	.11	.10	.08
crossing angle	mrad	59	14	3.8
disruption angle	mrad	6.7	.72	.25
chrom corr factor		22	24	28
quad radius	mm	19	2.1	.32
free length	m	.53	.56	.68
Intersection				
σ_y	nm	220	21	2.2
Oide min $\overline{\sigma_y}$	nm	43	8	1.7
σ_x/σ_y		180	170	177
σ_z	μm	460	180	70
disruption D		12	8	6.5
lum enhance H		1.3	1.4	1.6
beamstrahlung δ	%	.004	.27	11
dp/p physics	%	.18	.18	3.2
luminosity 10^{33}	cm^{-2} sec^{-1}	1.0	3.1	7.8

*** See text.

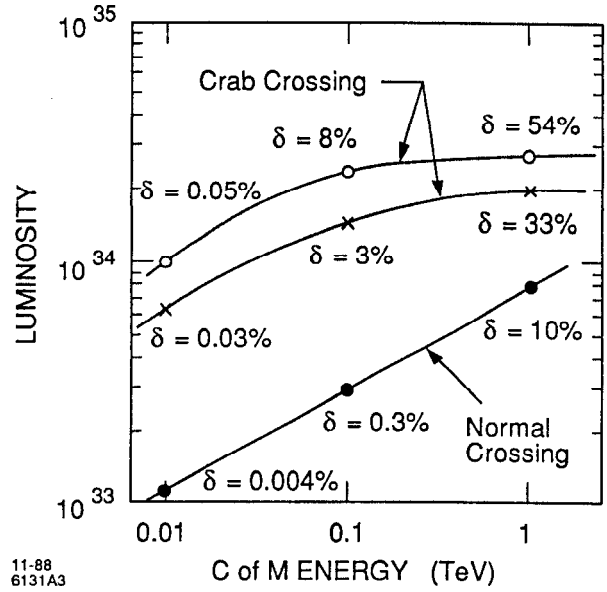

Fig. 1. Luminosity of linear collider designs as a function of energy.

3.2 An Intermediate Linear Collider

Instead of completely redesigning the machine as the energy is lowered, we can consider the performance of a collider with wavelength and repetition rate chosen for the 1 TeV case, but operating at a reduced energy, e.g., at one half energy. Two options are considered: (a) keep the gradient the same and half the length and (b) keep the length the same and half the gradient. In both cases, the final focus and damping rings have been reoptimized. The resulting parameters are shown in Table 2. The higher gradient version gives twice the luminosity and has a less severe vibration tolerance, both of which would be preferred. However, the dark currents and breakdown problems will be less in the low gradient case, and the stored energy is lower by a factor of two, so the power supply will be easier and cheaper.

3.3 Crab-Wise Finite Angle Crossing

The situation can be improved if "crab-wise" crossings are allowed. Such crossings would employ an RF deflector near the end of each linac to deflect the front of the bunches one way and the back the other way (so they now move somewhat crab-wise). If the angle of tilt of each bunch is correctly chosen, then the bunches pass through each other head on—even when the beams have a finite crossing angle (see Fig. 2). This technique removes the constraint on the width of the bunches that is normally present with finite angle crossing and allows a smaller aspect ratio.

Using this crab-wise crossing, machines were redesigned at the three energies [see Fig. 1 (crosses) and Table 3]. For the 10 GeV case, the total momentum spread is again kept below 0.2%; for the 100 GeV case, it is kept to 1% for Z production, and for 1 TeV it is kept to $\delta \leq .3$; *i.e.*, an rms momentum spread of 10%.

Figure 1 (circles) also shows designs with no restriction on momentum spread.

Table 2. Two designs for an intermediate energy collider.

		Low grad ILC	High grad ILC	TLC
General				
c.m. energy	TeV	.5	.5	1
RF wavelength	cm	1.75	1.75	1.75
repetition rate	kHz	.36	.36	.36
accel gradient	MV/m	93	186	186
number bunches		10	10	10
particles/bunch	10^{10}	.7	1.4	1.4
wall power	MW	52	103	210
Damping				
emittance x/y		100	100	100
emittance y (ϵ_n)	μm	.035	.06	.07
emittance z	m dp/p γ	.04	.04	.04
bunch spacing	m	.2	.2	.2
ring energy	GeV	1.1	1.0	1.0
ring radius	m	23	15	15
(avg B)/(peak B)		.17	.24	.24
damping time	msec	2.1	2.3	2.3
RF				
pulse length	ns	60	60	60
peak power/length	MW/m	146	580	580
total RF energy	KJ	51	103	210
Linac				
loading η	%	2.5	2.5	2.5
iris radius a	mm	3.5	3.5	3.5
section length	m	1.6	1.6	1.6
dp/p for BNS	%	.2	.4	.4
dp/p from wakes	%	.11	.11	.11
dp/p incl emit	%	.14	.14	.14
RF phase for BNS	deg	19	15	15
Linac tolerances				
alignment	μm	20	35	30
vibration	μm	.009	.017	.012
Final focus				
β_y^*	mm	.1	.12	.11
crossing angle	mrad	4.2	6.1	3.8
disruption angle	mrad	.23	.31	.25
chrom corr factor		29	29	29
quad radius	mm	.17	.25	.32
free length	m	.36	.43	.7
Intersection				
σ_y	nm	2.7	3.9	2.8
Oide max σ_y	nm	1.3	1.9	1.9
σ_x/σ_y		132	132	132
σ_z	μm	70	70	70
disruption D		5	5	5
lum enhance H		1.6	1.6	1.6
beamstrahlung δ	%	2	4	11
dp/p physics	%	.7	1.1	3.2
luminosity 10^{33}	cm^{-2} sec^{-1}	1.5	2.9	6.2

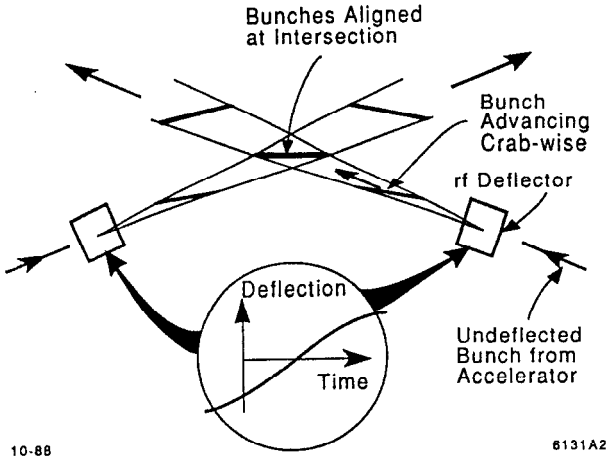

Fig. 2. Crab-wise crossing.

As in the case in Section 3.1, less effort has been spent on the low energy examples than on the TeV case, and there are the same problems in the B factory case. Nevertheless, the general trend is probably correct: a significant gain in luminosity is obtained in all cases, with the larger gain being realized in the lower energy examples.

4. POSSIBLE IMPROVEMENTS

1. Some improvements in the damping ring performance are probably possible. In the examples considered I used a wiggler ring but did not consider a combined function lattice that could alter the partition functions. If a combined function wiggler lattice is possible, we might gain a factor of two in the final luminosity.

2. I have assumed that not more than 25% of the energy stored in the cavities can be extracted with multiple bunches. This may be true for a traveling wave structure, but need not be so in a standing wave structure. A factor of two increase in efficiency, and thus luminosity, might be possible.

3. I assumed only 36% efficiency for the power source. Clusters of low perveance mini-klystrons might have much better efficiency. Another factor of two?

4. One can always hope that the dilutions that have been assumed are overly pessemistic. A maximum gain of about three is possible.

5. One can consider asymmetric arrangements in which a higher electron than positron current is employed. If electrons are available from a high brightness gun whose brightness is higher than that available from a damping ring then some gain in luminosity might be possible. For the low energy machines, one could also consider asymmetric energies with the same possible advantage.

At best there might be another order of magnitude to be won, but it will not be easy. Maybe there are other ideas!

Table 3. Parameters for colliders with crab-wise crossing.

		B factory	Z factory	TLC
General				
c.m. energy	TeV	.01	.1	1.0
RF wavelength	cm	15	5	1.75
repetition rate	kHz	1.8	1.0	.36
accel gradient	MV/m	46	93	186
number bunches		20	10	10
particles/bunch	10^{10}	19	6	1.4
wall power	MW	200	200	200
damping				
emittance x/y		100	100	100
emittance y	μm	2.7	.36	.05
emittance z (ϵ_n)	m dp/p γ	.004	.016	.04
bunch spacing	m	1.2	.5	.2
ring Energy	GeV	.64	.8	1.0
ring radius	m	1 ***	4	15
(avg B)/(peak B)		2 ***	.7	.24
damping time	msec	3.5	2.8	2.3
RF				
pulse length	ns	680	150	60
peak power/length	MW/m	260	380	580
total RF energy	KJ	40	70	210
Linac				
loading η	%	1.25	2.5	2.5
iris radius a	mm	44	10	3.5
section length	m	57 ***	4	1.6
dp/p for BNS	%	.02	.15	.4
dp/p from wakes	%	.07	.07	.12
dp/p incl emit	%	.19	.15	.08
RF phase for BNS	deg	14	28	15
Linac tolerances				
alignment	μm	8000	340	30
vibration	μm	3.8	.16	.012
Final focus				
β_y^*	mm	.34	.27	.2
crossing angle	mrad	150	45	9.2
Δz tolerance	μm	50	24	18
disruption angle	mrad	17	2.3	.58
chrom corr factor		26	23	28
quad rad	mm	200	18	1.8
free length	m	1.7	1.6	1.6
Intersection				
σ_y	nm	300	32	3.3
Oide min σ_y	nm	28	7	1.7
σ_x/σ_y (R)		24	35	49
σ_z	μm	340	150	70
disruption	D	15	14	10
lum enhance H		1.7	1.9	2
beamstrahlung δ	%	.03	2.7	33
dp/p physics	%	.2	.8	10
luminosity 10^{33}	cm^{-2} sec^{-1}	6	14	20

*** See text.

5. ADDENDUM–THE PAIR PROBLEM

Since the Snowmass meeting and since writing the above, we have become aware of the serious nature of the backgrounds due to electron positron pairs generated by beamstrahlung photons. These photons can be converted by at least two mechanisms. They can make pairs incoherently on the individual electrons in the oncoming beam.[2] They can also be converted in the coherent electromagnetic field of the entire oncoming beam.[3] There has not been time to give a thorough study of these backgrounds, and thus what follows is preliminary, and concerns only the 1 TeV cases discussed above.

5.1 Pair Production Cross Section

The cross section for the incoherent pair production[3] is relatively energy independent and has a value of the order of 6×10^{-26} cm^2. For the TLC parameters given above, approximately 10^6 electron positron pairs are generated per multibunch crossing.

The coherent production is negligible provided the beamstrahlung remains in the classical regime. Defining Υ as 2/3 times the critical energy divided by the beam energy, then

$$\Upsilon = \frac{.86 R_e \lambda\!\!\!^{-}_e \gamma N}{\sigma_z \sigma_x} \qquad (1)$$

where R_e (2.82×10^{-15}) is the classical electron radius, $\lambda\!\!\!^{-}_e$ is the classical electron wavelength (3.86×10^{-13}), γ is of the beam, N is the particles per bunch, and σ_z and σ_x are the rms length and width of the bunch.

The coherent production remains negligible compared to the incoherent effect provided Υ is less than 0.6.[3] If Υ is above that value the production rises very rapidly until the number of pairs is equal or even larger than the initial number of electrons. In the normal crossing TLC case given above the Υ is only 0.35 and the coherent production would not be a problem. But in the higher luminosity "crab crossing" case Υ is 1.1 and we would have massive coherent pair production.

5.2 Energy and Angular Distribution

Reflecting the bremstahlung spectrum of the photons, the number spectra of the pair electrons falls as the 2/3rd power of the energy. Their angles of production are of order $1/\gamma$, and therefore very much forward, but the magnetic fields at the bunch crossing deflect them to larger angles.

The maximum transverse momentum given to the pair electrons is, in our TLC examples, of the order of 160 MeV, but that is only given to relatively high energy electrons (approximately 50 GeV), and these emerge at relatively small angles (of the order of 2 mrad). With the finite angle crossings, discussed above, such high energy pair electrons would pass by the opposite quadrupole without causing trouble. For lower energy pair electrons, however, the situation is more serious and now depends on their charge.

In the case of the pair electron with the same charge as the beam from which it came, then the fields deflect it in towards the axis, and if its energy is low, trap it along the axis. When such a trapped electron leaves the bunch it emerges in a relatively forward direction, as do the beam electrons themselves when they have lost a large fraction of their energy.[4] The angles in our case are of the order of 1 mrad vertically, but 10 mrad horizontally, which would already be a problem. But the situation for the other sign is much worse.

For the pair electron with the opposite charge to its beam, then, the deflection is away from the axis and the final angle can be much larger. For low energy electrons (in our case less than approximately 50 GeV) the maximum angle can be expressed for flat beams (but I think only approximately) by

$$\Theta = 1.5\left(\frac{R_e N}{\gamma \sigma_z}\right)^{1/2} \qquad (2)$$

where R_e is the classical electron radius, N is the number of electrons in the oncoming bunch, γ is the γ of the pair electron and σ_z is the rms bunch length. In the TLC cases above, for a pair electron energy of 250 MeV the angle is 70 mrad. And there are approximately 100,000 electrons with energy less than 250 MeV!

5.3 Proposed Solution

I will assume that we should avoid operating in the quantum regime where massive coherent pair production is present. I will also assume that a number of electrons of the order of 100,000, of any energy, colliding with the face of an opposite quadrupole is unacceptable. They will either melt the magnet or at least give an albido that will be intolerable to the detector.

I then propose :

1. *Use crab crossing* to allow a crossing angle of the order of 80 mrad. At 1.6 m this corresponds to a distance of 13 cm. I will assume that we can make a quadrupole with a radius not larger than 4 cm, surrounded by a bucking coil (to shield the quadrupole from the experiments solenoidal field) of thickness not more than 3 cm. In this way only particles at angles greater than 40 mrad can hit the quad or bucking coil.
2. *Reduce the pair electron deflection angles* (Θ) by increasing σ_z and decreasing N. σ_z is increased until the momentum spread from the curvature of the sin wave of the rf is significant. I halve N and, at the same time, double the number of bunches, so as to keep the same total efficiency. The increase in transverse wakes caused by the bunch lengthening is compensated by the lower number of particles per bunch, so the alignment tolerances are the same. Despite the energy spread caused by the long bunch, the lower number of particles per bunch produces a smaller energy spread, and thus the same β can be obtained at the final focus.
3. *Reduce the bunch aspect ratio* $R = \sigma_x/\sigma_y$, and thus increase the luminosity, until the Υ reaches a still safe value of 0.32. The aspect ratio is then 60. The amplitude tolerance on the crab crossing rf separators

$$\frac{dA}{A} = \frac{\sigma_x}{\sigma_z \Theta_c} = 1.6\% \qquad (3)$$

where Θ_c is the crossing angle. The position tolerance on the separators is

$$dz = 2\frac{\sigma_x}{\Theta_c} = 4\ \mu \quad . \qquad (4)$$

Note that this position error is equivalent to a horizontal beam shift of 0.16 μ, and that the beams horizontal position will in any case have to be servoed. The 4 μ tolerance is a jitter tolerance and is not severe.

With these new parameters the luminosity is 10^{34} cm^{-2} sec^{-1}, as required, and other parameters quite reasonable. The maximum angle of pair electrons at 250 MeV is now 40 mrad, and we have chosen a crossing angle and magnet dimensions so that these will not hit the quad or bucking coil. But we must still do something to stop the lower momentum tracks from hitting these magnets.

4. *Use a kinked solenoidal field* to confine the low momentum tracks. If a solenoidal field can be obtained that is aligned along the outgoing beam axes, then low energy electrons will be guided along those axes. Electrons with 250 MeV or less will have transverse momenta of only 10 MeV or less. If the solenoidal field were 3 T then all such electrons would be constrained within a helix of 1 cm radius, *i.e.*, well away from the quadrupole and bucking coils. This maximum extent of the trapped electrons rises linearly with energy, while the maximum extent of untrapped electrons falls as the root of energy from Eq. (2). The maximum distance (Fig. 3) that any electron reaches from the outgoing axis is now 4 cm (at 500 MeV), which is over 2 cm from the bucking coil.

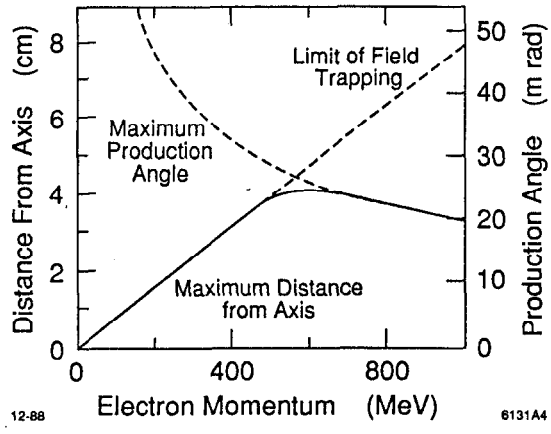

Fig. 3. Maximum radial extent of electrons from their axis at the entrace to the first quadrupole, plotted against their energy. At low energy the extent is limited by field trapping, at high energy by the production angles.

The problem remains as to how to make a solenoidal field that points along both outgoing beam directions; *i.e.*, how to make a solenoidal field with a kink of 80 mrad at the intersection. Such a field would be obtained with a current sheet in the mid plane of the detector, but that would be undesirable. Luckily it seems that the field that inevitably results when bucking coils are placed about the final quadrupoles has, at least to some approximation, the required kink [see Fig. 4(a)]. As shown in the figure, the bucking coils have been extended inward towards the intersection so as to improve the field shape. Further improvements could be made by the addition of horizontal low field (0.12 T) coils between the end of the bucking coils and the intersection. In the absence of bucking coils (e.g., if pure permanent magnet quads were used) such horizontal low field coils, but now much longer, could be used [Fig. 4(b)].

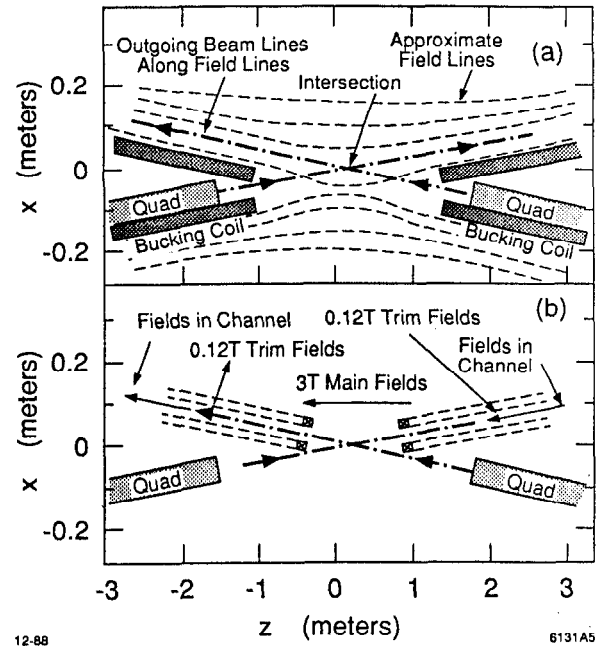

Fig. 4. Possible intersection region geometries in a large experimental solenoid; (a) with bucking coils to shield conventional quadrupoles; and (b) with permenant magnet quadrupoles and transverse trim coils. It is seen that in both cases the resulting fields have the qualitatively correct shape to guide low energy pair electrons away from the quadrupoles.

5.4 Conclusion

It appears that the pair production problem can be overcome, at least at 1 TeV, by a combination of modifications to the previously defined TLC. Crab crossing seems essential to allow a crossing angle of the order of 80 mrad. The high momentum pair electrons now pass well clear of the quadrupoles. The production angles of low momentum pair electrons can be reduced by halving the number of electrons per bunch and doubling the bunch length. Then, with the help of a solenoidal field, these too can be kept clear of the magnets.

A bunch aspect ratio of 60 keeps the beamstrahlung Υ to about 0.3, and the coherent pair production is supressed. Using these new parameters, and by increasing the number of bunches to 20, the luminosity can be maintained at 10^{34} cm^{-2} sec^{-1}.

REFERENCES

1. R. B. Palmer, "The Interdependence of Parameters for TeV Linear Colliders," SLAC-PUB-4295; Proceedings of Workshop on New Developments in Particle Accelerator Techniques, Orsay, France, June 1987.
2. V. Telnov, reported at SLAC Collider Workshop, November 1988.
3. P. Chen, reported at SLAC Collider Workshop, November 1988, and discussed in these Snowmass Proceedings.
4. K. Yokoya, Proceedings of Linear Accelerator Conference, Williamsburg, Virginia, 1988.

Damping Ring Designs for a TeV Linear Collider*

T. O. RAUBENHEIMER, L. Z. RIVKIN, R. D. RUTH

Stanford Linear Accelerator Center, Stanford University, Stanford, California 94309

ABSTRACT

In this paper we present a damping ring design for the TLC (TeV Linear Collider). The ring operates at 1.8 GeV. It has normalized emittances of $\gamma\epsilon_x = 2.8\,\mu$mrad and $\gamma\epsilon_y = 25.4$ nmrad. The damping times are $\tau_x = 2.5$ ms and $\tau_y = 4.0$ ms. To achieve these extremely low emittances and fast damping times, the ring contains 22 m of wigglers.

1. INTRODUCTION

In this paper we discuss a damping ring for the TLC, a TeV linear collider.[1] The basic design goals of the TLC damping ring are compared with those of the Stanford Linear Collider (SLC) damping rings in Table 1. The normalized horizontal emittance of the TLC ring is an order of magnitude smaller than that of the SLC ring, and the desired repetition rate has increased by a factor of two. Furthermore, the TLC ring needs to achieve an emittance ratio of 100:1. Thus the vertical emittance must be damped to a value three orders of magnitude smaller than the SLC emittance. This implies that TLC ring will either have much faster damping times than the SLC ring or be much larger, thereby damping more bunches at once.

The present design of the TLC operates in a multi-bunch mode. The linac accelerates batches of bunches, where the bunches within a batch are separated by roughly 20 cm and each bunch contains 2×10^{10} particles. To prevent multi-bunch instabilities we need to use a specially designed RF system; a discussion of multi-bunch instabilities is found in Ref. 2. In addition, we would like to operate the ring below the longitudinal microwave instability threshold. Thus, the threshold current must be 30% larger than that in the SLC ring. To achieve this without increasing the longitudinal emittance significantly, the TLC ring must have a very low impedance and a large momentum compaction.

Table 1. Basic parameters of the SLC and TLC damping rings.

	TLC	SLC
Energy	$1 \sim 2$ GeV	1.15 Gev
Emittance, $\gamma\epsilon_x$	$3.0\,\mu$mrad	$36.\,\mu$mrad [3]
Emittance, $\gamma\epsilon_y$	30. nmrad	–
Repetition rate	360 Hz	180 Hz
Bunch length	4 mm	5 mm [4]
Threshold Current	batches of 10 bunches of 2×10^{10}	1.5×10^{10} [4]

In the next section we discuss the design goals. Then using simple scaling laws, we show the dependance of the various design parameters such as the lattice, main bending field, bending angle per bend, etc. This is applied to illustrate problems with the wiggler damping ring,[5] an option that seemed promising for low emittances and fast damping times. We then discuss the effect of damping wigglers and methods of changing the damping partitions. Because the parametric dependances become complex, we use a computer program to search for a lattice which satisfies the design criteria and uses a minimal length of wigglers.

In Sec. 3 we present a design which meets all of the specified requirements. We discuss the various portions of the ring, the arcs, the insertion regions, and the wigglers. We then detail the chromaticity correction scheme and the resulting dynamic aperture. Finally, in Sec. 5 we discuss tolerances and methods of loosening the tolerances on alignment and on the extraction kickers.

* Work supported by the Department of Energy, contract, DE – AC03 – 76SF00515

2. DESIGN CONSIDERATIONS

2.1. Basic Parameters

There are two main parameters we need to consider when designing a damping ring: the ring's emittance and the damping times. The emittance of an extracted beam is

$$\epsilon = \epsilon_i e^{-2t/\tau} + (1 - e^{-2t/\tau})\epsilon_{\rm ring} \ , \qquad (2.1)$$

where ϵ_i is the emittance of the injected beam and $\epsilon_{\rm ring}$ is the ring emittance including the effects of intrabeam scattering. Here, τ is the horizontal or vertical damping time, and t is the time the bunch is in the ring. The present TLC design requires that the extracted beam have normalized emittances of $\gamma\epsilon_x \leq 3 \times 10^{-6}$ and $\gamma\epsilon_y \leq 3 \times 10^{-8}$. We assume an injected beam emittance of $\gamma\epsilon_i = 3 \times 10^{-3}$, which is realistic for a positron beam and an order of magnitude too large for an electron beam. Thus the vertical emittance needs to be decreased by five orders of magnitude. Damping the bunch for seven vertical damping times will reduce the first term of Eq. (2.1) by six orders of magnitude. The limit on the vertical emittance of the ring is then

$$\gamma\epsilon_{y\,\rm ring} \leq 2.7 \times 10^{-8}\,{\rm mrad} \ . \qquad (2.2)$$

In a storage ring built in the horizontal plane the vertical emittance is mainly determined by the coupling between the horizontal and vertical planes. Intrabeam scattering, which increases the horizontal emittance, has a very small effect on the vertical.[6,7] We will discuss the tolerances necessary to achieve the limit — Eq. (2.2) — in Sec. 5.

The required damping times are determined from the desired repetition rate (360 Hz) the number of damping times per bunch (7) and the number of batches stored in the ring at once (N_b)

$$\tau_x, \tau_y \leq \frac{1}{f_{\rm rep}} \frac{N_b}{\#\text{ of damping times}} = N_b 0.397\,{\rm ms} \ . \qquad (2.3)$$

The maximum number of batches stored in the ring is limited by the kickers needed for injection/extraction. We assume that the time for the kickers to turn on, extract/inject a batch, and turn off is less than 100 ns.[8] Thus the batches must be separated by at least 50 ns. Since the number of batches is roughly proportional to the size of the ring we can define an effective damping time as

$$\tau_{\rm eff} \equiv \tau \frac{50\,{\rm ns}}{T_0} \leq 0.397\,{\rm ms} \ , \qquad (2.4)$$

where T_0 is the revolution time of the ring.

For reasons we will discuss later, it is desirable that the horizontal damping time be less than or equal to the vertical; thus only the vertical damping time is limited by Eq. (2.3). Furthermore, assuming that $\tau_x \lesssim \tau_y$, the horizontal emittance of the extracted beam is very nearly equal to the horizontal emittance of the ring. Thus

$$\gamma\epsilon_{x\,\rm ring} \leq 3 \times 10^{-6}\,{\rm mrad} \ . \qquad (2.5)$$

Equations (2.4) and (2.5) determine the basic parameters. Initially, to study these parameters, we make the assumption that all the bending magnets are the same and we ignore the effect of intrabeam scattering. Now we can write simple expressions for $\gamma\epsilon_{x0}$ and $\tau_{y\,\rm eff}$,[9] the two quantities we want to minimize:

$$\tau_{y\,\rm eff} = 8.47 \times 10^6 \frac{\rho_B f_w}{J_y \gamma^3} \qquad (2.6)$$

$$\gamma\epsilon_{x0} = 3.84 \times 10^{-13} \frac{\gamma^3}{J_x} \frac{\langle \mathcal{H} \rangle_{\rm mag}}{\rho_B} \ . \qquad (2.7)$$

Here, ρ_B is the *local* bending radius of the bend magnets and $\langle \mathcal{H} \rangle_{\rm mag}$ is the Courant-Snyder dispersion invariant which equals the average of $\mathcal{H} \equiv \gamma\eta_x^2 + 2\alpha\eta_x\eta_x' + \beta\eta_x'^2$ over the bending magnets. Also, $J_{x,y}$ is the horizontal (vertical) damping partition number, and f_w is equal to ρ_B divided by the average bending radius in the bending magnets, ρ_0. Note that with normal bends $f_w = 1$, but in a wiggler ring[5] where the bending magnets bend in both directions, $f_w < 1$.

The emittance of a ring can be reduced by reducing the dispersion in the bend magnets, reducing the strength of the bends, or decreasing the energy of the ring. Unfortunately, the damping times are *increased* by reducing the bend magnet strength or decreasing the energy of the ring. This implies that the dispersion in the bends is the only free parameter. Unfortunately, it is constrained by the longitudinal microwave instability which increases the longitudinal emittance.

At this point it is worth discussing three additional parameters which constrain the design: (1) the longitudinal microwave instability which was just mentioned, (2) the dynamic aperture, and (3) the energy of the ring. The microwave instability, also called turbulent bunch lengthening, occurs at a given current when the longitudinal impedance is larger than a threshold, denoted $(Z/n)_t$. We want to keep this threshold as large as possible to avoid bunch lengthening and longitudinal instabilities. It can be estimated as

$$(Z/n)_t \approx \frac{(2\pi)^{3/2} E \sigma_\epsilon^2 \sigma_z \alpha}{N e^2 c} \mathcal{F} \ , \qquad (2.8)$$

where E is the energy, σ_ϵ is the relative energy spread, and σ_z is the bunch length. In addition, α is the momentum compaction, N is the number of e^+/e^- per bunch, and e and c are the electron charge and the speed of light. Finally, $\mathcal{F}$ is a form factor which is greater than 1.[10] At the 1987

ICFA workshop on Low Emittance Beams,[11] an impedance of

$$Z/n \geq 0.2\,\Omega \tag{2.9}$$

was determined to be the minimum reasonable, physically attainable value.

Next we should consider the dynamic aperture. The dynamic aperture of the ring is a function of the sextupoles needed to correct the chromaticity. To prevent particle losses the dynamic aperture should be many times the *injected* beam size. Unfortunately, rings with small emittances tend to have high tunes and large uncorrected chromaticities. This makes the desired dynamic aperture difficult to achieve. Thus we would like to choose a lattice which naturally has a large dynamic aperture.

Finally, the other parameter we mentioned is the ring energy which we would prefer to have low. There are three primary reasons for this: (1) it makes the magnets cheaper, (2) it keeps the longitudinal emittance small, and (3) it makes bunch compression easier. The TLC requires that the damping ring bunch be compressed longitudinally by, roughly, a factor of 100. Since one does not want an uncorrelated energy spread much greater than 1% in the linac, we need to perform at least a portion of the bunch compression at an energy 10 times that of the damping ring.[12] Unfortunately, at higher energies it becomes more difficult to perform the compression without degrading the beam emittances.

2.2. Scaling

Now we can combine these expressions to determine the dependencies of the parameters. Using the definition of and maximum value for $\tau_{y\,\mathrm{eff}}$ — Eqs. (2.6) and (2.4) — we find an expression for the energy of the ring as a function of the bending field and f_w:

$$B_0(KG)\gamma^2 = f_w \frac{1.44\times 10^5}{\tau_{y\,\mathrm{eff}}}\,. \tag{2.10}$$

In this equation, J_y is assumed to be equal to 1, since it cannot be changed without introducing vertical dispersion which would degrade the vertical emittance. Note that for our parameters, a normal ring, with saturated bending magnets (20 KG), must operate at 2.2 GeV to meet the damping time requirements.

In a similar manner, using Eqs. (2.7) and (2.10), we find an equation for the emittance as a function of f_w, $\langle\mathcal{H}\rangle_{\mathrm{mag}}$, and J_x:

$$\gamma\epsilon_{x0} = \frac{3.25\times 10^{-6}}{\tau_{y\,\mathrm{eff}}}\frac{\langle\mathcal{H}\rangle_{\mathrm{mag}} f_w}{J_x}\,. \tag{2.11}$$

Next we use Eq. (2.10), along with an equation for the relative energy spread in the ring:[9]

$$\sigma_\epsilon^2 = \frac{C_q\gamma^2}{J_\epsilon\rho_B} = 2.25\times 10^{-11}\frac{\gamma B(KG)}{J_\epsilon}\,, \tag{2.12}$$

to re-write the expression for $(Z/n)_t$ (Eq. (2.8))

$$(Z/n)_t \approx \mathcal{F}\frac{5.43\times 10^{11}}{N}\frac{\sigma_z}{\tau_{y\,\mathrm{eff}}}\frac{\alpha f_w}{J_\epsilon}\,. \tag{2.13}$$

Notice that the energy no longer appears in Eqs. (2.11) and (2.13). It is determined by the main bending field and the desired damping time, $\tau_{y\,\mathrm{eff}}$ (Eq. (2.10)).

In Eq. (2.13) we have ignored the constraints on the energy spread. A large energy spread reduces the lifetime and increases the longitudinal emittance. In practice we are limited to a relative energy spread of a couple tenths of a percent and thus there is a lower bound on α. Using $(Z/n)_t = 0.2\,\Omega$, this bound is:

$$\alpha \geq 1.19\times 10^{-18}\frac{N}{\mathcal{F}\gamma\sigma_\epsilon^2\sigma_z}\,. \tag{2.14}$$

Notice that the bound is inversely proportional to the energy, implying that a higher energy is desirable. In contrast, the energy does not appear in Eq. (2.13) where the energy spread is a free parameter. In most cases, we will find that we cannot increase the energy spread sufficiently to gain from the $1/\gamma$ dependance of Eq. (2.14).

If we assume that $\sigma_z \approx 4\,\mathrm{mm}$, we see that given an effective damping time, we only have six quantities: J_x, J_ϵ, f_w, B, $\langle\mathcal{H}\rangle_{\mathrm{mag}}$, and α, which can be varied to fit the requirements on the energy, the emittance, and the longitudinal impedance threshold. Unfortunately, the system is more tightly constrained since the six variable parameters are not independent.

The bending field, B_0, is determined by the energy and f_w. We are then left with fitting the emittance and the impedance threshold, one of which we would like small and the other large. The parameter f_w can be removed by considering the ratio $(Z/n)_t/\gamma\epsilon_{x0}$. To optimize this ratio, *i.e.* make it large, we can increase J_x at the expense of J_ϵ and/or increase the ratio $\alpha/\langle\mathcal{H}\rangle_{\mathrm{mag}}$. The easier option is that of changing the damping partition numbers. They can be changed by using combined function bending magnets or a Robinson wiggler.[13,14] Unfortunately, we do not wish to increase J_x much beyond 2. Thus, we also have to consider maximizing the ratio of $\alpha/\langle\mathcal{H}\rangle_{\mathrm{mag}}$.

For a given lattice design, we can write down some approximate scaling laws. In most lattices, assuming that the phase advance per cell is held constant, $\langle\mathcal{H}\rangle_{\mathrm{bend}} \propto \Theta^3\rho_{\mathrm{ave}} \propto \Theta^2 L_{cell}$ and $\alpha \propto \Theta^2$. Thus the ratio of $\alpha/\langle\mathcal{H}\rangle_{\mathrm{bend}}$ is inversely proportional to the length of the cell. Notice that unlike normal scaling laws for damping rings, the bend angle is not at our disposal for minimizing the emittance; it is determined by $(Z/n)_t$.

2.3. LATTICES

In choosing a lattice we want one that naturally has a large dynamic aperture and a large ratio of $\alpha/\langle\mathcal{H}\rangle_{\rm mag}$. The three lattices that seem best suited to our requirements are the FODO lattice, the triple bending achromat (TBA) lattice proposed by Vignola,[15] and the TME lattice described by Steenbergen.[16] Wiedemann has compared the double focusing achromat (DFA) and triplet achromat lattices with the FODO lattice.[17] He found that the FODO lattice had significantly better chromatic properties than the other two.

The TBA lattice has been studied by Bisognano[18] with application to a 750 MeV storage ring for FEL's and by Jackson[19] for a 1–2 GeV synchrotron light source. It has the advantage of probably being less expensive to construct than a FODO structure since fewer cells are needed to achieve the same emittance. In addition, the lattice, potentially, has a larger ratio of $\alpha/\langle\mathcal{H}\rangle_{\rm mag}$. Unfortunately, the lattices proposed to date have $\alpha/\langle\mathcal{H}\rangle_{\rm mag}$ ratios that are an order of magnitude too small.

The TME lattice would also be cheaper to build than a FODO lattice and it should be investigated further. In addition, another lattice worth examining would be an extreme version of the FODO lattice where combined function bends completely replace the defocusing quadrupoles. This would be the most compact and could offer the best ratio of $\alpha/\langle\mathcal{H}\rangle_{\rm mag}$. Unfortunately, it may not be feasible to achieve the necessary gradients in the bends.

For our initial design we chose to use a FODO lattice. This choice was based mostly upon the superior dynamic aperture characteristics of the lattice. Another advantage of the FODO lattice is that it allows for local chromatic correction, *i.e.* placing the correcting sextupoles next to the quadrupoles which generate the chromaticity. This results in looser tolerances on the vertical orbit; see the discussion in Sec. 5.

While we can create a simple FODO design on paper that would satisfy the requirements, the necessary magnetic fields make it technically unfeasible. The problems arise because extremely strong magnetic fields are needed in the quadrupoles to keep the cell length short. This leaves us the option of: (1) using combined function bends to minimize the cell length, (2) varying J_x and J_ϵ, and (3) possibly using wigglers to decrease the required main bending field and increase the energy spread. Before discussing the use of separate wigglers, we feel it is useful to quickly discuss the wiggler ring option.

2.4. WIGGLER RING

The wiggler ring design has excellent damping times at low energies. It achieves this, as wigglers do, by bending the particle a lot while generating very little dispersion. Since the damping times can be much shorter than a conventional ring, the wiggler ring can operate at lower energies and thus achieve the necessary low emittances. Unfortunately, the $(Z/n)_t$ of a wiggler lattice is lower than that of a comparable conventional ring. To understand this we have to compare $\langle\mathcal{H}\rangle_{\rm bend}$ and α in the two designs.

$\mathcal{H}$ can be written as the sum of two squares: $\mathcal{H} = \eta_x^2/\beta + (\eta_x\alpha + \eta_x'\beta)^2/\beta$. Since the second term depends upon η_x' which does not contribute to α, we would like to keep it small. The wiggler magnet bends in both the positive and negative x direction, and thus η_x and η_x' will oscillate. This will force the second term in $\langle\mathcal{H}\rangle_{\rm bend}$ to be larger. One could minimize the effects of the oscillations by making the wiggler period shorter, but one runs into technical limitations quickly. Another problem is that the length of the cells in the wiggler ring will be longer than in a normal ring. Using the scaling laws discussed at the end of Sec. 2.2, we can see that this increases $\langle\mathcal{H}\rangle_{\rm mag}$ without increasing α.

Before concluding this section, we note that many wiggler ring designs were presented at the 1987 ICFA workshop.[11] Unfortunately, these all had very long bunch lengths ($\sigma_z > 15\,$mm). The long bunch lengths are necessary to meet the impedance limitations and to reduce the effect of intrabeam scattering. However, if the $(Z/n)_t$ is not an issue or if the bunch length is allowed to be longer, the wiggler ring is an attractive option.

2.5. DAMPING WIGGLERS

As was mentioned in Sec. 2.2, it is very hard to build a conventional or wiggler ring which meets all of the design criteria. This leads us to consider the effects of including separate damping wigglers in regions of zero dispersion. By locating the wigglers in regions of zero dispersion, $\langle\mathcal{H}\rangle_{\rm mag}$ in the wigglers will be small, and thus one can significantly reduce both the damping times and the emittance. In addition, damping wigglers increase the energy spread in the ring. Thus, despite the slight decrease in α resulting from the increased length of the ring, damping wigglers can significantly improve the ratio of $(Z/n)_t/\gamma\epsilon_{x0}$.

The scaling formulas Eq. (2.10) thru (2.13) can be modified to include the effects of damping wigglers:

$$B_0(KG)\gamma^2(1+F_w) = \frac{1.44\times10^5}{\tau_{y\,\rm eff}} \tag{2.15}$$

$$\gamma\epsilon_{x0} = \frac{3.25\times10^{-6}}{\tau_{y\,\rm eff}J_x}\frac{\left(\langle\mathcal{H}\rangle_{\rm bend} + 6\overline{\beta_x}F_w\rho_0/5\pi k_w^2\rho_w^3\right)}{(1+F_w)^2} \tag{2.16}$$

$$(Z/n)_t \approx \mathcal{F}\frac{5.43\times10^{11}}{N\tau_{y\,\rm eff}}\frac{\sigma_z\alpha}{J_\epsilon}\frac{(1+8F_w\rho_0/3\pi\rho_w)}{(1+F_w)^2}\,, \tag{2.17}$$

where the parameter F_w is a measure of the effectiveness of the wigglers,

$$F_w \equiv L_w\rho_0/4\pi\rho_w^2\,. \tag{2.18}$$

Here, L_w and B_w are the length and peak field of the wiggler; $\overline{\beta_x}$ is the average beta function in the wiggler, and k_w

is the wiggler wave number, $k_w = 2\pi/\lambda_w$ where λ_w is the wiggler period. Also, ρ_0 and ρ_w are the bending radii of the main bends and the wiggler. Both bending radii are proportional to the energy over the respective magnetic fields. We have assumed sinusoidal wigglers, and thus the integral of $B_w^2(s)$ over the wiggler is equal to $1/2B_w^2$. In addition, we assume that $\overline{\beta_x} \gg \lambda_w/2\pi$ so that the $\eta_x'^2\beta_x$ term dominates in $\langle\mathcal{H}\rangle_{\rm wig}$. We do not consider decreasing $\overline{\beta_x}$ significantly since that would increase the chromaticity of the ring and might decrease the dynamic aperture.

Looking at Eqs. (2.15) thru (2.17), we can see that the largest effect occurs when $\rho_0 \gg \rho_w$ and F_w is large, *i.e.* when $B_0 \ll B_w$. Unfortunately, we are limited when increasing B_w since the η_x' created by the wigglers will blowup the emittance. This constrains the period of the wiggler and can be expressed

$$B_w^3\overline{\beta_x}\lambda_w^2\frac{F_w}{(1+F_w)} \ll 1.33\times10^9\gamma\epsilon_{x0}J_x\ . \qquad (2.19)$$

We consider two cases, relatively long Nd-Fe-B hybrid wigglers and short superconducting wigglers. In the Nd-Fe-B hybrid wigglers the maximum field can be specified as a function of the gap and the period[20]

$$B_w \le 3.44\exp\left[-\frac{g}{\lambda_w}\left(5.08-1.54\frac{g}{\lambda_w}\right)\right]\ , \qquad (2.20)$$

for $0.08 < g/\lambda_w < 0.7$. To achieve a field of $B_w = 22$ KG with a gap of 2 cm, λ_w must be at least 20 cm. This is much less than the limit imposed by Eq. (2.19); with $\overline{\beta_x} \approx 4$ m, Eq. (2.19) limits $\lambda_w \ll 35$ cm. In the superconducting case we use a 40 KG field and a 20 cm period. This is (arbitrarily) scaled from the 50 KG superconducting wiggler in the DCI ring at LURE[21] with a 65 mm gap and 26 cm period. Assuming that $\overline{\beta_x} \approx 1$ m since the wigglers are shorter, the 20 cm period is less than the limit specified by Eq. (2.19): $\lambda_w \ll 29$ cm.

If we assume that the condition Eq. (2.19) is met, we can use the simple scaling for $\langle\mathcal{H}\rangle_{\rm bend}$ and α, discussed earlier in Sec. 2.2, to express $\gamma\epsilon_{x0}$ and $(Z/n)_t$:

$$\begin{aligned}\gamma\epsilon_{x0} &\propto \frac{\Theta^2 L_{cell}}{J_x(1+F_w)^2}\\ (Z/n)_t &\propto \frac{\Theta^2}{J_\epsilon(1+F_w)^2}\frac{(1+8F_w\rho_0/3\pi\rho_w)}{1+L_{\rm wig}/L_{\rm ring}}\ ,\end{aligned} \qquad (2.21)$$

where $L_{\rm wig}$ is the length of the wigglers and the associated insertion regions and $L_{\rm ring}$ is the total length of the ring. We would like to keep the wiggler lengths short, and thus it is desirable to maximize the wiggler fields and minimize the bending field. While decreasing the main bending field increases the cell length, it still decreases the emittance without decreasing the impedance threshold. Unfortunately, decreasing the main bending field and the length of the wigglers forces us to higher energies.

Because the additional parameters make the analysis complex, a simple computer program was written that calculates $\gamma\epsilon_{x0}$ and $(Z/n)_t$. It uses Eqs. (2.15) thru (2.17) and the relations for $\langle\mathcal{H}\rangle_{\rm bend}$ and α in FODO cells[22] for the calculation. We chose phase advances per cell of $\nu_x = 0.3$ and $\nu_y = 0.1$; while these phase advances do not minimize the emittance, they are chosen to be regions where the chromaticity does not increase rapidly. The cell lengths are calculated by adding the length of two bending magnets to 0.8 m, length for the drifts and quadrupoles. We then calculate the ring length from the number of cells required plus three times the length of wigglers required, allowing space for dispersion suppression, quadrupole doublets, etc. in the insertion. We use the wiggler parameters: $B_w = 22$ KG, $\lambda_w = 20$ cm, $\overline{\beta_x} = 4$ m and $B_w = 40$ KG, $\lambda_w = 20$ cm, $\overline{\beta_x} = 1$ m, and solve for solutions with $\gamma\epsilon_{x0} = 2.0\times10^{-6}$ and $(Z/n)_t = 0.2\,\Omega$; the value of $\gamma\epsilon_{x0}$ was chosen to allow for the increase in emittance due to intrabeam scattering. Finally, since wigglers are expensive, we attempt to minimize the length included. Tables 2 and 3 list our solutions with the shortest wigglers for three energies.

Notice that the solutions for the superconducting case in Table 3 have a higher main bending field and smaller bending angles than those in Table 2. This occurs because the stronger wigglers cause a larger energy spread, lowering the momentum compaction required to meet the impedance threshold $(Z/n)_t = 0.2\,\Omega$. Thus one can decrease the bending angle per bend, increase the main bending field and decrease the length of the wigglers, see Eq. (2.21). Since we feel that the wigglers calculated are too expensive, and we do not wish to go much higher in energy, we need to also consider changing the damping partitions. This will further increase the energy spread and lower the emittance, allowing us to increase the main bending field and thereby decrease the length of the wigglers.

Table 2. Solutions for a FODO lattice with 22 KG wigglers: $\gamma\epsilon_{x0} = 2.0\times10^{-6}, (Z/n)_t = 0.2\,\Omega$.

Energy	# of cells	B_0	L_w	$L_{\rm ring}$
1.75 GeV	58	5.0 KG	39 m	210 m
2.0 GeV	70	4.5 KG	33 m	225 m
2.25 GeV	80	4.0 KG	28 m	250 m

Table 3. Solutions for a FODO lattice with 40 KG wigglers: $\gamma\epsilon_{x0} = 2.0\times10^{-6}, (Z/n)_t = 0.2\,\Omega$.

Energy	# of cells	B_0	L_w	$L_{\rm ring}$
1.75 GeV	90	8 KG	11 m	142 m
2.0 GeV	102	6.5 KG	9 m	170 m
2.25 GeV	112	6.0 KG	7.5 m	185 m

2.6. DAMPING PARTITIONS

The damping partitions describe the relative rates of the horizontal, vertical and longitudinal damping. Since the injected longitudinal emittance is usually much closer to the damped value than is the horizontal or vertical, it is reasonable to increase the horizontal and/or vertical partitions at the expense of the longitudinal. As was mentioned earlier the vertical partition is effectively fixed, but we can increase the horizontal damping partition and thereby lower the horizontal emittance. In addition, decreasing the longitudinal damping partition increases the energy spread, and thereby $(Z/n)_t$.

The damping partitions in a ring can be changed by using combined function bending magnets or Robinson wigglers.[13] The partitions can be written:[9]

$$J_x = 1 + \frac{\oint \eta_x/\rho(1/\rho^2 + 2K_1)ds}{\oint ds/\rho^2} \qquad J_\epsilon = 3 - J_x \ , \quad (2.22)$$

where K_1 is negative for a horizontally focusing quadrupole field.

In the case of a Robinson wiggler, Eq. (2.22) becomes

$$J_x = 1 + \frac{\overline{\eta_x} L_{\rm Rob} K_1}{2\pi(1+F_w)} \frac{\rho_0}{\rho_{\rm Rob}} \ , \quad (2.23)$$

where $L_{\rm Rob}$ and $\rho_{\rm Rob}$ are the length and bending radius of the Robinson wiggler. Thus we see that we would like to place it in a region of high dispersion. Unfortunately, this causes the emittance to increase. The emittance blowup is

$$\Delta\gamma\epsilon_x = \frac{3.25\times10^{-6}}{\tau_{y\,\rm eff}} \frac{1}{J_x(1+F_w)^2} \frac{L_{\rm Rob}}{4\pi^2} \frac{\overline{\eta_x}^2}{\overline{\beta_x}} \frac{\rho_0^2}{\rho_{\rm Rob}^3} \ . \quad (2.24)$$

To keep the emittance increase small, the wiggler should be built so both $\rho_{\rm Rob}$ and $|K_1|$ are large and it should be placed in a region where β_x is large also. For example with the parameters: $\eta_x = 20\,$cm, $\beta_x = 10$ m, $\rho_0 = 5$ m, and $K_1 = 17\,{\rm m}^{-2}$, a wiggler length of 4 m will increase J_x by 1.1 and increase the emittance by less than 5%. The problems with this are: (1) extra length is required for the wiggler insertion and (2) to achieve the strong quadrupole fields the wiggler would have to be built as large aperture quadrupoles with the beam passing off-center; technically this might present a problem.

The other option, that of using combined function bends, seems to be easier. In this case Eq. (2.22) is

$$J_x = 1 + \frac{\alpha K_1 \rho_0 L_{\rm ring}}{\pi(1+F_w)} \ . \quad (2.25)$$

Here the emittance is not increased by the combined function bends; in fact it should decrease slightly since the defocusing quadrupoles could be made smaller, increasing the filling factor. Furthermore, an additional insertion, which would decrease α, is not required.

Table 4. Solutions for a combined function FODO lattice with 22 KG wigglers. $\gamma\epsilon_{x0} = 2.0\times10^{-6}, (Z/n)_t = 0.2\,\Omega$.

Energy	# of cells	B_0	K_1	L_w	$L_{\rm ring}$
1.75 GeV	73	13.0 KG	$4.8\,{\rm m}^{-2}$	27 m	145 m
2.0 GeV	90	12.5 KG	$4.2\,{\rm m}^{-2}$	18 m	160 m
2.25 GeV	108	12.5 KG	$3.7\,{\rm m}^{-2}$	11 m	160 m

Table 5. Solutions for a combined function FODO lattice with 40 KG wigglers: $\gamma\epsilon_{x0} = 2.0\times10^{-6}, (Z/n)_t = 0.2\,\Omega$.

Energy	# of cells	B_0	K_1	L_w	$L_{\rm ring}$
1.75 GeV	96	15.0 KG	$3.4\,{\rm m}^{-2}$	7.25 m	113 m
2.0 GeV	112	14.5 KG	$3.3\,{\rm m}^{-2}$	4.75 m	125 m
2.25 GeV	120	14.0 KG	$3.2\,{\rm m}^{-2}$	2.75 m	140 m

Since this is the more promising route, we calculate $\gamma\epsilon_{x0}$ and $(Z/n)_t$ as we do in Tables 2 and 3, except we include the effect of a defocusing field on J_x. Obviously, it is desirable to have the largest defocusing field possible, consistent with limits on the energy spread. We calculate K_1 by choosing the larger of two expressions:

$$K_1 = \frac{14\,{\rm KG} - B_0}{B\rho\ 0.0125} \qquad K_1 = \frac{20\,{\rm KG} - B_0}{B\rho\ 0.025} \ . \quad (2.26)$$

The first expression estimates the field achievable in an off-center quadrupole, assuming 14 KG pole tip fields and a beam pipe radius of 1.25 cm. The radius of the quadrupole is then the beam pipe radius plus the offset. The second expression estimates the field in a bending magnet with modified poles. We assume 20 KG maximum field with poles that extend to twice the beam pipe radius of 1.25 cm.

The results for the conventional and superconducting wigglers are listed in Tables 4 and 5. Notice that when compared to Tables 2 and 3, the number of cells has increased and the main bending field has increased. Because the main bends are stronger, the required length of wiggler has decreased by roughly a factor of two. Obviously this is desirable. Unfortunately, increasing the number of cells and increasing the bend strength means that the bends becomes very short, 13 cm for the 1.75 GeV case in Table 5. It is difficult to achieve the necessary field quality in such short bends since the end fields become significant.

We use the results from Table 4 to pick a starting point for our ring. We start with the lowest energy, conventional wiggler, design. This was chosen for the reasons mentioned previously in Sec. 2.1; namely, low energy makes the subsequent bunch compression easier and the magnets are easier to build. In addition, although the low energy design requires more wigglers, it is smaller and therefore (hopefully) cheaper; we have not attempted to optimize costs in a rigorous manner.

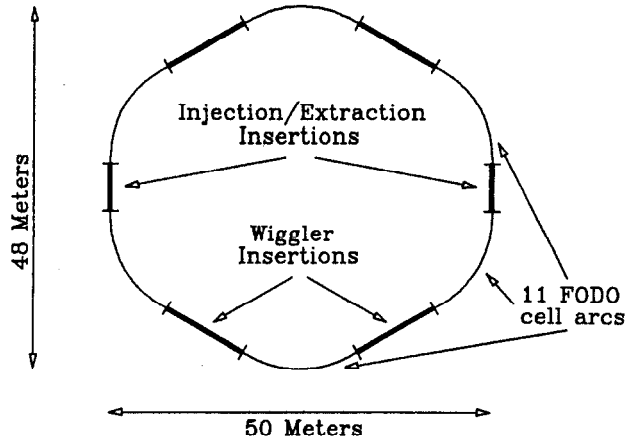

Fig. 1. Schematic of the TLC damping ring.

Table 6. TLC damping ring parameters.

Energy	$E_0 = 1.8$ GeV
Length	$L = 155.1$ m
Momentum compaction	$\alpha = 0.00120$
Tunes	$\nu_x = 24.37, \quad \nu_y = 11.27$
RF frequency	$f_{RF} = 1.4$ GHz
Current	10 batches of 10 bunches of $2 \times 10^{10} e^+/e^-$

3. BASIC LATTICE

A design for the TLC damping ring is illustrated in Fig. 1. The ring has a circumference of 155 m and operates at an energy of 1.8 GeV. There are six insertion regions, two for injection/extraction and four for wigglers. The arcs between each insertion region are composed of 11 combined function FODO cells. The ring has a superperiodicity of two. The parameters are listed in Tables 6 and 7. Table 6 lists general parameters while Table 7 lists parameters for the ring with the wigglers on and off. The optical functions β_x and β_y and the dispersion function η_x for half of the ring are plotted in Fig. 2.

The ring would operate with 10 batches of 10 bunches of 2×10^{10} electrons/positrons. The bunches in a batch are separated by 1 RF period, approximately 20 cm. Each batch is then separated by 50 ns, leaving 100 ns for the kicker pulse to rise and fall. When the wigglers are on, the normalized horizontal emittance, including the intrabeam scattering effects calculated by ZAP,[23] is 2.75×10^{-6}mrad. Because the ring operates at a relatively high energy, necessary to achieve the required damping rates, the intrabeam scattering contribution to the emittance is fairly small — about 27% of the ring emittance. The damping times are $\tau_x = 2.50$ ms and $\tau_y = 3.98$ ms. This allows each batch to remain in the ring for seven vertical damping times (vdt) when operating at a repetition rate of 360 Hz. Ignoring coupling of the horizontal and vertical planes, 7 vdt will damp a positron beam with an initial normalized emittance of 3×10^{-3} to an emittance of 2.7×10^{-9}mrad. The alignment tolerances required to achieve the 100:1 emittance ratio are discussed later in Sec. 5.

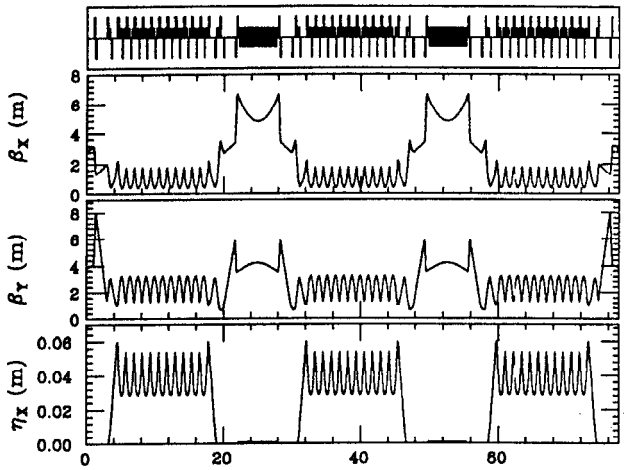

Fig. 2. Optical functions for half of the ring.

Table 7. TLC damping ring parameters.

	Wigglers Off	Wigglers On
Natural $\gamma\epsilon_x$	2.46 μmrad	2.00 μmrad
$\gamma\epsilon_x$ w/ intrabeam	3.33 μmrad	2.74 μmrad
Damping, τ_x	3.88 ms	2.50 ms
Damping, τ_y	9.19 ms	3.98 ms
Rep. rate, $f_{\rm rep}$	155 Hz	360 Hz
Damp. partition, J_x	2.37	1.59
Energy spread, σ_ϵ	0.00128	0.00104
Radiation/turn, U_0	203 KeV	468 KeV
Bunch length, σ_z	5.6 mm	5.2 mm
Synch. tune, ν_s	0.0068	0.0058
$(Z/n)_t$	$\mathcal{F} \times 0.32\,\Omega$	$\mathcal{F} \times 0.20\,\Omega$
Natural chrom., ξ_x	-28.35	-28.07
Natural chrom., ξ_y	-25.10	-22.27

We wish to operate the ring below or close to the turbulent bunch lengthening threshold. The threshold is $(Z/n)_t = \mathcal{F} \times .2\,\Omega$ where $\mathcal{F}$ is a form factor greater than one.[10] While this impedance is very low (by conventional standards) we plan to achieve such a value by using a constant size beam pipe throughout the ring. The planned

pipe has a 1 cm inner radius which is slightly smaller than the SLC damping rings and is approximately seven times the beam size of an injected positron beam.

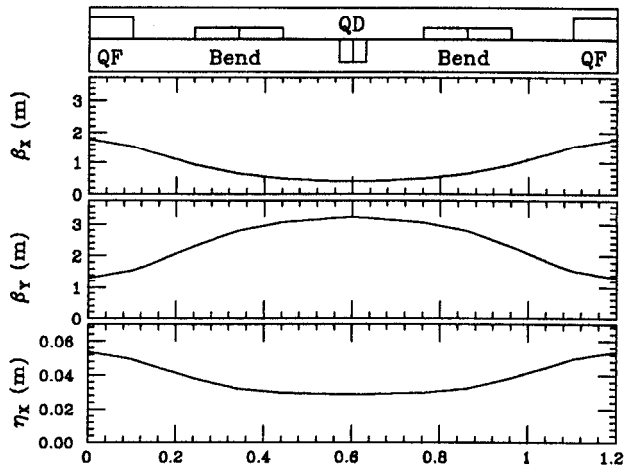

Fig. 3. Arc cell optics and magnets.

3.1. Arcs

The six arcs are constructed of 11 combined function FODO cells. The bends have an additional defocusing quadrupole gradient which re-partitions the damping. The optical functions and the magnet positions are plotted for a single cell in Fig. 3. The bend magnets bend an angle of 2.5° and have normalized defocusing gradients of $K_1 = 5.0\,\mathrm{m}^{-2}$, *i.e.* a gradient of 300 KG/meter. The QF's, the focusing quadrupoles, which are the strongest quadrupoles in the ring, have normalized gradients of $-15.7\,\mathrm{m}^{-2}$. Using a magnetic radius of $r = 1.2\,\mathrm{cm}$, 2 mm greater than the beam pipe, the QF's have pole tip fields of 11.3 KG.

This design has a little more space between magnets than the SLC damping rings do, but it is still tightly packed. There is 14 cm between the QF's and the bends and 13 cm between the bends and the QD's. Note that since the bends have large defocusing fields the QD's are very short. Since space is tight and very strong sextupoles will be needed to correct the chromaticity, we plan to use permanent magnet sextupoles similar to those successfully used in the SLC damping rings.[24]

3.2. Injection/Extraction Insertion

The injection/extraction insertion regions have a 2 m drift space for septum magnets. On either side of the insertion drift there are additional 1.6 m drift spaces. The horizontal phase advance from the middle of the insertion drift to the center of these side drifts is approximately $\pi/2$, thus making them useful for the placement of the kicker magnets needed for injection/extraction. The optical functions for half an insertion are plotted in Fig. 4.

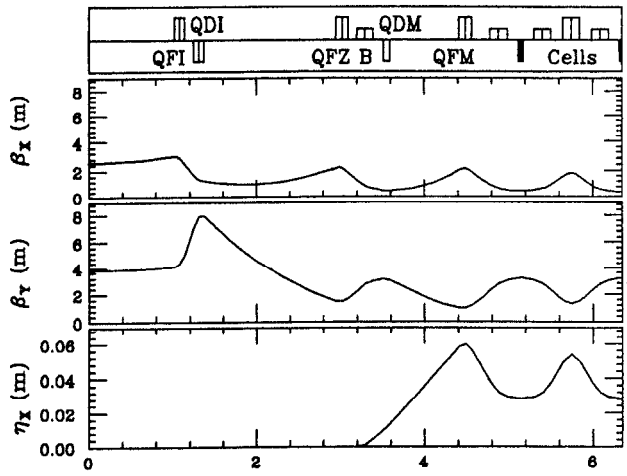

Fig. 4. Half of the injection/extraction insertion.

The dispersion is set to zero in all six of the insertion regions. This is done in the injection/extraction regions to make it easier to match the extraction transport line to the ring. Experience on the SLC has shown that properly matching the various components of the collider is crucial for obtaining small spots at the collision point. In addition, zero dispersion should make injection of the large positron beams easier.

3.3. Wiggler Insertions

The wiggler insertions are very similar to the injection/extraction insertions. Both insertions use the same dispersion suppression arrangement. The main drift in the wiggler insertion is 6 m rather than 2 m. There is also an additional quadrupole so that the wigglers can be continuously varied from full on to off while keeping the phase advance across the region constant. The lattice functions for 1/2 the insertion with the wigglers off are plotted in Fig. 5 and the same with the wigglers on is plotted in Fig. 6. Notice that the vertical focusing due to the wigglers allows β_y to have negative curvature across the insertion.

3.4. Wigglers

Wigglers are required to reduce the damping times by a factor of approximately 2.5. Thus, high peak fields are needed. Unfortunately, to prevent the wigglers from blowing up the emittance, short wiggler periods are also necessary. We chose a wiggler with a 24 KG peak field and a period of 20 cm. With this short period the wigglers actually lower the emittance. The wiggler contribution to the emittance is dominated by the η_x' generated by in the wigglers. Since β_x is approximately 4 m in the wiggler, the dispersion in the wiggler would have to be roughly 15 cm before its contribution to the emittance is comparable. We could have lowered β_x in the wiggler, but this would increase the chromaticity and likely decrease the dynamic aperture because stronger sextupoles would be needed for chromatic correction.

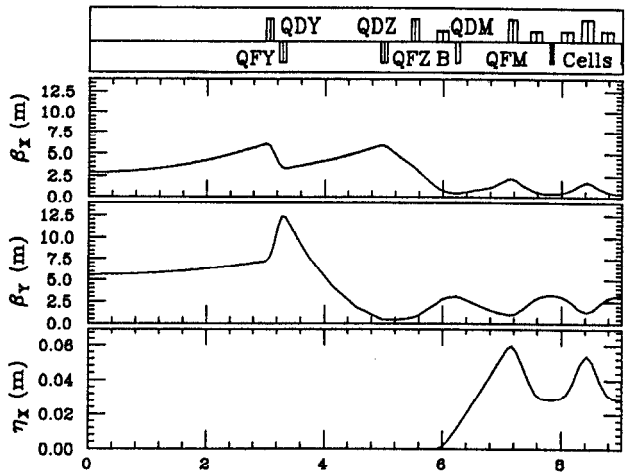

Fig. 5. Half of the wiggler insertion with wigglers off.

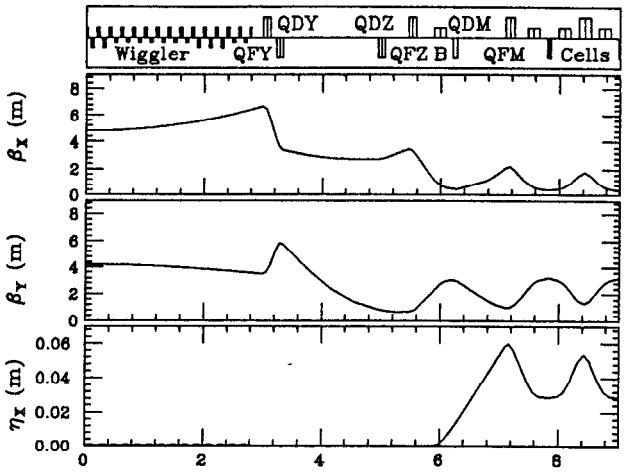

Fig. 6. Half of the wiggler insertion with wigglers on.

The period and the peak field were chosen to be within 15%[25] of the limits for Nd-Fe-B hybrid wigglers as specified in Ref. 20. If such a high peak field is not feasible, we can increase the energy of the design to 1.9 GeV and decrease the peak wiggler fields to 21 KG, the maximum field specified in this reference. The vertical damping time remains 3.98 ms and the natural horizontal normalized emittance increases to 2.29×10^{-6}mrad; intrabeam scattering further increases this to 2.85×10^{-6}mrad. The small increase in emittance occurs because the horizontal damping partition J_x increases as the wiggler gets weaker, see Eq. (2.25).

The wigglers are 5.6 m long, leaving 20 cm between the wiggler and the insertion quadrupoles. We modelled them in the lattice using hard-edged rectangular bends with the same peak field, 24 KG. The poles are 1/4 of a period long and the drifts separating the poles are also a 1/4 period long. Thus the model wigglers generate the same amount of synchrotron radiation as sinusoidal wigglers would, but the vertical focusing contribution is incorrect. With this model we should be over-estimating the vertical focusing and the four quadrupoles in the wiggler insertions should be able to easily compensate the weaker focusing.

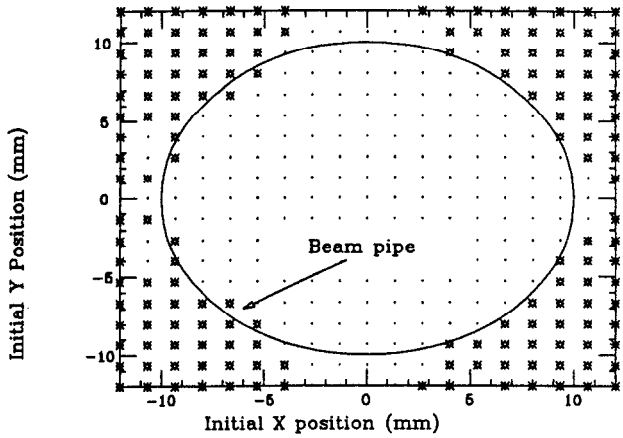

Fig. 7. Dynamic aperture for the chromatically corrected ring.

4. CHROMATIC CORRECTION

Before attempting to optimize the ring, we need to demonstrate that the chromatically corrected ring can have reasonable dynamic aperture. We currently correct the chromaticity with only two families of sextupoles located in the arcs. The integrated sextupole strengths are: $K_{2\,\mathrm{SF}} = -52.0\,\mathrm{m}^{-2}$ and $K_{2\,\mathrm{SD}} = 68.7\,\mathrm{m}^{-2}$.

The phase advance of the cells is adjusted to cancel most of the first order geometrics over an arc, 11 cells. The amplitudes of the first order geometric perturbations are proportional to:[26]

$$\int_{\mathrm{arc}} ds\beta_x^{3/2}K_2(e^{i3\psi_x} + e^{i\psi_x} + CC)$$
$$\int_{\mathrm{arc}} ds\beta_x^{1/2}\beta_y K_2(e^{i\psi_x+2\psi_y} + e^{i\psi_x} + e^{i\psi_x-2\psi_y} + CC) \tag{4.1}$$

where CC represents the complex conjugate. Since the cells are periodic, these integrals can be minimized by making the arc phase advances integral multiples of 2π. We chose cell phase advances of $\nu_{x\,c} = .270$ and $\nu_{y\,c} = .086$. Thus

$$\begin{aligned} 11\,\nu_{x\,c} &\approx 3 \qquad & 11(3\nu_{x\,c}) &\approx 9 \\ 11(\nu_{x\,c} + 2\nu_{y\,c}) &\approx 5 \qquad & 11(\nu_{x\,c} - 2\nu_{y\,c}) &\approx 1\ . \end{aligned} \tag{4.2}$$

While this choice of phase advance cancels the first order geometrics over an arc, it drives the octupole difference resonance, a second order geometric effect of sextupoles. Although we have not tried, we should be able to minimize the higher order geometric and higher order chromatic effects with additional sextupole families.

We have not attempted any optimization other than adjusting the cell phase advances as described above. The dynamic aperture is, for the most part, larger than the physical aperture. The results of tracking 1000 turns are plotted in Fig. 7. Note that the plot is distorted; the beam pipe is be round. The dynamic aperture will decrease when errors and realistic wiggler induced non-linear fields are included, but with more sophisticated chromatic correction schemes it should not present a problem.

5. TOLERANCES

5.1. ALIGNMENT

We need to calculate the effects of misalignments on both the dynamic aperture and the emittances. Errors in the machine decrease the dynamic aperture by causing tune shifts and higher order multipole fields on the closed orbit. In addition, errors will couple the horizontal and vertical planes and generate vertical dispersion, causing an increase in the vertical emittance. As mentioned in the previous section we have not yet attempted to optimize the chromatic correction scheme and the dynamic aperture; thus we only discuss the tolerances necessary to achieve the desired emittance ratio.

In an ideal uncoupled ring there is no vertical dispersion or linear coupling. Thus the synchrotron radiation opening angle, which is very small, determines the vertical emittance. In practice, this is not the case. First, vertical dipole errors and a non-zero vertical orbit in the quadrupole magnets will directly introduce some vertical dispersion. Second, a non-zero vertical orbit through the sextupole magnets, vertical sextupole misalignments, or rotational misalignments of the quadrupoles couple the horizontal and vertical planes. This coupling has two effects both of which increase the vertical emittance. It couples the horizontal dispersion to the vertical, causing an increase in the vertical, and it couples the x and y betatron motion so that energy is transferred between the two.

Assuming uncorrelated misalignments, the vertical emittance due to the dispersion generated by quadrupole rotations and sextupole misalignments is:

$$\begin{aligned}
\gamma\epsilon_y &\approx \frac{2C_q\gamma^3}{J_y}\frac{\langle\eta_y^2\rangle}{\beta_y}\frac{\oint ds/\rho(s)^3}{\oint ds/\rho(s)^2} \\
\frac{\langle\eta_y^2\rangle}{\beta_y} &\approx \frac{1}{2\sin^2\pi\nu_y}\sum_{\{\text{quads}\}}(K_1L)^2\beta_y\Theta^2 \\
\frac{\langle\eta_y^2\rangle}{\beta_y} &\approx \frac{1}{8\sin^2\pi\nu_y}\sum_{\{\text{sext}\}}(K_2L)^2\beta_y y_m^2 \ ,
\end{aligned} \tag{5.1}$$

where $C_q = 3.84 \times 10^{-13}$ m, Θ is the rotation angle, and y_m is the vertical sextupole misalignment. K_1L and K_2L are the integrated normalized quadrupole and sextupole strengths. Likewise, the increase in the vertical emittance due to linear coupling is:

$$\begin{aligned}
\epsilon_y &\approx \epsilon_x\overline{\alpha}\frac{1-\cos\Psi_x\cos\Psi_y}{(\cos\Psi_x-\cos\Psi_y)^2}\sum_{\{\text{quads}\}}(K_1L)^2\beta_x\beta_y\Theta^2 \\
\epsilon_y &\approx \epsilon_x\overline{\alpha}\frac{1-\cos\Psi_x\cos\Psi_y}{4(\cos\Psi_x-\cos\Psi_y)^2}\sum_{\{\text{sext}\}}(K_2L)^2\beta_x\beta_y y_m^2 \ ,
\end{aligned} \tag{5.2}$$

where $\Psi = 2\pi\nu$, and $\overline{\alpha} = (\alpha_x+\alpha_y)/\alpha_y$; $\alpha_{x,y}$ is the horizontal (vertical) damping rate. Note that both the formula for the dispersion and linear coupling have resonant denominators. The vertical dispersion grows as ν_y approaches an integer and the linear coupling contribution increases as ν_y approaches the linear sum or difference resonance. To minimize both these we chose the operating tunes $\nu_x = .37$ and $\nu_y = .27$.

It is harder to estimate the effects of the dipole errors since, in addition to generating vertical dispersion, dipole errors cause a vertical orbit which is correlated from point to point. We consider the limit of an orbit fully corrected with dipole correctors. We then approximate the orbit by assuming that it is correlated between correctors, but uncorrelated on either side of a corrector. In this case the vertical dispersion can be approximated as

$$\frac{\langle\eta_y^2\rangle}{\beta_y} \approx \frac{\langle y^2\rangle_{\text{res}}}{\beta_y}\left[1+\frac{1}{16\sin^2\pi\nu_y}\times \left(N_{\text{cell}}(4\pi\xi_{y\,\text{cell}})^2+N_{\text{ins}}(4\pi\xi_{y\,\text{ins}})^2\right)\right] \ , \tag{5.3}$$

where $\langle y^2\rangle_{\text{res}}/\beta_y$ is the residual orbit after correction and $\xi_y = -1/4\pi\int\beta_y(K_1+K_2\eta_x)ds$ is the local vertical chromaticity of one cell or insertion region. Also, N_{corr} is the number of correctors being used and N_{ins} is the number of insertion regions. Note that this formula illustrates the advantage of local chromatic correction. The vertical dispersion due to a vertical closed orbit is a quadratic function of the *local* vertical chromaticity between correctors. This is one advantage of the FODO and TME[16] lattices over the Chasman-Green type structures. In the FODO or TME lattices, sextupoles can surround each quadrupole, whereas, in the Chasman-Green lattice all of chromatic correction is done at the center of each cell structure where the dispersion is non-zero. In our current design we have not yet attempted to minimize the chromaticity locally by correcting the arcs and insertions separately; all chromatic correction is done in the arcs.

Using the same approximation, that the orbit is uncorrelated across the correctors, the emittance due to the linear coupling is:

$$\epsilon_y = \frac{\epsilon_x\overline{\alpha}}{64}\frac{\langle y^2\rangle_{\text{res}}}{\beta_y}\sum_{\Delta\nu,\Delta\phi}\frac{N_{\text{corr}}}{\sin^2\pi\Delta\nu\sin^2\pi\Delta\phi_{\text{cell}}}\times \left(\sum_{i,j\in\text{cell}}(K_2L)_i(K_2L)_j\beta_{y\,i}\beta_{y_j}\sqrt{\beta_{x\,i}\beta_{x\,j}}\cos\Delta\phi_{i,j}\right) \ , \tag{5.4}$$

where the first sum is over the two values of $\Delta\nu$, $\Delta\nu =$

$\nu_x \pm \nu_y$, and two values of $\Delta\phi$ for each value of $\Delta\nu$:

$$\Delta\phi_{i,j} = \begin{cases} \phi_{x\,i,j},\ \phi_{x\,i,j} + 2\phi_{y\,i,j}; & \Delta\nu = \nu_x + \nu_y \\ \phi_{x\,i,j},\ \phi_{x\,i,j} - 2\phi_{y\,i,j}; & \Delta\nu = \nu_x - \nu_y\ . \end{cases} \quad (5.5)$$

Here, $\phi_{i,j}$ is the phase advance between sextupole i and j in the cell and $\phi_{\rm cell}$ is the cell phase advance. Notice that the expression becomes large when the tunes are close to the linear coupling resonances and when the cell phase advances are close to the sextupole coupling resonances.

Summing all of these contributions, we have

$$\gamma\epsilon_y \approx \Theta^2 8.9\times10^{-8} + y_m^2 10.5\times10^{-6} + \frac{\langle y^2\rangle_{\rm res}}{\beta_y} 1.8\times10^{-6}\ , \quad (5.6)$$

where Θ is the quadrupole rotational misalignment in milliradians and y_m and $y_{\rm res}$ are the sextupole misalignment and residual orbit in millimeters. Thus the vertical emittance depends strongly upon y_m and the residual orbit. We can specify tolerances by dividing most of the contribution between y_m and the closed orbit:

$$\Theta \le 0.25\,\text{mrad}, \quad y_m \le 30\,\mu\text{m}, \quad y_{\rm res} \le 100\,\mu\text{m}\ , \quad (5.7)$$

where $\overline{\beta}_y$ was assumed to be 2 m. Notice that random sextupole misalignments y_m are far more damaging than the residual orbit. In addition, with a vertical corrector in each cell, the residual orbit is strongly dependant on the BPM tolerances and only weakly dependant upon the magnitude of the dipole errors. Thus the BPM's must be aligned to a tolerance of $100\,\mu$m *minus* the BPM measurement sensitivity.

These results were verified with a computer program which, like PETROS, calculates the fully coupled emittances given a distribution of errors in the ring. Using 10 distributions of errors, the program consistently corrects the orbit due to $200\,\mu$m quadrupole misalignments to less than the $100\,\mu$m orbit tolerance. Furthermore, the average value of $\gamma\epsilon_y$ is very close to the results of these analytic formulas. Unfortunately, the rms of $\gamma\epsilon_y$ is quite large, about 70% of the average value, implying that we would need to tighten the tolerances to have confidence in the final emittance ratio.

Fortunately, we can correct much of the coupling. Linear coupling can be corrected with four orthogonal skew quadrupoles. Of course to correct the linear coupling, one has to measure the amount of coupling, and then separate the linear coupling from the effects of vertical dispersion. One option would be to use a number of profile monitors around the ring. The effects of the vertical dispersion could be subtracted off using the fact that the dispersion should oscillate at a harmonic next to the tune. Alternatively, we should be able to find the amplitude and phase of the linear coupling by measuring the phase and amplitude of the $\nu_x \pm \nu_y$ tune lines relative to the ν_x and ν_y lines.[27] We hope to test this technique on the SLC in the future.

We can also correct the vertical dispersion. Skew quads in regions of horizontal dispersion act much like dipole correctors when correcting a closed orbit. Just as when correcting a closed orbit, the first few correctors, skew quads in this case, do most of the correction. Obviously to correct both the linear coupling and the dispersion, we have to perform the corrections in an orthogonal manner.

5.2. KICKERS

It is extremely important that the extraction kicker have very small jitter. Assuming linear optics, a one sigma jitter at the extraction septum becomes one sigma jitter at the IP. Actually, without BNS damping[28,29] the jitter would be magnified many times by transverse wakefields in the linac. But with weak BNS damping, the linear approximation is fairly accurate.

We would like to achieve a jitter tolerance of one tenth of the beam size $\sigma_{x,y}$ at the IP. This specifies a tolerance on the kicker. Assuming that the septum plate is 90° in phase downstream of the kicker,

$$\frac{\Delta\Theta}{\Theta} \le \frac{\sigma_{\rm jit}}{x_{\rm kick}} \quad \text{where} \quad \sigma_{\rm jit} \le \frac{1}{10}\sigma_x\ , \quad (5.8)$$

where $x_{\rm kick}$ is the transverse displacement of the kicked beam at the septum. It is a sum of the distance between the closed orbit and the septum plate plus the septum thickness and some extra space for the extracted beam.

This tolerance can be written in a more transparent form:

$$\frac{\Delta\Theta}{\Theta} \le \frac{1}{10}\frac{\sqrt{\gamma\epsilon_{\rm ext}\beta_{x\,\rm sept}}}{x_{\rm sept\ plate} + 1\,\text{mm} + N_s\sqrt{\gamma\epsilon_{\rm inj}\beta_{x\,\rm sept}}}\ , \quad (5.9)$$

where $\gamma\epsilon_{\rm ext}$ and $\gamma\epsilon_{\rm inj}$ are injected and extracted beam emittances. N_s is the distance between the closed orbit and the septum plate in units of the injected beam size. To prevent particle loses, the septum plate must be many sigma from the stored beam just after *injection* when the beam is the largest; we assumed $N_s = 7$. The only other quantity in the tolerance is the septum plate thickness. Because a pulsed septum will introduce more jitter problems, we need to use a DC septum. The septum plate in a DC septum with strong fields cannot be made much thinner than 3 mm.[30] Assuming $\overline{\gamma\epsilon}_{\rm inj} = 3\times10^{-3}$ mrad and $\beta_x \approx 3$ m, the jitter tolerance on the kicker is

$$\frac{\Delta\Theta}{\Theta} \le 3\times10^{-4}\ . \quad (5.10)$$

Notice that this tolerance is mainly determined by the ratio of the extracted beam emittance to the injected emittance. The only way to minimize the tolerance is to reduce N_s, increasing the particle loses due to scraping, or to reduce the injected emittance.

Such a tolerance will be difficult to achieve. One solution would be to use two kickers, separated by a phase advance of π, to cancel the jitter. One kicker would be placed before the septum and one located in the extraction line. Unfortunately, this approach requires that the two kickers track each other over the time needed to extract a batch, $\sim$ 7 ns. Since the tolerance for this bunch to bunch tracking is equal to the jitter tolerance, getting the two kickers to track maybe as difficult a problem as having a single kicker to achieve the jitter tolerance. An alternate approach would be to use a current source with feedback instead of a thyratron. Unfortunately, with current technology, it is not apparent that such a system could provide the necessary current.[8] To conclude, we have not yet found a viable solution to the kicker problem and it requires further research.

6. SUMMARY

In this paper we present a design for a damping ring for a TeV linear collider. The ring is based upon a FODO lattice where the bending magnets contain a gradient to re-partition the damping. In addition, damping wigglers are used to lower the operating energy and to increase the energy spread. If the length of wiggler required is too much, we have solutions at higher energies that need less.

We demonstrate, using a very simple chromatic correction scheme, that the chromatically corrected ring has reasonable dynamic aperture. We also calculate the tolerances on the alignment and the vertical orbit necessary to achieve a 100:1 emittance ratio and then discuss methods of correcting the coupling. Finally, we calculate tolerances on the extraction kickers and find that they are very tight. Unfortunately this tolerance depends mainly upon the ratio of the injected beam emittance to the extracted emittance and it is not easy to decrease.

Finally, we note that we have more work in optimizing the injection/extraction insertion regions to loosen the requirements on the extraction kickers. We need to improve the chromatic correction scheme and we should calculate the effect of errors on the dynamic aperture. We also should also take detailed looks at designs based upon the TME lattice and a version of a FODO lattice without separate defocusing quadrupoles.

ACKNOWLEDGEMENTS

We would like to thank Bill Gabella for help with the preliminary design, Phil Morton and Martin Lee for many useful suggestions, and Martin Donald for discussions on chromatic correction.

REFERENCES

1. See references in these proceedings.
2. K. Thompson and R. D. Ruth, "Multibunch instabilities in Subsystems of 0.5 and 1.0 TeV Linear Colliders", *in these proceedings* and SLAC–PUB–4800 (1988).
3. L. Z. Rivkin, "Damping Ring for the SLC", Ph.D. Thesis, California Inst. Tech. (1986).
4. L. Z. Rivkin, *et. al.*, "Bunch Lengthening in the SLC Damping Ring", SLAC–PUB–4645 (1988).
5. R.B. Palmer, "Exotic Damping Ring Lattices", SLAC–PUB–4329 (1987).
6. J.D. Bjorken and S.K. Mtingwa,"Intrabeam Scattering", *Particle Accelerators*, **13**, 115 (1983).
7. Using the formalism of Bjorken and Mtingwa, Pisin Chen estimated the effect of intrabeam scattering on the vertical emittance and found it negligible.
8. F. Bulos, private communication.
9. M. Sands, "The Physics of Electron Storage Rings", SLAC–121 (1970).
10. J. M. Wang and C. Pellegrini, *Proceedings of the 11th Int. Conf. on High Energy Acc.*, Geneva, Switzerland (1980), p. 554.
11. *Proceedings of the ICFA Workshop on Low Emittance e^--e^+ Beams*, BNL, March 20-25 1987.
12. S. Kheifets, "Bunch Compression for the TLC", *in these proceedings* and SLAC–PUB–4802 (1988).
13. K.W. Robinson, *Phys Rev.*, **111**, 373 (1958).
14. A. Hofmann, "Emittance Reduction in PEP with a Robinson Wiggler", SSRL–ADC–NOTE-40 (1986).
15. G. Vignola, "The Use of Gradient Magnets in Low Emittance Storage Rings", *Nucl. Instr. and Meth.*, **A246**, 12 (1986).
16. A. van Steenbergen, "Collider Damping Ring, Theoretical Minimum Emittance Structures", *Proceedings of the ICFA Workshop on Low Emittance e^--e^+ Beams*, BNL (1987), p. 60.
17. H. Wiedemann, "Design of Low Emittance Storage Rings", *Nucl. Instr. and Meth.*, **A246**, 4 (1986).
18. J. Bisognano *et. al.*, "Feasibility Study of a Storage Ring for a High-Power XUV Free-Electron Laser", *Particle Accelerators*, **18**, 223 (1986).
19. A. Jackson, "A Comparison of the Chasman-Green and Triple Bend Achromat Lattices", LBL–21279 (1986).
20. K. Halbach, *J. Appl. Phys.*, **57**, 3605 (1985).
21. C. Bazin, *et. al.*, "A Five-Pole Superconducting Wiggler for the DCI Positron Ring at LURE", *Nucl. Instr. and Meth.*, **A266**, 132 (1988).
22. H. Wiedemann, "Emittance in a FODO Lattice", PEP-303 (1979).
23. M. Zisman *et al.*,"ZAP User's Manual", LBL–21270 (1986).
24. J.E. Spencer, "Permanent Magnet Sextupole Protocol and Tolerances for the Damping Rings", SLAC–CN–309 (1985).
25. Klaus Halbach, private communication.
26. T. O. Raubenheimer and R. D. Ruth, "Superconvergent Tracking", *Particle Accelerators*, **23**, 197 (1988).
27. J. Bengtsson, "Non-Linear Transverse Dynamics for Storage Rings", CERN 88-05 (1988).
28. V. Balakin, A. Novokhatsky, V. Smirnov, *Proceedings of the 12th Int. Conf. on High Energy Accelerators*, Fermilab (1983), p. 119.
29. K. Bane, *IEEE Trans. Nucl. Sci.*, **NS-32**, 2389 (1985).
30. G. Fisher, private communication.

BUNCH COMPRESSION FOR THE TLC. PRELIMINARY DESIGN*

S. A. KHEIFETS, R. D. RUTH, J. J. MURRAY AND T. H. FIEGUTH

Stanford Linear Accelerator Center, Stanford University, Stanford, California 94309

ABSTRACT

A preliminary design of a TLC bunch compressor as a two-stage device is described. The main parameters of the compressor as well as results of some simulations are presented. They show that the ideal system (no imperfections) does the job of transmitting transverse emittances without distortions (at least up to the second-order terms) producing at the same time the desired bunch length of 50 μm.

1. INTRODUCTION

There are several reasons to choose a short TLC bunch length :

(a) short bunch length is required for controlling the adverse effects caused by the transverse wake field.

(b) the high luminosity of the linear collider is achieved by decreasing the value of the beta-function at the interaction point. Such a decrease is effective only when the value of the beta-function is greater than the effective bunch length.

(c) the cost of the RF power supplies, which is one of the largest cost ingredients of the linear collider, tends to decrease for higher frequencies of the accelerating field; to keep the particle energy spread tolerable for a small wave length one needs a small bunch length.

On the other hand, the adverse effects of the longitudinal wake fields, which become more pronounced when the bunch length decreases, limit the length of the bunch from below.

As a compromise, a bunch length of the order of 70 μm has been chosen for the present design of the TLC.[1] A bunch of this length is not readily obtainable from a damping ring and, hence, a compressor will be needed to transform a long bunch with small momentum spread $\Delta p/p$ into a short bunch with a larger momentum spread.

But there is a limit on how large the resultant momentum spread can be, which is determined by the momentum acceptance of the linac. For the bunch extracted from the TLC damping ring the momentum spread will be typically $\Delta p/p \approx 10^{-3}$ with a bunch length of $l \approx 5$mm. Compression of this bunch length to 50 μm would then require increasing the momentum spread to 10%. That is clearly unacceptable when chromatic aberrations and practical aperture limitations are considered. Therefore, a two-stage compressor with an intermediate acceleration is assumed in the present design. The relevant input parameters of the beam as well as the corresponding desired output parameters for each stage are collected in Table 1.

Table 1.
Compressor input and output parameters.

N	Parameter	1st Stage	2nd Stage
1	Energy (GeV)	1.8	16.2
2	$\Delta l_{\rm in}$ (mm)	5.0	0.46
3	$\Delta p/p_{\rm in}$ (%)	0.1	0.12
4	$\Delta l_{\rm out}$ (mm)	0.46	0.037
5	$\Delta p/p_{\rm out}$ (%)	1.1	1.6
6	$\gamma\epsilon_x$ (Mrad)	2.10^{-6}	2.10^{-6}
7	$\gamma\epsilon_y$ (Mrad)	2.10^{-8}	2.10^{-8}
8	$\sqrt{\epsilon_x\beta_x}$ (μm)	54.9	24.4
9	$\sqrt{\epsilon_y\beta_y}$ (μm)	3.11	1.20
10	$\sqrt{\epsilon_x/\beta_x}$ (μrad)	10.35	2.33
11	$\sqrt{\epsilon_y/\beta_y}$ (μrad)	1.83	0.475

* Work supported by the Department of Energy, contract DE–AC03–76SF00515.

2. THE CONCEPTUAL COMPRESSOR DESIGN

The design of each compressor stage is conceptually similar to the design of the SLC compressor.[2] A bunch extracted from the damping ring first passes through a matching section, where the beta- and eta-functions of the ring are matched to the corresponding periodic functions of the compressor.

The compressor itself consists of two stages. Each stage starts with an acceleration section where a momentum shift $\Delta p/p$ is introduced for each particle dependent upon its longitudinal position Δl within the bunch. The bunch then passes through a transport line where the path length depends upon particle momentum. The linear part of the path length dependance upon momentum is adjusted in such a way as to obtain a minimal bunch length on its exit. As in Ref. 3, the design of the transport line uses the concept of a second-order achromat[3] to prevent the emittance growth due to the second-order aberrations and chromatic effects. There is an intermediate accelerator between the stages 1 and 2 where particles are accelerated from 1.8 GeV to 16.2 GeV. The momentum spread with which the bunch enters the second stage is thus reduced to $\approx 0.1\%$.

The achromat in each stage is built out of four identical cells with 90° betatron phase advance in each plane. That makes the overall first-order transverse transfer matrix of the line equal to unity. Two families of the sextupole magnets compensate the natural first-order chromaticities eliminating at the same time all the second-order chromatic aberrations.[3,9] Cells are chosen to be symmetric, since that makes the phase ellipses of the line admittance on the entrance to the achromat upright and facilitates matching of the phase ellipses of the particle distribution and the amplitude functions.

Figures 1 and 2 present the horizontal and the vertical amplitude functions for each stage, respectively. Figures 3 and 4 give the horizontal dispersion functions and the bunch length along both achromats. Tables 2 and 3 contain the list of magnetic elements and the parameters of each of them in the TRANSPORT[5] notation. Two-dimensional TURTLE[6] scatter plots of a thousand randomly chosen particles in the $(\Delta l, \Delta p/p)$ plane at the exit of the each stage are presented in Figs. 5 and 6.

Table 4 contains the main parameters of both compressor stages.

3. EMITTANCE CHANGE DUE TO RADIATION AND NON-LINEAR EFFECTS

Of special concern is the emittance increase due to the quantum character of the radiation in a magnetic field. The design should provide that such a growth is small

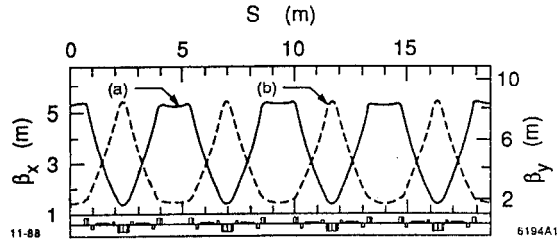

Fig. 1. Horizontal (a) and vertical (b) β-functions for the first compressor stage.

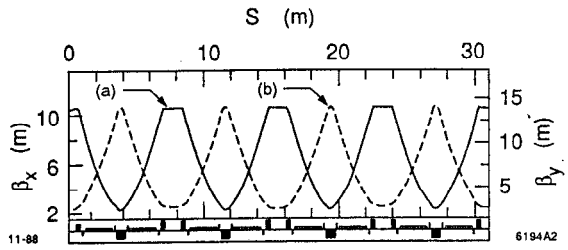

Fig. 2. Horizontal (a) and vertical (b) β-functions for the second compressor stage.

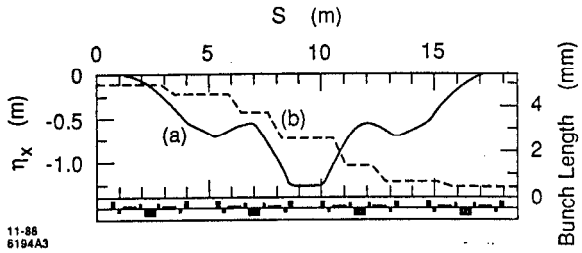

Fig. 3. Horizontal dispersion function (a) and the bunch length (b) along the first compressor stage.

compared to the transverse emittance of the bunch. The effect is evaluated by Sands.[7] The absolute and relative emittance increases due to this effect are to be found in Table 4.

The simulation results, in particular Figs. 5 and 6, show that the ideal designed system (without imperfections) does the job of transmitting transverse emittances without distortions (at least up to the second-order terms) producing at the same time the desired bunch length of 50 μm.

In the last row of Table 4 the main non-linear term of the accelerating field is evaluated and is seen not to

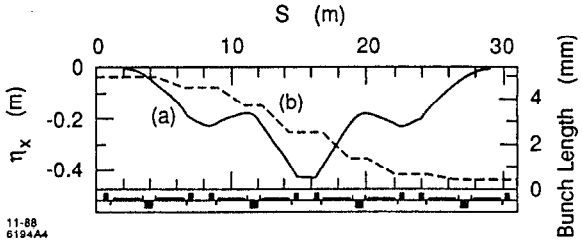

Fig. 4. Horizontal dispersion function (a) and the bunch length (b) along the second compressor stage.

Table 2. Lattice of Stage 1.

	9.	4.		;
Element	Label	Length (m)	Field (kG)	Pole Radius (mm)
3.0	"BGND"	0.61351;		
5.00	"Q1A"	0.19070	1.24505	10.0000;
3.0		0.12000;		
18.00	"SEXA"	0.10000	-0.03078	10.0000;
3.0		0.12000;		
4.000	"BH1"	0.60000	-12.58428	0.0;
3.0		0.12000;		
18.00	"SEXB"	0.10000	0.043344	10.0000;
3.0		0.12000;		
5.00	"Q1B"	0.25000	-0.89500	10.0000;
3.0	"SYM"	0.00000;		
5.00	"Q1B"	0.25000	-0.89500	10.0000;
3.0		0.12000;		
18.00	"SEXB"	0.10000	0.043344	10.0000;
3.0		0.12000;		
4.000	"BH1"	0.60000	-12.58428	0.0;
3.0		0.12000;		
18.00	"SEXA"	0.10000	-0.03078	10.0000;
3.0		0.12000;		
5.00	"Q1A"	0.19070	1.24505	10.0000;
3.0	"BGND"	0.61351;		
	9.	0.		;

Table 3. Lattice of Stage 2.

	9.	4.		;
Element	Label	Length (m)	Field (kG)	Pole Radius (mm)
3.0	"BGND"	0.60000;		
5.00	"Q1A"	0.30000	3.95726	10.0000;
3.0		0.12000;		
8.00	"SEXA"	0.10000	-0.36189	10.0000;
3.0		0.12000;		
4.000	"BH1"	2.00000	-6.41640	0.0 ;
3.0	"DRVA"	0.12000;		
18.00	"SEXB"	0.10000	0.58043	10.0000;
3.0		0.12000;		
5.00	"Q1B"	0.30000	-3.71447	10.0000;
3.0	"SYM"	0.00000;		
5.00	"Q1B"	0.30000	-3.71447	10.0000;
3.0		0.12000;		
18.00	"SEXB"	0.10000	0.58043	10.0000;
3.0	"DRVA"	0.12000;		
4.000	"BH1"	2.00000	-6.41640	0.0;
.0		0.12000;		
18.00	"SEXA"	0.10000	-0.36189	10.0000;
3.0		0.12000;		
5.00	"Q1A"	0.30000	3.95726	10.0000;
3.0	"BGND"	0.60000;		
	9.	0.		;

produce any significant changes in the momentum spread for both compressor stages. The same is true for the non-linearity due to second-order terms in the transformation matrix (T_{556} terms in TRANSPORT notation). Since the bunch length is about 10 times longer in the compressor RF section than in the linac, the wake fields are about 10 times stronger. However, since the section is short this would lead to only a small effect. In addition, since the correlation induced by the RF yields lower momentum of particles at the tail of the bunch, the bunch is stabilized by BNS damping[6] throughout part of the structure.

To conclude it is important to note that these two designs are simply examples and are not unique, e.g., the final compressor might be included in a 180° bend in order to keep the site shorter. Several examples of 180° arcs

Table 4. Main compressor parameters.

N	Parameter	1st Stage	2nd Stage
1	Length (m)	18.67	31.04
2	Bend Angle/magnet (°)	7.205	1.361
3	Number of Magnets	8	8
4	Radius of curvature (m)	4.771	84.218
5	Total Angle Bend (°)	57.64	10.89
6	Correlation $(\Delta p/p)/l$ (%/mm)	0.21517	3.4012
7	RF (GHz)	3.0	17.0
8	λ (cm)	10.0	1.76
9	$\theta = 2\pi l/\lambda$	0.314	0.164
10	V_o (MV)	57.3	1058.5
11	$\{H/\rho\}$	$2.5 \cdot 10^{-2}$	$1.6 \cdot 10^{-5}$
12	$\Delta\epsilon$(Mrad)	$2.03 \cdot 10^{-12}$	$4.45 \cdot 10^{-12}$
13	$\Delta\epsilon/\epsilon$ (%)	0.36	7.8
14	$\Delta(\Delta p/p) = \theta^2/6$	0.016	0.0045

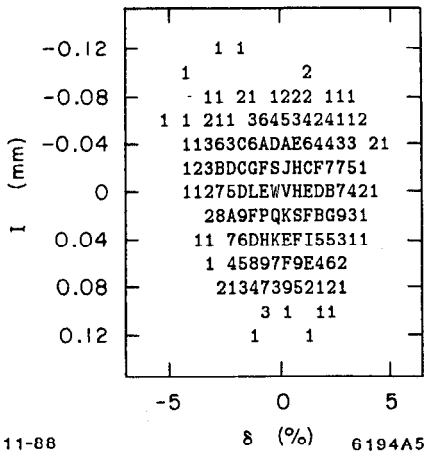

Fig. 5. Scatter plot in the horizontal phase space $(\Delta\ell, \Delta p/p)$ of 1,000 rays at the exit of the first compressor stage. Rms half widths are $(\Delta p/p)_{rms} =$ 1.088%, $(\Delta\ell)_{rms} = 0.487$ mm.

which accomplish this have been calculated with favorable results.[9]

ACKNOWLEDGEMENT

The design of the second stage has been fulfilled during the Workshop. We are grateful to the Workshop organizers for a stimulating working environment.

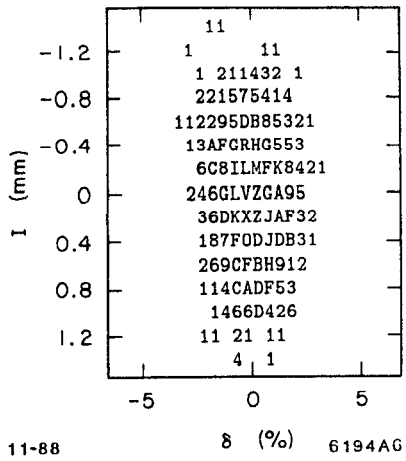

Fig. 6. Scatter plot in the longitudinal phase space $(\Delta\ell, \Delta p/p)$ of 1,000 rays at the exit of the second compressor stage. Rms half widths are $(\Delta p/p)_{rms} =$ 1.591%, $(\Delta\ell)_{rms} = 0.037$ mm.

REFERENCES

1. Palmer, R., SLAC-PUB-4707 (1988) and in these proceedings (1988).
2. Fieguth, T. H. and Murray, J. J., *Proceedings of the 12th International Conference on High Energy Acceleration,* Fermilab, Batavia IL, **401** (1983).
3. Brown, K. L., SLAC-PUB-2257, (February 1979); IEEE Trans. Nucl. Sci. NS-26 (3) p. 3490 (1979).
4. Kheifets, S. A., Fieguth, T. H. and Ruth, R. D., SLAC-PUB-4569, (March 1988).
5. Brown, K. L. et al., CERN Report CERN 80-04, Geneva (1980).
6. Carrey, D. G. et al., SLAC Report-246, UC-28, (March 1982).
7. Sands, M., SLAC Report-121, UC-28, (1970); SLAC Report SLAC/AP-47 (December 1985).
8. Balakin, V., Novokhatskii, A. and Smirnov, V., *Proceedings of the 12th International Conference on High Energy Accelerators*, Fermilab (1983).
9. Kheifets, S. A., Ruth, R. D. , Murray, J. J. and Fieguth, T. H., in preparation.

RF BREAKDOWN AND FIELD EMISSION

G. A. LOEW AND J. W. WANG

*Stanford Linear Accelerator Center**
Stanford University, Stanford, California 94309

One of the crucial parameters in the design of TeV $e^{\pm}$ linear colliders is the maximum electric field gradient that can be attained and used safely in the accelerating structure. In the absence of definitive knowledge on the availability and cost of RF power sources, the optimum machine length for a given energy cannot be determined at this time. However, the designs considered in this report could require gradients as high as 200 MV/m at RF frequencies of 11.424 GHz or 17.136 GHz, corresponding to peak powers of up to 1 GW/m. On the basis of research done at SLAC and at Varian, it now appears that such gradients are reachable, at least in short standing-wave (SW) structures.[1] Considerably more work, however, is needed to determine if the required gradients are achievable in long and complicated structures, and to verify that the accompanying field emitted currents which can absorb power, cause parasitic wakefields and spurious x-rays along the accelerator, are tolerable.

All experiments reported in Ref. 1, except for one X-band test started in collaboration with LLNL but not yet completed, were performed on SW structures. The equivalent traveling-wave accelerating fields were then calculated using the SUPERFISH computer program. S-band experiments were done on a seven-cavity disk-loaded ($2\pi/3$-mode) structure and on a two-cavity nose-cone-shaped (π-mode) structure, powered by a klystron operated up to 47 MW. C-band and X-band tests, done in collaboration with Varian, used nose-cone-shaped half-cavity structures powered by ~1 MW magnetrons. The overall results are shown in Table 1. For the pulse lengths used in the measurements (~1.5-4 μs), the breakdown-limited copper surface electric fields scale roughly as

$$E_s \sim 195[f(\mathrm{GHz})]^{1/2} \quad ,$$

(about seven times the levels predicted by the Kilpatrick limit). If this empirical relationship is valid at higher frequencies, then breakdown-limited surface fields of 660 and 807 MV/m could be reached at 11.424 GHz and 17.136 GHz respectively (corresponding to 264 and 323 MV/m accelerating fields, assuming $E_s/\bar{E}_{acc} = 2.5$). This extrapolation assumes no improvements due to the much shorter pulse lengths required at these higher frequencies (~20 to 100 ns), and conversely no worsening due to the probable need for more complex damped structures (see next section) with slots in the disks.

The structures used in the above measurements were equipped with RF couplers, temperature sensors to measure disk temperature, internal probes to measure field emission (FE), glass and copper windows, external magnets, a spectrometer and Faraday cup to measure the intensity and energy of extracted currents, an x-ray pinhole camera, radiation monitors, a TV camera with video recorder to look at breakdown sparks, pumps and a residual gas analyzer (RGA). Intensive studies were carried out of both pre-breakdown and breakdown phenomena, during and after RF processing. Upon completion of RF processing, Fowler-Nordheim plots of FE currents versus $1/E_s$ yielded β-field enhancement factors of ~60 at 2.856 GHz and 38 at 4.998 GHz. (For more details, see below.) RF-focused beams with peak currents as high as 25 mA and energies up to 13 MeV were extracted from the seven-cavity structure, and energy spectra in agreement with theoretical calculations were analyzed.

The pre-breakdown currents produced intense x-ray fields around the seven-cavity structure, in excess of 0.75 Mrad/h. When breakdown took place at a given RF power input, the resulting reflected RF pulse was invariably accompanied by a momentary current jump by a factor of 20 to 40 (as measured by internal transverse probes), the appearance of a spark, generally on the edge

* Work supported by the Department of Energy, contract DE-AC03-76SF00515.

Table 1. Experimentally obtained breakdown-limited gradients.

	S-band		C-band	X-band	
	Disk-loaded ($2\pi/3$-mode)	With nose cone (π-mode)	Half-cavity	Half-cavity	Disk-loaded ($2\pi/3$-mode)
Frequency, f (MHz)	2856	2858	4998	9303	11424
Total length (cm)	24.5	10.5	1.507	0.806	26.25
Filling time* (μs)	0.77	1.0	0.172	0.082	0.028
Pulse length (μs)	1.5-2.5	1.5-2.5	3.5	3.8	0.025†
Peak power input (MW)	47	10.8	0.8	1.2	200†
Peak surface field, E_s (MV/m)	313	- 340	445	572	303†
Corresponding traveling-wave accelerating field‡	161	175	229	295	133†

* For critical coupling in the case of standing-wave structures.

† Preliminary results, limited by available RF power and not by breakdown.

‡ Assuming SLAC structure, working in the traveling-wave mode, in which $E_s/\overline{E}_{acc} = 1.94$, except for X-band disk-loaded TW structure which was built with $E_s/\overline{E}_{acc} = 2.28$.

of the disk, and a marked increase in CH_4, CO and CO_2 gas at the RGA. As the gas burst was pumped away and RF processing was continued, the FE current gradually subsided to its pre-breakdown level and could eventually be decreased to a lower level for a given RF power input. Further RF breakdown events could then be triggered by increasing the RF power until the quasi-asymptotic levels shown in Table 1 were reached.

All SW structures listed in Table 1 were RF-processed for periods of 3 to 20 hours. Afterwards, they all showed considerable damage in the form of numerous pits and craters, mostly around the high-field points on the disk edges and/or nose cones. It is interesting to note, however, that this damage did not prevent the structures from continuing to operate at the highest electric field levels.

Our conjecture of what happens during RF processing can be understood by considering the expression for the Fowler-Nordheim average FE current density in an RF cavity:

$$\vec{j}_{FE} = \frac{K}{\phi^{1.75}} (\beta E_s)^{2.5} \exp\left(-\frac{6.53 \times 10^9 \times \phi^{1.5}}{\beta E_s}\right)$$

where ϕ is the metal work function in eV and β, the surface field enhancement factor, is a composite equal to $\beta_1\beta_2$: here β_1 is due to surface microprotrusions and β_2 is due to dielectric surface impurities. When RF processing starts, β_1 is relatively low (~2) except perhaps for a few whiskers which burn up early in the process, and β_2 is relatively high (~60-120) because of the thickness of the dielectric layer. As RF processing proceeds, the dielectric surface impurities are gradually desorbed and β_2 decreases; however, as a breakdown "event" takes place through explosive electron emission[1] (EEE), a crater is formed and β_1 grows. When RF processing reaches the asymptotic state (in our case, $\beta_1\beta_2$ ~60 at S-band), β_2 may be reduced to ~10 but β_1 is raised to ~6 because of the craters. The idea that comes to mind is that it may be possible to prevent β_1 from growing by processing the structure more gently, possibly with argon. There is evidence already that this procedure can at least reduce the "clean-up" time. If, in addition, it could reduce the number of craters, then the ultimate β_1 could perhaps be reduced by a factor of two. By operating at gradients at least 10 to 20% below breakdown, the so-called "dark current" due to captured FE current could be reduced considerably. Furthermore, to get the "dark current" per unit length, the above expression for the current density must be multiplied by the area available for FE per disk (which varies as f^{-2}) and the number of disks (which varies as f), yielding a net scaling as f^{-1}, thus favoring the higher frequencies. It is hoped that the experiments at X-band with a traveling-wave section will soon be performed, thus confirming some of these conjectures and predictions.

References

1) Loew, G. A., and Wang, J. W., "RF Breakdown Studies in Room Temperature Electron Linac Structures," SLAC-PUB-4647, May 1988 .

DAMPED ACCELERATOR CAVITIES*)

R. B. Palmer

Stanford Linear Accelerator Center, Stanford University, Stanford, California 94309
and
Brookhaven National Laboratory, Upton, New York 11973

ABSTRACT

Structures with slots to strongly damp higher-order longitudinal and transverse modes should allow the use of multiple bunches in linear colliders, and thus attain luminosities of over 10^{34} cm^{-2} sec^{-1}. Preliminary measurements on model structures suggest that such damping can be achieved.

1. INTRODUCTION

The luminosity of a linear collider[1] is severely limited by the total beam power and thus, since wall power is limited, by the efficiency with which RF power is transferred to the beam. There are, of course, many other applications that would benefit from high efficiency, so this is also a general problem.

The primary bound on the loading (and thus on the efficiency) comes from the fields—known as wakefields[2]—generated by the bunches, themselves, in the structure. Acting back on the bunches, these fields cause unacceptable distortion, momentum spread or deflection. Those that cause momentum variations are referred to as longitudinal wakes and generate momentum variations. Those that cause deflections are referred to as transverse wakes. In this case, they are only generated if the bunch is itself off-center, but cause subsequent bunches to be deflected further off-center, thus leading to the possibility of an instability, known as beam breakup. If the beam is displaced, quadrupole and higher wakes will also be excited, but these will have little effect unless the displacement is large and the bunch broad.

In a linac loaded with many bunches, each bunch sees fields generated by itself and by a sum of all previous bunches. The effects from the bunch itself, at least for short bunches, are dominated by the iris hole diameter. Besides using the largest possible iris, there is nothing much one can do about the fields themselves, although BNS damping[3] can be used to reduce their effects. The maximum fraction of RF energy extracted by one bunch is then bounded to a few percent, the exact amount depending on detailed assumptions. If more efficiency is required, it is imperative to use multiple bunches.

*)Work supported by the Department of Energy, contracts DE-AC03-76SF00515 (SLAC) and DE-AC02-76C0016 (BNL).

When there are many bunches, the fields seen by a particular bunch are a sum of those from all previous bunches. These wakefields have many different frequencies that are not in general multiples of the bunch spacing and will not add coherently. Thus, for a large number of very small bunches, the contributions of the wakefields are relatively less and higher efficiencies can be obtained.

For colliders, unfortunately, we need both relatively high individual bunch loading plus multiple bunches for high efficiency, and—in this case—both momentum spread and beam breakup become unacceptable unless something is done. In this paper, we study the possibility of damping the wakefields generated by each bunch before later bunches are introduced. Clearly, this damping must be very rapid; i.e., very low Q's are required for all unwanted wakefields.

2. RF MODES

For these studies, I have considered a traveling wave structure similar to that in the SLAC accelerator, except that I have chosen a relatively larger iris to wavelength ratio (.2 instead of .1) and—as a result—a larger group velocity (.07 c instead of .007 c). This choice was made[4,5] to reduce the single bunch wakefields. A multicell model of this structure was constructed at one-half SLAC scale. Figure 1 shows this structure. Figure 2 shows the measured mode frequencies as a function of phase advance.

2.1 Wakefield Requirements

Current parameter lists of TeV linear colliders are limited to luminosities of the order of 10^{33}cm^{-2} sec^{-1} for a wall power consumption of the order of 100 MW. Such designs employ only single bunches and use only from one[4] to a few[6] percent of the stored RF energy in the cavity. If multiple bunches can be employed, then as much as 25% of the energy can be extracted.[7] However, it has been shown[8] that with normal cavities and the required loading, beam breakup is unacceptable with more than one or two bunches. In addition, higher modes of longitudinal wakes will cause unacceptable momentum variations.[9]

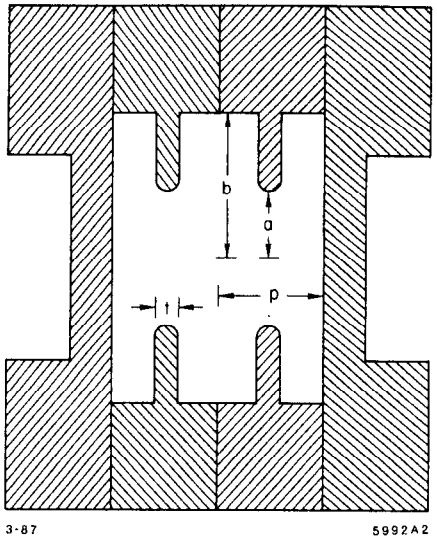

Fig. 1. Cross section of high group velocity accelerating structure.

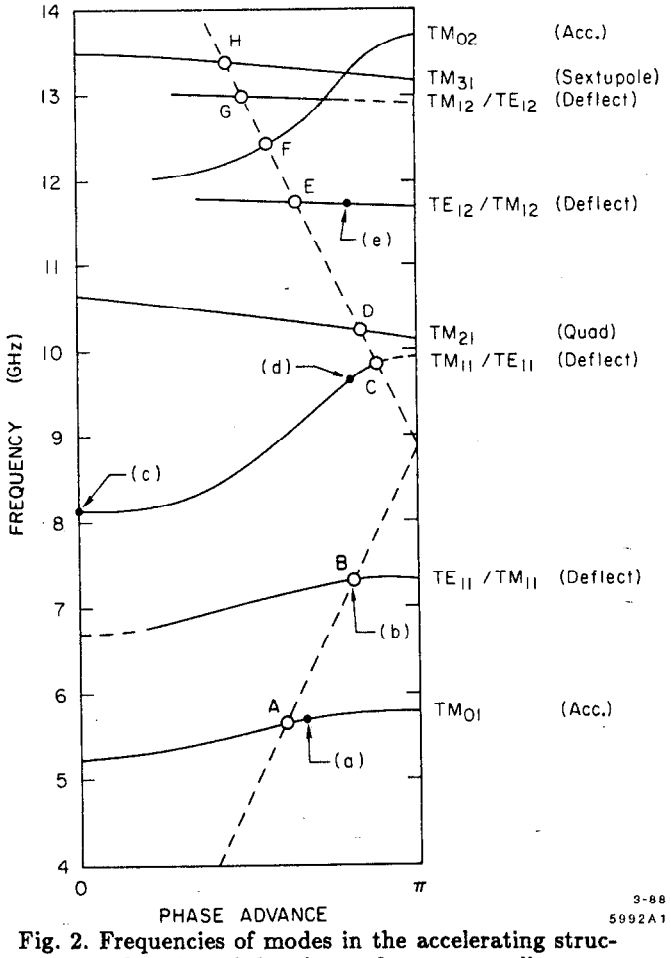

Fig. 2. Frequencies of modes in the accelerating structure as a function of the phase advance per cell.

If, however, the transverse modes can be strongly damped, then the beam breakup will be controlled. If the higher longitudinal modes can also be damped, then the momentum variations will also be controlled. It should then be possible to extract of the order of 25% of the energy and obtain working luminosities of over 10^{34} cm^{-2} sec^{-1} with the order of 200 MW.

In principle, all transverse modes and longitudinal modes other than the first—i.e., all higher modes—should be damped to a negligible value between bunches. This requirement can be eased if we arrange that the bunch spacing is equal to an integer times a half wavelength of the most serious modes. If the bunch spacing is n cycles of the fundamental, f_0 is the frequency of the fundamental and f_i is that of the mode; then this requires that $f_i/f_0 = n/m$, where m and n are integers. With the cavity being considered, $f_i/f_0 \approx 1.3$ so, with some slight adjustment of dimensions, $f_i/f_0 = n/m$ will be satisfied for the first deflecting mode (with $n = 4$ and $m = 3$); i.e., with one bunch every three cycles.

A study of the transverse wake problem[10] has shown that even with this condition, the wakefields for many bunches are still unacceptable. However, the study has shown that if the modes are damped, the effects can be controlled, provided condition two is satisfied with some reasonable tolerance.

The longitudinal wake problem is less severe than that in the transverse direction, because no instability is involved. The wakes from each bunch simply add up and, since they have random phases, they add incoherently. Nevertheless, with the parameters being considered, they add to give an unacceptable momentum spread between bunches. A study of the problem[9] shows that the problem is controlled if all higher modes are damped with Q's less than about 80, and this will be taken as a requirement in this study.

3. STRUCTURES WITH HIGHER MODE DAMPING

Higher modes could, in principle, be damped by the introduction of resistive materials into the structure, but it would be hard in this way to damp one and not another mode. Instead, we have studied damping by coupling the unwanted modes into a waveguide and damping the fields externally. Such coupling is accomplished by cutting into the basic cavity with slots leading to waveguides that can be chosen to have a cutoff higher than the fundamental. Thus, such slots will not damp this accelerating mode, but will allow all unwanted higher modes to propagate out of the structure.

In placing the cuts to couple fields to a mode in the waveguide, we can place the slot so as to interrupt currents that would normally be flowing in the cavity wall, thereby inducing such currents to enter the waveguide and induce a traveling wave in the guide. Figure 3(a) shows these currents for the fundamental accelerating mode, and Fig. 3(b) for the first transverse mode. The dotted lines indicate two possible cuts that would interrupt the transverse mode currents. The circumferential cut is seen also to interrupt the currents of the accelerating mode, but the "radial cut" does not interrupt such currents, and would therefore not damp the accelerating mode. Because of their relative simplicity, we first considered circumferential cuts, but these were unable to provide sufficient damping without adversely affecting the accelerating mode, so then—because of their lack of effort on the acceleration—we considered radial cuts.

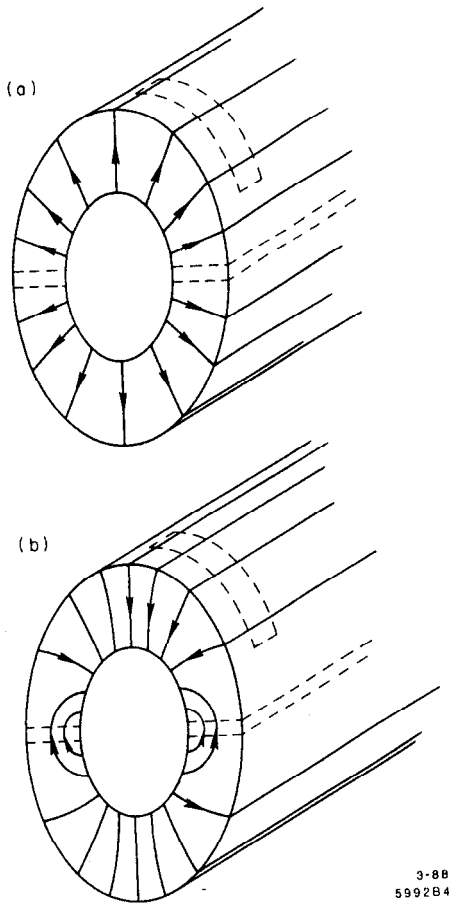

Fig. 3. Sketch showing approximate directions of current flow in the iris and wall of a structure: a) for the first accelerating mode and b) for the first transverse mode.

In all cases, the measurements were made on a single aluminum cell and only π modes were examined. Future studies will be reported using multiple cavities. Also in all cases, the fields in the waveguides were damped by inserting a cone of resistive plastic foam into the exits of the waveguides. When this was not done, the Q's of damped modes were, in general, a factor of two higher. This was because of the approximately 50% reflection of power at an open-ended waveguide.

3.1 Longitudinal Slot

Since the circumferential slots described above were unable to obtain sufficient damping of the transverse mode, we also tried a longitudinal slot. Initially, a slot was tried without a cut through the iris but, as Fig. 3 suggests, this was not effective for the first transverse mode (although it did damp some of the higher modes).

The longitudinal slot with cut iris is shown in Fig. 4. The length of the slot was chosen to have a cutoff about 7% above the accelerating mode and was 15% below the first transverse mode. Its length was then 2.4 cm and thus longer than the individual cell length (of 1.75 cm).

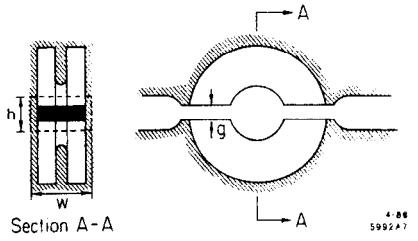

Fig. 4. Diagram of test cell with slot cut longitudinally in the cell wall and extending through the iris.

There is nothing obviously wrong with this, but it does mean that multiple cells cannot all have such slots at the same azimuthal angle (see the next section).

The width of the waveguide was 1 cm, but just prior to its entry to the cavity, this was reduced to a slot of only .5 cm—this being done to minimize the effect on the accelerating mode. The cut in the iris was only .27 cm. The object here was again to minimize the effect on the accelerating mode and, in particular, to minimize the increase in peak electric fields where the iris was cut.

We initially observed:

- (a) a negligible effect on the accelerating mode, in frequency or Q;
- (b) a negligible effect on the first higher longitudinal mode;
- (c) the apparent disappearance of the first transverse mode.

A study was then undertaken to observe the first transverse mode as the gap width was gradually varied from closed to its full width of 2.7 mm. This revealed that as the gap was opened, the transverse mode both widens and moves, and that its direction of motion is towards the undamped zero phase advance transverse mode at 8.1 GHz. Estimations of the final Q were then made both by observing the width and by tracking the amplitude of the resonance—extrapolating, in the case of the width observation, to the fully open case. Unfortunately, a fully consistent picture did not emerge. Both methods were complicated by the presence of the 8.1 GHz signal. We could only conclude that the Q of the mode was in the range between 10 and 20, with the width suggesting the higher value and the amplitude the lower. In either case, the requirement of a Q less than or equal to 20 seems to have been achieved. Further measurements by other methods are needed.

3.2 Combined Slot for Transverse/Longitudinal Modes

A basically longitudinal slot was tried whose length and cut iris was as described in Sec. 3.2, but the width of the slot was opened up to 1.4 cm (see Fig. 5). This width was chosen to have a cutoff in the lateral direction of 10.7 GHz, which is below the first longitudinal mode to be damped.

As expected, the first transverse mode was again damped to a Q of between 10 and 20. The first longitudinal mode was observed to have a Q of 80. Note that in a linac, one will wish to damp both horizontal and vertical transverse modes, and that there will thus have to be

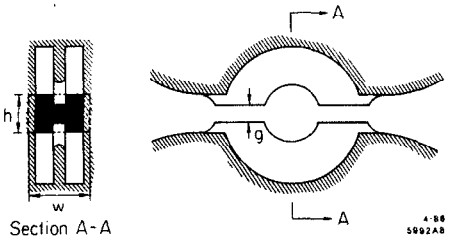

Fig. 5. Diagram of test cell with rectangular waveguide entering the cell wall and with a cut extending through the iris.

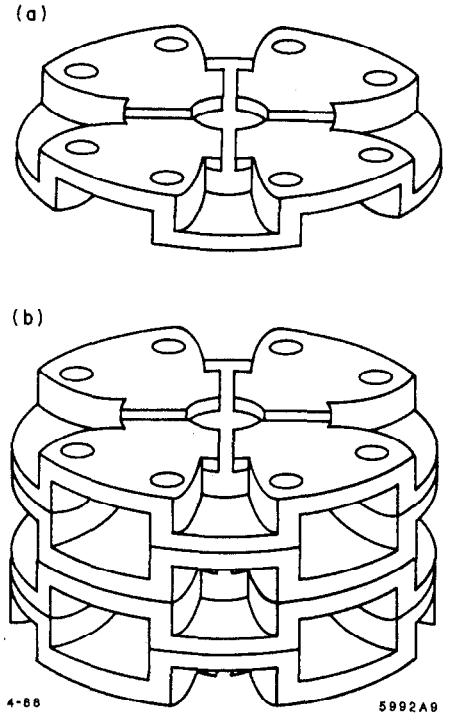

Fig. 6. Conceptual design of damped structure with a) a single cell and b) a stack of four such cells. Each cell is rotated 45° with respect to its neighbors.

twice as many slots as in these model tests. As a result, the longitudinal damping will be twice as strong; i.e., a Q of 40 would be expected where we require 80, which is certainly okay.

The Q of the acceleration mode was lowered by 20% which, with double the number of slots, would become 40% but because of the bolted nature of the test cavity, this is presumably an overestimate. A preliminary study with the three-dimensional computer code "MAFIA" indicated a loss of only 2%.

We appear to have a solution that has required damping of both the first transverse and longitudinal modes. A brief look for higher modes suggested that these will also meet our requirements, although a more careful study is needed.

4. A PRACTICAL REALIZATION

The design of a multicell linac employing such damped accelerating cavities is not simple. Four slots per cell are required, and succeeding slots cannot be at the same azimuthal angles. Each slot should open out before exiting the structure, so as to minimize reflections at their outer ends. The entire structure would then be supported inside a larger vacuum chamber, which may have to contain RF damping resistors or at least be made of a relatively high-resistance material. Since the structure is inside the vacuum container, water cooling would have to be integral to the structure. It should be noted that despite its complication, such a design will have the advantage of providing very good vacuum pumping to the inside of the cavities; something that is probably essential, and something that would be impossible to obtain without slots or holes of some kind. Figure 6 illustrates what a one cell (a) and a multicell structure (b) might look like, but it should be clear from this preliminary paper that much work remains to be done.

REFERENCES

1) Wilson, P. B., "Linear Accelerators for TeV Colliders," *Proceedings of the 2nd Workshop on Laser Acceleration,* Malibu, CA (AIP Conf. Proc. No. 130, 1985); SLAC–PUB–3674 (1985).

2) Bane, K. L. F., Wilson, P. B. and Weiland, T., "Wakefields and Wakefield Acceleration," in *Physics of High Energy Particle Accelerators,* Month, M., Dahl, P. F. and Dienes, M. eds., (AIP Conf. Proc. No. 127, New York, 1985), pp. 875–928.

3) Balakin, V., Novokhatskii, A. and Smirnov, V., *Proceedings of the 12th International Conference on High Energy Accelerators,* Fermilab (1983).

4) Palmer, R. B., "The Interdependence of Parameters for TeV Linear Colliders," *Proceedings of the Workshop on New Developments in Particle Accelerator Techniques,* Orsay, France, June 1987, CERN 87–11, p. 80; SLAC–PUB–4295.

5) Farkas, Z. D. and Wilson, B., "Comparison of High Group Velocity Accelerating Structures," SLAC–PUB–4088 (1987).

6) Schnell, W., CERN–LEP–RF/86–27 (1986).

7) Ruth, R. D., SLAC–PUB–4541 (1988).

8) Yokoya, K., DESY 86–084 (August 1976).

9) Palmer, R. B., to be published.

10) Thompson, K. A. and Ruth, R. D., "Controlling Multibunch Beam Breakup in TeV Colliders," SLAC–PUB–4537 (1988).

RELATIVISTIC KLYSTRON RESEARCH FOR LINEAR COLLIDERS†

M. A. ALLEN, R. S. CALLIN, H. DERUYTER, K. R. EPPLEY, K. S. FANT, W. R. FOWKES, W. B. HERRMANNSFELDT, T. HIGO,* H. A. HOAG, R. F. KOONTZ, T. L. LAVINE, T. G. LEE, G. A. LOEW, R. H. MILLER, P. L. MORTON, R. B. PALMER, J. M. PATERSON, R. D. RUTH, H. D. SCHWARZ, Y. TAKEUCHI,* A. E. VLIEKS, J. W. WANG, AND P. B. WILSON

Stanford Linear Accelerator Center, Stanford University, Stanford, California 94309

D. B. HOPKINS AND A. M. SESSLER

University of California, Lawrence Berkeley Laboratory, Berkeley, California 94720

W. A. BARLETTA, D. L. BIRX, J. K. BOYD, T. HOUCK, D. S. PRONO, R. D. RYNE, G. A. WESTENSKOW, AND S. S. YU

University of California, Lawrence Livermore National Laboratory, Livermore, California 94550

ABSTRACT

Relativistic klystrons are being developed as a power source for high gradient accelerator applications which include large linear electron-positron colliders, compact accelerators, and FEL sources. We have attained 200 MW peak power at 11.4 GHz from a relativistic klystron, and 140 MV/m longitudinal gradient in a short 11.4 GHz accelerator section. We report here on the design of our relativistic klystrons, the results of our experiments so far, and some of our plans for the near future.

1. INTRODUCTION

Large linear electron-positron colliders, compact accelerators, and FEL sources require a new generation of high gradient accelerators. Conceptual designs for large linear electron colliders for research at the frontier of particle physics call for beam energies of 250–1000 GeV and luminosities of 10^{33}–$10^{34}\,cm^{-2}sec^{-1}$. Accelerating gradients of 100–200 MV/m are desired in order to keep the accelerator length within acceptable limits. Frequencies of 10–30 GHz are desired in order to keep peak and average power requirements and beam loading reasonably small. The peak power necessary to drive a traveling-wave structure in the desired frequency range with the desired gradient is of order 1 GW/m with a pulse length of 50–100 ns.

Pulsed beams of such high peak power can be obtained using the technologies of magnetic pulse compression and induction acceleration.[1] Beam pulses of 1 kA current and 50–100 nsec duration are routinely accelerated to several MeV at Lawrence Livermore National Laboratory (LLNL). These beams contain several gigawatts of peak power.

† Work supported by the U.S. Department of Energy under contracts DE-AC03-76SF00515 (SLAC), DE-AC03-76SF00098 (LBL), and W-7405-ENG-48 (LLNL), and by the U.S.-Japan Collaboration on High Energy Physics.

* Visitor from KEK, National Laboratory for High Energy Physics, Oho, Tskuba, Ibaraki 305, Japan.

The first demonstration of RF power extraction from such a beam yielded an impressive 1 GW at 35 GHz, using a free electron laser.[2] A. M. Sessler and S. S. Yu, following a suggestion by W. K. H. Panofsky, proposed a more direct method for energy extraction by bunching a relativistic beam and passing it through extraction cavities.[3] Sessler and Yu suggested that if only part of the beam energy were extracted, the beam could be reaccelerated and energy could be extracted again. Repeated reacceleration and extraction was the concept they called a "relativistic klystron two-beam accelerator."[3] The idea of a relativistic klystron, however, is not limited to the two-beam accelerator concept. Relativistic klystrons can be imagined which span the range from a 1 GW device powering 1 m of accelerator, to a 10 GW device powering 10 m, to a two-beam device extending several kilometers. These ideas have led to a collaboration between Stanford Linear Accelerator Center (SLAC), Lawrence Berkeley Laboratory (LBL), and LLNL to study the combination of the klystron concept with induction accelerator and magnetic pulse compression technology. The first experiments have been done at the Accelerator Research Center (ARC) at LLNL using as a gun an induction accelerator designed to produce 1 kA currents with 1.2 MeV kinetic energy for up to 75 nsec duration. Four klystrons have been tested with this injector. They are, in chronological order as tested,

(1) SL3, a multicavity klystron with a conventional gun designed to operate at 8.6 GHz (three times the frequency of the SLAC linac),

(2) SHARK, a two cavity subharmonic drive relativistic klystron with 5.7 GHz drive and 11.4 GHz output,

(3) SL4, a high gain relativistic klystron at 11.4 GHz (four times SLAC frequency) designed specifically for the high power pulsed beam,

(4) SHARK-2, a three-cavity version of SHARK.

In this paper we discuss the design of these klystrons, report on the results of our experiments so far, and discuss some of our plans for the near future.

2. KLYSTRON SCALING

To motivate the increase in energy of the beam in an otherwise conventional klystron, it is useful to discuss the physics of the klystron interaction. In a two cavity klystron, the beam is velocity modulated by an RF drive cavity and allowed to drift until the velocity modulation bunches the beam. The bunched beam then is passed through another cavity which may be used to extract RF power. In practice, such a two cavity device has low gain. In most klystrons, there are several intermediate "idler" cavities. The first cavity bunches the beam. The bunched beam drives the second cavity to an RF voltage an order of magnitude greater than the first, which in turn bunches the beam more strongly. This process continues until the final idler cavity of the "linear gain region" of the klystron. The bunching is determined primarily by the voltage on the final idler cavity. After this cavity the bunches are allowed to drift until the RF current is maximum. At this point the beam is passed through two more cavities: a highly detuned "penultimate" cavity which sweeps still unbunched electrons into the bunch, and an output cavity which extracts energy by decelerating the beam. The output cavity could be replaced by a series of cavities or by a traveling wave structure.

An important parameter in klystron scaling is the beam plasma wavelength. Velocity modulation bunches a DC beam. However, space charge repulsion (modified by the drift tube) causes the beam to debunch. In the linear region, this process produces oscillations. The distances between cavities in a klystron are chosen to be approximately one-quarter of a plasma wavelength for optimal bunching. For a long relativistic beam of current I and radius a in a narrow tube of radius b the plasma wavelength on axis is

$$\lambda_p \simeq \lambda_{RF}\sqrt{\frac{17\,\mathrm{kA}}{I}\frac{(\beta\gamma)^5}{1+2\ln(b/a)}}$$

where λ_{RF} is the free-space RF wavelength, $\beta = v/c$, and $\gamma = 1/\sqrt{1-\beta^2}$. Increasing the beam energy ameliorates longitudinal space charge effects but increases the bunching distance. Increasing the frequency reduces the bunching distance. Our choice of 2.6 cm RF wavelength makes possible a multicavity klystron design that can bunch a 1 MV, 1 kA beam efficiently and extract power from it in a total distance of 1 m. For higher energy beams, bending magnets can be used to create differences in path length for particles of different energies. This permits bunching of higher energy beams even though their velocity is nearly independent of energy.

Another important parameter in klystron scaling is the magnetic field necessary to focus the beam. For a beam of uniform charge density and normalized edge emittance ϵ_n, the solenoid field B necessary to confine the beam current I to radius a is

$$B = \frac{2m_e c^2}{ea}\sqrt{\frac{2I}{17\,\mathrm{kA}}\frac{1}{\beta\gamma} + \frac{{\epsilon_n}^2}{a^2}}.$$

The constant, $2m_e c^2/e$, is 3.4 kG-cm.

In the relativistic klystrons discussed here both γ and I are greater than in conventional klystrons. At shorter wavelengths higher magnetic fields are needed to focus the beam since the radius of the drift tube scales with the wavelength. An estimate of the required field must include the effects of beam bunching. The peak current in the bunched beam typically is about four times the initial DC current. Thus, for a space charge dominated beam, the magnetic field required is typically twice that calculated for focusing a DC beam.

3. EXPERIMENTAL APPARATUS

3.1 Induction Accelerator

Most of the experimental studies described here were performed using the Snowtron injector at the ARC facility at LLNL. Snowtron is a linear induction injector composed of ten 150 kV induction cells driven by pulsed magnetics.[1] For klystron experiments, a triode electrode configuration was used with a cathode of 12.5 cm diameter and 35.6 cm spherical radius. The inner diameter of the anode drift tube was 8.8 cm. The cathode was placed 35 cm from the downstream end of the injector. Accelerating voltages up to 1.2 MV, beam currents up to 1.4 kA, and pulse widths up to 75 nsec FWHM have been obtained for the klystron experiments. The greatest stress on the injector is 260 kV/cm on the cathode shroud at peak voltage. The DPC computer code, which was used to design Snowtron, predicts peak currents of 2.3 kA at 1.2 MV.[4] However, the operating pressure of the injector led to cathode contamination which precluded uniform space charge limited emission.

3.2 Beam Transport

The distance from cathode to klystron was 4 m for the SL3 test and is 1.6 m for the SHARK and SL4 tests. Just downstream from the injector is a 30 cm taper where the beam pipe narrows from 8.8 to 1.9 cm diameter. The pipe diameter is narrowed further to 9.2 mm in the SHARK and SL4 klystrons. Nine 2.5 kG solenoid coils powered by five separate power supplies focus the beam between the cathode and the klystron. Three independently controlled 5 kG solenoids focus the beam in the relativistic klystron. Four sets of dipole magnets for horizontal and vertical steering are used to correct for beamline misalignments.

Beam transport calculations with the ST code have been used to estimate the required strengths of the focusing fields for 100% transmission of current through the klystron.[4] The result of such a calculation is shown in Fig. 1.

3.3 Klystrons

Parameters of the three relativistic klystrons tested are summarized in Table 1. Further descriptions are given below.

SL3 is a conventional high gain klystron designed to operate at 8.6 GHz with a conventional gun. With its design gun replaced by an induction accelerator, it served as an expedient first demonstration of a relativistic klystron. SL3 was driven by a 1 kW X-band TWT amplifier.

SHARK is a two cavity sub-harmonic drive relativistic klystron. The input cavity is driven by an RF source of several MW at 5.7 GHz which modulates the beam velocity. After drifting, the beam current has large Fourier

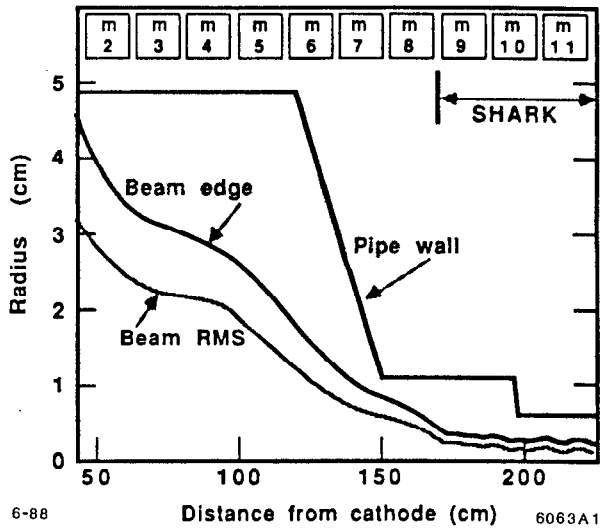

Fig. 1. Beam size calculated through SHARK.

Table 1. Parameters of relativistic klystrons tested.

	SL3	SHARK	SL4	SHARK-2
Output freq. (GHz)	8.57	11.4	11.4	11.4
Drive freq. (GHz)	8.57	5.7	11.4	5.7
Output power (MW)				
Peak (max)	75	47	200	117
Flat pulse (max)	75	47	68	80
Design gain (dB)	54	20	65	25
Efficiency (%)				
Design	60	20	40	40
Operation (max)	55	25	50	32
Beam Voltage (kV)				
Design	330	1200	1200	1200
Operation (max)	1000	1200	1000	1200
Beam Current (A)				
Design	300	1000	1000	1000
Operation (max)	350	750	750	800
Number of cavities	5	2	6	3
Total length (cm)	31	25	98	33
Beam-off loaded Q				
Input cavity	250	725	280	742
Idler cavities	4000	—	120	—
Penultimate cavity	4000	—	3800	3800
Output cavity	44	40	20	20
Drift tube diam (mm)	11	19, 9.2	14, 9.2	19, 9.2

components at 5.7, 11.4, and 17.2 GHz. Resonant cavities tuned to the higher harmonics can be used to extract power and measure breakdown fields at the higher frequencies. The 11.4 GHz output cavity is positioned after a 25 cm drift for maximum RF current at that harmonic. With only two high Q resonant structures in this klystron, problems with beam breakup instabilities are minimized. However, the gain of a two cavity tube is low. Therefore, in order to achieve beam-to-RF power conversion comparable to that in multicavity tubes, a conventional 5 MW, 5.7 GHz klystron is used to drive SHARK. The RF fields in the input and output cavities are comparable for 2 MW of drive and 50 MW of output because of the different Q's.

SHARK was designed to serve as a test bed for cavity design to be used in relativistic klystron research. Its design allows study of a wide range of beam parameters and minimizes difficulties with beam propagation. The drift pipe and output cavity are easy to replace, making it possible to use SHARK to study different output cavities at several frequencies.

SL4 is a high gain, six cavity, relativistic klystron at 11.4 GHz which was designed specifically for the 50 nsec pulsed 1.2 MV, 1 kA Snowtron beam. Therefore, unlike most klystrons, it was designed without an integral gun assembly. In order to make the RF filling time of the SL4 cavities much shorter than the 50 nsec beam pulses, three of the gain cavities are coupled by irises and waveguides to absorptive ceramic wedges. This results in loaded Q's of 120, and filling times of 2–3 nsec for these cavities.

To reduce the difficulty of maintaining a well-focused electron beam over a 1 m drift length, the SL4 drift tube was tapered. The drift tube diameter in the first four cavities is rather wide, 14 mm. The tube then is tapered to 9.2 mm just upstream of the penultimate cavity. Tapering permits the use of solenoid magnets with axial field of 2.7 kG for most of the length of the klystron. A 5 kG solenoid surrounds the region of the penultimate and output cavities.

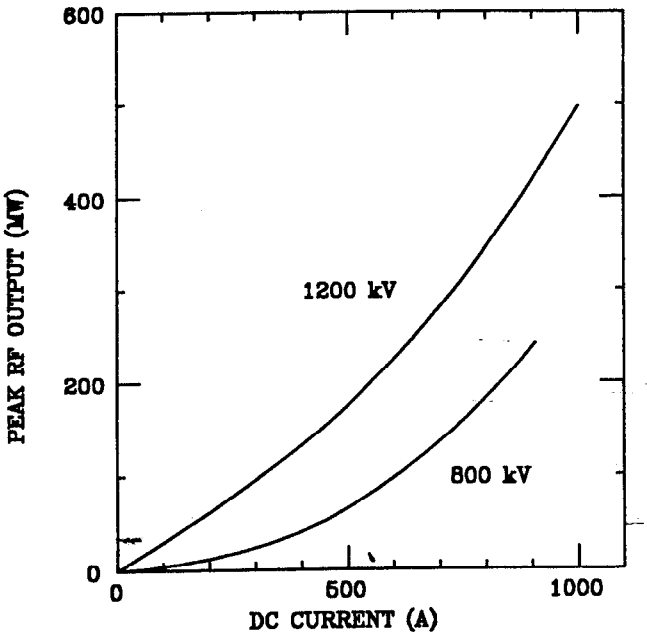

Fig. 2. MASK simulations of SL4 output power.

The design gain and efficiency for SL4, 65 dB and 40%, respectively, are obtained using the MASK computer code.[5] MASK simulations were used to optimize the SL4 design parameters and to predict the efficiency and gain at several different beam currents and voltages.

Some simulation results are shown in Fig. 2. The saturation RF drive power is approximately 200 W, which is supplied by a 1 kW X-band TWT amplifier.

Because of the high peak electric fields in the penultimate and output cavities good vacuum is necessary to prevent cavity breakdown. Consequently, a 500 liter/sec cryopump evacuates the klystron collector section and two 8 liter/sec vac-ion pumps evacuate the output waveguide. In this configuration waveguide and collector pressures can be maintained at 10^{-8} Torr.

SHARK-2 is a modification of SHARK in which a third cavity resonant at 11.8 GHz was inserted between the input and output cavities to increase klystron gain and efficiency. In addition, the outer cylindrical wall of the cavity was fabricated from low carbon steel to shield the cavity interior from the axial magnetic field for reasons discussed below in Section 4.3.

3.4 Diagnostics

The pulsed DC beam current is monitored in three places: at the injector, upstream from the input cavity, and downstream from the output cavity. The DC current monitors measure image currents in the beam pipe wall. An RF current monitor is placed downstream from the SHARK output cavity. The RF current diagnostic for SHARK was a pickup loop, recessed azimuthally in the beam pipe wall, which measured $\dot{B}_\phi$. The RF current diagnostic for SHARK-2 was a pair of probes, recessed radially in the beam pipe wall, which measured $\dot{E}_r$.

Forward and reflected RF drive power signals are sampled using 20 dB broad band waveguide directional couplers. Relativistic klystron output power and, in the SL4 experiment, the RF reflected back from the high gradient accelerator test section, were sampled using 56 dB waveguide directional couplers. The sampled RF signals are transported on individually calibrated, 25 m long, high quality Heliax cables from the couplers to the control room where they are measured with calibrated HP 8470B crystal diode detectors. Calorimetric measurement methods so far have been precluded by the low pulse repetition rate (less than 10 pulses/sec) necessitated by inadequate shielding.

3.5 High Gradient Accelerator

To complement the SL4 experiment, a 26 cm long section of 11.4 GHz accelerator structure operating in the $2\pi/3$ traveling wave mode has been built. The constant impedance structure consists of 30 cells and has $r/Q = 14\,\mathrm{k\Omega/m}$. The attenuation parameter is 0.14 nepers. The group velocity is 0.031c, giving a filling time of 28 nsec. The iris diameter was chosen to be 7.5 mm. Parameters were calculated by the SUPERFISH code and confirmed by cold test measurements. Coupler dimensions were approximated by extrapolation from S-band data, and finalized by cold test. The accelerator was fabricated from machined "cups" which were stacked and brazed. A special tool permitted each cavity to be tuned up or down in frequency in order to obtain the correct phase advance per cell.

4. EXPERIMENTAL RESULTS

4.1 Beam Transmission

The design goal of 100% beam transmission through the klystrons has not been achieved experimentally, even after focusing adjustments were performed by empirical optimization using a diagnostic such as transmitted current or output RF. The maximum current transported through SHARK is 750 A, only 65% of the maximum current entering the klystron. Up to 80% transmission has been achieved at 400 A. Transmission achieved through SL4 (which is four times longer than SHARK) is 55% at 800 A, and is 65% at 500 A. Transmission is observed to be independent of RF drive for SHARK. However, for SL4 and SHARK-2, a slight decrease in transmission was noted at high RF output levels. (There was no downstream current monitor in the SL3 tests; transmission through SL3 was not measured.)

4.2 SL3 Demonstration

The SL3 test was designed to be a demonstration of the effects of putting a conventional klystron tube (stripped of its gun) in a high power pulsed beam. No unusual or unexpected phenomena were observed. No evidence of multipactor, breakdown, parasitic oscillations, nor other instabilities was observed. RF pulse risetimes were 5–10 nsec. RF pulses reproduced the shape of the beam current pulses quite well. SL3 performance at beam energies much greater than design is illustrated in Fig. 3. Peak power of 75 MW was attained with an 800 kV, approximately 250 A beam. Observed output power agreed well with the predictions of the MASK simulation code.

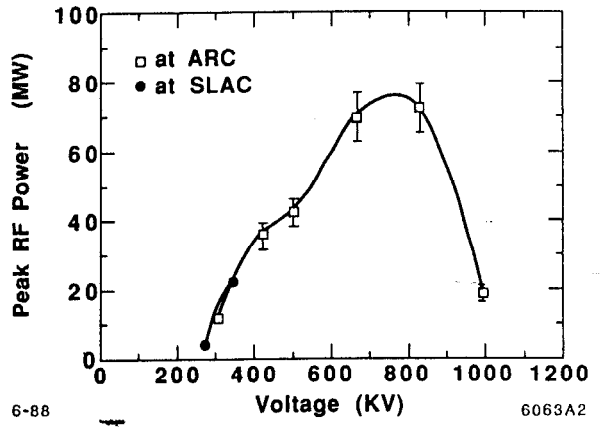

Fig. 3. SL3 performance.

4.3 SHARK and SL4

Peak output power of 200 MW at 11.4 GHz was attained with the SL4 relativistic klystron design using a 930 kV, 420 A beam. SL4 has not yet operated at its 1000 A design current. However, agreement is excellent between output power measured at lower currents and the MASK predictions (Fig. 2) for operation at these currents. The 200 MW peak power delivered by SL4 to the

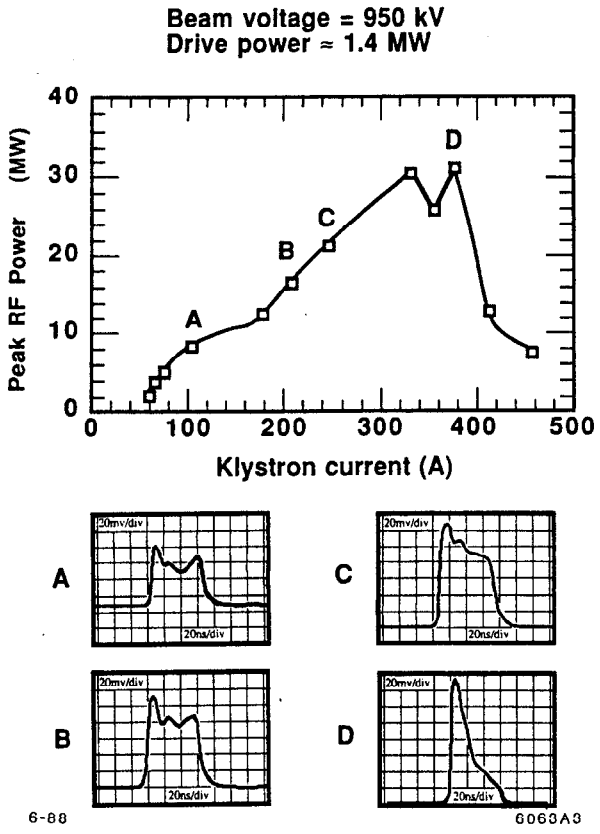

Fig. 4. RF pulse shortening observed in SHARK tests.

11.4 GHz accelerator corresponds to a longitudinal accelerating gradient of 140 MV/m. Early indications are that there is appreciable dark current in the accelerator when the accelerating gradient exceeds 90 MV/m.

In our tests of both SHARK and SL4, we observe that as the beam current through the klystron is increased up to a certain level, the output power pulses remain relatively flat. However, if the beam current is increased beyond this level, the trailing edges of the output power pulses diminish in amplitude, while the leading edges continue to grow with the beam current. This behavior in SHARK tests is illustrated in Fig. 4. We have demonstrated that our ability to obtain flat output power pulses is affected by beam current, RF drive level, and focusing magnetic field strength. The practical importance of these observations is that even though 200 MW of RF was produced with SL4, the maximum reasonably flat RF pulse achieved in our initial tests was only 68 MW. Low and high peak power SL4 pulses are illustrated in Fig. 5. The pulse shortening phenomenon is a serious impediment to making flat high power RF pulses. It is not beam breakup because the transmitted DC beam current pulse does not shorten with the RF pulse.

To understand the mechanism for output pulse shortening in SHARK, an experiment was performed in which simultaneous data on reflected power from the input cavity and on output power were recorded at a critical point for the onset of the shortening phenomenon. With no external changes in the beam condition and/or input power, the output alternated from pulse to pulse between the rectangular and triangular pulse shapes. When the beam turns on, there is a significant dip in the drive power reflected from the SHARK input cavity. Two distinctly different states have been observed in the reflected drive, as shown in Fig. 6, one having a much greater reflection during the beam-on time. Furthermore, the state with large reflection is correlated repeatedly with the narrow output pulse.

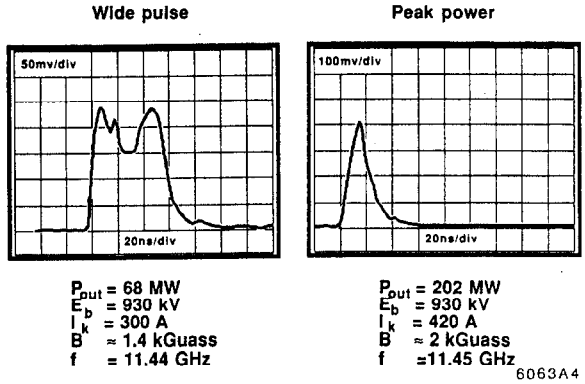

Fig. 5. Low and high peak power pulses in SL4 tests.

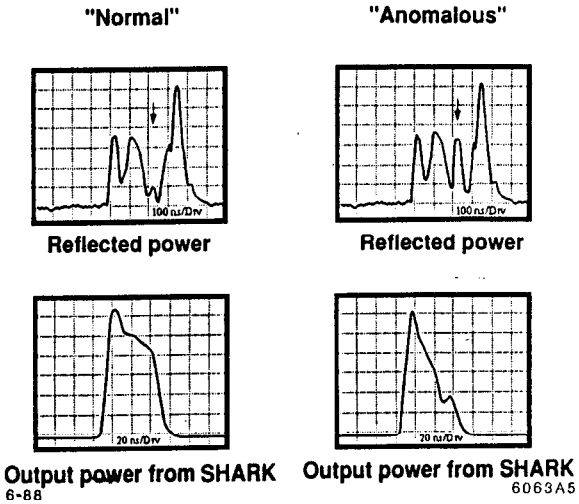

Fig. 6. SHARK reflected drive and output power. Arrows indicate the 50 nsec beam time in the reflected power.

This observation can be reproduced with our computer code for transient analysis. In the code, we use a circuit model to compute the time varying voltage across the input gap. The reflected power is calculated from the time-varying voltage by power balance. Results of the

transient calculation are shown in Fig. 7 where the relatively flat output pulse with the low beam-on reflected power was obtained by using a beam loading generally consistent with MASK calculations and measurements. The narrow output pulse and increased reflection were obtained by arbitrarily increasing beam loading by a factor of 2.5.

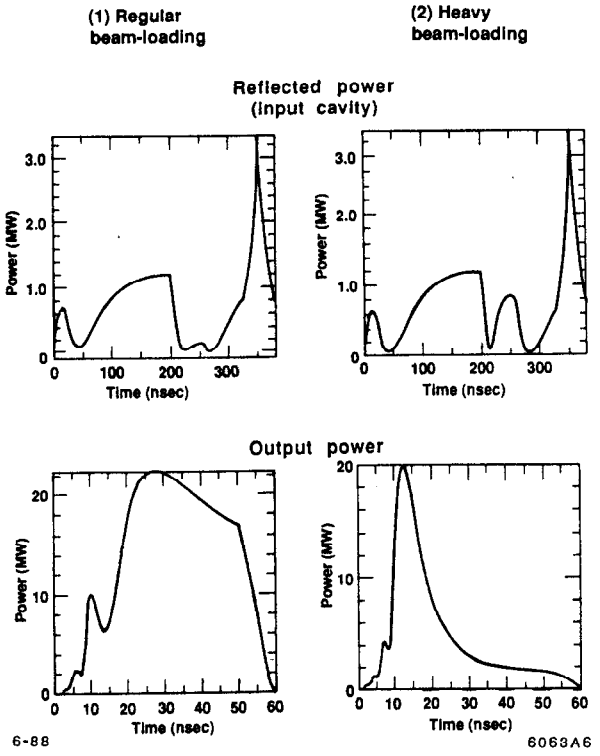

Fig. 7. Calculations of the effect of anomalous beam loading on SHARK reflected drive and output power.

The anomalous heavy beam loading which we believe causes pulse shortening appears to be a phenomenon similar to multipactor to the extent that it is sensitive to changes in focusing magnetic field and RF power level. The anomalous beam loading in fact may be multipactor.

Further studies of the SL4 relativistic klystron have demonstrated anomalous input cavity loading by charged particles when the RF drive level exceeds 40 W, even under cold cathode, beam-off conditions. Sometime after the onset of the RF drive pulse, the input cavity absorbs all of the incident RF drive that otherwise would be reflected from the beam-off, unloaded cavity. This power absorption is a function of drive level, and of axial magnetic field surrounding the cavity. No power absorption is present when the axial magnetic field is zero. This cavity loading phenomenon, which we have observed in the SL4 input cavity, both with and without beam, may occur in any of the cavities of a multicavity klystron and may be associated with pulse shortening.

The power threshold for RF pulse shortening was observed to increase with decreasing magnetic focusing field. Consequently, we tested a SHARK (5.7 GHz subharmonic) input cavity surrounded by iron which shunts the focusing field away from the beam axis in the region of the cavity gap. Figure 8 shows the effect of the iron on the axial magnetic field profile near the SHARK input cavity. The iron input cavity does not exhibit anomalous loading, with or without beam. Output pulse shortening continues to occur above a threshold in output power. However, the output pulse shortening in the configuration with the iron input cavity occurs at a higher power threshold than in the original SHARK tests with a copper input cavity, and the output pulse shortening apparently starts in the output cavity. The evidence that pulse shortening occurs in the output cavity is that no correlation is observed between the output pulse shortening and either the input cavity reflected power or the RF current as monitored by an RF probe in the drift downstream from the input cavity. Figure 9 shows multiple exposure photos of the output power pulses simultaneous with the input power reflected from the input cavity. The pulses in the figure were recorded during operation at the pulse shortening threshold. Both long and short output pulses are observed, while all reflected input pulses exhibit normal beam loading.

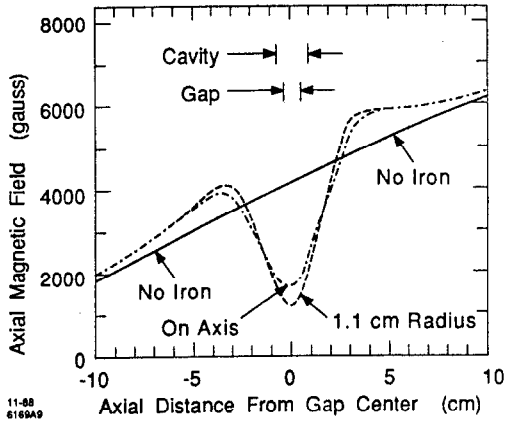

Fig. 8. Calculation of the axial magnetic field near the SHARK input cavity with and without iron. The cavity noses are at 1.1 cm radius.

4.4 SHARK-2

The observation that RF pulse shortening did not occur in the iron SHARK input cavity but did occur in the copper SHARK output cavity, as discussed in the previous section, prompted us to test a three cavity subharmonic drive klystron configuration consisting of the iron SHARK input cavity and copper penultimate and output cavities. (The penultimate and output cavities are the output section of the modularly designed SL4 relativistic klystron.) In this configuration we expect lower electric fields in the output cavity because the external Q of this output cavity is half that of the original SHARK output cavity. Results with this three cavity configuration, named SHARK-2, are summarized in Table 1.

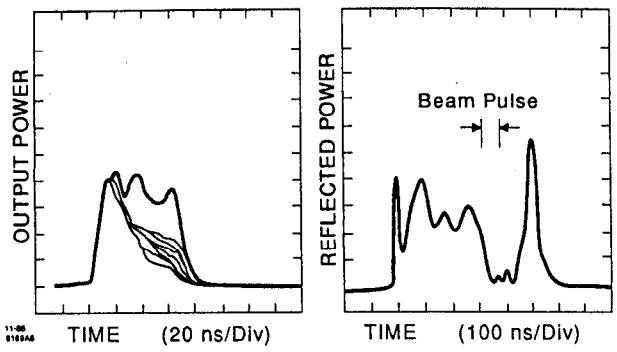

Fig. 9. Multiple exposure photos of long and short output power pulses simultaneous with "normal" reflected input power pulses in the SHARK with the magnetically shielded input cavity operating at the pulse shortening threshold.

Output pulse shortening is observed in the three cavity SHARK-2 at some point downstream from the iron input cavity. However, the power threshold is higher than in the two cavity iron input SHARK, presumably due to the lowered external Q of the output cavity. Flat output pulses of 80 MW amplitude and 45 nsec duration (FWHM) have been obtained from the three cavity subharmonic SHARK-2 before the onset of pulse shortening. This is 70% more flat-top RF power than we obtained from the two cavity SHARK.

Some improvement in the pulse shortening threshold has been observed with high power RF conditioning at 10 pulses/sec.

5. FUTURE PLANS

We are incorporating RF field probes in our designs of new intermediate cavities in order to ascertain where pulse shortening first occurs in multicavity relativistic klystrons, such as SL4.

In light of the apparent success of the iron magnetic shield at suppressing pulse shortening in the SHARK and SHARK-2 input cavities we plan to apply several techniques commonly used for multipactor suppression in order to raise the threshold for pulse shortening. We plan to add iron magnetic shields to downstream cavities. Consequently, we are studying the effect of the iron on the relativistic beam dynamics. We are fabricating and plan to test a cavity with slotted noses (as an alternative to iron). We plan to employ RF conditioning at higher pulse repetition rates with improved radiation shielding.

A traveling wave output structure which has been fabricated will be used in place of an output cavity in a relativistic klystron. This structure will have lower electric fields than a single output cavity and consequently the output power threshold for pulse shortening may be higher.

As soon as rectangular high power RF output pulses of sufficient duration are obtained, further studies of the high gradient accelerator structure described in Section 3.5 are planned. These tests will include studies of breakdown at 11.4 GHz and measurement of the accelerating gradient.

6. SUMMARY

We have been working to develop a high power (500 MW) short wavelength (2.6 cm) relativistic klystron with beam kinetic energy greater than 1 MeV. Four different klystrons have been tested. Peak RF power of 200 MW has been achieved, but only with an RF flat top much shorter than the beam current pulse. This pulse shortening phenomenon is by far the most serious problem encountered. It is clearly not beam breakup since it does not correlate with shortening of the DC current pulse. Experimental evidence from one of the klystrons (SHARK) indicates that pulse shortening is caused by loading of the input cavity by anomalous charged particle currents. The loading is believed to be due to either secondary electrons or to photoelectrons produced by the copious supply of x-rays caused by beam interception. The power threshold for pulse shortening is sensitive to magnetic focusing field and to RF field strength. Magnetically shielding a klystron input cavity raised the power threshold for pulse shortening. A second and perhaps related problem is rather poor beam transmission through the klystrons, which has not exceeded 65%. The shortened 200 MW peak RF pulses have been transmitted into a 26 cm long high gradient accelerator structure. This power corresponds to an accelerating gradient of 140 MV/m.

ACKNOWLEDGEMENTS

We thank R. J. Briggs, G. J. Caporaso, M. Chodorow, H. Gasquet, Y. Goren, J. Haimson, E. W. Hoyt, V. K. Neil, A. C. Paul, C. Pearson, D. S. Prono, L. L. Reginato, A. C. Smith, K. Whitham, D. Yu, and L. Zitelli for their assistance. The authors from SLAC thank LLNL for its continuing hospitality.

REFERENCES

1. L. L. Reginato and D. L. Birx, "Pulsed High Power Beams" and "Recent Advances in Magnetically Driven Induction Linacs" in Proceedings of the European Particle Accelerator Conference, Rome, Italy, June 7–11, 1988.
2. T. J. Orzechowski *et al.*, "High Efficiency Extraction of Microwave Radiation from a Tapered Wiggler Free Electron Laser," *Phys. Rev. Lett. 54*, 889 (1985).
3. A. M. Sessler and S. S. Yu, "Relativistic Klystron Two-Beam Accelerator," *Phys. Rev. Lett. 58*, 2439 (1987).
4. J. K. Boyd, "Snowtron Numerical Calculations," LLNL-RM-87-48 (November 1987).
5. K. Eppley, "Algorithms for the Self-Consistent Simulation of High Power Klystrons," SLAC-PUB-4622 (May 1988), to be published in the proceedings of the Linear Accelerator and Beam Optics Codes Workshop, San Diego, California, January 19–21, 1988.

RF PULSE COMPRESSION AND ALTERNATIVE RF SOURCES FOR LINEAR COLLIDERS*

P. B. WILSON

Stanford Linear Accelerator Center, Stanford University, Stanford, California 94309

ABSTRACT

Future linear colliders will require a very high peak power per meter of accelerating structure at a relatively high frequency—greater than 10 GHz—but at a relatively short pulse length—less than 100 ns. One technique for generating the required peak power is to use a more or less conventional microwave power source, which produces power at a pulse length typically on the order of 1 μs, together with RF pulse compression. Some parameters are given for a Binary Power Multiplier (BPM) pulse compression system operating at 17.1 GHz with an output pulse length of 60 ns. The peak power gain for a three stage system is estimated to be 6.6 (82% compression efficiency). Some possible long-pulse microwave sources which—when coupled with such a pulse compression system—would be suitable for driving a linear collider are briefly discussed.

1. INTRODUCTION

The peak power requirement for a recent TLC design[1] is 586 MW/m at a frequency of 17.1 GHz and a pulse length (equal to the structure filling time) of 60 ns. The relativistic klystron[2] is capable of producing sufficient peak power at this pulse length to power several meters of structure. More conventional microwave power sources operating at beam voltages of 500 kV or less could be expected to produce at most about 100 MW at this frequency. However, the natural pulse length for such sources, using conventional or near-conventional modulator technology, is on the order of 1–2μs. If a one microsecond pulse could be compressed to 62 ns by some technique, the gain factor in peak power would be $G = 16\ \eta_c$, where η_c is the compression efficiency. Thus, a 100 MW source coupled with pulse compression at 80% efficiency would produce 1.3 GW, which is comparable to the power to be expected from a relativistic klystron. In the next section we take a brief look at the capabilities and limitations of RF pulse compression.

2. PULSE COMPRESSION SYSTEMS

A number of pulse compression methods have been proposed and a few have been experimentally tested. The SLED scheme, for example, is in routine operation at SLAC. However, the peak power gain for SLED is limited to about a factor of three for a reasonable compression efficiency, and the system delivers a strongly time-varying output waveform. Energy storage cavities which are pumped up slowly by a relatively low power source with a long pulse length, and then dumped rapidly using a high power plasma switch, have also been proposed. However, the technological problems of a suitable switch have not been solved, and again the output waveform is highly nonuniform.

A pulse compression system with a potentially high peak-power gain, which gives a flat output waveform, is the Binary Power Multiplier (BPM) suggested by Z. D. Farkas[3]. The system uses a series of over-moded waveguide delay lines as low-loss energy storage elements, and 3 dB directional couplers—triggered by a pattern of phase reversals—as switching elements. It is important to note that in this pulse compression scheme two high power amplifiers and one set of delay lines are required for each BPM system. The phase reversal pattern is imposed at a low RF power level on the input drive to the amplifiers. The RF components used in a BPM system (3 dB directional couplers, transitions from rectangular to circular guide, 180° turn-arounds and right angle bends) must be carefully designed to avoid mode conversion. The theory of the BPM method is given in Ref. 3, and some initial experimental results on a prototype system (which did not, however, use all low-loss components) are reported in Ref. 4.

Let us look at a 17 GHz n–stage BPM system designed to compress an input pulse of $2^n \times 60$ ns to an output of 60 ns. Each stage compresses the pulse length by a factor of two and increases the peak power by a factor of $2\eta_n$, where η_n is the compression efficiency of the n^{th} stage. To calculate the compression efficiency, we assume a loss of 0.18 dB (transmission efficiency $\eta = 0.96$) per stage for a coupler and turn-around. The delay-line loss at 17 GHz for standard 2.81 inch I.D. copper pipe is .06 dB/100 ns (transmission efficiency of 0.99/60 ns). The length of line per 60 ns is 17.1 m ($v_g/c = 0.95$). The delay line lengths and efficiencies are given in Table I. Two efficiency figures are given for each stage. The top figures give the component and total efficiencies for that particular stage. The bottom figures give the cumulative efficiencies for all stages up to and including the n^{th} stage. Thus, a complete system of either one, two, three or four stages would have a net efficiency of 0.95, 0.89, 0.82 and 0.73, respectively.

*Work supported by the Department of Energy, contract DE-AC03-76SF00515.

Table I. BPM Pulse Compression System at 17.14 GHz with 60 ns output pulse length

Stage Number	0	1	2	3	4
Delay time (ns)	0	60	120	240	480
Line length (m)	0	17	34	68	137
Efficiencies:					
η_{coup}	—	0.96 0.96	0.96 0.92	0.96 0.89	0.96 0.85
η_{line}	—	0.99 0.99	0.98 0.97	0.96 0.93	0.92 0.86
η_n η_{cum}	1.00 1.00	0.95 0.95	0.94 0.89	0.92 0.82	0.88 0.73
RF Source:					
T_k (ns)	60	120	240	480	960
$P_K/feed$ (MW)	938	493	263	143	80

Note that the coupler and delay line losses are equal in the third stage. The cumulative losses due to the couplers and delay lines are approximately equal in a four-stage system. The pulse length required from the RF source is given by T_k. The peak source power per feed, P_k, is given for Palmer's TLC design parameters:[1] peak accelerating gradient, 186 MV/m; RF power per meter, 586 MW; distance between feeds, 1.60 m.

It is useful to note that a BPM system can be programmed to deliver more than one output pulse per RF source pulse. For example, suppose a three stage system is desired, which would nominally require a 480 ns source pulse. It may be more convenient and more efficient to design a modulator-source combination which delivers 3×480 ns ≈ 1.5 μs. The BPM phasing pattern is then simply repeated three times in succession, giving three 60 ns output pulses spaced 480 ns apart. The disadvantage is that the effective repetition rate of the collider is reduced by a factor of three; for example, from 360 Hz to 120 Hz in the TLC design in question[1]. This, in turn, reduces the effectiveness of feedback in controlling emittance growth due to the high-frequency component of magnet jitter from ground motion. However, the 120 Hz rate may still be acceptable. This multipulse scheme also has implications for the damping rings, but the necessary design modifications are acceptable[5] if the number of output pulses per klystron pulse is not too large.

Assembly of components for a low-loss 11.4 GHz BPM prototype system, which will compress 320 ns to 40 ns in three stages, is now underway at SLAC. The experiment will test the insertion loss of components (couplers, delay lines, 180° turn-arounds and transitions), the overall power gain of the system, and effects due to mode conversion and dispersion. Initial measurements at low power will be reported[6] early next year. The expected compression efficiency is 80% to 85%, giving a peak power gain of 6.5 to 7.0. The next step will be to make the system vacuum tight, so that it can be tested at high power.

In order to test a BPM compression system, accelerating structures and other RF components at a frequency and power level of interest for a linear collider, an appropriate near-term high-power RF source is needed. A 100 MW, 11.4 GHz klystron is under design[7] at SLAC which meets this need. The tube operates at 440 kV, and uses a combination of electrostatic and magnetic beam compression to achieve a high compression ratio and a reasonable cathode loading. K. Eppley[8] has simulated the dynamics of this tube, and finds an efficiency of 43% using a double-gap output cavity. Diode tests on the tube will begin early in 1989.

Some other possible microwave sources which can be used together with RF pulse compression to power a linear collider are discussed in the next section.

3. ALTERNATIVE RF SOURCES

By "alternative" we mean RF power sources which produce moderate peak power levels at a pulse length on the order of one microsecond, as opposed to very high peak power devices such as relativistic klystrons which operate at a much shorter pulse length equal to the structure filling time. Alternative sources can be driven by modulators using presently existing technology, and must be followed by several stages of RF pulse compression.

An example of such an alternative RF source, mentioned in the previous section, is the 100 MW, 11.4 GHz klystron now under design at SLAC. This power level is probably close to the limit that can be produced at this frequency using conventional klystron technology and a beam voltage less than 500 kV. It is well known that the efficiency of a klystron depends on the perveance, defined as $K = I_0/V_0^{3/2}$, where I_0 is the beam current and V_0 the beam voltage. A typical plot of efficiency (defined as the RF output power divided by the beam power I_0V_0) as a function of perveance is given in Ref. 9. The efficiency typically falls below 50% at a perveance of about $2 \times 10^{-6} A/V^{3/2}$. This fact alone limits the output power of a klystron to about 180 MW, independent of frequency, if it is to have reasonable efficiency at a beam voltage less than 500 kV. However, at shorter wavelengths cathode loading imposes an additional constraint. The cathode area is related to the beam cross-section area by the area compression ratio R_A. In turn, the beam area cannot exceed about $\pi(\lambda/8)^2$ if the coupling to the rf gaps is to be adequate. The output power for an efficiency η greater than about 50% is therefore

$$P \approx (\lambda/8)^2 R_A I_A V_0 \eta \ , \qquad (1)$$

where I_A is the cathode loading in A/cm^2. Choosing $I_A = 10 A/cm^2$ (reasonable but not conservative), $R = 200$ (probably near the upper limit), $V_0 = 400$ kV and $\eta = 50\%$, we have

$$P(MW) \approx 20\,[\lambda(cm)]^2 \ . \qquad (2)$$

Thus at 17 GHz we can expect at most about 60 MW from such a "pushed technology" klystron.

A number of devices have been suggested which get around the λ^2 scaling in Eq. (2). The gyroklystron, for example, employs an annular beam with a thickness which scales with wavelength, but a circumference which to first order can be independent of wavelength. The area of the beam, and hence the power output, then scales roughly in proportion to λ. Thus, the gyroklystron is more suited to the production of high power at high frequencies than

the klystron. As an example, a gyroklystron is being developed at the University of Maryland which will produce 40 MW at 10 GHz. It is estimated that the device could be scaled to produce 110 MW at 17.1 GHz.[10]

Strip beam, or sheet beam, tubes are another class of device which can get around the λ^2 scaling law that round beam tubes must follow. Consider, for example, a sheet beam of width w and thickness t. To couple to the RF circuit, the thickness must be a fraction of the wavelength, say $t \approx \lambda/5$. Thus the power output of a sheet beam device is roughly

$$P \approx 0.2\lambda w R_t I_A V_0 \eta \ . \qquad (3)$$

Here, R_t is the transverse beam compression ratio (ratio of cathode width to beam thickness). We take R_t to be 10, although detailed gain design calculations are needed to determine a realistic limit. Again, take $I_A = 10A/cm^2, V_0 = 400$ kV and $\eta = 0.5$. Equation (3) then gives

$$P(MW) \approx 4\,[\lambda(cm)]\,[w(cm)] \ . \qquad (4)$$

At 17 GHz such a sheet beam device with a width of 25 cm would produce 175 MW.

The perveance of sheet beam devices is also an important consideration. Longitudinal and transverse space charge effects in a sheet beam depend on the perveance per square K_s, defined terms of the current in the beam per square, I_s, as

$$K_s = I_s/V_0^{3/2} \approx I_A R_t (\lambda/5)^2 V_0^{-3/2} \ . \qquad (5)$$

For $I_A = 10A/cm^2, R_t = 10, V_0 = 400$ kV and $\lambda = 1.76$ cm (17 GHz), $K_s = 0.05$. Space charge effects are relatively small at this low a perveance. In fact, a sheet beam device with the same output power as a round beam device has a perveance per square which is lower than the round beam perveance by a ratio on the order of $\lambda/5w$. These concepts also apply to annular beams, where w is the circumference of the beam.

The design of a sheet beam X-band (11.4 GHz) klystron has been considered by Eppley, Herrmannsfeldt and Miller.[11] The device, shown in Fig. 1, uses permanent magnets with alternating polarity to focus the beam (wiggler focusing). The tube was not actually built, but in simulations it produced an output power of 2 MW per centimeter of beam width at a beam voltage of 200 kV with an efficiency of about 50%. The perveance per square was about 0.1×10^{-6}. The calculations indicated that the output power could be raised above 10 MW/cm at somewhat higher voltage and perveance with no loss in efficiency, giving an output power of 250 MW for a 25 cm wide beam. A number of problems with the sheet beam klystron concept need more detailed investigation, in particular the design of suitable RF cavities and potential feedback between cavities which can result from construction asymmetries.

It is possible to envision a variety of other sheet beam devices, for example sheet beam traveling wave tubes. The concept of a deflection modulated sheet beam device also looks interesting. Such a device is based on the interaction of the beam with the transverse beam-breakup mode. The tube can use discrete cavities to amplify the deflection (the Deflectron), or a continuous periodic structure (the Deflection Wave Amplifier). All sheet beam devices could in principle also be constructed as annular beam devices.

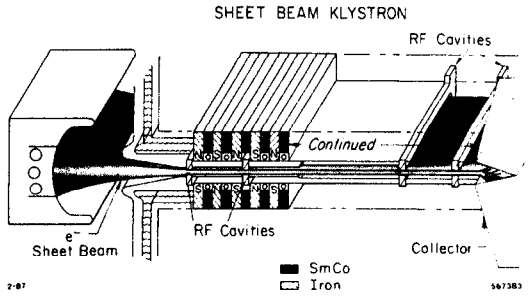

Fig. 1. Sheet beam X-band klystron.[11]

To obtain high output power at a relatively low voltage from a linear beam device, it is clear that the beam cross section area must be increased so that in one dimension it becomes large compared to the RF wavelength. Only a few relatively simple possibilities for such extended beam area devices have been considered in this brief survey. More exotic concepts using annular or sheet beams have been proposed, such as the Gigatron[12]. Crossed-field amplifiers, which inherently operate at a high perveance (microperveance on the order of ten), have not been discussed. It has recently been suggested[13] that such devices are capable of being scaled to high power levels. In conclusion, there are a number of potential RF sources which can be used in conjunction with RF pulse compression to power a high gradient linear collider. The difficult problems are not so much in concept as in the detailed engineering and development needed to advance the technology on a reasonable time scale.

REFERENCES

1. R. B. Palmer, TLC Parameter List (1988). See also R. B. Palmer, "Energy Scaling of Linear Colliders," these Proceedings.
2. M. A. Allen *et al.*, these Proceedings; see also SLAC-PUB-4733.
3. Z. D. Farkas, IEEE Trans. MTT-34, 1036 (1986); also SLAC-PUB-3694.
4. Z. D. Farkas, and J. N. Weaver, SLAC/AP-59 (1987).
5. R. D. Ruth, private communication.
6. Z. D. Farkas, G. Spalek and P. B. Wilson, "RF Pulse Compression Experiments at SLAC," to be submitted to the 1989 Particle Accelerator Conference.
7. T. G. Lee, private communication.
8. K. Eppley, "Design of a 100 MW X-Band Klystron," to be submitted to the 1989 Particle Accelerator Conference.
9. Jean V. Lebacqz, Proceedings of the 1979 Linear Accelerator Conference, BNL Report 51134 (1979); pp. 327–335. Also SLAC-PUB-2380 (August 1979).
10. V. L. Granatstein, "Gyroklystrons for Linear Supercolliders: An assessment of Feasibility and Cost." Invited lecture at the International Workshop on Next Generation Linear Colliders, Stanford Linear Accelerator Center, Nov. 28–Dec. 9, 1988.
11. K. R. Eppley, W. B. Herrmannsfeldt and R. H. Miller, Proceedings of the 1987 Particle Accelerator Conference, IEEE Cat. No. 87CH2387-9 (IEEE, New York, 1987). pp. 1809–1811.
12. H. M. Bizek, P. M. McIntyre, D. Raparia and C. A. Swenson, IEEE Trans. Plasma Sci. 16, No. 2, 258 (1988).
13. M. A. Allen and J. Feinstein, private communication.

RF POWER AMPLIFICATION BY ENERGY STORAGE AND SWITCHING

WAYNE VERNON
University of California, San Diego, La Jolla, California 92093

During the last decade there have been several suggestions for RF storage and switching schemes.[1-6] The principle behind these schemes is simply that energy from a source which is on for a long time at moderate power can be stored in a resonant cavity and dumped ("switched") in a short time to yield higher power. This is also the basis of SLED[7] which is driving the SLC, but the major difference is in the switching and the proposed power gains. In the case of SLED there is no switch, only a "phase agile" RF source, and the maximum power gain is about a factor of 3. Proposed storage and switching schemes are often based on larger ratios of charge to discharge times, say 5 μsec/50 nsec = 100 which could be the power amplification ratio.

An early demonstration of the switching of a superconducting cavity was reported by Birx, et al.,[1] in 1977. They observed a peak power gain of 9 at low power levels with a cold cavity and a room-temperature switch. The switch was a He gas filled tube positioned in the leg of a waveguide T so that a $\lambda/2$ stub turned into a $\lambda/4$ stub when the gas broke down and became a good conductor. All switches encountered to date are some variant of this technique; the stub reflects back an out-of-phase signal which cancels the one from the cavity so that no power escapes while the low-loss dielectric tube is non-conducting.

Simple discharge of a cavity results in an exponential decay of the power, and it may be more useful to have a length of waveguide be the resonant element so that a constant power pulse is generated with a width equal to twice the waveguide's propogation time. Such a test was reported from the USSR in 1979;[5] power levels of 70 MW with a pulse width of 15 nsec were obtained for the S-band waveguide (1.2 m length) being driven by a 1.6 MW source. This was a room temperature system with a storage time constant of about 1 μsec. During the workshop Roger Miller suggested that a circular waveguide operating in low loss mode (TE_{01}) might allow the charging time constant to increase to 5 μsec which could result in large power amplification with 50 nsec output pulses.

A related development involves RF storage in superconducting cavities filled with sapphire.[8,9] The single-crystal pieces of sapphire fit inside the cavity with a small (1 mm) gap between the crystal and the superconducting wall and the electric and magnetic fields at the wall are quite a bit lower than in the empty cavity (for the same stored energy). If cavity modes can be found which keep the surface electric fields low, then energy densities of 25 mJ/cm^3 for X-band RF should be possible (the dielectric constant is of order 10 for these frequencies). If a dielectric loaded waveguide with a 6 cm^2 cross section and a length of 1.6 m is used as the resonant cavity, then that one liter crystal could store 25 Joules of RF and return it as a 50 nsec long pulse of 0.5 GW accelerator drive power. Single-crystal sapphire costs about $ 10,000/liter, which is modest in this context. Power amplifications of 10^4 at GW output power levels might be possible.

It would appear that further evaluation of these schemes is warranted, especially if the switch part of the problem can be shown to work. The next generation of "SLED" will probably use "phase switching" with many stages of delay lines;[10] this rather complicated approach comes about because of the absence of trustworthy switch technology. One switching technique which seems to not have been tried with RF is the use of high resistivity silicon which is made to conduct with a laser pulse. It may be that the silicon can survive the high electric fields associated with the large stored energy in the resonant structure. If one of these energy storage approaches turned out to be moderately priced and reliable, then the high cost of peak RF power would cease to be the dominant problem in linear collider design.

REFERENCES

1. D. Birx, G. J. Dick, W. A. Little, J. E. Mercereau and D. J. Scalapino, *Microwave Power Gain Utilizing Superconducting Resonant Energy Storage*, Appl. Phys. Lett. **32**, 68 (1978).

2. Kazuo Minami and Kenji Hosoyama, *Proposal of a High-power Microwave Pulse Source Utilizing a Superconducting Cavity for Energy Storage*, Japanese Jour. of Appl. Phys. **18**, 85 (1979).

3. D. L. Birx and D. J. Scalapino, *A Cryogenic Microwave Switch*, IEEE Trans. on Magnetics, **MAG–15**, 33 (1979).

4. D. L. Birx and D. L. Scalapino, *Microwave Energy Compression Using a High-Intensity Electron Beam Switch*, J. Appl. Phys., **51**, 3629 (1979).

5. N. D. Devyatkov, A. N. Didenko, L. Ya. Zamyatina, S. V. Razin and Yu. G. Yushkov, *Formation of Powerful Pulses With Accumulation of UHF Energy in a Resonator*, Radio Eng. and Electron Phys., **25(6)**,87 (1980).

6. K. Saeki, T. Kimura, H. Kubo, K. Minami, M. Ohtsuka and M. Awano, *Microwave Pulse Source Utilizing a Superconducting Cavity*, Oyo Buturi, **54(8)**, 812 (1985); in Japanese.

7. Z. D. Farkas et al., *SLED: A Method of Doubling SLAC's Energy*, Proceedings of the 9th International Conference on High Energy Accelerators, p. 576, May 1976.

8. V. B. Braginsky and V. I. Panov, *Superconducting Resonators on Sapphire*, IEEE Trans. on Magnetics, **MAG–15**, 30 (1979).

9. D. G. Blair and S. K. Jones, *A High-Q Sapphire Loaded Superconducting Cavity Resonator*, J. Phys. D: Applied Physics **20**, 1559 (1987); see also IEEE Trans. on Magnetics, **MAG–21**, 142 (1985).

10. Z. D. Farkas, *Binary Peak Power Multiplier and its Application to Linear Accelerator Design*, IEEE Trans. on Microwave Theory and Tech., **MTT–34**, 1036 (1986).

A CLUSTER KLYSTRON*

ROBERT B. PALMER and ROGER MILLER

Stanford Linear Accelerator Center, Stanford University, Stanford, California 94309

ABSTRACT

We consider a honeycomb-like array of 126 individual klystrinos all fed from a single high-voltage source and all focused by a single axial magnetic field. It is argued that such a device may be a practical and economic power source for a TeV Linear Collider. It could be used either as a source of $\frac{1}{2}$ μsec rf pulses to be binary pulse compressed or, with a grid cathode and oil line energy storage, as a direct source of power.

1. INTRODUCTION

For a .5 on .5 TeV Linear Collider we need (for example)[1]

wavelength $\lambda = 17.5$ mm
power/length $P \approx 600$ MW/m
length/feed $\ell_{\text{feed}} = 1.6$ m
power/feed $P_{\text{feed}} = 930$ MW
no feeds $n_{\text{feed}} = 3.6$ K
pulse length $\tau = 60$ nsec
energy/length $J = 36$ Joules/m
total length $\ell_{\text{cavity}} \approx 6$ Km
total energy $J_{\text{TOTAL}} \approx 200{,}000$ Joules
total power $P_{\text{TOTAL}} \approx 3.4$ TWatts

If we consider the use of "conventional" klystrons operating at a voltage of the order of 400 KV then space-charge considerations (perveance ≤ 2) limit the current to 500 amps and the power output (at 50% beam-to-rf efficiency) per tube to 100 MW. And even this would be hard to achieve at 17 GHz. With 100 MW/tube, 34,000 tubes would be required. To avoid this two approaches are possible: either raise the voltage thus allowing higher currents; or use sheet or multiple beams so as to provide the very large number of "tubes" required without excessive cost.

The objections to raising the voltage are now becoming clear:

A) Higher voltage implies intense X-ray production, requiring significant shielding, and probably forcing the location of such klystrons in the accelerator tunnel rather than in a gallery.

B) Very high voltages are best obtained with Induction Linacs rather than a simple gun. Such Linacs are excessively expensive unless the drive current is relatively high (e.g., $\sim$ 10K amps). But such high currents require even higher beam energies with corresponding problems and development time.

C) The power supplies (e.g., magnetic compressors) to drive the required Induction Linacs with short pulses are also expensive.

For these reasons it is worth considering the other alternatives.

A) The Sheet-beam klystron has been studied by R. Miller et al.[2] Several problems were revealed: The efficiency was relatively low; there is a problem with maintaining the phase stability in the cavities, and there is a danger of feedback from the output to the input cavity of transversely polarized rf.

B) These problems are, of course, absent in a multi-klystrino approach as proposed by G. Loew.[3]

The present note represents an alternative packaging of Greg's basic idea.

2. PARAMETERS OF AN INDIVIDUAL KLYSTRON

We will consider two cases: 1) with a cathode of 8 amps/cm^2 and 2) with 32 amps/cm^2 and compare these

*Work supported by the Department of Energy, contract numbers DE-AC02-76CH00016 and DE-AC03-76SF00515.

with a conceptual design[4] of a 100 MW 12 GHz tube (refer to the table on the following page).

It is seen that the parameters of examples (1) are universally conservative, and of example (2) conservative in everything but the cathode current. Let me assume that we adopt example (1) for phase I of our TLC (i.e., 250 + 250 GeV) and hope that the higher current will become available for the full TLC (500 + 500 GeV). Then the number of tubes required is:

		Klystrino	
	Ref Design	Exp1(1)	Exp1(2)
$f\ gH_z$	12	17	
$j_{\text{cathode}}\ A/\text{cm}^2$ [1]	8	8	(32)
diam (cathod) mm	90	18	
I amps	500	20	(80)
V kVolts	400	400	
Perveance [2]	$2\ 10^{-6}$	$.08\ 10^{-6}$	$(.32\ 10^{-6})$
efficiency [3]	50	75	(70)
P_{out} MWatts	100	6	(24)
B Tesla [4]	0.5	0.15	(0.3)
diam (drift tubes) mm	9	6	
$R = \frac{\text{cathode diam}}{\text{drift tube diam}}$ [5]	10	3	
J_{in} for 62 nsec		5	(20)
J_{in} for 75 nsec		6	(24)
J_{in} for 520 nsec		42	(166)

Notes:

[1] 8 amps/cm^2 is standard SLAC 5045 performance and thus very conservative. 32 amps/cm^2 is claimed to be now available from Varian, although its vacuum requirements and lifetime seem uncertain; it represents a less conservative but not unreasonable goal.

[2] Perveance is defined by

$$Pv = \frac{I(\text{amps})}{V^{\frac{3}{2}}(\text{Volts}^{\frac{3}{2}})}$$

and is a measure of the severity of space-charge effects.

[3] The efficiency of converting beam power to rf power could, if there were no space-charge effects, approach 100%. In practice the efficiency obtainable falls as the perveance rises (fig. 1),[6] and the assumed efficiencies used have reflected this empirical observation.

[4] The field required to balance the space-charge forces in the beam is given by:

$$B \propto \frac{1}{\lambda}(\frac{I}{\beta\gamma})^{\frac{1}{2}} \quad .$$

In these examples I have scaled from the 17 GHz 100 MW design.[4]

[5] The ratio of cathode to drift tube diameters is a measure of the precision with which the gun must be designed and built. There may be no theoretical limit to this ratio but in practice ratios larger than about 7 are hard to achieve without beam loss.

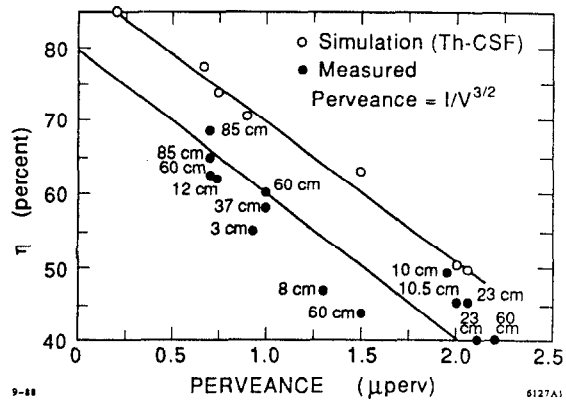

Fig. 1. Klystron efficiences plotted as a function of perveance. The wavelengths of examples are given by each measured point. The lines represent an approximate fit to the simulated and measured values.

a) With 8× pulse compression at 85% efficiency[5]

$$n = \frac{3.4\ \ 10\ 12\ \text{Watts}}{.85 \times 24\ \ 10\ 6\ \text{Watts}} \times \frac{1}{8} = 29{,}000 \quad ;$$

b) with no pulse compression

$$n = \frac{3.4\ \ 10\ 12}{24\ \ 10\ 6} = 140{,}000 \quad .$$

These are formidable numbers. How can one build them at reasonable cost?

3. THE HONEYCOMB CONCEPT

It is proposed here to build the klystrons into honeycomb-like structures. Each structure containing 126 individual klystrons. The number of such structures is now

a) with 8× pulse compression at 85% efficiency

$$w_s = \frac{18{,}000}{.85 \times 126} \approx 170 \quad (1 \text{ per } 35 \text{ m}) \quad ,$$

b) with no pulse compression

$$\overline{n_s} = \frac{140{,}000}{126} = 1140 \quad (1 \text{ per } 6 \text{ m}) \quad .$$

Both of which seem reasonable. Indeed, if such clusters can be built for a reasonable cost, and if a method to power the tube for $\approx$ 60 nsec can be provided, then pulse compression would seem unnecessary.

It is proposed here to group the klystrons into clusters of 18 (see fig. 2a). Each cluster would have its own input and output wave guide. Within a cluster the cavities of all 18 tubes would be strongly coupled and thus locked in

phase and amplitude. Each cluster of tubes would act as a single klystron, with the only difference that the current is broken up into sub beams, and, as a result the space charge forces greatly reduce.[7] Seven of these clusters would form a single structure with 126 individual tubes (see fig. 3a).

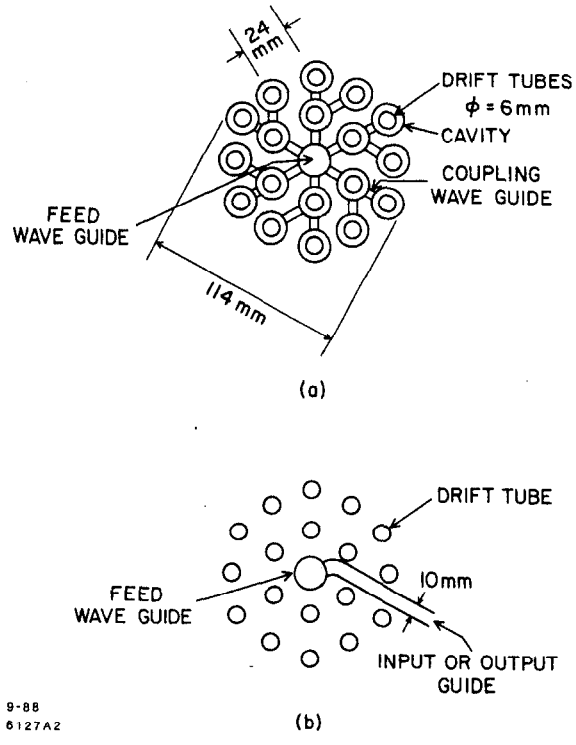

Fig. 2. A single cluster of 18 klystrinos; a) showing the cavities with rf feed at center; b) showing drift tubes between cavities with input or output guide to the feed.

The waveguides to feed, damp or extract power from a cluster of cavities could consist of short longitudinal mode guides at the center of each cluster. In the case of the output cavities these longitudinal guides could continue out through the beam dump. For the input guides they would extend just into the space before the next cavity, and there convert to conventional guides passing between the drift tubes (fig 3b). They could then couple again into longitudinal guides outside the honeycomb and pass thus out through the beam dump.

The object in this design is to minimize the number of parts. The input, output, or intermediate cavities, of all 126 tubes would be machined into discs of Copper, as would the feed waveguides (fig. 4). Though each disc would involve complex machining, the number of such discs would be no more than the number of parts in a single klystron.

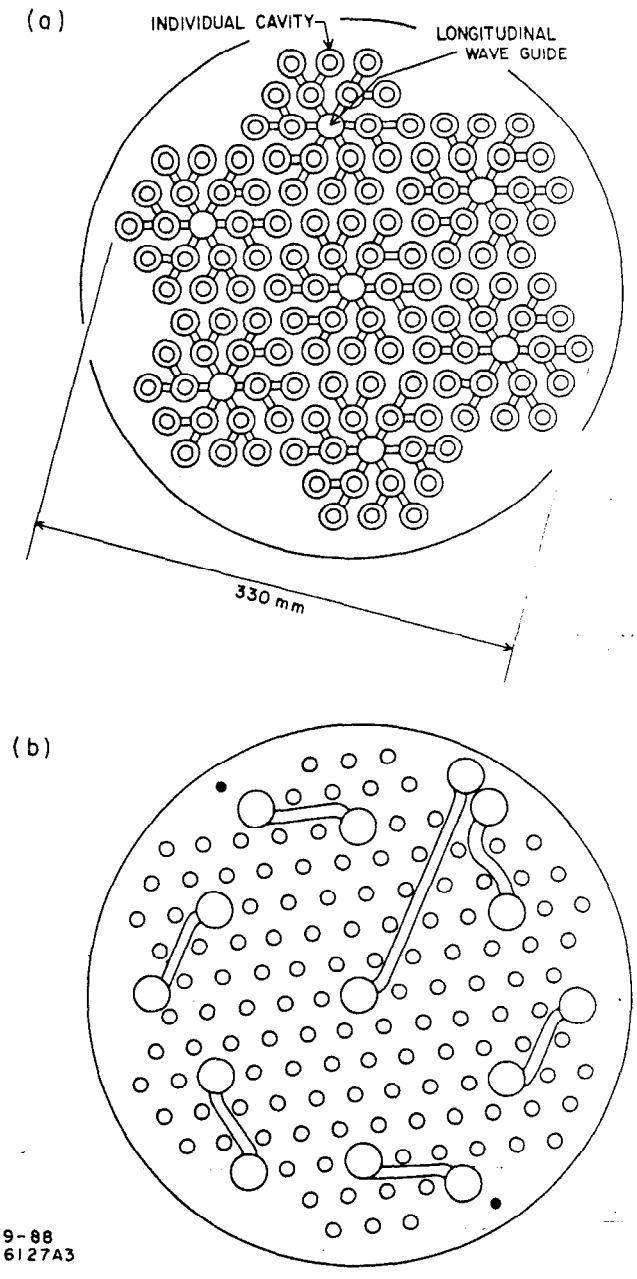

Fig. 3. Seven clusters in a single copper block; a) showing cavities; b) showing guides joining cluster feeds to external axial wave guides.

4. GUN DESIGN

Focusing within the honeycomb of klystrons can be provided by a uniform axial magnetic field. In order to keep the beams within the drift tubes the transverse fields must be small and the field quality requirement for the 275 mm diameter area should be of the order of:

$$\frac{\Delta B}{B} \leq 2 \times 10^{-3} \quad .$$

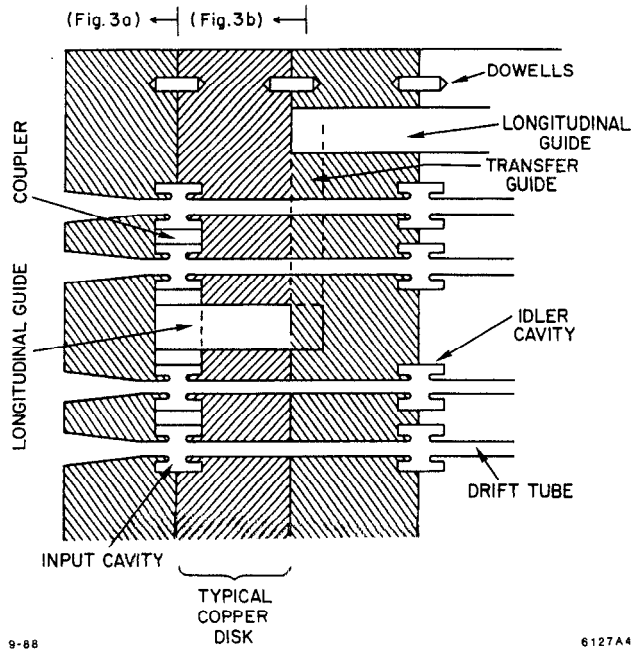

Fig. 4. Section showing construction.

At the cathode end the situation is more complicated. The field must be reduced in order to allow the current to converge from the larger cathode area into the smaller drift tubes. The method proposed is to use an iron end plate with holes in it to effectively end the axial fields (fig. 5).

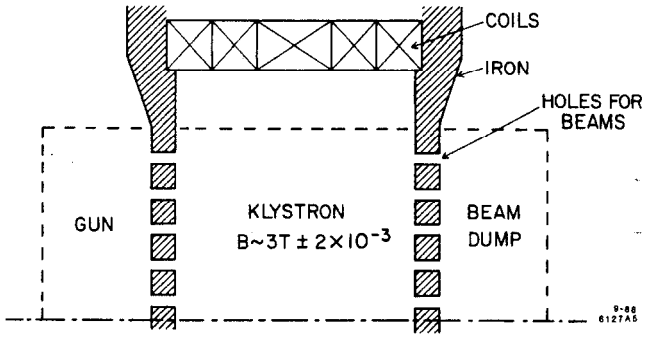

Fig. 5. Magnet with perforated iron end plates to restrict field to the klystron region.

The required thickness t of the iron plate depends on the focusing field B_k, the allowed field in the iron B_{Fe}, the hole radii r, the hole spacing s and the total honeycomb radius R

$$t = \frac{R}{2}\frac{B_k}{B_{Fe}}\frac{s}{s-r} \quad .$$

For the high j_c example: $B_k = 0.3$ Tesla, $B_{Fe} = 1$ Tesla R = 140 mm, r = 10 mm and s = 24 mm. Then, t = 43 mm (or 22 m for the lower current density).

Outside the iron plate the gun geometry would be relatively conventional (fig. 6). The design is complicated by the relatively late application of the magnetic field, but is eased by the low reduction ratio from the cathode to drift tube (3×).

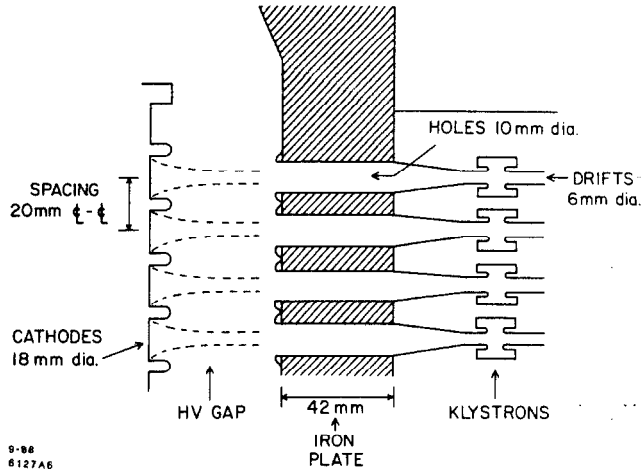

Fig. 6. Conceptual view of gun.

5. POWER SUPPLIES AND EFFICIENCY

A. Binary Pulse Compression

If used with 8× pulse compression then an initial pulse of 520 nsec would be required (60 nsec output pulses with 6 nsec between pulses to allow time for the phase to change). A 400 KV 520 nsec modulator could presumably be designed along more or less conventional lines. If the rise and fall times of such a modulator were ≈ 100 nsec, and the power supply efficiency were 90% than the overall efficiency would be:

$\eta_a =$	·9 ×	·8 ×	·7 ×	·9 ×	·85	= ·38
	↑	↑	↑	↑		
	Power Supply	Rise & Fall	Klystron	Time to Change Phase	Pulse Compression	

It would be reasonable to put a separate pulse compressor on each pair of clusters. For the 32 amp per square cm case, the output power is 432 MW per cluster of 18 tubes (18 * 24). Using two such clusters as input to an eight-fold compressor, the output (at 85% efficiency) would be 2.8 G watts emerging from each of two waveguides. These would have to be divided into three to give the required .9 G watt per feed. There would then be:

1 klystron/21 feeds, (1 klystron/35 m)

1 compressor/6 feeds, (1 compressor/10 m)

Total: 3.6 K feeds

600 compressors

171 klystrons

B. Magnetic-Pulse Compressor

If no pulse compression were used then a power supply is needed that can give 400 KV for a 60 nsec pulse. Magnetic compressors could do this. The rise and fall time would be of the order of 15 nsec leading to an overall efficiency:

$$\eta_b = \underset{\substack{\uparrow \\ \text{Power Supply}}}{\cdot 9} \times \underset{\substack{\uparrow \\ \text{Magnetic Compressor}}}{\cdot 9} \times \underset{\substack{\uparrow \\ \text{Rise \& Fall}}}{\cdot 75} \times \underset{\substack{\uparrow \\ \text{Klystron}}}{\cdot 7} = \cdot 42$$

C. Grid-Controlled Cathode

Another way to obtain the required 60 nsec pulse of 10,000 Amps would be to leave essentially full voltage on the gap but switch the current with a grid placed close to the cathode. The gun gap would be connected to a suitable oil delay line (fig. 7a), recharged by a power supply between pulses. The voltage wave from the gap would be as shown in fig. 7b; and the maximum gap voltage V_0 will be given by:

$$V_0 = V_k \frac{1 + Z_0}{R_k} \quad ,$$

where V_k = klystron voltage = 400 KV, R_K = klystron impedance = $\frac{400\text{KV}}{10{,}000\text{A}}$ = 40 Ω 's (160 Ω 's for the lower current density) and Z_0 = impedance of the line.

The energy stored in the line U_0 is given by:

$$U_0 = U_K \frac{R_K}{4Z_0} \left(1 + \frac{Z_0}{R_K}\right)^2 \quad ,$$

where U_K is the energy required by the klystron.

$$Z_0 = 10\Omega (40\Omega \text{ for the lower current density})$$

and the energy stored in the line is

$$U_0 = 1.56\, U_K \quad .$$

It is not unreasonable to expect a rise time for the grid voltage, and thus currents, of the order of 2 nsec—significantly faster than that for the magnetic compressor. We will assume a 6 nsec rise time for the klystron. The efficiency of the oil line will be near 100%. Assuming a 90% efficiency for the power supply then the overall efficiency would be:

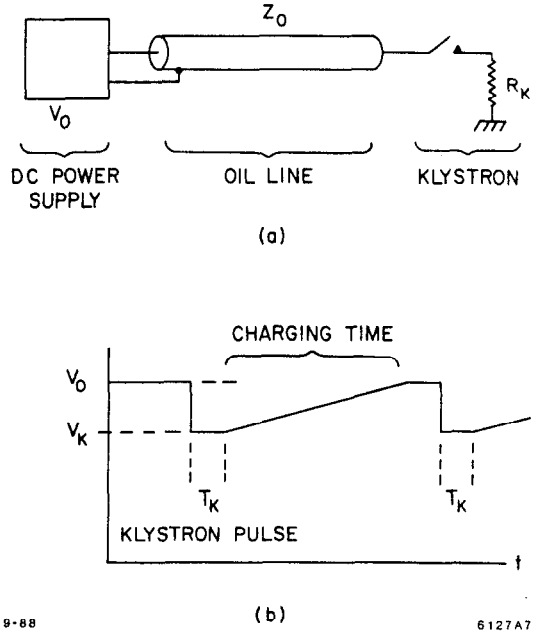

Fig. 7. Power supply for a grid controlled klystron a) schematic; b) voltage at end of oil line as a function of time.

$$\eta_c = \underset{\substack{\uparrow \\ \text{Power Supply}}}{\cdot 9} \times \underset{\substack{\uparrow \\ \text{Rise \& Fall}}}{\cdot 9} \times \underset{\substack{\uparrow \\ \text{Klystron}}}{\cdot 7} = \cdot 57$$

Although the grid-controlled cathode and oil lines require significant R&D the higher efficiency that could be obtained would be well worthwhile.

6. COST ESTIMATES

It is clearly very hard to estimate costs at this time. We do it only to see if there is any hope of the costs being significantly lower than other methods.

In the case using binary pulse compression the modulator can be scaled from SLAC at about .5 \$/Joule input. For the pulse compressor we use 100K\$ per unit which is twice P. Wilson's estimate (physicists are usually a factor of 2 low).

For the magnetic compressor we have used prices from W. Barletta at Livermore of .7 \$/Joule input including the power supply. Bayless' estimates are similar.

For the oil line and power supply we took .4 \$/Joule, a little less than the SLAC Modulator cost. This is a very unreliable guess.

For the klystron itself we have guessed a figure of 200K\$ per unit. This is four times the SLAC 5045 cost, and is based on the observation that the cluster klystron is likely

Table 1.

A. With Binary Pulse Compression and Conventional Modulators ($\epsilon \approx 38\%$)			
	Units	K$/Unit	M
Modulators	170	1000 (250)	180 (50)
Klystrons	170	200	30
Binary Compressors	600	100	60
Total rf Source			270 (140)
B. With Magnetic Compression and no BPC ($\epsilon \approx 42\%$)			
	Units	K$/Unit	M
Magnetic Compressor + PS	1100	200 (50)	200 (60)
Klystrons	1100	200	220
Total rf Source			440 (280)
C. With Grid Cathode and no BPC ($\epsilon \approx 57\%$)			
	Units	K$/Unit	M
PS + Oil Line	1100	100 (25)	110 (30)
Klystrons	1100	200	220
Total rf Source			330 (250)

to weigh about four times more!

Using these assumptions, we estimate costs in Table 1. The parenthesized numbers in the table are for the lower current Phase I.

From Table 1 we conclude:

1) These costs are low and efficiencies higher, compared with those obtained for current moderate energy ($\lesssim$ 2 MeV) relativistic klystron designs.

2) There seems no advantage in using the magnetic compression example (B).

3) If 32 amps/cm^2 cathodes are okay then there is little significant cost difference between the approaches (A) and (C). The grid cathode and oil line (example C) is then preferred for its higher efficiency and pulse flatness.

4) If the cathodes only operate at 8 amps/cm^2 then there is probably a cost advantage in using binary pulse compression (example A).

But these conclusions may change when more is known. Note that other combinations such as grid control plus some Binary pulse compressions were not considered but may be a good compromise.

7. WORK TO BE DONE

1. See if the gun design is possible. Note that it may *not* be possible. Multiple Iron plates might be needed to raise the field more gently. Intermediate potential electrodes may be needed between cathode and anode to shape the fields and or shield space-charge effects.
2. Make a better cost estimate of the klystron. What will a 1.5 or 3 Kg magnet with 10^{-3} field quality cost? What are the machining costs? Can the iron be a brazed part of the klystron?
3. Design the Klystrino itself. Emphasis should be given to achieving the high efficiency that the low perveance should make possible. Double output cavities are essential and R. Ruth's phase-space swirling should be studied.
4. Get information on performance and cost of oil lines and 500KV DC supplies. It is important to gain order of magnitude cost estimates early to avoid wasted effort if they are too high.
5. Get better engineering, including installation cost estimates for binary pulse compression as a function of the number of stages.
6. Get more information on 32 amp/cm^2 cathodes, including information from LBL on LaB_6 thermionic cathodes.
7. Build a single cluster gun with a *single* klystrino on the central cathode. Tuning and variable damping should be available for all cavities to fix these parameters prior to #8.
8. Build a full single-cluster klystron with 18 tubes giving 108 MWatts.
9. Start R&D Program on high current cathodes.
10. Start R&D Program on grid-controlled cathodes (conditional on #4).

REFERENCES

1. Palmer, R.B., *The Interdependence of Parameters for TeV Linear Colliders*, SLAC-PUB-4295 (1987) and *Proceedings of the Workshop on New Developments in Particle Acceleration Techniques*, June 29–July 1987, Orsay, France; CERN 87-11; ECFA 87-110. R. B. Palmer, *Linear Collider Energy Scaling*, SLAC-PUB-4707 (1988) and *Proceedings of the DPF Workshop*, June 27, 1988, Snowmass, Colorado.
2. Eppley, K. R., W. B. Hermansfeldt and R. H. Miller, *Proceedings of the 1987 IEEE Particle Physics Conference*, March 16–19 1987, Washington D.C.
3. Loew, G., *Considerations of r.f. Frequency and Power Generation in Linear Colliders Using Conventional Technology*, SLAC Internal Report AAS #22.
4. Eppley, K. R., private communication.
5. Farkas, Z. D., *Binary Peak Power Multiplier and Its Application to Linear Accelerator Design*, SLAC-PUB-3694 and IEEE Trans. on Microwave Theory and Techniques, **MTT-34**, No. 10, p. 1036 (1986).
6. Simulation data is from Thompson-CSF, private communication.
7. The use of multiple channels to suppress space charge effects has been proposed for light ion acceleration by A. W. Maschke, Brookhaven National Laboratory Report, BNL 51209 (1979).

A MICROWAVE POWER DRIVER FOR LINAC COLLIDERS
GIGATRON

Hana M. Bizek*, Stephen M. Elliott, Peter M. McIntyre, Alireza Nassiri, Milorad B. Popovic, and Deepak Raparia
Department of Physics, Texas A&M University, College Station, Texas 77843-4242

and

Henry F. Gray
Code 6844, Naval Research Lab., Washington, D.C. 20375

*Present address: Advanced Photon Source, Argonne Nat'l Lab., 9700 S. Cass Ave., Argonne, IL 60439

ABSTRACT

The gigatron is a new rf amplifier tube designed for linac collider applications. Three design features permit extension of the lasertron concept to very high frequencies. First, a gated field-emitter array is employed for the modulated cathode. Second, a ribbon beam geometry mitigates space charge depression and facilitates efficient output coupling. Third, a traveling wave output coupler is used to obtain optimum coupling to the ribbon beam. This paper describes recent developments in the gigatron design, and progress towards experimental tests.

I. INTRODUCTION

This paper describes recent progress in the development of gigatron as a high-power microwave driver for future e⁺e⁻ linac colliders.[1] The gigatron design concept has been described previously.[2] We have evaluated its design for the parameters required for most TeV linac collider designs:

rf frequency 10-30 GHz
rf power >100 MW
efficiency >50%.

The only rf devices with comparable capability are the relativistic klystron[3] and the gyroklystron[4]. By comparison to either of these the gigatron offers a simple, compact structure and low capital cost.

In the gigatron a bunched electron beam is extracted from a field emitter array (FEA) cathode, and accelerated through a pulse-modulated high-voltage diode as shown in Figure 1. The resulting beam is fully modulated at high energy without the requirements of modulator and drift region that characterize all conventional amplifier tubes. RF energy is then extracted from the beam in an output coupler. Since the bunching process is a dominant limitation to high power-high frequency operation in conventional tubes, this approach results in high performance for the above design parameters.

Three features of the gigatron design extend its performance to very high frequency and peak power. First, a ribbon beam geometry is adopted rather than the conventional round beam. Second, a traveling wave output coupler is used to achieve optimum output coupling across a wide beam. Third, a gated field emitter array (FEA) is employed for the cathode; this appears to offer a simple, reliable modulated cathode for microwave applications.

By the beginning of the past year we had calculated the beam dynamics in gigatron and verified the impressive performance estimated earlier. During the past year we have addressed three design issues raised in reviews of the gigatron technology. First, it was suggested that the ribbon beam might be unstable, since many previous ribbon beam devices have proven unstable. Detailed calculations have demonstrated that the gigatron beam is in fact extremely stable to a variety of perturbations over the full range of parameters contemplated. The reason for this is simply that the gigatron approaches a switch tube geometry: the beam has no time in which for instabilities to grow. From cathode to collector is ~6 rf cycles.

Second, it was suggested that the traveling wave coupler might have parasitic modes that could compromise the coupling to the desired loop-resonant traveling wave. We have shown that, by distributing the beam-wave coupling along ~ half the circumference of a loop-resonant circuit, higher-order modes (corresponding to different harmonics of the loop-resonant frequency) are in fact naturally suppressed. Only transverse harmonics remain; these occur at multiples of the operating frequency and are weakly coupled to the beam. The waveguide coupler thus appears to be a particularly benign structure for this traditional tube designer's headache.

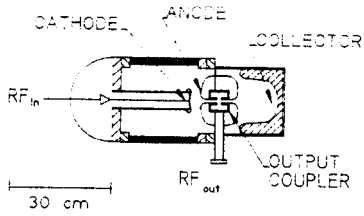

Figure 1. Cross section of gigatron.

The third problem is more substantial: microwave modulation of the FEA cathode. FEA cathodes have been built by several groups,[5,6,7] and have achieved impressive performance. Currents of >100A/cm² have been achieved. Extended life-cycle tests show no deterioration during a year of continuous operation. But these results were obtained in DC operation. The FEA gate structure presents a highly capacitive load to a modulation driver. The charging resistance R through the silicon substrate appears in series with the gate capacitance C and renders the FEA cathode configurations built by previous authors unworkable at microwave frequencies.

During the past year we have developed several specific improvements to FEA cathode design that together overcome this problem. First, a base layer metalization is incorporated so that charging currents flow in metal rather than silicon. Second, we configure the cathode as a lumped-constant resonant circuit (Q ~100), which is matched to a 50 Ω modulator input. With these improvements the system gain of gigatron is ~25-30 dB.

II. GIGATRON DESIGN CONCEPT

The gigatron is a design for a compact, efficient microwave power amplifier tube. It employs the lasertron concept,[8,9] in which a bunched electron beam is extracted from a modulated cathode and accelerated through a high-voltage diode structure. Several significant innovations have been introduced to achieve high efficiency, high frequency, and high power. The principle of operation is illustrated in Figure 2. A fully modulated ribbon electron beam is produced from a strip cathode of gated field-emitter array (FEA). The ribbon beam is accelerated through a high-voltage diode structure, and enters a drift slot leading to the output coupler. The output coupler consists of a slotted waveguide connected to form a resonant loop. The waveguide slot is configured to permit passage of the ribbon beam through the waveguide, parallel to the electric field of a traveling wave. The electron beam is decelerated by the wave, and thereby drives the wave amplitude. Optimum phase match to the electron beam is maintained over an arbitrary beam width by phasing the electron beam emission from the cathode to tilt the ribbons with respect to the direction of acceleration. By a

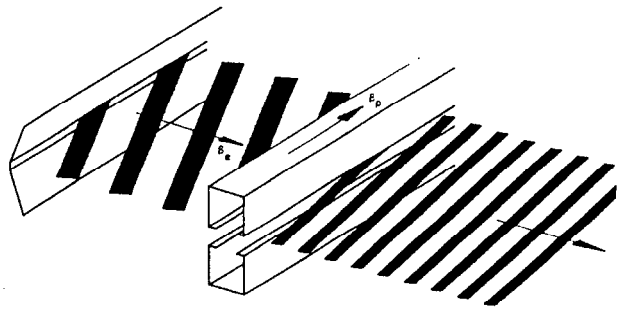

Figure 2. Ribbon beam geometry and traveling wave coupler.

suitable matching condition, the transverse position of the electron packet traversing the coupler slot can be made to move sideways at the same rate as the phase velocity of the traveling wave. The beam "surfs" with the wave, and optimum coupling can be preserved over an arbitrary beam width.

The advantages of the gigatron include a) low-loss coupling of input power to the FEA structure; b) e-beam fully modulated before acceleration; c) elimination of space-charge limits to high power/high frequency by using ribbon beam geometry; d) close coupling to the ribbon beam in the output coupler reduces phase dispersion at high frequency; e) provision of optimum output coupling over a wide beam front, using the traveling wave coupler; e) elimination of the requirement for static guide fields that characterize nearly all high frequency power tubes; f) simple, compact structure. Table I summarizes the important parameters of a particular design which has been evaluated recently.[2] The following text describes each aspect of the gigatron design. Numerical calculations are specific to the parameters of Table I.

1. Gated field-emitter cathode. The gated field-emitter (FEA) cathode appears to offer an attractive new technology for achieving a high current, fully modulated electron beam directly from a cathode structure.[5] C.S. Spindt et al.[5] and H. Gray et al.[6] have developed microfabrication techniques by which they can prepare planar arrays of field-emitting points. Gray uses directional etching techniques to produce atomically sharp needle and knife-edge arrays directly on silicon. A silicon-insulator-metal gate structure is then deposited on the cathode substrate, and plasma-etched to form a planar array of micro triodes. Application of a modest (25 V rms) gate-cathode voltage results in full modulation of emission current. Currents of >100 A/cm² have been routinely achieved. There is no evidence of in-service deterioration during extended life tests.[5]

We have improved upon the fabrication procedure of Gray in two respects that are critical to achieve high-frequency modulation.

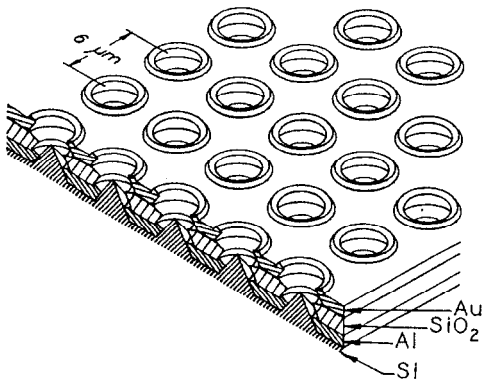

Figure 3. Gated field emitter array cathode.

First, the silicon surface is metalized after formation of the field-emitting tips, as shown in Fig. 3. This provides a metal base surface for low-impedance charging of the FEA tips. In the devices fabricated by Gray[6] and Spindt[5], charging current must flow through the bulk of the silicon substrate. Even with heavy doping, the silicon substrate presents an unacceptable charging resistance ($\rho > .01\ \Omega$ cm) at high frequency.

Second, a fabrication process has been devised whereby an optimum field geometry can be produced for quiesent electron optics. The optics of the electron beam emission from the FEA cathode determines the initial emittance of the beam in the gigatron. We have calculated the beam dynamics during field emission using the computer code MASK[7]. Beam is assumed to be emitted from the tip into a cone of half-angle $\pi/4$. Figure 4 shows the transport at several time intervals after emission. The tip/gate geometry of the cathode forms an approximate point-to-parallel optical lens. As a result the emitted beam will have a much smaller emittance than the previous estimates based simply on assuming a transverse temperature $T_\perp \sim eV_m$. The beam divergence produces negligible transverse growth at the anode aperture, and hence does not pose a limitation to gigatron performance. If in fact the effective emittance is very small, the improved FEA cathode may be an excellent candidate for electron sources for linacs, FEL's etc.

2. Resonant input coupler. The field-emitter array presents a highly reactive load to a modulation driver. Matching can be optimized by configuring the cathode within a sequence of coupled lumped-constant resonant circuits, as shown in Figure 5. The gate/base junction of the FEA constitutes a capacitance C_1. A metalized quartz fiber is mounted adjacent to the FEA, and the metal-insulator-metal layers (without tips) are continued laterally to form a tuning capacitance C_2. The gate layer metalization and quartz fiber metalization are interrupted along the region where the fiber contacts the insulating layer, so that rf currents to/from the gate layer must flow around

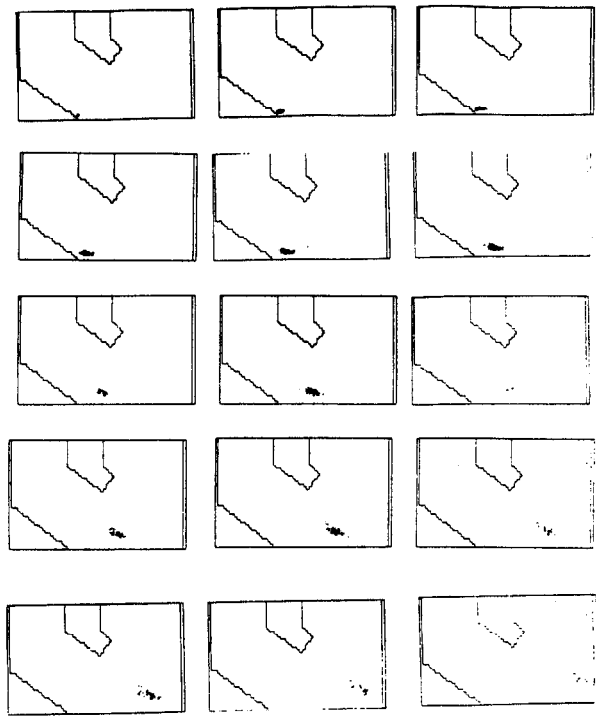

Figure 4. Acceleration of an electron bunch from an FEA cathode.

the fiber - it is an inductor L. The system C_1 - L - C_2 then forms a resonant circuit whose frequency can be controlled by choice of the radius r of the inductive fiber:

$$L = \mu_o \pi r^2 / x \qquad (1)$$

The cathode and resonant coupler are divided lengthwise into segments of equal length x = 5 mm. The metalized inductor is fabricated separately and bonded to the gate layers of C_1 and C_2 by conventional ultrasonic bonding.

Figure 6 shows an equivalent circuit of the cathode system, including dc bias network, resonant network, and impedance matching network. Each resonant circuit is capacitively coupled (C_c) to an impedance matching network which matches rf power from a waveguide into the sequence of input couplers. Resonance occurs at an angular frequency

$$\omega = \frac{1}{\sqrt{LC_o}} \qquad (2)$$

where C_o is the equivalent capacitance of C_1, C_2, C_c. The resistance R in the equivalent circuit is the effective series resistance to current flow in the resonant circuit:

$$R = (\tfrac{2}{3} w + 2\pi r)\, R_s / x \qquad (3)$$

where $R_s = .04\ \Omega$ is the surface resistance of the metalizations.

The Q of the resonant circuit is

$$Q = \frac{1}{\omega C_o R} \simeq \frac{1}{\omega C_1 R} \qquad (4)$$

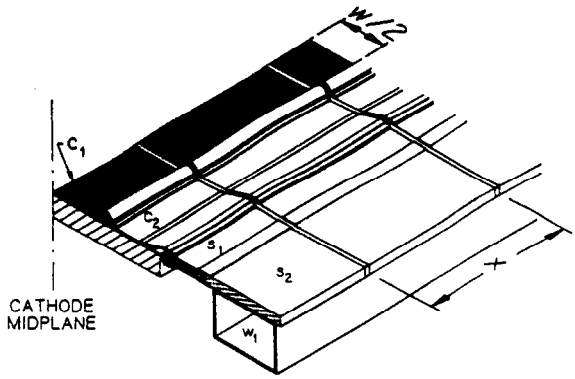

Figure 5. FEA cathode and resonant coupler.

The resulting load impedance Z_L for critical coupling is

$$Z_L = \left(\frac{1}{1+1}\right) Q^2 R/4 \qquad (5)$$

Using parameters of Table I, each resonant network has

$$\begin{aligned} C_1 &= C_2 = 72 \text{ pF} \\ C_c &= 5 \text{ pF} \\ L &= 2.2 \text{ pH} \\ r &= 50 \ \mu\text{m} \\ R &= 9 \times 10^{-3} \ \Omega \\ Q &= 28 \\ Z_L &= 2 \ \Omega \end{aligned} \qquad (6)$$

The emission current corresponding to the above modulation characteristic is $I_m = 390$ A peak, $I_o = 8$ A from a (14 cm x 1 mm) cathode. The power supplied from the input modulator that is required to supply this emission is

$$P_e = I_m V_m \frac{\sin(\Delta\phi/2)}{\pi} = 2.2 \text{ kW} \qquad (7)$$

The input power P_m required to drive each resonant network is

$$P_m = R(\omega C_1 V_m)^2/2 = 350 \text{ W} \qquad (8)$$

In the overall cathode there are $N = 2\ell/x = 56$ networks. The total input rf power requirement is

$$P_{in} = P_e + NP_m = 22 \text{ kW} \qquad (9)$$

The rf gain of gigatron is therefore

$$G = \log (P_{out}/P_{in}) = 27 \text{ dB}. \qquad (10)$$

3. Traveling Wave Coupler. The traveling wave coupler naturally suppresses all parasitic modes. The resonant loop of waveguide has a total length chosen to be an integral number M of phase wavelengths:

$$2\ell = 2\pi M \frac{\beta_p c}{\omega} \qquad (11)$$

For the parameters of Table I, an appropriate choice would be $M \simeq 14$. In principle, parasitic modes could be excited at frequencies corresponding to neighboring integral harmonics $M' \neq M$. The coupling to each mode M' must, however, be averaged over the length ℓ of the ribbon beam. The ribbon beam tilt is adjusted

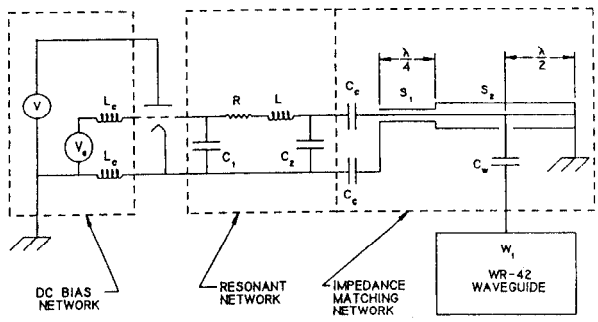

Figure 6. Equivalent circuit of FEA cathode and resonant coupler.

to achieve the phase-match condition. The phase shift between the electron bunch and a traveling wave of harmonic M' varies linearly along the ribbon beam:

$$\Delta\phi(x) = 2\pi(M' - M) \left(\frac{x}{2\ell}\right) \qquad (12)$$

Averaging over the width ℓ of the ribbon gives a coupling for each parasitic mode:

$$\frac{E}{E_o} = \int_0^{\ell} \cos \Delta\phi(x) \frac{dx}{\ell} = \begin{cases} 0 & M' \neq M \\ 1 & M' = M \end{cases} \qquad (13)$$

All parasitic modes $M' \neq M$ thus receive no net coupling. This feature is a result of the distributed beam waveguide coupling, and is unique among electron tube designs.

III. DEVICE PERFORMANCE

We have calculated beam transport through the gigatron. Calculations were performed using the MASK computer code. Fig. 7 shows the trajectories of successive bunches through the diode region. Fig. 8 shows the trajectories of two successive ribbons through the coupler structure. Trajectories are shown on five points across each ribbon. Both transverse position and energy are shown for each trajectory. Slot width and height, coupler peak field, RF phase, and beam phase width were varied to optimize RF efficiency while transporting residual beam to the collector. For the optimized parameters, RF conversion efficiency of 74 % is obtained. No beam is intercepted before entering the collector structure.

We now have operational FEA cathodes at Texas A&M. The IV curves of these cathodes are presented below. The cathodes were made for us by C.S. Spindt, and employ the traditional fabrication approaches. We have built a vacuum assembly for testing the IV characteristics of cathodes in pulse mode, including provision for rf modulation. We have also built the complete vacuum structure for a round-beam gigatron prototype, with design parameters 12 GHz, 40 kW.

REFERENCES

1) P.B. Wilson, "Design Concepts for TeV Linac Colliders," SLAC-PUB-3674 (1985.
W. Schnell, "CERN Linear Collider Design Study," CERN-LEP-RF/86-06 (1986).

2) Hana M. Bizek, Peter M. McIntyre, Deepak Raparia and Charles A. Swenson, "Gigatron," IEEE Trans. on Plasma Sci., 16, No. 2, (1988).

3) S. Yu, "Physics of Relativistic Klystrons," Workshop on new developments in particle accelerator technology. Orsay, France (1987).

4) W. Lawson et al., "A High Peak Power, X-Band Gyroklystron for Linear Accelerators," Proc. 1986 Linac Conference.

5) C.A. Spindt et al., "Field Emission Array Development," Proc. 33rd Int. Field Emission Symp. (1986).

6) D.J Campisi and H. Gray, "Microfabrication of Field Emission Devices for Vacuum Integrated Circuits using Orientation Dependent Etching," Proc. Mat. Res. Soc. Meeting. 1986.

7) J. Fisher and T. Srinivasan-Rao, "Fabrication and Performance of Knife-Edge Field-Emitter Structures on Silicon," 1987 Workshop on New Technology for Future Accelerators. Orsay. 1987.

8) M.T. Wilson and P.J. Tallerico, U.S. Patent #4,313,072 (1982).

9) C.K. Sinclair, "The SLAC Lasertron Project," SLAC-PUB-4111 (1986).
Y. Fukushima et al., "Lasertron," Nucl. Instr. Math. A238, 215 (1985).

TABLE I
Parameters of Example Gigatron

$\omega/2\pi$	rf frequency	18 GHz
P_o	rf peak power	10 MW
G^o	power gain	27 dB
	rf efficiency	74%
V	beam voltage	200 kVDC
	peak beam current	390 A
ϕ	rf phase	230°
$\Delta\phi$	beam phase width	60°
$\ell \cdot w$	cathode size	14 x .1 cm²
$a \cdot b$	waveguide coupler (WR42)	1.1 x .4 cm²
g,h	slot width, height	.2 cm, .3 cm
β	electron velocity/c	.70
β^ϵ	phase velocity/c	1.37
θ^p	ribbon tilt angle	27°
Ψ	magnetic bend angle	22°
E_o	peak rf field	125 MV/m

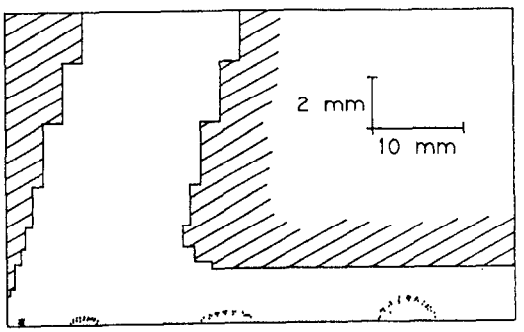

Figure 7. Calculated ribbon beam trajectories through diode region.

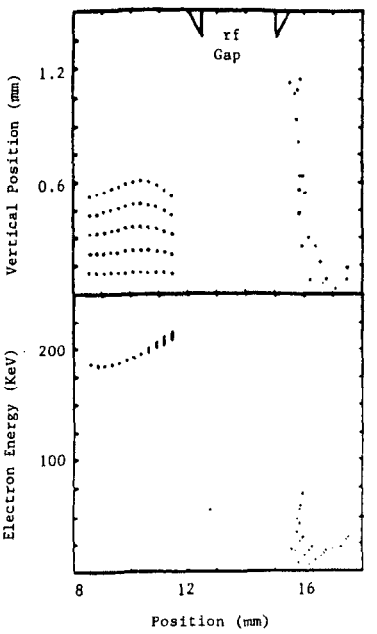

Figure 8. Electron energy and bunch motion through the traveling wave coupler.

ACKNOWLEDGEMENTS

It is a pleasure to acknowledge stimulating discussions with W. B. Herrmannsfeldt, K. R. Epley, R. Miller, R. Taylor, J. Welch of SLAC, C. A. Spindt of SRI, K. Chang, D. L. Parker and R. Rogers of Texas A & M. This work is supported by U. S. Department of Energy contract number DE-AC02-85ER40236.

FINAL FOCUS SYSTEM FOR TLC*

Katsunobu Oide†

Stanford Linear Accelerator Center, Stanford University, Stanford, California 94309

ABSTRACT

A limit of the chromaticity correction for the final focus system of a TeV Linear Collider (TLC) is investigated. As the result, it becomes possible to increase the aperture of the final doublet with a small increase of the horizontal β function. The new optics design uses a final doublet of 0.5 mm half-aperture and 1.4 T pole-tip field. The length of the system is reduced from 400 m to 200 m by several optics changes. Tolerances for various machine errors with this optics are also studied.

1. INTRODUCTION

One of the merits of the flat-beam scheme for a future linear collider is that it makes the final focus system very simple, because one can mainly concentrate on the chromaticity correction of one dimension. Actually, a consistent design of the final focus system for TLC with R. B. Palmer's parameters[1] has been given,[2] and the number of optical elements is much fewer than that for a round beam final focus system like SLC[3] owing to the single-family sextupole chromaticity-correction scheme. Table 1 and Fig. 1 show the main parameters and these optics.

Although this design proved the existence of a final focus system for the TLC, it still needs many improvements and further optimization. One major problem is the aperture of the final quadrupole. It requires 100 μm half-aperture and 1.4 T pole-tip field, but until today only 5 mm with 1.25 T has been built as a high-gradient quadrupole.[4] The 100 μm aperture corresponds to 6 σ of the vertical beam size of this design, however, it is proved in this workshop that it must be at least 10 σ to prevent the synchrotron radiation in the final doublet from hitting the surface of itself.[5] A large aperture quadrupole can only be achieved by extending its length, unless one can get higher surface field. This makes the chromatic effect of the quadrupole larger in general and, thus, we need to know the limit of the chromaticity correction. This will be discussed in the next chapter and a design with larger aperture quads will be given in Chap. 3.

Another problem with the final focus system is the tolerances to various machine errors. In Chap. 4 we will briefly estimate several of them.

Table 1. Parameters for the final focus system of Fig. 1.

Center-of-mass energy	$E_{CM} = 1$ TeV
Beta function at IP	$\beta_x^* = 14$ mm
	$\beta_y^* = 43$ μm
Normalized emittance	$\varepsilon_{Nx} = 2.5 \times 10^{-6}$ m
	$\varepsilon_{Ny} = 2.5 \times 10^{-8}$ m
Momentum bandwidth	$\lvert\Delta p/p\rvert \leq 0.30$ %
Pole-tip field	$B_0 = 1.4$ T
Length of the experimental area	$\ell^* = 0.4$ m
Quadrupole half-aperture	$a = 100$ μm

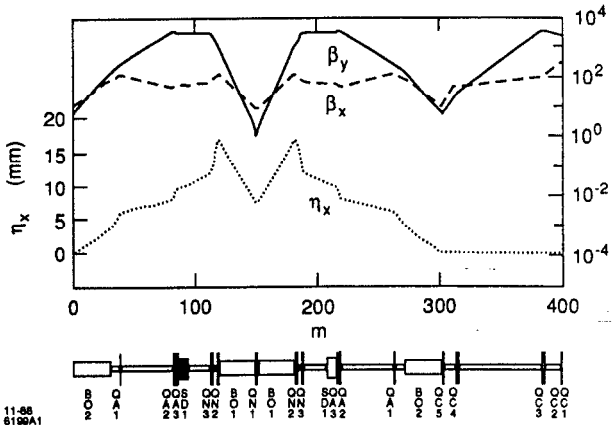

Fig. 1. A final focus optics for TLC with the single-family sextupole chromaticity correction scheme. The first character of each element specifies the type of the element as B:bend, Q:quadrupole, and S:sextupole.

*Work supported by the Department of Energy, contract DE–AC03–76SF00515.

†Visiting from KEK, National Laboratory for High Energy Physics, Oho, Tsukuba, Ibaraki 305, JAPAN.

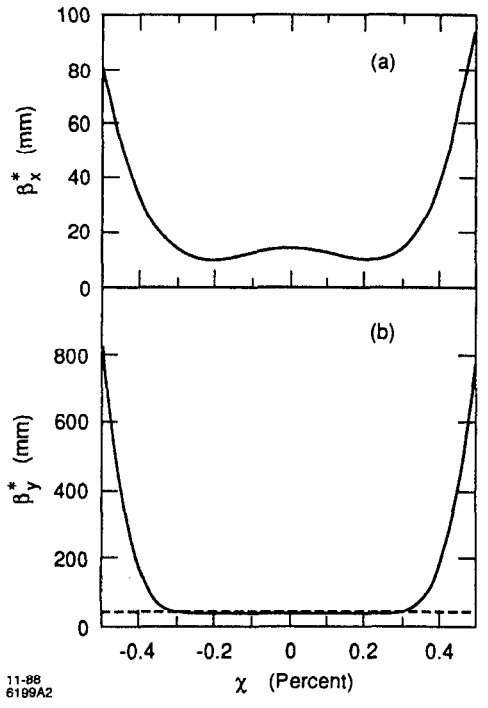

Fig. 2. The momentum dependence of the β functions at IP with the optics of Table 2. The horizontal axis is the parameter $\chi \equiv (p - p_0)/p$. The dashed line in β_y^* is the chromatic effect from the elements except the bad phase quadrupoles QC4 and QC5.

2. LIMIT OF THE CHROMATICITY CORRECTION

Figure 2 shows the momentum dependence of β functions at the interaction point with the previous optics. The behavior of the horizontal β function has been fully analyzed in Ref. 2 and the bandwidth for horizontal δ_x is determined by the horizontal chromaticity ξ_x

$$\delta_x = \frac{1}{\xi_x} \quad , \qquad \xi_x \equiv \int K \beta_x \, ds \quad , \tag{1}$$

where K is the focusing gradient of the final quadrupoles. When we use large aperture quadrupoles, we have to increase β_x^* to keep the desired bandwidth, as long as we use the single-family sextupole-correction scheme. Figure 3 shows how β_x^* depends on the aperture while keeping the bandwidth constant. We see in this figure that β_x^* is roughly proportional to $a^{\frac{1}{2}}$.

On the other hand, the behavior of the vertical β function has not been completely studied. We know that it is possible to cancel the momentum dependence up to fourth order by placing a sextupole at the phase difference $N\pi$ (N: integer) from the final doublet and setting the strength

$$k' \eta \beta_{Sy} = \xi_y \quad , \tag{2}$$

where η, β_{Sy} and ξ_y are the dispersion, vertical β function at the sextupole, and the vertical chromaticity of the

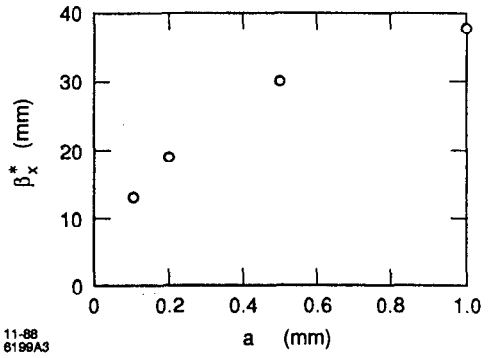

Fig. 3. The dependence of β_x^* on the aperture of the final doublet. The bandwidth is kept at $\pm$ 0.3 %. Here we fixed ℓ^*, β_y^*, and B_0 to 40 cm, 40 μm, and 1.4 T, respectively.

final lenses. We see in Fig. 2 a large sixth-order term appears in β_y^* which gives the same bandwidth as β_x^*. We need to investigate this sixth-order term and determine the limit of the vertical chromaticity correction.

There are a lot of candidates for the sixth-order term. The doublet scheme, the finite thickness of quadrupoles and a higher order term in the dispersion at the sextupole give this effect, but estimations on these effects give a few percent bandwidth in this optics, far smaller than the actual strength of the sixth-order term. An analysis below will reveal the real source: the answer is the chromatic effect of quadrupoles between the sextupole and the final quadrupoles.

Consider a quadrupole with a strength k_1 which is placed at a position with a phase difference μ_1 from the collision point. The Twiss parameters are β_1 and α_1 at the quadrupole. We consider the system by a thin-lens approximation as shown in Fig. 4. Here we omit the suffix y, but the arguments below are only applied to the vertical dimension. We represent the effect of the final doublet by one thin lens as Ref. 2. Therefore, the chromaticity of the final doublet is written as $\xi_0 = k_0 \ell^2 / \beta^*$. After a simple thin-lens calculation, we find that it is not possible to cancel the chromatic terms completely even below the fourth order, but the main aberration appears in the sixth-order term

$$\frac{\Delta\beta^*}{\beta^*} = \xi_0^4 \xi_1^2 \left(\cos\mu_1 - \frac{\beta^*}{\ell} \sin\mu_1 \right)^4 \chi^6 \quad , \tag{3}$$

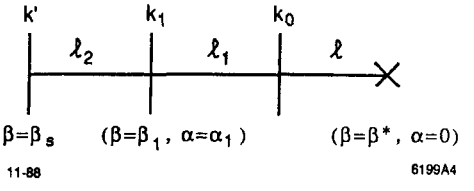

Fig. 4. A thin lens model of the final focus system. Here, ℓ is the length from the center of the final quadrupole to the collision point.

where $\xi_1 \equiv k_1\beta_1$ is the chromaticity of the intermediate lens and $\chi \equiv (p - p_0)/p$. Equation (2.3) tells us that a quadrupole gives a large sixth-order effect, unless the phase advance μ_1 is close to $(N + \frac{1}{2})\pi$. In our previous optics the quadrupoles QC4 and QC5 are at the bad positions $\mu_1 = 0.58\pi$ and $\mu_1 = 0.97\pi$, respectively. According to Eq. (2.3), the quadrupoles limit the bandwidth to $\pm 0.27\%$, which is defined at the point where

$$\frac{\Delta\beta^*}{\beta^*} = 1 \quad . \tag{4}$$

This result agrees well with the behavior of β_y^* of Fig. 4. If both QC4 and QC5 were achromatic lenses, the behavior of the β function of this optics would become the dashed line of Fig. 4. It is a remarkable effect that despite the fact that the chromaticities of these lenses ($\xi_1 = 2.1$ and $\xi_1 = 0.4$ for QC4 and QC5, respectively) are much smaller than that of the final doublet ($\xi_0 = 14800$), they give the main contribution in the sixth-order term. For a lens which is at the phase advance $\mu_1 \approx (N + \frac{1}{2})\pi$, the sixth-order term given by Eq. (2.3) is smaller by the factor $(\beta^*/\ell)^4$ than those which are at the bad phase position.

What we have learned here is: "do not place a quadrupole at a position where the phase is not $(N + \frac{1}{2})\pi$ from the collision point." It is possible to remove these bad-phase quadrupoles, but at least one quadrupole is necessary to make the π phase advance between the sextupole and the final doublet.

We now consider the simplest system, which consists of one final lens, one sextupole and one intermediate lens which sets the phase advance to π. Let us denote the distances from the intermediate lens to the final lens and the sextupole as ℓ_1 and ℓ_2, respectively, as shown in Fig. 4. The π phase advance is achieved by setting the strength of the intermediate lens as

$$k_1 = \frac{\ell_1 + \ell_2}{\ell_1 \ell_2} \quad ; \tag{5}$$

therefore the residual sixth-order given by Eq. (3) becomes

$$\frac{\Delta\beta^*}{\beta^*} = \xi_0^4 \frac{\beta^* L^2}{\beta_S \ell^2} \chi^6 \quad , \tag{6}$$

where L is the distance between the sextupole and the final doublet. Equation (6) gives the final limit of chromaticity correction. The bandwidth for the vertical correction is written

$$\delta_y = \left(\xi_{y0}^2 \sqrt{\frac{\beta_y^*}{\beta_{yS}}} \frac{L}{\ell} \right)^{-\frac{1}{3}} , \tag{7}$$

which corresponds to the condition of Eq. (4), and we have restored the y suffix. This bandwidth is proportional to $\beta_y^{*(1/2)}$ if the other parameters are fixed. The strength of the sextupole is still expressed as Eq. (2), but ξ_y at the right hand side of Eq. (2) is given not only by the final lenses but also by all quadrupoles of the system.

Figure 5 shows the band widths for both x and y achieved by actual designs, compared to the calculations from Eqs. (2.1) and (2.7). The agreement in vertical bandwidth is a little worse than the horizontal one, but Eq. (2.) still gives a rough estimation of the vertical bandwidth. The total bandwidth of the system is determined by the smaller of the horizontal and vertical band widths.

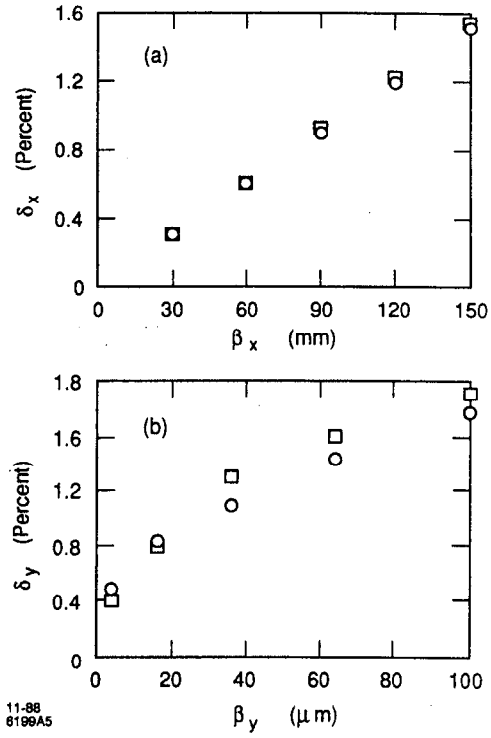

Fig. 5. The bandwidth δ_x and δ_y as functions of β_x^* and β_y^*. Here a final doublet with 0.5 mm half-aperture, 1.4 T pole-tip field, and $\ell^* = 40$ cm is used. The circles show the band widths achieved by actual designs, and squares the calculated values by Eqs. (2.1) and (2.7).

3. A LARGE APERTURE FINAL FOCUS SYSTEM

Although it is still not clear for us how small a quadrupole aperture is really available, here we use 0.5 mm half-aperture with 1.4 T pole-tip field for final doublet as an example. It is about one tenth of the aperture of quadrupole actually constructed.[4] According to the results of the last chapter, it is possible to design an optics with this aperture and a bandwidth of 0.3%. In this case, the bandwidth is only determined by the horizontal chromaticity, and we have to increase β_x^* from 14 mm to 30 mm to achieve this bandwidth, as indicated in Fig. 3. The vertical β function is 40 μm and almost the same as before. Although we have enough acceptance in β_y^*, it is worthless to decrease β_y^* any more because it has already hit the synchrotron-radiation limit of the final quadrupole.[6]

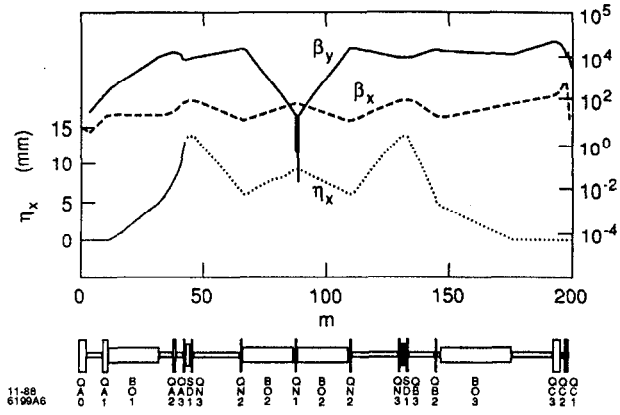

Fig. 6. A new design of the final focus optics with the 0.5 mm half-aperture final doublet.

Figure 6 shows a design of the final focus system with 0.5 mm half-aperture final doublet. This aperture is made by stretching the length of the final quadrupole QC1 from 40 cm to 120 cm and also QC2 from 40 cm to 68 cm. The pole-tip field and the length of the experimental area are the same as for the previous design. The system length is decreased to 200 m, which is just half of the previous one. In the previous design the mirror symmetry of the chromaticity correction section is kept from the first bend to the last bend, which is followed by a focusing section of 100 m length. The new design has kept the symmetry only between two sextupoles, and the dispersion suppressor and the telescope are merged into one complex. Another improvement is done to obtain a bigger dispersion/bending angle ratio. These two changes contribute to reducing the total length.

The vertical chromaticity is increased as the increase of the aperture and it needs strong sextupoles, which make the geometric aberrations large. One cure is to increase the dispersion at the sextupole, as in the paragraph above. Another cure is to shorten the length of the sextupoles. Although the shorter sextupole is the better in the geometric effects, owing to the $-I$ transformation between the two sextupoles, it is unclear how small an aperture sextupoles can be reduced to and still remain actually possible. Here we set the half-aperture to 0.4 mm, with a pole-tip field of 1.0 T, which is a modest value compared to those of the final quadrupoles.

Now the 200 m final focus system is short enough for the 500 GeV accelerator. This system has been checked by a multiparticle tracking simulation, and the total vertical aberration caused by synchrotron radiation and geometric nonlinearity is about 10% of the nominal beam size. The luminosity is decreased from the previous design due to the increase of β_x^*, but it can be recovered by changing other parameters of the collider.

Although a design with 1 mm half-aperture quadrupoles is also made, and it will be possible to increase the aperture more, a large aperture increases the chromaticity of the system and makes the tolerance of the system tighter, as shown in the next chapter.

Table 2. The optics parameters for the new design of the final focus system.

MARK

INPUT = (ALPHAX = 0 ALPHAY = 0
BETAX = 10.0 m BETAY = 10.0 m
EMIX = 2.5D-12 m EMIY = 2.5D-14 m
DP = 0.003)

DRIFT

LA0 = (L = 6.9938532) LX0 = (L = 0.1000000)
LA1 = (L = 0.1000000) LB2 = (L = 10.6758039)
LA2 = (L = 5.2890761) LB1 = (L = 1.5095633)
LA3 = (L = 3.1396575) LC4 = (L = 16.4694946)
LS2 = (L = 0.1000000) LC3 = (L = 1.8851826)
LN2 = (L = 0.1000000) LX2 = (L = 0.0400000)
LN1 = (L = 18.9086844) LX1 = (L = 0.4000000)

BEND

B01 = (L = 21.0000000 , ANGLE = 0.000499346458)
B02 = (L = 21.0000000 , ANGLE = 0.000300000000)
B03 = (L = 29.0000000 , ANGLE = 0.000300000000)

QUAD

QA0 = (L = 3.0000000 , K1 = 0.2847124)
QA1 = (L = 2.0000000 , K1 = 0.2160445)
QA2 = (L = 1.0000000 , K1 = −0.1020459)
QA3 = (L = 1.0000000 , K1 = 0.0933806)
QN3 = (L = 1.0000000 , K1 = 0.0349031)
QN2 = (L = 1.0000000 , K1 = −0.0664416)
QN1 = (L = 1.0000000 , K1 = 0.0651954)
QB3 = (L = 1.0000000 , K1 = 0.0489054)
QB2 = (L = 1.0000000 , K1 = −0.0892923)
QC3 = (L = 3.0000000 , K1 = −0.2265658)
QC2 = (L = 0.6800000 , K1 = 1.1431554)
QC1 = (L = 1.2000000 , K1 = −2.0005762)

SEXT

SD1 = (L = 2.0000000 , K2 = −132.0000000)

LINE

FFS = (INPUT	QA0	LA0	QA1	LA1
B01	LA2	QA2	LA3	QA3	LS2
SD1	LN2	QN3	LN1	QN2	LX0
B02	LX0	QN1	LX0	B02	LX0
QN2	LN1	QN3	LN2	SD1	LS2
QB3	LB2	QB2	LB1	B03	LC4
QC3	LC3	QC2	LX2	QC1	LX1)

Table 2 lists the parameters of these optics in the same format as Ref. 2.

4. TOLERANCES FOR MACHINE ERRORS

What we discuss in this chapter are the tolerances for various machine errors which reduce luminosity. In this section we discuss tolerances to abrupt changes of components from pulse to pulse. This is usually called jitter. For the flat beam collider, the tolerances are much tighter in the vertical dimension than the horizontal, because the final spot size is smaller and the chromaticity is higher in the vertical. We will show some simple expressions to estimate the tolerances for only the vertical, but these are easily applicable to the horizontal dimension. Figures in

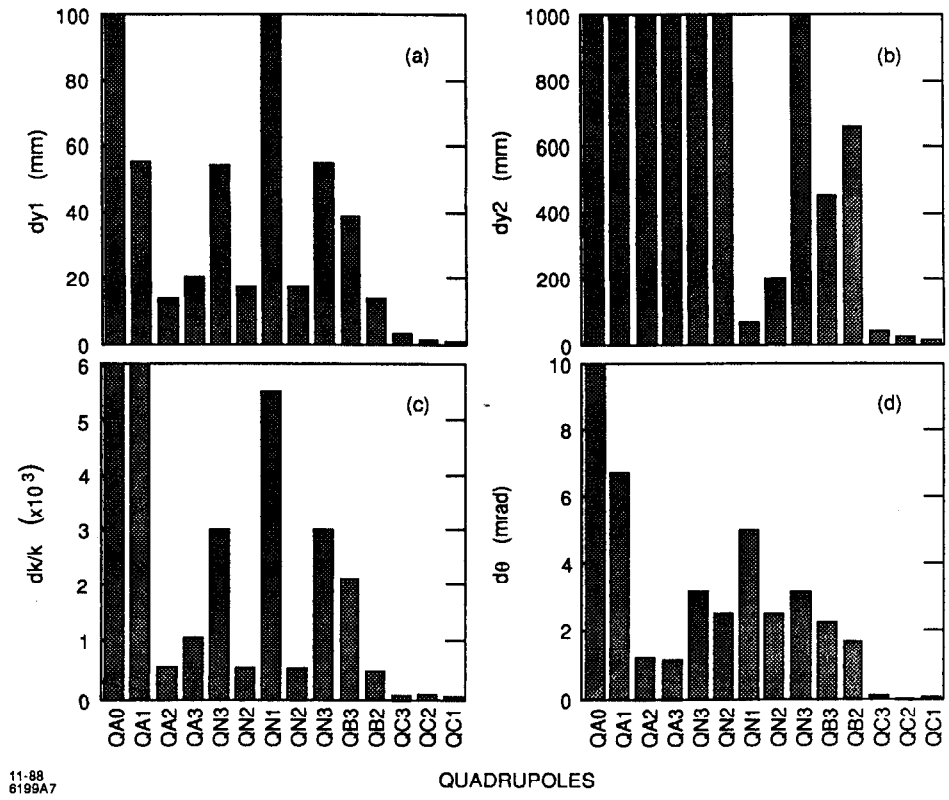

Fig. 7. Tolerances for vertical misalignments dy_1 and dy_2, strength error dk/k, and roll ang

this chapter show the values of machine errors for each quadrupole which reduce the luminosity to $1/\sqrt{2}$ of the nominal value. The new optics described in the last chapter is used in this calculation. We take into account only the first order optics and its first order momentum dependence.

The first kind of the error is the simplest one. The misalignment dy_1 of each quadrupole vertically shifts the beam spot and prevents the head-on collision. The amount which reduces the luminosity by $1/\sqrt{2}$ is

$$dy_{1i} = \frac{\sqrt{2\log 2}}{k_i \sin\mu_i}\sqrt{\frac{\varepsilon_y}{\beta_{yi}}} \quad , \tag{8}$$

where μ_i, β_{yi}, and k_i are the phase difference from the IP, the vertical β function, and the strength of the i-th quadrupole, respectively.

There is another effect of a misalignment of a quadrupole. A vertical displacement makes the vertical spot size larger due to the vertical dispersion created by the vertical displacement in the final doublet. The tolerance to this effect is written as

$$dy_{2i} = \frac{\sqrt{3}}{k_i\xi_y \cos\mu_i\delta}\sqrt{\frac{\varepsilon_y}{\beta_{yi}}} \quad , \tag{9}$$

where ξ_y is the chromaticity of the system, and we have assumed the beam has a uniform energy distribution of the full width 2δ. This effect becomes weaker for quadrupoles between two sextupoles, because about the half of the chromaticity is corrected, and ignorable for the quadrupoles before the chromaticity correction section.

Quadrupole strength error dk/k and roll $d\theta$ along its longitudinal axis also make the vertical spot size larger. The tolerances for them are written

$$\frac{dk_i}{k_i} = \frac{1}{k_i\beta_{yi}\sqrt{\sin^2\mu_i + \xi_y^2\delta^2\left[\frac{\sin^2 2\mu_i}{2} + \left(\frac{1}{3} + \frac{\xi_y^2\delta^2}{5}\right)\cos^4\mu_i\right]}} \tag{10}$$

and

$$d\theta_i = \frac{\sqrt{\frac{\varepsilon_y}{\varepsilon_x}}}{k_i\sqrt{\beta_{xi}\beta_{yi}\left(\sin^2\mu_i + \frac{\xi_y^2\delta^2\cos^2\mu_i}{3}\right)}} \quad . \tag{11}$$

Figure 7 shows above tolerances for each quadrupole used in this system. We see in this figure all tolerances are about one order more severe for the final three quadrupoles than other quadrupoles.

Tolerances for sextupoles can be estimated similarly. The tolerances for the horizontal displacement is calculated in the same expression as Eq. (4.3) by replacing dk

with $k'dx_S$. The vertical tolerances is also obtained from Eq. (11) by replacing $k_i d\theta$ with $k'dy_S$. These values are $dx_S = 0.82$ μm and $dy_S = 0.85$ μm. The tolerance for the sextupole strength dk'/k' is written

$$\frac{dk'}{k'} = \frac{\sqrt{3}}{k'\eta\beta_{yS}\delta} \quad , \tag{12}$$

which gives $dk'/k' = 3.4 \times 10^{-2}$.

5. DISCUSSIONS

In this paper we have a rough evaluation of the limit of the vertical chromaticity correction. This limit is still far from the present requirement of β_y^* and the actual bandwidth is determined only by β_x^*, due to the single-sextupole scheme. We have to abandon this scheme when we need smaller β_x^*, and use a two-family sextupole scheme instead. What limits the chromaticity correction with two-family sextupole scheme has not been studied, but another sixth-order terms from the coupling of these two families will appear, and the limit will be tighter than the single-family scheme.

We have achieved improvements of the final focus optics in the aperture of the final doublet and the total length. These will give more reality to TLC.

We have estimated the tolerances for several machine errors. The values estimated here give the maximum jitters of the components discussed. There are also other kinds of machine errors which have dc or very low frequency components. These are correctable by monitoring beam position and size in various points in principle, but there are some limits to the correction due to the finite errors of monitors and additional aberrations induced by correctors like synchrotron radiation. This problem also depends on the correction scheme with the specific optics.

ACKNOWLEDGMENT

The author would like to express his sincere thanks to Dr. R. D. Ruth for valuable suggestions.

REFERENCES

1. R. B. Palmer, SLAC–PUB–4295 (1987).
2. K. Oide, SLAC–PUB–4660 (1988).
3. Stanford Linear Accelerator Center, *SLC Design Handbook,* 1984.
4. W. O. Brunk and D. R. Walz, SLAC–PUB–3672 (1985).
5. T. Himel, SLAC–PUB–4804 (1988) and these Proceedings.

FINAL FOCUS SUPPORTS FOR A TEV LINEAR COLLIDER*

W. W. Ash

Stanford Linear Accelerator Center, Stanford University, Stanford, California 94309

ABSTRACT

Final focus quadrupoles supported from structures in the endcap region of a physics experiment appear to meet the high-frequency vibration and stability criteria for a TeV Linear Collider (TLC). The support stays within a ten-degree cone, minimizing interference with the experimental apparatus.

SUPPORTING BEAM

Final focus optics and a small-bore quadrupole have been discussed in early studies of a TLC.[1] The quadrupoles would be about 2 centimeters tall and 40 centimeters long and would weigh about 1.5 kg. The support must keep the vertical position of each doublet stable to a few percent of the vertical collision-point height of about 10^{-9} m.

Consider supporting the quadrupole doublet on a mechanical beam that fills the ten-degree region and anchors to a firm, seismically damped base in the endcap region as shown in Fig. 1. (A model for this is the SLD detector at the SLC. The central detector and two endcaps are roughly comparable in size. Supporting machine components from the endcaps minimizes interference with physics components.)

The tapered, cantilevered mechanical supporting beam[2] has a static deflection of about 0.6 μm and a simple vibration frequency, $\nu = \sqrt{g/y}$, of about 600 Hz.

SEISMIC ISOLATION

The seismic isolation is based on the system used in the Caltech gravity wave detector,[3] illustrated in Fig. 2. Although their detector is elegant, the basic idea in the passive part of the support is not high-tech — it is comparable to the "granite table on rubber tires" mentioned in R. Palmer's talk at this conference.

With this arrangement the Caltech group measured a seismic vibration spectrum as shown in Fig. 3, which is

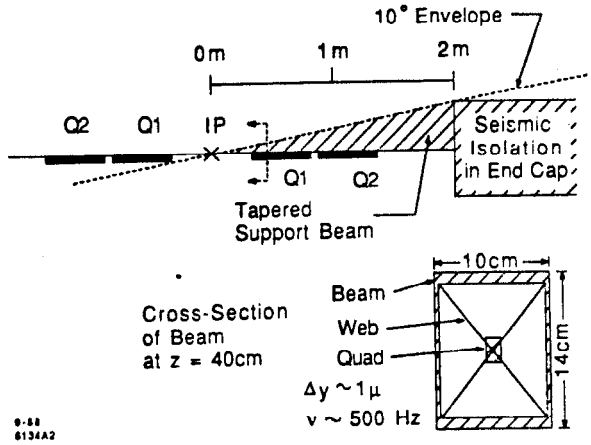

Fig. 1. Conceptual layout of a mechanical support beam for the small quadrupole doublet. The insert shows the cross section of the beam and the drawing shows the beam tapered to fill the available dead region. The beam is cantilevered from a heavy, seismically damped mass in the endcap region of a detector.

adapted from their report. (The isolation is too efficient to measure the effect directly so they used a mechanical thumper very close to their support and then scaled the vibrations down.)

The low-frequency curve is the normal Pasadena ground motion plotted directly on the curve in the region where the damping can do no good. The extrapolation is a guess at what to expect in between.

The adaptation here would exploit the mass of the endcap of the physics experiment, possible isolation in the floor under the endcap, and a suspension system inside the ten-degree cone. Seismic vibrations will drive the cantilevered beam with the amplitude enhanced at the beam's resonance. The Caltech data shows a similar resonance from the wire-support system around 800 Hz. Given the very rapid falloff of the motion, this effect is not serious.

* Work supported by the Department of Energy, contract number DE–AC03–76SF00515.

Contributed paper at the DPF Summer Study Snowmass '88, High Energy Physics in the 1990's, Snowmass, Colorado, June 27–July 15, 1988

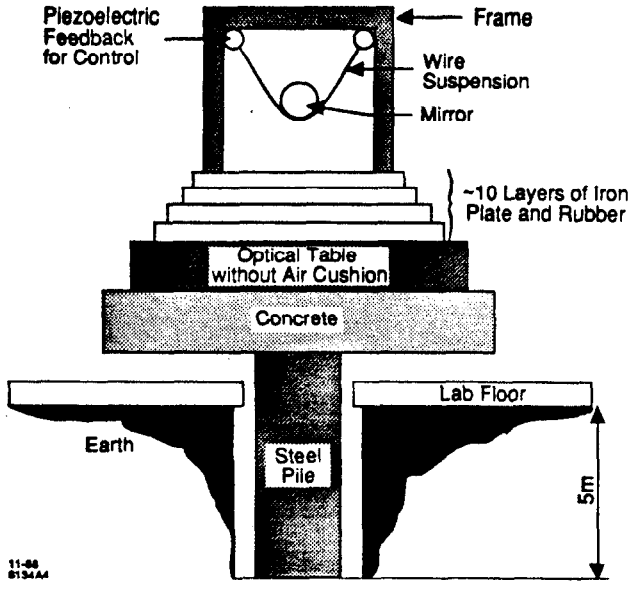

Fig. 2. Schematic layout of the passive seismic isolation for the Caltech interferometric gravity wave detector. In the application to a collider final focus, the heavy mass is the experiment's endcap, the floor might be appropriately modified, the optical table fits into the ten-degree dead region, and the final focus support beam hangs on the suspended "mirror".

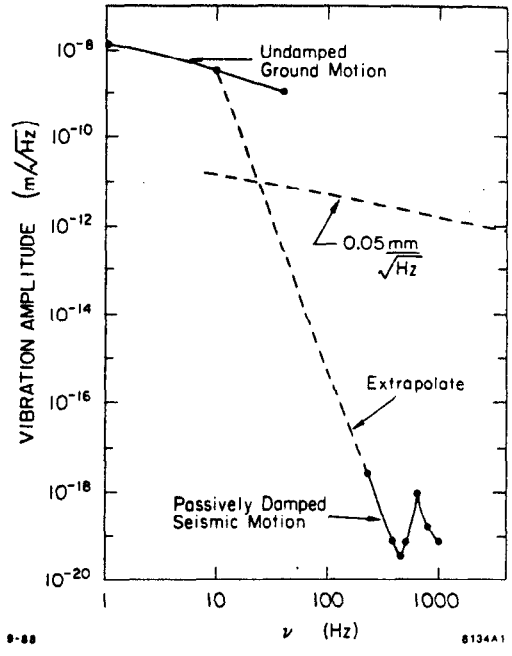

Fig. 3. This graph, adapted from the Caltech work, shows the noise measured on the kind of suspension sketched in Fig. 2. The extrapolation joins the indirect high-frequency data with undamped low-frequency seismic vibrations. The curve marked $0.05\ mm/\sqrt{Hz}$ *is an estimate of the collider requirement.*

The dashed curve falling off as $1/\sqrt{\nu}$ is the assumed criterion for supporting the linear collider final focus to give acceptably small vibrations over the frequency band.*

SLOW FEEDBACK

Above 100 Hz the isolation looks very good. Below around 10 Hz, however, the seismic noise becomes too large as the isolation becomes ineffective. Low frequency drifts, including rubber creep and thermal effects, will overpower the isolation of the doublets so something else is required to maintain alignment.

Steering coils would normally provide for this correction of the spot position. This is limited, however, to a few μm or the synchrotron radiation from the bending of the beam in the final quadrupoles may degrade performance.[1] Something else is needed to keep the system mechanically stable to around 1 μm.

The Caltech experiment has a similar problem in maintaining the orientation of their detector components. A system of low-power lasers, reflecting mirrors and photodiode detectors operate below 30 Hz on piezoelectric transducers at the final suspension. (Note: this is a simple system and not the elegant high-power optical-cavity laser system used as the primary detector.) This achieved control in angles at the μrad level adequate to keep static tolerances of μm.

A combination of this active support control and steering correctors must be used to manage the low-frequency end. These problems are probably much harder to solve than the high frequency seismic case addressed in this note.

* The curve comes by integrating a $1/\nu$ function for the square of the amplitude from frequencies too low to isolate up to those too high to affect the beam, and then requiring the overall rms amplitude to be of order 10% or less of the final spot size.

REFERENCES

1. Palmer, R. B., SLAC–AAS–36 (1988) and Oide, K., SLAC–PUB–4660 (June 1988).
2. Roark, R. J. and Young, W. C., *Formulas for Stress and Strain*, Fifth Edition, McGraw-Hill (1982). The standard formulas for simple bending are tabulated on page 98 and the conversion factors for tapered sections are given on page 174. The stiffening factor of about 50 requires some extrapolation.
3. Suspension systems and seismic background are discussed in the NSF proposals for a Laser Interferometer Gravitational Wave Observatory by Caltech and MIT. The relevance was noted by W. Atwood (SLAC) during visits to the site and in discussions there with R. W. P. Driver. For a more thorough discussion, see Fischer, G. E. and Mayoud, M., *Some Thoughts on Linear Collider Alignment and Mechnical Stability*, CERN–LEP–RF–SU–88–07 (March 1988).

DISRUPTION, BEAMSTRAHLUNG, AND BEAMSTRAHLUNG PAIR CREATION*

PISIN CHEN

Stanford Linear Accelerator Center, Stanford, California 94309

ABSTRACT

The two major effects from the interaction of e^-e^+ beams — beamstrahlung and disruption — are reviewed, with emphasis on flat beam collisions. For the disruption effects we discuss the luminosity enhancement factor, the maximum and *rms* disruption angles, and the "kink instability". All the results are obtained from computer simulations, and scaling laws based on these are deduced whenever possible. For the beamstrahlung effects, we concentrate only on the final electron energy spectrum and the deflection angle associated with low energy particles. In addition to the generic studies on the beam-beam effects, we also list the relevant beam-beam parameters obtained from simulations on two sample designs: the TLC and the ILC. As an addendum, the newly discovered phenomenon of coherent beamstrahlung pair creation, together with the incoherent process, are discussed.

INTRODUCTION

There are two major phenomena induced by the beam-beam interaction which are important to the design of high energy linear colliders. Namely, the *disruption* process where particle trajectories are bent by the field provided by the oncoming beam, and the *beamstrahlung* process where particles radiate due to the bending of the trajectories. The most important impact of disruption is the deformation of the effective beam sizes during collision, which causes an enhancement on the luminosity. In addition, the disruption angle affects the constraints on the final quadrupole aperture. When the two beams are colliding with certain initial offset, the disruption effect between the two beams would induce a kink instability, which imposes a constraint on beam stability. Ironically, this instability helps to relax the offset tolerance for flat beams, because the offset beams tend to find each other during the initial stage of the instability. Under a multi-bunch collision mode, however, the kink instability will largely degrade the luminosity through the relatively long growth time. On the other hand, the direct impact of beamstrahlung is the loss of the available energy for high energy events, and the degradation of beam energy resolution because of the stochastic nature of the radiation.

* Work supported by the Department of Energy, contract number DE–AC03–76SF00515.

Most of the issues raised above can be studied by decoupling the disruption and the beamstrahlung effects. The energy loss due to beamstrahlung may modify the luminosity enhancement but this effect can be ignored since we are only interested in the case where the average energy loss is small. Conversely, the average energy loss and the final energy spectrum can be studied by assuming no disruption without compromising too much on accuracy. There is, however, one issue where the two effects are strongly coupled. This is the maximum disruption angle associated with the large deflections from particles that have suffered severe energy loss.

In this report we summarize what has been studied on these issues with emphasis on flat beam collisions. The computer simulations are performed using the code ABEL (Analysis of Beam-beam Effects in Linear colliders) described in Ref. 1, but improved considerably since it was first written. Some results given here are still preliminary and will be refined in later papers, but their qualitative features will not be changed.

LUMINOSITY ENHANCEMENT

Our primary interest is the enhancement of luminosity due to the mutual pinching of the two colliding beams. The details have been discussed in Ref. 2 for round beams and will be given in Ref. 3 for flat beams. As was pointed out in Ref. 2, the luminosity is infinite if the initial beam is paraxial and the computation is perfectly accurate. This is because a paraxial beam can be focused to a singular point. In reality, however, a beam will always have certain inherent divergence, and the singularity is only approached asymptotically. To account for this effect, a parameter $A_{x,y} = \sigma_z/\beta^*_{x,y}$ is introduced,[2] which is proportional to the emittance for a given beam size $\sigma_{x,y}$. The computed enhancement factor $H_D = L/L_0$, where L_0 is the geometrical luminosity without the effect of the depth of focus related to $A_{x,y}$ taken into account, is plotted in Fig. 1 as a function of D_y and A_y for flat beams.

The data in Fig. 1 are obtained by using a distribution function which is uniform in x and Gaussian in y and z (UGG), instead of a three-dimensional Gaussian distribution (GGG), for easiness of computation. The enhancement factor of GGG distributions for a given D_y can be

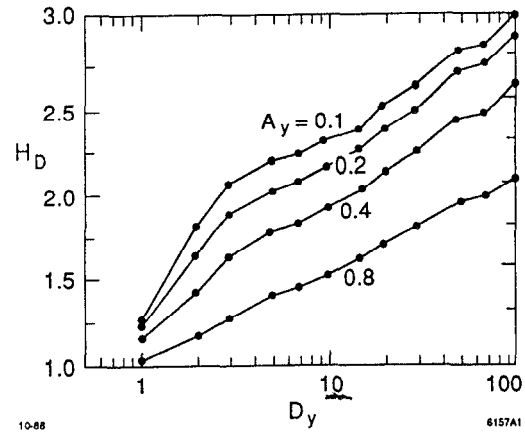

Fig. 1. Luminosity enhancement factor for flat beams.

deduced from a superposition of UGG results with disruption parameters ranging from 0 near the horizontal edge to $\sqrt{6/\pi}D_y$ at the beam center. The enhancement factor for round beams is shown in Fig. 2.

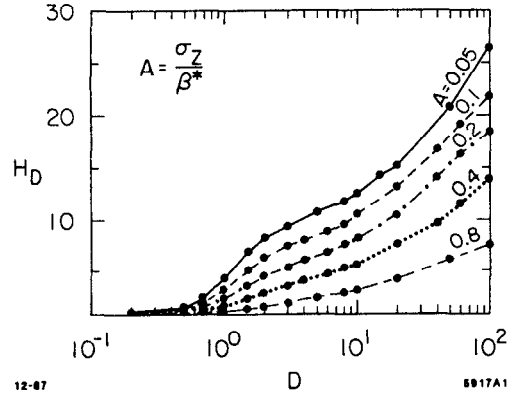

Fig. 2. Luminosity enhancement factor, round beams.

By comparing Figs. 1 and 2, one finds that the enhancement factor for flat beams scales roughly as the cube-root of the corresponding value for round beams; which obeys the following empirical scaling law that fits all data points in Fig. 2 to within 10% accuracy:

$$H_D = 1+D^{1/4}\left(\frac{D^3}{1+D^3}\right)\left[ln(\sqrt{D}+1)+2ln\left(\frac{0.8}{A}\right)\right] \quad . \quad (1)$$

The reason for the flat beam enhancement not being scaled as a square root of the corresponding value for the round beam is because the horizontal focusing can enhance the vertical pinch effect (and vice versa) in the round beam case, whereas for flat beams the pinch in the major (horizontal) dimension can hardly affect the disruption in the minor dimension.

In both cases, our results indicate a logrithmic divergence of H_D as a function of A, or A_y. In addition, H_D is monotonically increasing as a function of D, or D_y, at least up to D =100. This second finding of ours is qualitatively the same as that found by Fawley and Lee[4] but in contradiction to Holebeek[5] and Solyak,[6] where the enhancement factor first saturates before eventually decreases at large D's.

The difference appears to be due to the different ways of handling stochastic errors. In a Monte Carlo simulation such as ours, the initial condition is generated by random numbers, which introduces a statistical fluctuation, and therefore an asymmetry, of the order $1/\sqrt{N_p}$, N_p being the number of macro particles. This asymmetry will be amplified during collision (i.e., kink instability) due to the beam-beam force, especially when the disruption parameter is large. The fact that the number of macro particles in a simulation is typically much smaller than the actual particle number, this fluctuation is artificially enhanced if no proper action is taken. To minimize this computation error, the particle distribution function is symmetrized at every time step in our calculation, so that the beam-beam force has the up-down symmetry at all times for the flat beam case. Similarly, in the round beam case only the radial force is computed. This process eliminates the possible instability triggered by computation errors.

The actual collisions are expected to have some unavoidable initial offset in alignment and skewness in distributions. Since the asymmetry in distributions tend to shift the center-of-gravity of the beams, it gives rise to the same effect as the initial alignment offsets. For this reason our study on the effect of imperfections is concentrated on initial offsets only.

As will be discussed in the next section, an initial offset triggers a kink instability, especially when the disruption parameter becomes large. As it occurs, this instability is not always harmful because, in the initial phase of the instability, the beams always tend to find each other, which prevents the otherwise rapid degradation of the luminosity for large initial offsets. Figure 3 shows the luminosity enhancement factor as a function of offset Δ_y (in units of σ_y) for various values of D_y. The dotted curve is the geometrical enhancement factor without beam-beam force, which is equal to $\exp(-\Delta_y^2/4)$. UGG distribution is used and A_y =0.2 for all curves. The up-down symmetry is not enforced except for the cases at Δ_y =0.

From Fig. 3 one finds that the tolerance on alignment offset reaches an optimum for values of D_y between 5 and 10. Within this range of D_y, H_D is still above unity even at $\Delta_y \sim 3$. Beyond this region of D_y the beam-breakup becomes severe while below which the beam-beam attraction is not yet strong enough.

The same data as in Fig. 3 is replotted in Fig. 4 as a function of D_y and each curve corresponds to a fixed value of Δ_y. (The region of large D_y and small Δ_y is not very accurate because of its sensitivity to computing errors.) One sees a saturation and decrease of H_D as a function of D_y unless $\Delta_y = 0$. One also notices that the curves with small offsets, e.g., $\Delta_y = 0.2$, resemble the results in Refs. 5 and 6, except that our offset was explicitly

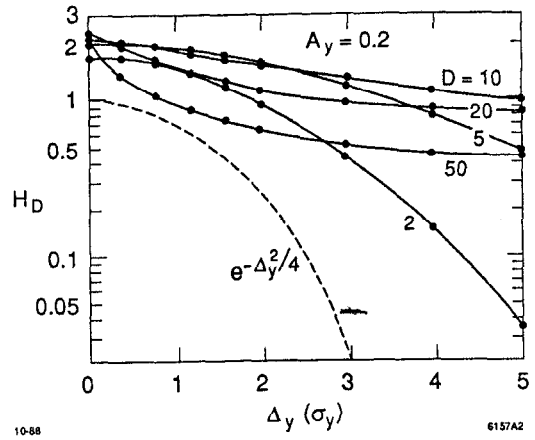

Fig. 3. H_D as a function of offset; Flat beams.

introduced. In designing a linear collider, one needs to estimate H_D for the chosen D and A. This depends on the assesment of potential imperfections of beam-beam collision. Though arbitrary, it may be safer to adopt the curve for $\Delta_y = 0.2$ or 0.4, instead of $\Delta_y = 0$, as the effective enhancement factor.

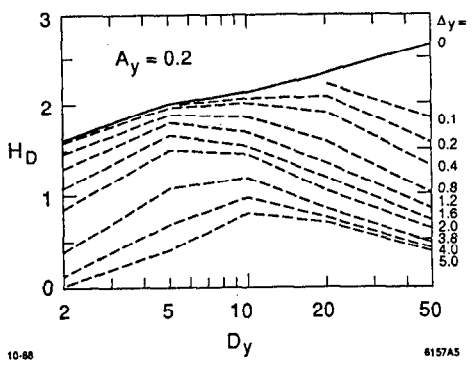

Fig. 4. H_D as a function of D_y; Flat beams.

Similar exercise for round beams are shown in Fig. 5 for D up to 50. Here we find the generic behavior as in the case for flat beams.

DISRUPTION ANGLE

Information on the final direction of the electron trajectory after collision is necessary in designing the interaction region, especially for the aperture of the final quadrupole magnets. If the disruption parameter is very small, the transverse location of a particle during collision is nearly constant. Then we can estimate the disruption angle θ_x

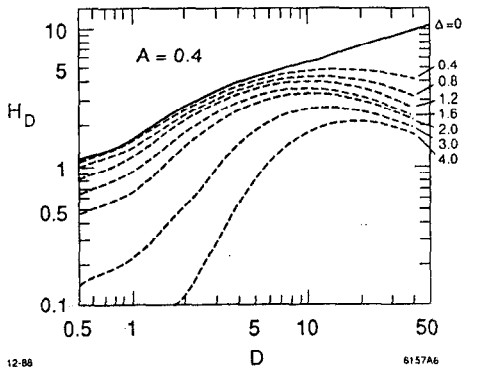

Fig. 5. H_D as a function of offset; Round beams.

and θ_y as functions of the initial transverse coordinates x_0 and y_0. For very flat Gaussian beams we have

$$\theta_x = -\sqrt{\frac{\pi}{2}} D_x \frac{\sigma_x}{\sigma_z} \mathcal{I}m\left[\frac{i}{\pi}\int_{-\infty}^{+\infty} \frac{\exp(-t^2)dt}{(x_0/\sqrt{2}\sigma_x) - t - i0}\right] \quad , \quad (2)$$

$$\theta_y = -\sqrt{\frac{\pi}{2}} D_y \frac{\sigma_y}{\sigma_z} \left[\frac{2}{\sqrt{\pi}} \int_0^{y_0/\sqrt{2}\sigma_y} e^{-t^2} dt\right] e^{-x_0^2/2\sigma_x^2} \quad , \quad (3)$$

where the quantities in the square brackets can be expressed by the complex error function $w(x_0/\sqrt{2}\sigma_x)$ and the real error function $\mathrm{erf}(y_0/\sqrt{2}\sigma_y)$. Here the emittance is ignored. One finds that the maximum and *r.m.s.* disruption angles to be

$$\theta_{x,max} = 0.765 D_x \frac{\sigma_x}{\sigma_z} \quad , \quad (x_0 = 1.31\sigma_x) \quad (4)$$

$$\theta_{y,max} = \sqrt{\pi/2} D_y \frac{\sigma_y}{\sigma_z} \quad , \quad (x_0 = 0,\ y_0 = \infty) \quad (5)$$

$$\theta_{x,rms} = \sqrt{\pi/(6\sqrt{3})} D_x \frac{\sigma_x}{\sigma_z} \quad ,$$

$$\theta_{y,rms} = \sqrt{\pi/(6\sqrt{3})} D_y \frac{\sigma_y}{\sigma_z} \quad . \quad (6)$$

(Rigorously speaking, for flat beams with large but finite aspect ratio, θ_y reaches a maximum near $y_0 \sim \sigma_x$ and then decreases; but this is not important.)

The distribution functions of θ_x and θ_y are shown in Fig. 6. The actual singularities at $\theta_x = \theta_{x,max}$ and $\theta_y = 0$ are not supposed to be as sharp as those in Fig. 6 because of finite emittance, various errors, and the disruption effect. However, we found from simulations that the qualitative difference between the horizontal and vertical angles still holds even for $D_{x,y}$ not much less than unity.

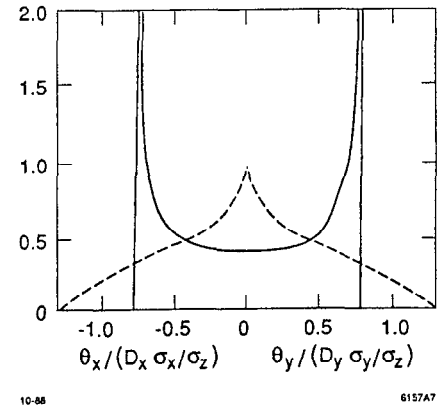

Fig. 6. Distribution of $\theta_{x,y}$ ~~for~~ small $D_{x,y}$.

Figure 7 shows the maximum and *r.m.s.* vertical disruption angle, in units of $D_y\sigma_y/\sigma_z$, as a function of D_y. Here we consider the case for small D_x only. The four curves corrrspond to A_y = 0.1, 0.2, 0.4, 0.8, respectively. The dependence on A_y is not as significant as in the case of H_D except for the small D_y region, where the beam divergence is emittance dominated. (The distribution of initial $\sigma_{x'}$ is truncated at 2.5 standard deviations in the simulation.)

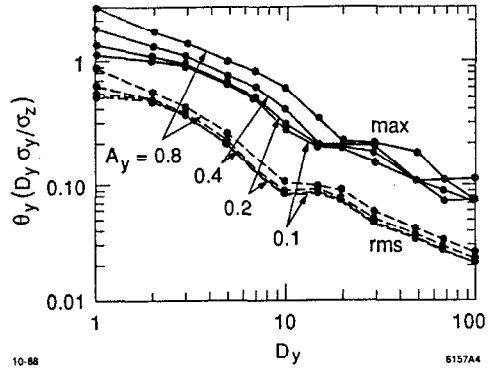

Fig. 7. Maximum and r.m.s. vertical disruption angle.

The simulation results can roughly be fitted by

$$\theta_{y,rms} \sim \sqrt{\frac{\pi}{6\sqrt{3}}}\frac{\sigma_y}{\sigma_z}\frac{D_y}{[1+(0.5D_y)^5]^{1/6}} \quad . \tag{7}$$

and $\theta_{y,max} \sim 2.5\theta_{y,rms}$. Here the contribution of the initial emittance ($= A_y\sigma_y/\sigma_z$ for $\theta_{y,rms}$) has not been included. The reason that the angle does not increase linearly in D_y is that the particle trajectories are bent backwards and oscillate when D_y is large.

So far, the collision is assumed to be head-on. For flat beams the disruption angle in the presense of vertical offset is also important in determining the aperture of the final quads. The mean deflection angle of the entire bunch can be written in the form[7]

$$\Theta_y = \frac{1}{2}\frac{\sigma_y}{\sigma_z}D_y H_c(D_y,\Delta_y) \quad , \tag{8}$$

where Δ_y is the vertical offset in units of σ_y and the weak dependence on A_y is ignored. For small disruptions, the function H_c approaches the following analytic form

$$H_c(D_y,\Delta_y) = \int_0^{\Delta_y} e^{-y^2/4}dy \quad . \tag{9}$$

Figure 8 shows H_c as a function of Δ_y computed by simulations, where UGG distribution is assumed.

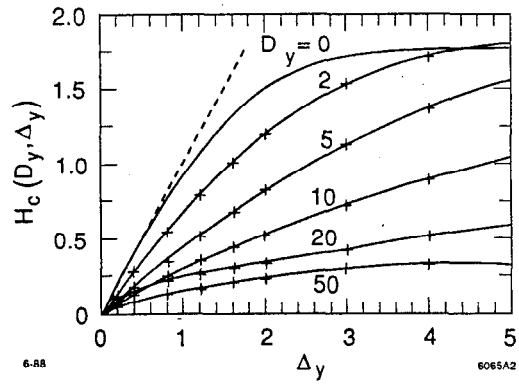

Fig. 8. Effective center-of-mass deflection.

Roughly speaking, the maximum disruption angle in the presense of offsets is the sum of the center-of-mass deflection angle Θ_y and the maximum angle in the absense of offsets, $\theta_{y,max}$.

KINK INSTABILITY

If one of the beams is displaced vertically for some reason, this offset triggers a vertical oscillation and, when D is large, the oscillation is enhanced by the beam-beam force. This phenomena is known as the *kink instability*. Figure 9 shows a specific example.

In the above figure the bunch is sliced longitudinally and the vertical coordinate y of the center-of-mass of each slice (in units of σ_y) is plotted against the longitudinal coordinate s (in units of σ_z). Each graph corresponds to a snapshot of the beam vertical position at a particular time t (in units of σ_z/c). The development of the instability can be seen in time sequence. The initial offset in this example is chosen to be $0.2\sigma_y$ (full) and the disruption parameter is $D_y = 20$.

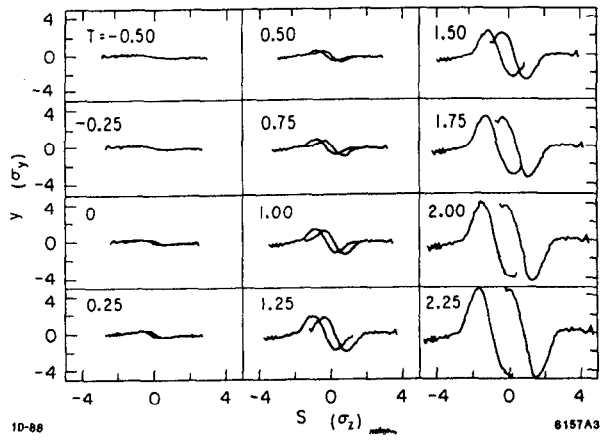

Fig. 9. An example of kink instability.

e^- and e^+ beams is varified to be $\pi/3$, and the growth rate is as predicted. Furthermore, Fig. 9 clearly demonstrates the standing-wave nature of the kink instability, which agrees with the description of Eq. (11).

So far our discussion on the kink instability deals with collisions of two bunches. Another type of kink instability occurs during the collision of two bunch trains, each consists of N_B bunches. One of the major problems of such a multibunch operation is the interactions between bunches before and after their collisions at the central collision point. The i^{th} bunch in the electron bunch train will collide not only with the i^{th} bunch in the positron train, but also with the $j(<i)^{th}$ positron bunch before its coming to the central collision point. Colliding two flat beams at a relatively large crossing angle can help to avoid unwanted direct encounters between the outgoing bunch debris and the incoming fresh bunches. However, due to the long-

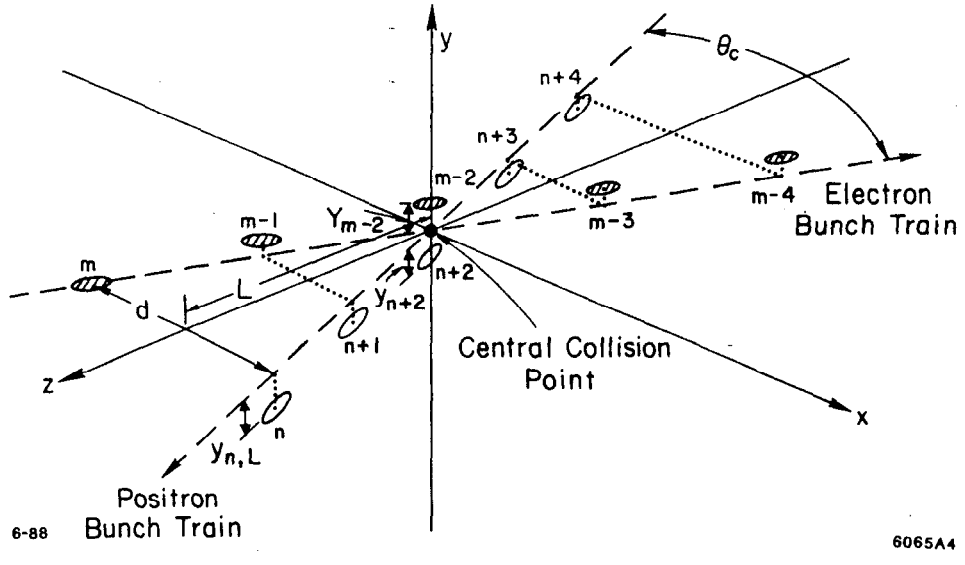

Fig. 10. Schematic diagram for collisions of bunch trains.

For uniform beams and small amplitude oscillations, the equation of motion for the beam particles can be obtained from fluid dynamics (the flat beam version of the equation is given in Ref. 8),

$$\left[\frac{\partial}{\partial t} \pm \frac{\partial}{\partial s}\right]^2 y_\pm = -\omega_0^2 (y_\pm - y_\mp), \quad \omega_0^2 = \frac{\sqrt{2\pi}}{6}\frac{D_y}{\sigma_z^2} \quad , \quad (10)$$

where $y_\pm$ is the y coordinate of $e^+$and e^- beams. The most unstable solution is found to be

$$y_\pm = \text{const.} \times \exp\left[\pm i\left(\frac{\sqrt{3}}{2}\omega_0 s - \frac{\pi}{6}\right) + \frac{1}{2}\omega_0 t\right] \quad . \quad (11)$$

This solution is in reasonable agreement with the simulation shown in Fig. 9. Namely, the phase difference between

range nature of the Coulomb interaction, there still exists undesirable interference between two separated bunches at a distance. Since the crossing angle cannot be made arbitrarily large due to the luminosity consideration, this long range interaction cannot be entirely suppressed. In fact, it imposes a severe restriction on the stability of the beams.

Consider the encounter between the n^{th} positron bunch after collision and the m^{th} $(m > n)$ electron bunch before collision at a distance L from the collision point. A schematic diagram of the system is shown in Fig. 10. We assume that all the bunch encounters occur within the drift space around the central collision point.

According to Eq. (8), the center-of-mass deflection angle for the n^{th} positron bunch is

$$\Theta_{yn} = \frac{1}{2}\frac{\sigma_y}{\sigma_z} D_y H_c(D_y, \Delta_{yn}) \quad , \quad (12)$$

where Δ_{yn} is the relative offset between the m^{th} electron and the n^{th} positron bunch, in units of σ_y, at their closest encounter. The cumulative offset for the m^{th} bunch before arriving at the central collision point is therefore

$$\Delta_m = C \sum_{n<m} H_c(D_y, \Delta_n) + \delta_m \quad , \tag{13}$$

where δ_m is the initial offset of the m^{th} beam, and the coefficient C is

$$C = D_x D_y \left(\frac{\theta_d}{\theta_c}\right)^2 \quad , \tag{14}$$

and $\theta_d = \sigma_x/\sigma_z$ is the diagonal angle of the bunch.

The cumulative offset Δ_m (in units of $\delta(1+C)^{m-1}$) is plotted as a function of the number of bunches in Fig. 11. Since the factor θ_d/θ_c must be larger than unity in order that the crossing angle does not reduce the luminosity significantly, the condition for negligible growth of the instability, i.e., $\Delta_{yn} \lesssim \delta$, according to Fig. 11, is roughly

$$(N_B - 1)\, D_x D_y \lesssim 2 \quad . \tag{15}$$

This imposes a constraint on the allowable number of bunches per train.

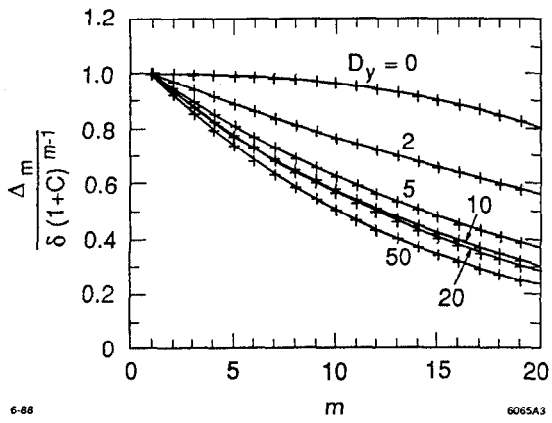

Fig. 11. Cumulative offset as a function of the number of bunches.

ENERGY SPECTRUM OF FINAL ELECTRONS

The energy spectrum of the electrons is important for two reasons: The *tip* of the spectrum, i.e., the distribution near the initial beam energy, provides information on the energy resolution for high energy physics events. On the other hand, the *tail* of the spectrum, i.e., the distribution of the low energy electrons, which had suffered severe energy loss through hard beamstrahlung, reveals the likelyhood of finding large disruption angles. This second issue will be addressed in the next section.

The energy spectrum of radiation can be characterized by the beamstrahlung parameter Υ, defined as

$$\Upsilon = \gamma \frac{B}{B_c} \quad , \tag{16}$$

where B is the effective field strength of the beam, and $B_c = m^2c^3/e\hbar \sim 4.4 \times 10^{13}$ Gauss is the Schwinger critical field. For historical reasons, this parameter is related to the parameter ξ introduced by Sokolov and Ternov, by a simple factor

$$\xi = \frac{(\text{critical energy})}{(\text{initial energy})} = \frac{3}{2}\frac{r_e\gamma^2}{\alpha\rho} = \frac{3}{2}\Upsilon \quad , \tag{17}$$

where ρ is the instantaneous radius of curvature. Since the two parameters are trivially related, we shall employ either of them depending on the convenience of the situation. The typical value of ξ during collision is

$$\xi_1 = \frac{r_e^2\gamma N}{\alpha\sigma_z\sigma_y}\frac{2}{1+R} \quad . \tag{18}$$

The average value of ξ is a bit smaller than Eq. (18) (by about a factor 2/3) but we adopt Eq. (18) for the better description of the spectrum tail which is contributed more effectively from beamstrahlung with larger ξ.

The number of emitted photons per electron is

$$N_\gamma = N_{cl} U_0(\xi_1), \text{ with } N_{cl} = 2.12\frac{\alpha r_e N}{\sigma_x + \sigma_y} \quad , \tag{19}$$

where N_{cl} is the number of photons computed by the classical formula and $U_0(\xi)$ is the ratio of the quantum-theoretical number of photons to that from the classical theory, and is found to be[9]

$$U_0(\xi) = \frac{1 - 0.598\xi + 1.061\xi^{5/3}}{1 + 0.922\xi^2} \quad , \tag{20}$$

where the relative error is within 0.7%.

An approximate formula for the energy spectrum of electrons after collision has been derived recently. The details will be given in Ref. 10. Here we only quote the results. The distribution function $\psi(\varepsilon)$ ($\varepsilon = E/E_0$), normalized as $\int \psi(\varepsilon)d\varepsilon = 1$, can be written as

$$\psi(\varepsilon) \simeq e^{-N_\gamma}\left[\delta(\varepsilon - 1) + \frac{e^{-y}}{1-\varepsilon}h(N_1 y^{1/3})\right] \quad , \tag{21}$$

with

$$\begin{aligned} h(x) &= \frac{1}{2\pi i}\int_{\lambda-i\infty}^{\lambda+i\infty} \exp(xp^{-1/3} + p)dp \quad (\lambda > 0) \\ &= \sum_{n=1}^{\infty} \frac{x^n}{n!\Gamma(n/3)} \end{aligned} \tag{22}$$

and

$$y = \frac{1}{\xi_1}(\frac{1}{\epsilon} - 1) \quad ,$$

$$N_1 = \frac{1}{1+\xi_1 y} N_{cl} + \frac{\xi_1 y}{1+\xi_1 y} N_\gamma \quad . \qquad (23)$$

(This formula does not exactly satisfy the normalization condition except for $\xi_1 \to 0$ which leads to $N_1 = N_\gamma = N_{cl}$.) The function $h(x)$ can be estimated very accurately by with relative error less than 2%. Figure 12 compares Eq. (21) with the simulation results using the parameters for the TLC and the ILC.[11] The design parameters of the two colliders are summarized in Table 1. The histograms in Fig. 12 are from simulations and the dotted data are computed from Eq. (21). The agreement is excellent.

Table 1. Parameters for TLC and ILC ($\lambda_{rf} = 17mm$)

	TLC	ILC
E_0[TeV]	0.5	0.25
N	8×10^9	7×10^9
σ_x[nm]	190	440
σ_y[nm]	1	3
$\sigma_z[\mu m]$	26	65
R	190	147
ϵ_x [mrad]	2.58×10^{-12}	5.2×10^{-12}
ϵ_y [mrad]	2.33×10^{-14}	5.2×10^{-14}
D_x	0.033	0.027
D_y	6.27	3.9
A_x	0.0002	0.0017
A_y	0.60	0.37
* L/L_0	1.61	1.71
* δ	0.15	0.01
* N_γ	1.33	0.38
ξ_1	3.43	0.19

* Quantities computed by simulations.

MAXIMUM DEFLECTION ANGLE UNDER BEAMSTRAHLUNG

The particle which once lost a large fraction of its initial energy through beamstrahlung would in principle be severely deflected by the beam-beam field and cause background problems for high energy experiments. Consider an electron which emits a hard photon at a particular time during the collision and results in an energy ϵE_0,

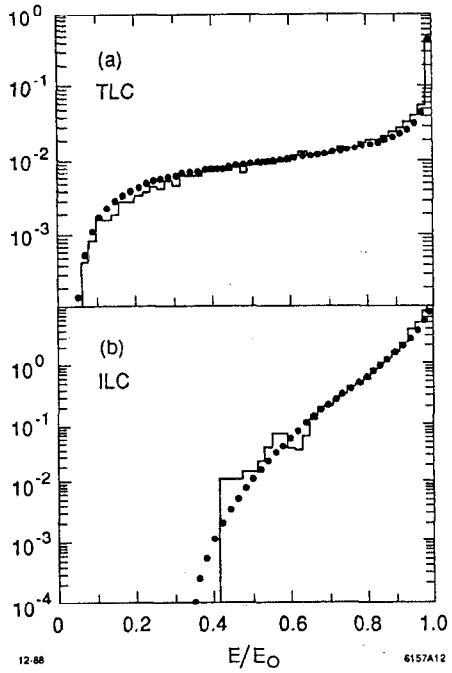

Fig. 12. Electron energy spectrum for TLC and ILC parameters.

with $\epsilon \ll 1$. The effective disruption parameter for this particle becomes D_x/ϵ and D_y/ϵ. One might think that Eqs. (4) and (5) are still applicable by replacing D by D/ϵ. However, the collision of a single particle on a beam with the disruption parameter D/ϵ is different from the collision between two beams with D/ϵ, although the qualitative feature is the same; i.e., the disruption angle increases linearly in D for $D \lesssim 1$ and more slowly for $D \gtrsim 1$.

A simulation was done by monitoring low energy test particles through the collision process. The maximum deflection angle for a given ϵ is found to be roughly

$$\theta_{max} \sim \frac{\sigma}{\sigma_z} \frac{D/\epsilon}{\sqrt{1+(0.75D/\epsilon)^{4/3}}} \quad , \quad (\epsilon \ll 1) \qquad (24)$$

where $D = D_x(D_y)$ and $\sigma = \sigma_x(\sigma_y)$ for the horizontal (vertical) angle.

The minimum value of ϵ can in principle be as small as $1/\gamma$. But the real problem is about how small a ϵ should one care. Since the number of photons N_γ per beam particle for linear colliders in the near future is of order unity, the spectral function $\psi(\epsilon)$ given in Eq. (21) is always dominated by the factor e^{-y} in the spectrum tail, where $y \gg 1$ (in logarithmic sense). Therefore, if the acceptable background counts is n out of N electrons, then the minimum ϵ of concern is approximately determined by $y = \log(N/n)$, or

$$\epsilon_{min} = \frac{1}{1+\xi_1 \log(N/n)} \quad . \qquad (25)$$

With this value of ϵ, one can directly estimate the maximum deflection angle using Eq. (24). Since the dependence

on n is only logarithmic, one can set $n = 1$. Thus, for example, $\varepsilon_{min} = 0.013(0.188)$, $\theta_{x,max} = 10$ (0.95) mrad and $\theta_{y,max} = 0.4$ (0.15) mrad for TLC (ILC) parameters.

ADDENDUM: BEAMSTRAHLUNG PAIR CREATION

After the completion of this paper, the author has discovered a new phenomenon called "coherent beamstrahlung pair creation",[12] which, together with the incoherent process studied earlier,[13,14] would have impacts on linear collider designs. Recall that in the case of radiation by $e^-(e^+)$ during beam-beam collision, there are essentially two mechanisms that induce the radiation. Namely, there is an "incoherent" process, or Bremsstrahlung, associated with the individual e^-e^+ scatterings, and there is also a "coherent" process due to the interaction between the radiating charged particle and the macroscopic beam–beam EM field. At high energies and strong fields, the coherent process tends to dominate over the incoherent one. This is actually why our discussion on beam energy loss has been focused only on the beamstrahlung process.

The beamstrahlung photons once emmited would have to travel through the remainder of the oncoming beam before entering into free space, and would therefore turn themselves into e^-e^+ pairs. Analogous to the case of radiation, photon pair creation also involves coherent and incoherent processes. Here again, at high energies and strong fields the coherent process will dominate over the incoherent one. Once the e^-e^+ pairs are created with lower energies in general, one of the two particles in each pair will have the same sign of charge as the oncoming beam (For the sake of argument, consider a low energy e^+ moving against the positron beam). Unlike the case of low energy e^- moving against a positron beam, where the potential tends to confine the particle in the beam profile, in the case of a positron the potential is unconfining, and the particle can in principle be deflected by a large angle and thus create severe background problems. This effect would therefore impose a contraint on the final focus design.

It is well known that the cross section for incoherent pair creation is

$$\sigma(\gamma e \to e e^+ e^-) \sim \frac{28}{9}\alpha r_e^2 \log\Big(\frac{2\omega E}{m^2}\Big)\mathrm{cm}^2 \quad , \qquad (26)$$

which is a very slowly varying function of the photon energy ω. For TLC, $\gamma = 1 \times 10^6$, the cross section is $\sim 5\times10^{-26}$ cm^2 for photons at full energy. The beam parameters for TLC listed in the above Table gives the average number of the beamstrahlung photon per beam particle as $N_\gamma \sim 1.3$. On the other hand, it can be shown[13] that the effective luminosity for such a cascading process is 1/2 of the original. Thus, the number of e^-e^+ pairs created per bunch crossing can be easily evaluated to be

$$N^i_{e^+e^-} = \frac{1}{2}\sigma(\gamma e \to e e^+ e^-)\frac{N_\gamma L_{ee}}{f_{\rm rep}} \sim 2\times10^5 \quad , \qquad (27)$$

where $L_{ee} = 1.3 \times 10^{33}\mathrm{cm}^{-2}\mathrm{sec}^{-1}$, and $f_{\rm rep} = 220$ sec^{-1} in this design. To be sure, this process provides a non-negligible amount of e^-e^+ pairs.

The rate of photon pair creation in a homogeneous magnetic field has been studied by many people,[15] and has been generalized to inhomogeneous fields by Baier and Katkov.[16] In the asymptotic limits the rate can be expressed as

$$\frac{\mathrm{d}I}{\mathrm{d}t} = \begin{cases} \frac{3\sqrt{3}}{16\sqrt{2}}\,\frac{\alpha\Upsilon}{\lambda_c\gamma}e^{-8/3\chi} & , \ \chi \ll 1 \ ; \\ \frac{15}{\pi}\left(\frac{2}{3}\right)^{1/3}\frac{\Gamma(5/6)}{\Gamma(1/6)}\,\frac{\alpha\Upsilon}{\lambda_c\gamma}\chi^{-1/3} & , \ \chi \gg 1 \ . \end{cases} \qquad (28)$$

Here $\chi = \Upsilon\omega/E$ plays the similar role as Υ in the case of beamstrahlung. Notice that χ is independent of the initial particle energy γ, as the process does not care where the photon was originated from. Let

$$\frac{\mathrm{d}I}{\mathrm{d}t} \equiv \frac{\alpha\Upsilon}{\lambda_c\gamma}T(\chi) \quad . \qquad (29)$$

To a very good approximation,[17]

$$T(\chi) = 0.16\chi^{-1}K^2_{1/3}\Big(\frac{4}{3\chi}\Big) \quad , \qquad (30)$$

for all values of χ.

Integrating over the collision time — again, only half of the e^-e^+ collision time — we have

$$\begin{aligned} I &= \frac{\sqrt{3}}{2}\frac{\sigma_z\alpha\Upsilon}{\lambda_c\gamma}T(\chi) \\ &= \frac{1}{2}n_{cl}T(\chi) \quad . \end{aligned} \qquad (31)$$

Next we evaluate the mean value of $T(\chi)$ by weighting over the beamstrahlung spectral function,

$$\frac{\mathrm{d}n_b}{\mathrm{d}\omega} = \frac{1}{\pi}\frac{\alpha\sigma_z}{\gamma^2}\left\{\int_y^\infty K_{5/3}(x)\mathrm{d}x + \frac{\xi^2y^2}{1+\xi y}K_{2/3}(y)\right\} \quad , \qquad (32)$$

and

$$\langle T(\Upsilon)\rangle = \int_0^E T(\chi)\frac{\mathrm{d}n_b}{\mathrm{d}\omega}\mathrm{d}\omega \Big/ \int_0^E \frac{\mathrm{d}n_b}{\mathrm{d}\omega}\mathrm{d}\omega \quad . \qquad (33)$$

The total number of e^-e^+ pairs created through this coherent process is therefore

$$N^c_{e^+e^-} = \frac{1}{2}N_\gamma n_{cl}\langle T(\Upsilon)\rangle \quad . \qquad (34)$$

A plot of $\langle T(\Upsilon)\rangle$ is shown in Fig. 13, where the solid curve is from the exact form of $dn_b/d\omega$ in Eq. (32), and the dashed curve corresponds to an asymptotic expression for $dn_b/d\omega$ at large y. The closeness between the two curves

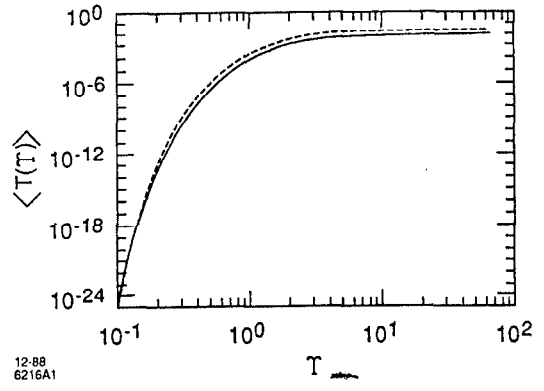

Fig. 13. The function $\langle T(\Upsilon)\rangle$ vs. Υ.

suggests that only the spectrum tip contribute effectively to the coherent pair creation process. From the TLC parameters, $n_{cl} \sim 1.9$, so we find that

$$N^c_{e^+e^-} \sim 5 \times 10^7 \quad , \tag{35}$$

which is much larger than the incoherent process.

It should be noticed, however, that $\langle T\rangle$ drops exponentially for $\Upsilon \lesssim 1$. Therefore, for next generation linear colliders at the range of 1 TeV, which would typically have $\Upsilon \sim 1$, it is not at all difficult to redesign the machine such that the coherent process can be entirely suppressed. For the above-mentioned TLC parameters the condition is $\Upsilon \leq 0.3$. This, ironically, is an over-kill of the issue since the incoherent process corresponds to $\Upsilon \sim 0.6$, as can be read from Fig. 13.

Since to a large extent N_γ is of the order unity and quite insensitive to other parameters, and since we usually choose to fix the luminosity in a design, the incoherent e^-e^+ pairs can not be easily suppressed. It is thus important to evaluate the energy spectrum of the pair created e^+. Assuming constant probability in finding the e^+ at energy $\varepsilon E \leq \omega$, the spectrum can be derived to be

$$N_{e^+}(\varepsilon) = \frac{7(3/2)^{2/3}}{18\pi^2\Gamma(1/3)}\frac{\alpha^3}{\gamma m} N D_y \Upsilon^{2/3} F(\varepsilon,\Upsilon) \quad . \tag{36}$$

The spectral function $F(\varepsilon,\Upsilon)$ is plotted in Fig. 14 for $\Upsilon = 0.2$. At the small ε limit, $F(\varepsilon,\Upsilon) \propto 1/\varepsilon$.

Finally, we evaluate the deflection angle of these low energy positrons by the beam–beam field. As a rough estimation, we assume that the vertical field beyond the beam height extents constantly to a distance equal to the beam width σ_x. It is then easy to show that the deflection angle for the $e^+$with energy ε is

$$\theta_\varepsilon = \begin{cases} \frac{2}{3^{1/4}}\frac{\sigma_x}{\sigma_z}\sqrt{\frac{D_x}{\varepsilon}} & , \quad \theta_\varepsilon \geq \frac{2}{\sqrt{3}}\theta_d \quad ; \\ 2\frac{\sigma_x}{\sigma_z}\frac{D_x}{\varepsilon} & , \quad \theta_\varepsilon \leq \frac{2}{\sqrt{3}}\theta_d \quad . \end{cases} \tag{37}$$

The deflection angle in the above expression is plotted in Fig. 15. For a 1 GeV e^+, $\theta_\varepsilon \sim 45$ mrad. The information

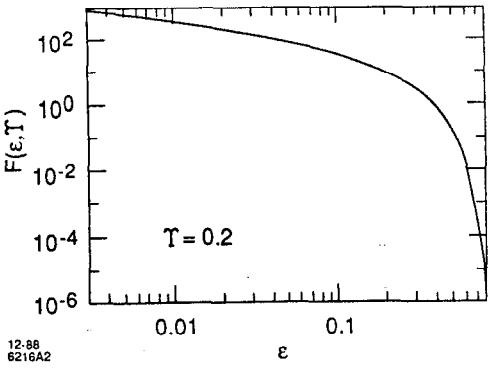

Fig. 14. The spectral function for incoherent pair created e^+.

on the transverse monemtum can be easily deduced from the above expressions via $p_\perp = \varepsilon\theta_\varepsilon$.

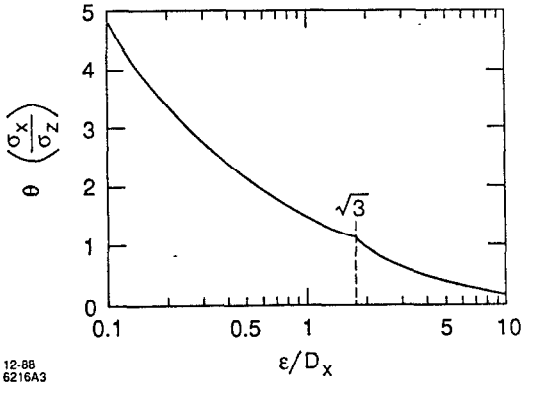

Fig. 15. The deflection angle as a function of e^+ energy.

REFERENCES

1. K. Yokoya, *A Computer Simulation Code for the Beam–Beam Interaction in Linear Colliders*, KEK Report 85-9, Oct 1985.
2. P. Chen and K. Yokoya, *Disruption Effects from the Interaction of Round e^+e^- Beams*, Phys. Rev. D 38, 987 (1988).
3. P. Chen and K. Yokoya, *Disruption Effects from the Interaction of flat e^+e^- Beams*, in preparation.
4. W. M. Fawley and E. P. Lee, *Particle in Cell Simulations of Disruption*, in "New Developments in Particle Acceleration Techniques", Orsay 1987, CERN 87–11, ECFA 87/110.
5. R. Holebeek, *Disruption Limits for Linear Colliders*, Nucl. Ins. Meth. 184 (1981).
6. N. A. Solyak, *Collision Effects in Compensated Bunches of Linear Colliders*, Novosibirsk Preprint IYF–88–44, 1988.

7. K. Yokoya and P. Chen, *Multiple Bunch Crossing Instability*, SLAC–PUB–4653, June 1988.

8. Y. H. Chin, *Stability of a Colliding Beam in a Linear Collider*, DESY January 1987.

9. K. Yokoya and P. Chen, *Depolarization due to Beam-Beam Interaction in Electron–Positron Linear Colliders*, SLAC–PUB–4692, September 1988; and in the *Proceedings for the Eighth International Symposium on High Energy Spin Physics*, 1988.

10. P. Chen and K. Yokoya, *Final Electron Energy Spectrum and Maximum Deflection Angle under Beamstrahlung*, in preparation.

11. R. B. Palmer, *Interdependence of Parameters for TeV Linear Colliders*, SLAC–PUB–4295, April 1987; and SLAC–AAS–39, November 1988.

12. P. Chen, *Review of Beam–Beam Interaction*, summary talk given at the International Workshop on the Next Generation Linear Colliders, November 28–December 9, 1988, SLAC, Stanford.

13. M. S. Zolotarev, E. A. Kuraev and V. G. Serbo, *Estimates of Electromagnetic Background Processes for the VLEPP Project*, Inst. Yadernoi Fiziki, Preprint 81–63, 1981; English translation SLAC TRANS–0227, 1987.

14. I. F. Ginzburg, G. L. Kotkin, V. G. Serbo and V. I. Telnov, *Colliding γe and $\gamma\gamma$ Beams Based on the Single–Pass Accelerators*, Inst. Nucl. Phys. (Novosibirsk) Preprint 81–102, 1981.

15. See, for example, W. Y. Tsai and T. Erber, Phys. Rev. D **10**, 492, 1974; and references therein.

16. V. N. Baier and V. M. Katkov, Soviet Phys. JETP **26**, 854, 1968.

17. T. Erber, Rev. Mod. Phys. **38**, 626, 1966.

QUANTUM BEAMSTRAHLUNG: PULSE SHAPING PROSPECTS FOR A PHOTON-PHOTON COLLIDER*

RICHARD BLANKENBECLER AND SIDNEY D. DRELL

Stanford Linear Accelerator Center
Stanford University, Stanford, California 94309

Beamstrahlung is the fractional energy loss to radiation as one beam pulse is accelerated by the electromagnetic field of the other pulse through which it passes in a collider. It is very important for high energy electron-positron linear colliders ($\sqrt{s} \sim \frac{1}{2} - 1\ TeV$) that are being studied.[1] In linear colliders the individual pulses must be formed with much larger charge densities to compensate for their much lower rate of interactions ($10^2 - 10^3$ per second) in comparison to storage rings (typically 10^5 per second). Therefore the electromagnetic fields generated by the charges in each pulse will be correspondingly larger, as will the acceleration they induce in the charges of the intersecting pulses; this in turn leads to a larger loss of energy to radiation. In the classical approximation the beamstrahlung is given by

$$\delta_{\text{classical}} = \frac{8\pi}{3} N^2 \gamma \frac{r_0^3}{\ell\{\pi B^2\}} \tag{1}$$

where N is the number of electrons (positrons) per pulse, for a uniformly charged cylindrical pulse of length ℓ and cross section πB^2; $\gamma = E/M$ is the beam energy and $r_0 \equiv 2 \cdot 8 \times 10^{-13}\ cm$ is the classical electron radius.

In this report we consider three questions:

1. What is the quantum result for beamstrahlung and when is the classical result valid?
2. How does the transverse beam geometry—*i.e.*, ribbon versus cylindrical pulse—affect the beamstrahlung?
3. Extending the quantum calculation to multiple photon emission, what is the photon flux and what are the prospects for a photon-photon collider?

* Work supported by the Department of Energy, contract DE-AC03-76SF00515.

1) Quantum beamstrahlung

Synchrotron radiation is a well-studied problem. Its application to beamstrahlung in the very high energy quantum limit was made in a seminal paper by Himel and Siegrist. The calculation can be done analytically[2] for the physical case of small disruptions—*i.e.*, for parameters such that the impact parameter of a beam particle changes fractionally only by a small amount as it traverses an intersecting beam pulse. Making this approximation which is an appropriate one for envisioned TeV colliders the quantum result for beamstrahlung for uniformly charged colliding pulses with cylindrical geometry is

$$\delta = \delta_{\text{classical}}\, F(C) \tag{2}$$

where the form factor $F(C) \to 1$ in the classical limit ($\hbar \to 0$, $C \to \infty$) and $F(C) \to C^{4/3}(0.83)$ for $C \to 0$ in the extreme quantum limit. The physical interpretation of C is the ratio of a transverse coherence length, $\ell_\perp$, to the radiation length, ℓ_{rad}:

$$C \propto \frac{\ell_\perp}{\ell_{\text{rad}}}\,. \tag{3}$$

$\ell_\perp$ is defined as the length along the trajectory of a beam particle as it traverses a pulse for it to acquire a transverse momentum $p_\perp \sim m$ from the field produced by the charges of the pulse; after travelling a distance $\ell_\perp$ the trajectory turns through an angle m/E. This angle is the same as the width of the radiation pattern from a relativistic charged particle; $\theta_{\text{tr}} \sim 1/\gamma = m/E$. Thus the radiation ceases to be coherent after a particle moves a length $\ell_\perp$ along the curving path. The second length, ℓ_{rad}, is defined as the length of the target that the electron coherently scatters from during the radiation process. According to the uncertainty principle, it is the reciprocal of the minimum longitudinal momentum transfer to the

target. As shown in ref. 2

$$C = \frac{1}{4\gamma y} \left\{ \frac{\ell}{\hbar/mc} \right\} \tag{4}$$

where

$$y \equiv \frac{Nr_0}{B} = r_0\sqrt{\pi\mathcal{L}} \tag{5}$$

is a dimensionless classical variable proportional to the square root of the luminosity per pulse, $\mathcal{L}$, and we inserted $\hbar$ and c as appropriate to show that $C \propto 1/\hbar$. In the classical limit the radiation occurs locally and by (3) and (4), $C \propto 1/\hbar \to \infty$ as claimed above. In all cases currently under study as practical in the TeV energy range both lengths $\ell_{\rm rad}$, $\ell_\perp \ll \ell$ and end effects of the pulse are small.[2] Using (5) we can rewrite (1) and (2) in terms of scaling variable C which, for fixed luminosity per pulse, $\mathcal{L}$, and for pulses of circular cross-section is the only parameter appearing:

$$\delta = \frac{2}{3}\,\alpha y\,\frac{F(C)}{C}\;; \quad \alpha \equiv \frac{1}{137}\,. \tag{6}$$

The classical approximation is valid for $C \gg 1$, $F(C) \to 1$, in which case the beamstrahlung is small since for practical values of $\mathcal{L} \lesssim 10^{30} cm^{-2}$, $y \lesssim 400$.

2) Ribbon Beams

The field strengths generated by the pulses are reduced when the circular cross section of a cylindrical pulse is distorted to an ellipse of the same area. Therefore the resulting acceleration of a beam particle is also reduced, as is the energy loss to radiation. As defined in ref. 2 this reduction can be summarized in the aspect ratio $1/G$ defined as the ratio of the mean value of the semi-major and minor axes to their average:

$$\frac{1}{G} = \frac{2\sqrt{a_x a_y}}{a_x + a_y} \leq 1\,. \tag{7}$$

The result is[2]

$$\delta^{\rm ellipse} = \frac{2}{3}\,\frac{\alpha y}{G}\,\frac{F(CG)}{(CG)}\,. \tag{8}$$

The fact that $\delta^{\rm ellipse}_{\rm classical} \propto 1/G^2$ follows from the fact that (acceleration)$^2 \propto$ (field strength)$^2 \propto (1/G)^2$. Since $G \geq 1$, the argument CG of the form factor increases with increasing values of the aspect ratio and we move toward the classical region for fixed C.

3) Multiple photon emission and prospects for a $\gamma - \gamma$ collider

Interest in this possibility is kindled by the fact that the expected gamma flux due to beamstrahlung for TeV linear colliders now under study is one to two orders of magnitude larger than that calculated in the Weiszacker-Williams equivalent-photon approximation, and the resultant photon spectrum is hard.[3]

This result introduces a new dimension into the design and application of $e^\pm$ linear colliders. For constant luminosity, the beam pulses can be shaped as desired in order to either maximize or minimize the fields and the resulting beamstrahlung. The beamstrahlung can be reduced by forming beams with very thin ribbon-like cross sections, *i.e.*, $G \sim 5$, permitting study of e^+e^- interactions at maximum energy and with narrow energy spread. Oppositely, in order to study high energy photon-photon processes, the collider can be tuned by shaping the beam pulses with smaller aspect ratio, *i.e.*, $G \sim 2$, in order to increase the flux of hard photons. We note that the multiple photon contributions substantially alter the spectral distribution of radiated photons but have little effect on the fractional energy loss δ.

The basic calculation proceeds from the rate equation for $P_e(x,t)$, defined as the probability of finding an electron with a fraction x of its incident momentum at a fractional depth t within the pulse:

$$\frac{dP_e(x,t)}{dt} = \int_x^1 dz\, T(x,z)\, P_e(z,t) - p(x)\, P_e(x,t)\,, \tag{9}$$

where the two terms on the right hand side are the standard "source" and "sink" contributions that represent falling into and out of the momentum fraction x as a result of radiating a photon. $T(x,z)\,dt\,dx$ is the probability that an electron with momentum fraction z will radiate a photon with momentum fraction $(z-x)$ and end up within dx of x after traversing a fraction dt of the pulse length $(0 < t < 1)$.

$$p(z)\,dt \equiv \int_0^z dx\, T(x,z)\,dt \tag{10}$$

is the probability that the electron with z radiates one photon while traversing dt.

Analogously, the rate equation for the probability of finding a photon with momentum fraction v at depth t is

$$\frac{dP_{ph}(v,t)}{dt} = \int_z^1 dx\, T(x-v,x) P_e(x,t)\,. \tag{11}$$

Equations (9) and (11) include only the first generation of shower development; neglected is subsequent pair conversion of the high energy radiation formed in the pulses. We have also proceeded classically above in calculating the probabilities for multiple photon emission since for $y \gg 1$ (see Eq. 5 and the subsequent discussion) we can chop the pulse into thin slices of thickness ℓ/y such that radiation from successive slices is incoherent.

Equations (9) and (11) can be integrated[3] numerically in terms of known single photon radiation probabilities, $T(x,z)$. We define the photon flux through a pulse

by

$$F(v) \equiv \int_0^1 dt\, P_{\rm ph}(v,t)\ .$$

The equivalent luminosity for beamstrahlung photon-photon collisions at total mass W is given by

$$\frac{d\mathcal{L}_{\gamma\gamma}}{dW^2} = \int_0^1 dv_1 \int_0^1 dv_2\, F(v_1)F(v_2)\,\delta(sv_1v_2 - W^2)\ ,$$

or

$$\frac{d\mathcal{L}_{\gamma\gamma}}{dz} = 2z \int_0^1 \frac{dv}{v}\, F(v)\, F\left(\frac{z^2}{v}\right)\ , \qquad (12)$$

where $z^2 = W^2/s = W^2/4E^2$.

Using this definition of $\mathcal{L}_{\gamma\gamma}$, the cross section to form a final state X at mass W is given by

$$\frac{d}{dz}\,\sigma_{\rm beamstrahlung}(e^+e^- \to e^+e^-X) = \left[\frac{d}{dz}\,\mathcal{L}_{\gamma\gamma}\right]\sigma_{\gamma\gamma\to X}(W)\ , \qquad (13)$$

In the narrow resonance approximation for a "particle" X of mass m_X (13) reduces to

$$\sigma_{\rm beamstrahlung}(X) = \left[z\,\frac{d}{dz}\,\mathcal{L}_{\gamma\gamma}\right]_{z=m_X/\sqrt{s}} \left\{\frac{4\pi^2(m_X \to 2\gamma)}{m_X^3}\right\}\ . \qquad (14)$$

The equivalent luminosity is shown in Figs. 1 and 2 for two choices of luminosity

$$C = 1.5\ \&\ y = 400,\ \text{or}\ \mathcal{L} \sim 0.7\ 10^{30} cm^{-2}\ \&\ \ell \sim 0.9mm$$

$$C = 0.5\ \&\ y = 800,\ \text{or}\ \mathcal{L} \sim 2.8\ 10^{30} cm^{-2}\ \&\ \ell \sim 0.3mm\ . \qquad (15)$$

The sensitivity to the beam geometry is illustrated by the three curves plotted in each figure corresponding to different values of the pulse aspect ratio, $G = 1$, 2 and 5 respectively. The latter values correspond to a flat beam with aspect ratios $a_x/a_y = 15$ and and 100, respectively. The virtual photon curves are drawn as dotted lines for a 1 TeV collider. For a 600 GeV collider with the same values of C and y, the results differ only slightly since the beamstrahlung photon-photon flux does not depend explicitly on the beam energy, and the virtual flux decreases only slightly due to its logarithmic energy dependence.

This calculation shows that two photon reactions via beamstrahlung can be significantly larger than previously appreciated on the basis of virtual photon processes. Note also that the beamstrahlung source works with electron-electron as well as positron-electron colliders. These hard photons may lead to troublesome backgrounds or, conversely, raise the attractive possibility of doing interesting

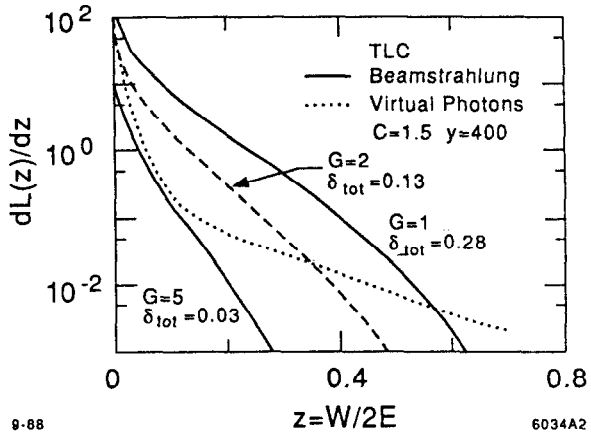

Figure 1. The photon-photon luminosity relative to the incident electron-positron flux is plotted for the case $C = 1.5$ and $y = 400$. The effect of pulse shaping is illustrated by the three values of G. The virtual two photon flux is also plotted as the dotted line for a collider energy of 1 TeV.

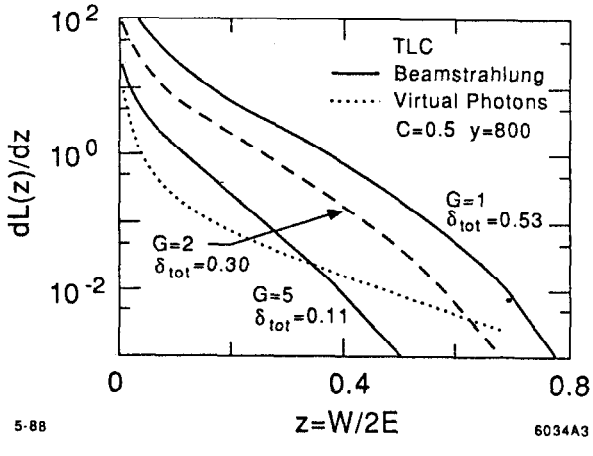

Figure 2. The same as Fig. 1 but for machine parameters of $C = 0.5$ and $y = 800$. The increase in luminosity is evident.

new physics with linear colliders in the 500 $GeV - 1\ TeV$ energy range that is now being studied. The colliders can be tuned by beam shaping to minimize or to maximize the beamstrahlung contribution as demanded by experiment.

REFERENCES

1. Palmer, R. B., SLAC-AAS-35 (1988), Stanford University preprint SLAC-PUB-4295 (1987), SLAC-AAS-31 (1987).
2. Blankenbecler, R. and Drell, S. D., Phys. Rev. D36, 277 (1987); D37, 3308 (1988).
3. Blankenbecler, R. and Drell, S. D., SLAC-PUB-4629 (1988), to be published.

CALCULATION OF DETECTOR BACKGROUNDS AT TEV LINEAR COLLIDERS*

T. Himel

Stanford Linear Accelerator Center, Stanford University, Stanford, California 94309
and
Brookhaven National Laboratory, Upton, New York 11973

ABSTRACT

It is necessary to carefully design masks and beam lines to prevent the high energy physics detector from being inundated with background particles from a high energy linear collider. Presented here are preliminary calculations on two of the three expected backgrounds: (1) photons from synchrotron radiation produced in the final focus quadrupoles, and (2) electrons which lose energy due to beamstrahlung and are then bent into a mask or quadrupole by the field of the opposite beam. The former can be controlled with proper masking. The later may pose a problem so further calculations are needed. Work was also done on the third expected source of background: electrons in the tail of the beam which hit masks where showers are made whose products enter the detector. This work was very preliminary and is not included in this write-up. All the calculations here are based on the 1 TeV center-of-mass linear collider design of R. Palmer and the final focus design of K. Oide which can be found in these proceedings. Extrapolations to other accelerator designs should be straightforward.

BACKGROUNDS FROM SYNCHROTRON RADIATION

As an electron goes through the bend and quadrupole fields of the final focus, it emits synchrotron radiation photons. These photons may enter the detector either directly or by penetrating or being reradiated from a mask. The goal of the mask design is to minimize the number of photons entering the detector. From SLC design studies, this number must be kept below about 1000 photons or the occupancy of the detector is high enough to degrade its pattern recognition capabilities. This is the first of many times the existing 100 GeV SLC design will be used as a benchmark to which our new 1 TeV Linear Collider (TLC) design will be compared.

The first step in the calculation is to make a scale drawing of the quadrupoles near the Interaction Point (IP). For the TLC the final quadrupoles have an inner bore 100 μm in radius and cover a distance of 0.4 to 1.2 meters from the IP. Using the β functions from Oide's design, the trajectory of a particle at five standard deviations is superimposed on the drawing. Since synchrotron radiation (SR) is emitted tangentially to the electron's trajectory (the opening angle of $1/\gamma$ is negligible) it is easy to estimate where the radiation will hit. One can also estimate the range of standard deviations of electrons which will generate photons to hit a certain mask or quadrupole. The number of photons radiated by an electron is given by

$$N_\gamma = 2.06\ (\frac{E_{\rm beam}}{100\ {\rm GeV}}) \cdot \theta\ ({\rm m}R)\ ,$$

where θ is the bend angle of the electron. Putting this all together with the fact that there are a total of 2×10^{11} incident electrons per pulse we can now calculate how many photons will hit the quadrupoles. Electrons between 2.8 and 3.6 σ will produce 1.1×10^9 photons which will hit the quadrupoles on the far side. Electrons outside 5σ will produce 1.4×10^5 photons which will hit the quadrupoles on the side of the incoming beam. The critical energy of these photons will be about 50 MeV.

This is a lot of photons especially when you consider that they are hitting a quadrupole which is inside the detector. Let's put in the best mask allowed by the constraints of detector acceptance (down to 10°) and see what happens. A 3.5 cm radius tungsten (because it is dense and has a large Z) rod which completely surrounds the quadrupoles and goes to within 20 cm of the IP just stays within the allowed 10°. In the center of this rod is drilled a 120 μm radius hole to a depth of 15 cm. For the next 5 cm the hole narrows to a 100 μm radius. For the next 80 cm we have the quadrupole with its 100 μm bore which is contained inside the tungsten mask. Making and aligning a mask with such a small hole in it may seem difficult, but compared to making the quadrupole it really isn't.

The purpose of this mask is to make it so the shower products from photons which hit the quadrupoles have a very small solid angle to enter the detector. The angles of the primary SR photons are so small that no photon can hit the 120 μm part of the hole since it is shadowed by the 100 μm part of the hole. So, to get to the detector a photon must either penetrate through the tungsten or make its way through a 15 cm long pin hole. The solid angle to get through the pin hole is 1000 times smaller than the equivalent in the SLC design. Photons penetrating the mask dominate.

*Work supported by Department of Energy contract DE-AC03-76SF00515.

Calculations of the penetration probability were done by H. DeStaebler using the electromagnetic shower simulation (EGS). Photons with a 50 MeV critical energy synchrotron radiation spectrum were simulated hitting the tungsten 15 cm from the end of the rod. For each incident photon only 0.004 came out the end. However, 0.17 came out the side of a 3.5 cm radius rod. Similarly, 0.02 and 0.002 came out of 6 and 10 cm rods, respectively. Given the 10^9 photons hitting the quadrupoles, this reduction factor is insufficient. Two improvements are needed to get an acceptable background.

The first improvement of 10^4 comes easily. We need to account for the 4 mR crossing angle of the beams, which is specified in the TLC design for other reasons. Because of this crossing angle, the outgoing beam doesn't have to go through the 100 μm bore of the quadrupole. Instead it goes 1.6 mm off to the side where there can be a larger hole. The crossing angle was originally put in the design so the disrupted electron beam would not have to pass through the center of the quadrupole. It has the same benefit for the outgoing SR photons. As long as the hole in the side of the quadrupole is at least 200 μm in radius no SR photons will hit it.

This still leaves us with the $0.17 \times 1.4 \times 10^5 = 2.4 \times 10^4$ photons which hit the quadrupole on the side of the incoming beam and penetrate the 3.5 cm thick mask around the quadrupole. This is a factor of 20 more than the detector can handle. The mask cannot be made thick enough to reduce this without encroaching on the solid angle reserved for the detector. The solution we arrived at was to increase the size of the quadrupole. Palmer redesigned the TLC with a quadrupole aperture of $10\sigma_{\rm beam}$ instead of $6\sigma_{\rm beam}$. This resulted in only a 10–20% reduction in the design luminosity while giving a very large reduction in the calculated synchrotron radiation background (there are many fewer particles outside 8σ than outside 5σ).

Having solved the toughest problem, let's look farther upstream to see if there are other magnets which will cause SR problems. The next quadrupole is 13 m from the IP. It is much weaker ($k = -.0249$ compared to the -3.416 of the quadrupole closest to the IP). It is also five times longer, so its field is very weak. The critical energy of the SR should be about 0.1 keV. This is so low that there is no problem stopping them from reaching the detector.

Finally, consider the last bend magnet which is 100 m from the IP. Only the last part of the bend which sweeps the beam past the 100 μm radius hole in the quadrupoles at the IP matters. This bend angle is $100\,\mu{\rm m}/100\,{\rm m} = 1\ \mu$ R. Hence, we expect 2×10^6 photons heading towards that hole. Note that only 1% of these photons will actually hit the inside bore of the quadrupole. The rest will pass right through and hit someplace well downstream of the detector. This still leaves 10^4 photons hitting the inside bore of the quadrupole inside the detector. Since the bend has a 0.144 kG field they will have a critical energy of 2.4 MeV. This is an uncomfortably large number of high energy photons being deposited inside the quadrupole. A significant number will penetrate the 3.5 cm thick mask. To fix this the last couple of microradians of the bend should be made with a lower field (a soft bend) to reduce the critical energy by about a factor of 25.

In summary, with moderate redesign we can avoid having synchrotron radiation contribute significantly to the detector's background. Note that the 100 μm radius of the quadrupoles sets the radius scale. Hence the minimum radius of a vertex detector will be determined by detector technology rather than the few hundred micron limit that background considerations set.

BACKGROUND DUE TO BEAMSTRAHLUNG FOLLOWED BY DISRUPTION

In the design of the TLC a maximum disruption angle is calculated. This is the maximum angle an outgoing electron has due to the kick it receives from the electromagnetic fields of the opposing positron bunch. The pinching of one beam by the other is included in the calculation. This maximum disruption angle is used to determine the crossing angle of the two beams to ensure there is a hole in the side of the quadrupole large enough to accept the outgoing beam. Not included in the calculation is the fact that an electron may lose energy due to beamstrahlung (synchrotron radiation in the field of the opposing beam) and thus be disrupted more. In some designs with a large beamstrahlung parameter it is possible for an electron to lose a large fraction of its energy in a single radiation event.

To see if beamstrahlung followed by disruption could be a source of background we made a simple computer model. The oncoming beam was considered to be Gaussian in z but very thin in y, and much wider in x than in y. Note that the TLC design has a 100:1 $x : y$ aspect ratio. Disruption of the oncoming beam was ignored. An electron was allowed to radiate up to 99.9% of its energy at any z from -0.5 to 3.5 σ_z. Electrons starting at 2, 3, 4, 6 and 8 σ_y were considered. The path of each electron was calculated by integrating the equations of motion out to $z = 5\sigma_z$. The outgoing angle was then calculated. For the case of no radiation the answer obtained agreed with previous calculations (0.25 mR). The largest disruption angle seen for an incident electron which radiated less than 99% of its energy at y less than $4\sigma_y$ was 1.1 mR. This should just manage to make it through the hole in the side of the quadrupole. However, the largest disruption angle seen when an electron was allowed to radiate up to 99.9% of its energy at a y up to $8\sigma_y$ was 2.7 mR. Such an electron would certainly hit the face of the quadrupole in the present design.

Time did not allow the calculation of the probability of such an event. The fact that there are 2×10^{11} electrons per pulse and that just a few electrons hitting the quadrupole will cause serious background problems for the detector certainly gives cause for worry. There are also arguments saying that the problem should be worse in the x direction than in the y direction. A more complete calculation is needed to see if we have a serious background here.

MULTIBUNCH INSTABILITIES IN SUBSYSTEMS OF 0.5 AND 1.0 TEV LINEAR COLLIDERS*

K. A. THOMPSON AND R. D. RUTH

Stanford Linear Accelerator Center, Stanford University, Stanford, California 94309

ABSTRACT

The acceleration of multiple bunches per RF fill of the linac accelerating structures is an important feature of the SLAC design for a next-generation linear collider, in order to use the RF as efficiently as possible and to obtain a higher luminosity. In this paper, we give simulation results on the control of multibunch instabilities in the subsystems of a 1.0 Tev linear collider (TLC) and an "intermediate" linear collider (ILC) of about 0.5 TeV center of mass energy.

INTRODUCTION

The acceleration of multiple bunches per RF fill of the linac accelerating structures is an important feature of the SLAC design for a very high energy linear collider (0.5 to 1.0 Tev). The reasons for multibunching are to use the RF as efficiently as possible and to obtain a higher luminosity. However, the problems of cumulative beam breakup in the linacs and coupled bunch instabilities in the damping rings must be addressed. In both cases, damped acceleration cavities may be a useful cure.[1] In such cavities, the transverse dipole wake is strongly damped by the use of axial slots through the irises of the RF structure coupled to radial waveguides. The Q of the fundamental transverse mode can be made as low as about 10 in this way, without significant adverse effect on the longitudinal accelerating mode, and the $Q's$ of higher order modes are expected to be at least as low as the Q of the fundamental.

Tuning the frequency of the fundamental transverse dipole mode to allow placement of the bunches near zero crossings of the wake fields will probably also be necessary in the main linacs. The transverse dipole wake for the accelerating structure considered here is strongly dominated by its fundamental mode and has zero crossings that are approximately equally spaced. Therefore it is possible to place all the bunches in a train near zero crossings of the wake field, if the ratio of the frequency of the fundamental dipole mode to the frequency of the accelerating RF is tuned to satisfy:

$$\frac{1}{2}\, n\lambda_{W_\perp} = m\lambda_{rf} = \ell \quad , \tag{1}$$

where ℓ is the bunch spacing, m and n are integers, and λ_{rf} and $\lambda_{W_\perp}$ are the wavelengths of the RF and the fundamental dipole wake mode.

The theoretical models and details of the computer simulations used in our study of multi-bunch instabilities have been discussed in more detail elsewhere.[2,3] The main emphasis of this paper will be on results for TLC and ILC parameter sets at the present stage of design.

MULTIBUNCH BEAM DYNAMICS

The bunches are taken to be point macroparticles, with an equal charge of N electrons in each bunch. The spacing ℓ between adjacent bunches is uniform and is an integral number of RF wavelengths in each subsystem.

The transverse dipole wake function is a sum of modes of the following form:

$$W_\perp(z) = \sum_m W_m \sin(K_m z) \exp\left(-\frac{K_m z}{2Q_m}\right) \quad , \tag{2}$$

where z is the distance behind the exciting bunch. K_m is the wavenumber and Q_m is the quality factor of mode m, and the $W'_m s$ are constant coefficients. The units of $W_\perp(z)$ are V/Coul/m^2.

2.1 Transverse Dynamics in Linacs

The acceleration is assumed to be linear: $\gamma = \gamma_0 + Gs$, where γ is the energy divided by the rest energy and G is a constant. We use the smooth-focusing approximation $k(s) = 1/\beta(s)$ for the focusing function, where $\beta(s)$ is the "average" betatron function at longitudinal position s. The focusing is assumed to vary as

* Work supported by the Department of Energy, contract DE-AC03-76SF00515.

$$k(s) = \left(\frac{\gamma_0}{\gamma(s)}\right)^{1/2} k_0 \quad , \tag{3}$$

unless stated otherwise. Taking acceleration into account, the equation of motion for the transverse offset x_n of bunch n is:

$$\gamma(s)x_n'' + \gamma'(s)x_n' + \gamma(s)k_n^2(s)x_n = F_n(s) \quad . \tag{4}$$

where the driving term due to the wake is:

$$F_n(s) \equiv \frac{Ne^2}{mc^2}\sum_{j=1}^{n-1} W_\perp[(n-j)\ell]\; x_j(s) \quad . \tag{5}$$

Here primes denote derivatives with respect to s, and m is the rest mass of the electron. The transverse offsets are taken to be all in one plane. The WKB solutions of the homogeneous equation are

$$\begin{aligned} x_n^{\pm}(s) &= x_n^{\pm}(0)\left[\frac{\gamma_0 k_n(0)}{\gamma(s)k_n(s)}\right]^{1/2} \exp\left[\pm i\int_0^s k_n(s')ds'\right] \\ &= x_n^{\pm}(0)\left[\frac{\gamma_0}{\gamma(s)}\right]^{1/4} \exp\left[\pm i\int_0^s k_n(s')ds'\right] \quad , \end{aligned} \tag{6}$$

where we have used Eq. (3) for the variation of k_n with γ. Assuming the acceleration is adiabatic and the blowup of the transverse offset is slow compared to a betatron oscillation, it is straightforward to show (see Ref. 2 or 3 for details) that the general solution to the inhomogeneous equation for bunch n is

$$x_n(s) = a_n^+ x_n^+(s) + a_n^- x_n^-(s) + \int_0^s G_n(s,s')F_n(s')ds' \quad , \tag{7}$$

where a_n^+ and a_n^- are arbitrary constants, the Green function is:

$$G_n(s,s') = [\gamma(s)\gamma(s')k_n(s)k_n(s')]^{-1/2}\sin\psi_n(s,s') \quad , \tag{8}$$

and

$$\psi_n(s,s') \equiv \int_{s'}^{s} k_n(s'')ds'' \tag{9}$$

is the phase advance for bunch n. If we take the "positive phase" WKB solution

$$x_1(s) = x_1(0)\left(\frac{\gamma_0}{\gamma(s)}\right)^{1/4} \exp\left[\psi_1(s,0)\right] \quad , \tag{10}$$

as the motion for the first bunch, assume $a_n^- = 0$ for all $n > 1$, and drop a term with rapidly oscillating integrand, the solution for the transverse motion of bunch n may be written:

$$\begin{aligned} x_n(s) = \Bigg[& x_n(0) + \\ & \frac{Ne^2}{2i\gamma_0 mc^2 k_n(0)} \int_0^s \left(\frac{\gamma_0}{\gamma(s')}\right)^{1/4} \exp[-i\psi_n(s',0)] \\ & \times \sum_{j=1}^{n-1} W_\perp[(n-j)\ell]x_j(s')ds' \Bigg] \\ & \times \left(\frac{\gamma_0}{\gamma(s)}\right)^{1/4} \exp[+i\psi_n(s,0)] \quad . \end{aligned} \tag{11}$$

We note that this result is equivalent (see Refs. 2 and 3) to that obtained ignoring acceleration, from the equations of motion

$$x_n'' + k_n^2 x_n = \frac{Ne^2}{E}\sum_{j=1}^{n-1} W_\perp[(n-j)\ell]x_j(s) \quad , \tag{12}$$

with solution

$$\begin{aligned} x_n(s) = \Bigg[& x_n(0) + \frac{Ne^2}{2iEk_n}\int_0^s e^{-ik_n s'} \times \\ & \sum_{j=1}^{n-1} W_\perp[(n-j)\ell]x_j(s')ds' \Bigg] e^{ik_n s} \quad , \end{aligned} \tag{13}$$

provided that we interpret E and the k_n to be the energy and the focusing functions at the beginning of the linac, and s to be not the true distance along the accelerator, but rather an "effective distance" $\psi(s)/k_0$, where $\psi(s)$ is the phase advance in the actual distance s along the linac and k_0 is the focusing function at the beginning of the linac:

$$\begin{aligned} s_{eff} &= \frac{\psi(s)}{k_0} = \frac{1}{k_0}\int_0^s k(s)ds \\ &= \frac{2\gamma_0^{1/2}}{G}\left[\gamma^{1/2} - \gamma_0^{1/2}\right] \quad . \end{aligned} \tag{14}$$

Note that if $\gamma(L) \gg \gamma_0$ at $s = L$, the end of the linac, the effective length of the linac is approximately

$$L_{eff} = 2\left(\frac{\gamma_0}{\gamma}\right)^{1/2} L \quad . \tag{15}$$

Solutions for the transverse blowup of each bunch as a function of s may be obtained by numerical integration of the above equations for $x_n(s)$, and we shall present results in later sections for parameter sets of interest.

Finally, we note that in cases where the wake field is strongly damped, a bunch will only see a significant wake from the immediately preceding bunch, and a simple "daisy chain" model gives excellent agreement with the simulation

results. Using the effective length approximation the equations of motion become:

$$x_1'' + k^2 x_1 = 0$$
$$x_n'' + k^2 x_n = \frac{Ne^2 W_\perp(l)}{E} x_{n-1} \qquad (n > 1) \quad . \tag{16}$$

Assuming $x_n(s) = a_n(s)e^{iks}$, the solution for the envelope function $a_n(s)$ for initial conditions $a_n(0) = 1$ is

$$a_n(s) = \sum_{j=0}^{n-1} \frac{(-i\sigma s)^j}{j!} \quad . \tag{17}$$

Since this is the first n terms of the Taylor series expansion of $\exp(-i\sigma_0 s)$, it is apparent that the criterion for little or no blow-up in the linac under these conditions is $|\sigma L| < 1$, that is:

$$\frac{Ne^2 |W_\perp(l)| L}{2kE} < 1 \quad , \tag{18}$$

where L is the effective length of the linac, and k and E are the values of focusing function and energy at the beginning of the linac.

In the main linacs of a TeV collider with damped acceleration cavities, we can have $|\sigma L| \sim 1$. Thus for n sufficiently large, $a_n(s)$ is approximately $\exp(-i\sigma s)$, and there is almost no blowup of the n^{th} bunch.

2.2 Transverse Dynamics in Damping Rings

We assume the damping ring impedance is dominated by the contribution of the RF cavities and that damped acceleration cavities are used. If the Q of the transverse modes is sufficiently low that turn-to-turn wakes are negligible, then the equations of transverse motion are similar to those for a linac, except for the presence of a coherent damping term due to tune spread and/or head-tail damping, which we parameterize in a constant α_{cd} (units m^{-1}):

$$x_n'' + 2\alpha_{cd} x_n' + k^2 x_n(s) = \frac{Ne^2}{E} \sum_{j=1}^{n-1} W[(n-j)\ell] x_j(s) \quad . \tag{19}$$

We divide the motion on one turn through the ring into two parts: (1) the motion through the RF cavities, where the effect of the wake fields is modelled by a localized kick, and (2) a mapping around the rest of the ring, with specified average beta function and phase advance. Let us define $x_n^-(x_n^+)$ and $x_n'^-(x_n'^+)$ to be the transverse offset and angular divergence of bunch n just before(after) the RF cavities (assumed to be clumped together). Then, assuming that $\beta' = 0$ at the location of the cavities,

$$\begin{pmatrix} x_n^- \\ x_n'^- \end{pmatrix} = e^{-\alpha_{cd} C} \begin{pmatrix} \cos\mu & \beta \sin\mu \\ -\frac{1}{\beta}\sin\mu & \cos\mu \end{pmatrix} \begin{pmatrix} x_n^{old\,+} \\ x_n'^{old\,+} \end{pmatrix} \quad . \tag{20}$$

Here $x_n^{old\,+}$ and $x_n'^{old\,+}$ are the transverse offset and angular divergence just after passing through the RF cavities on the preceding turn, C is the circumference of the ring, and μ is the coherent phase advance around the ring. One may also show (see Ref. 3):

$$\begin{pmatrix} x_n^+ \\ x_n'^+ \end{pmatrix} = \begin{pmatrix} x_n^- \\ x_n'^- + \frac{Ne^2}{E} L_{rf} \sum_{j=1}^{n-1} W[(n-j)\ell]\, x_j^- \end{pmatrix} \quad , \tag{21}$$

where L_{rf} is the total length of the RF cavities and $W(z)$ is the wake per unit length in the cavities. The results presented later on damping ring transverse instabilities are obtained using a tracking program based on these equations.

PARAMETERS OF COLLIDER SUB-SYSTEMS

We assume a train of ten bunches is to be accelerated on each RF fill, and that the interbunch spacing within the train is 21.0 cm (i.e., two wavelengths at S-band or twelve RF wavelengths at 17.1 GHz).

Table 1. Parameters for TLC.

Subsystem	Energy (GeV)	Particles per bunch
Injection accelerators	$0.18 \rightarrow 1.8$	2×10^{10}
Damping rings	1.8	2×10^{10}
Preaccelerators	$1.8 \rightarrow 18.0$	1.8×10^{10}
Main linacs	$18.0 \rightarrow 500.$	1.67×10^{10}

Table 2. Parameters for ILC.

Subsystem	Energy (GeV)	Particles per bunch
Injection accelerators	$0.18 \rightarrow 1.8$	1×10^{10}
Damping rings	1.8	1×10^{10}
Preaccelerators	$1.8 \rightarrow 18.0$	9×10^{9}
Main linacs	$18.0 \rightarrow 250.$	8.33×10^{9}

Other parameters of individual collider subsystems are given in Table 1 for the TLC design, and in Table 2 for the ILC design.

We shall discuss results for each of these subsystems in the TLC design, and for the main linacs of an ILC design. Since the parameters for other subsystems of the ILC will be assumed the same as those for the TLC except for a lower charge per bunch, it is clear that instabilities can be controlled in these subsystems of the ILC if they can be controlled in the corresponding subsystems of the TLC.

RESULTS FOR MAIN LINACS IN THE TLC

We assume a main linac accelerating frequency of 17.1 GHz, and a disk-loaded accelerating structure with

Table 3. Parameters for main linacs at 17.1 GHz.

Number of bunches	10
Number of particles per bunch	1.67×10^{10}
Bunch spacing ℓ	21.0 cm
Initial energy of linac	18 GeV
Final energy of linac	500 GeV
Linac length	3000 m
Initial beta function	3.2 m ($k_0 = 0.3125m^{-1}$)

cell length 5.83 mm, internal cell radius 7.47 mm, and relatively large iris radius of 3.47 mm.

The parameter set used is shown in Table 3. Each linac accelerates 10 bunches per RF fill, to an energy of 0.5 TeV. The spacing of 12 RF wavelengths between bunches (at the assumed RF frequency) is chosen in order to match the energy extracted by the bunch train to the energy input from the RF. This gives very nearly the same acceleration for every bunch in the bunch train.[4)]

The RF wavelength at 17.1 GHz is 1.75 cm, and the wavelength of the fundamental mode of the unmodified transverse dipole wake for our cavity design is 1.36 cm. If the frequency of the fundamental mode is shifted slightly, so that its wavelength is 1.31 cm, then Eq. (1) is satisfied with n=32, and we have

$$\frac{\lambda_{rf}}{\lambda_{W_\perp}} = \frac{4}{3} \quad . \tag{22}$$

When this relation is satisfied, the frequency of the fundamental transverse mode is 477.85 m^{-1}, which we shall denote by K_{W_0}.

In Fig. 1, we show "tuning curves" of the maximum transverse amplitude x_{max} in the bunch train as a function of the frequency of the fundamental transverse dipole mode, for values of Q = 30, 40, 50, and 60. The value of x_{max} is the maximum of the amplitudes reached by all bunches as they travel down the linac, normalized by dividing out the adiabatic damping factor $(\frac{\gamma_0}{\gamma})^{1/4}$. The central frequency, at which $\frac{\lambda_{rf}}{\lambda_{W_\perp}} = \frac{4}{3}$, is 477.85 m^{-1}. The range about the central frequency shown in the figure is only $\pm 0.1\%$, so the tolerance on tuning the frequency of the low-Q dipole mode with respect to the accelerating mode is rather tight compared to its bandwidth.

Note that at M bunch spacings behind a bunch, the wake field has damped by a factor of about

$$\exp\left(-\frac{K_{W_0}\ell M}{2Q}\right) \approx \exp\left(-\frac{50M}{Q}\right) \quad , \tag{23}$$

and so a given bunch can feel a significant wake field from several bunches ahead of it, unless it is near a node of these wakes and/or the value of Q is well below 50. Figure 2 shows tuning curves for the smaller values Q = 15, 20, and 25. The spread around K_{W_0} in this figure is $\pm 1\%$, and as can be seen from the figure, for Q = 15, we have $x_{max} < 2$ for frequencies within this range.

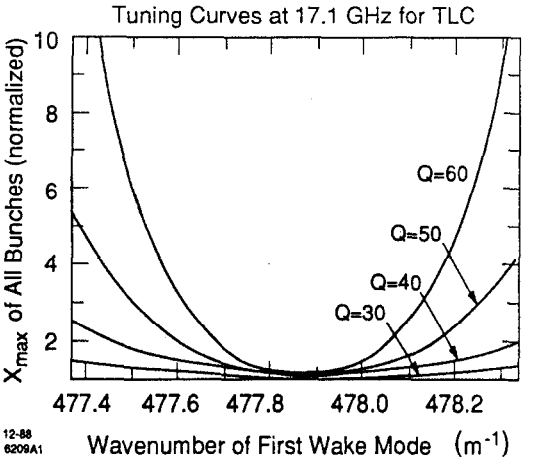

Fig. 1. Maximum transverse amplitude x_{max} (normalized) of all bunches as a function of the frequency of the fundamental transverse dipole mode, for values of Q = 30, 40, 50, and 60, at 17.1 GHz accelerating frequency. The central frequency, where $\lambda_{rf}/\lambda_{W_\perp} = 4/3$, is 477.85 m^{-1}. The spread shown about K_{W_0} is ± 0.1%.

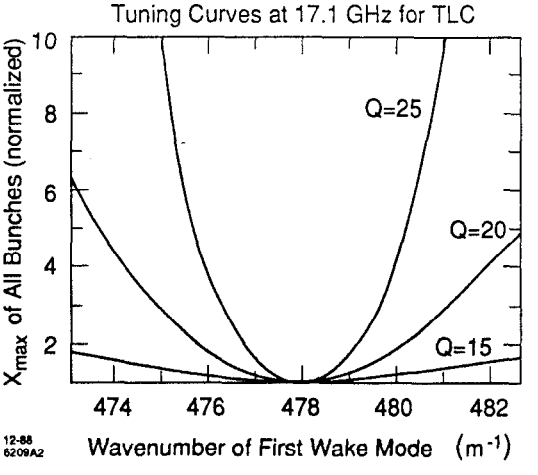

Fig. 2. Maximum transverse amplitude x_{max} (normalized) of all bunches as a function of the frequency of the fundamental transverse dipole mode, for values of Q = 15, 20, and 25, at 17.1 GHz accelerating frequency. The central value of the frequency, where $\lambda_{rf}/\lambda_{W_\perp} = 4/3$, is 477.85 m^{-1}. The spread shown about K_{W_0} is ± 1%.

For low values of Q, the frequency of the fundamental transverse mode becomes less sharply defined; the full width at half-maximum of the resonance around the central frequency K_{W_0} is $\Gamma \equiv K_{W_0}/Q$ (and the central frequency

is shifted slightly from that of the undamped mode). So it is also of interest to compare the ratio R of the tuning tolerance for a given Q to the full width Γ of the resonance at that Q:

$$R \equiv \frac{\Delta K_{W_0}}{\Gamma} \quad . \tag{24}$$

Table 4. Tuning parameters for the fundamental transverse dipole mode for TLC main linacs.

Q	$\Delta K_{W_0}(\mathrm{m}^{-1})$	$\Gamma = \frac{K_{W_0}}{Q}(\mathrm{m}^{-1})$	$\frac{\Delta K_{W_0}}{K_{W_0}}$	$\frac{\Delta K_{W_0}}{\Gamma}$
15	>11.0	31.9	>2.3%	>34%
20	4.37	23.9	0.91%	18%
25	2.56	19.1	0.54%	13%
30	1.60	15.9	0.33%	10%
40	0.87	11.9	0.18%	7.3%
50	0.57	9.56	0.12%	6.0%
60	0.38	7.96	0.08%	4.8%

In Table 4, we show the full-width tuning tolerance ΔK_{W_0} for the criterion $x_{max} \leq 2$, the full-width Γ of the resonance peak, the tuning tolerance expressed as a percentage of the undamped central frequency, and the ratio R. The parameters used and the values of Q tabulated are those used in Figs. 1 and 2. The lower values of Q, say up to 30 or so, seem to be the most desirable in that the tolerance on tuning is at least 10% of the bandwidth of the resonance; this should be straightforward to do. Such $Q's$ have already been achieved in models (Ref. 1).

RESULTS FOR MAIN LINACS IN THE ILC

It is also of interest to consider a design for an "intermediate" energy linear collider with half the center of mass energy. The parameters for the main linacs are as shown in Table 3 for the TLC, except that the final energy of each linac is 250 GeV and the number of particles per bunch is 8.33×10^9. The lower charge per bunch more than compensates for the fact that since the energy is lower the beam is less "stiff" (also, the initial focusing function is the same as in the TLC, but weakens less quickly with distance, according to Eq. (3)). The tuning curves for the ILC case are shown in Fig. 3.

The tuning parameters corresponding to Fig. 3 are shown in Table 5.

RESULTS FOR THE PREACCELERATORS (TLC)

We turn now to the question of beam breakup in the preaccelerators of the linear collider. We assume the same type of large-irised, and possibly damped, accelerating structure as in the main linacs, but scaled to S-band.

The bunch spacing chosen for the main linacs, about 21.0 cm, is two S-band wavelengths, and other parameters are as shown in Table 6. In the preaccelerator the problem of beam breakup is much less acute than in the main

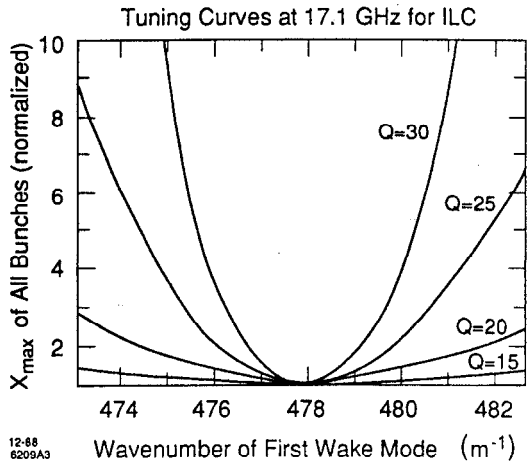

Fig. 3. Maximum transverse amplitude x_{max} (normalized) of all bunches as a function of the frequency of the fundamental transverse dipole mode, for values of Q = 15, 20, 25, and 30, using the ILC design parameters. The central frequency, where $\lambda_{rf}/\lambda_{W_\perp} = 4/3$, is 477.85 m^{-1}. The spread shown about K_{W_0} is ± 1%.

Table 5. Tuning parameters for the fundamental transverse dipole mode for ILC main linacs.

Q	$\Delta K_{W_0}(\mathrm{m}^{-1})$	$\Gamma = \frac{K_{W_0}}{Q}(\mathrm{m}^{-1})$	$\frac{\Delta K_{W_0}}{K_{W_0}}$	$\frac{\Delta K_{W_0}}{\Gamma}$
15	>15.0	31.9	>3%	>50%
20	7.20	23.9	1.5%	30%
25	3.73	19.1	0.78%	20%
30	2.51	15.9	0.53%	16%

Table 6. Parameters for preaccelerator.

RF accelerating frequency	2.856 GHz
Number of bunches	10
Number of particles per bunch	1.8×10^{10}
Bunch spacing ℓ	21.0 cm
Initial energy of preaccelerator	1.8 GeV
Final energy of preaccelerator	18 GeV
Acceleration gradient	50 MeV/m

linacs. It is not necessary to tune the frequency of the fundamental transverse dipole mode relative to the accelerating mode, so as to place all bunches near wake zero crossings. In our example the placement of the bunches is neither particularly favorable nor unfavorable.

Table 7. Transverse beam blowup at end of preaccelerators.

Initial β (meters)	Q	Max transverse blow-up factor
4.0	∞	1.22
2.0	∞	1.05
1.0	∞	1.01
4.0	40.0	1.05
2.0	40.0	1.01

Results for several choices of Q and focusing function are given in Table 7. Note that we are assuming that the transverse focusing weakens with distance along the linac according to Eq. (3), and that one might choose to keep it more nearly constant.

RESULTS FOR THE INJECTION ACCELERATORS (TLC)

Accelerators are also needed to take the bunches up to the damping ring energy of 1.8 GeV.

Table 8. Parameters for injection accelerator.

RF accelerating frequency	2.856 GHz
Number of bunches	10
Number of particles per bunch	2×10^{10}
Bunch spacing ℓ	21.0 cm
Initial energy	0.18 GeV
Final energy	1.8 GeV
Acceleration gradient	25 or 50 MeV/m

A representative parameter set is given in Table 8. We again assume an accelerating structure of the same type as in the main linacs, including damping if necessary, but scaled to S-band. Due to the lower energy, somewhat stronger focusing is needed here than is needed in the case of the preaccelerators.

Results are shown in Table 9 for two values of acceleration gradient, again assuming that the focusing scales according to Eq. (3).

In Table 10, we show the results obtained assuming the focusing function does not vary with s.

RESULTS FOR DAMPING RINGS (TLC)

We have carried out simulations for the damping ring parameters shown in Table 11, using two examples of RF cavity designs. One is the TLC main linac cavity described earlier, scaled to the damping ring frequency. The other is a scaled PEP cavity, which has nose cones and a relatively smaller iris. In both cases we assume the $Q's$ of the transverse modes may be lowered by modifying the cavities to include axial slots coupled to radial waveguides, as in the main linacs.

Table 9. Transverse beam blowup at end of injection accelerators.

Accel. gradient MeV/m	Initial β (meters)	Q	Max transverse blowup factor
50.0	4.0	∞	1.25
"	2.0	∞	1.05
"	4.0	40	1.05
25.0	4.0	∞	2.40
"	2.0	∞	1.20
"	1.0	∞	1.06
"	4.0	40	1.18
"	2.0	40	1.07

Table 10. Transverse beam blowup at end of Injection Accelerators with focusing assumed constant.

Accel. gradient MeV/m	β (meters)	Q	Max transverse blowup factor
50.0	4.0	∞	1.06
25.0	4.0	∞	1.32
"	2.0	∞	1.08
"	1.0	∞	1.02
"	4.0	40	1.08

Table 11. Damping ring parameters.

Number of bunch trains	10
Number of bunches per train	10
Number of particles per bunch	2×10^{10}
Particle energy	1.8 GeV
Ring circumference	154 m
RF frequency	1.428 GHz
Bunch spacing within a train	21.0 cm

For both cavities, the wavenumber K_1 of the fundamental transverse mode is approximately 40 m^{-1}. The number of e-foldings of this mode per turn around the circumference C of the ring is

$$\frac{K_1 C}{2Q} \approx \frac{3000}{Q} \quad , \tag{25}$$

and the number of e-foldings between bunch trains (assuming ten trains symmetrically placed in the ring) is about

$300/Q$. Thus we expect turn-to-turn and train-to-train wake effects to be negligible for sufficiently low $Q's$.

Simulations were done with the tracking program discussed earlier. For $Q = 30$ and a coherent damping parameter α_{cd} of at least $10^{-6}\mathrm{m}^{-1}$, none of the bunches ever get an amplitude larger than their initial injected amplitude, and the centroids of all the bunches have damped to small amplitudes after 50000 turns, due to the effect of α_{cd}. Note that this value of α_{cd} gives a coherent damping time of 3.33 msec, which corresponds to about 6500 turns. The amplitudes of the second and tenth bunches as a function of turn number are shown in Fig. 4, for the two cavities, for $Q = 30$ and $\alpha_{cd} = 10^{-6}\mathrm{m}^{-1}$.

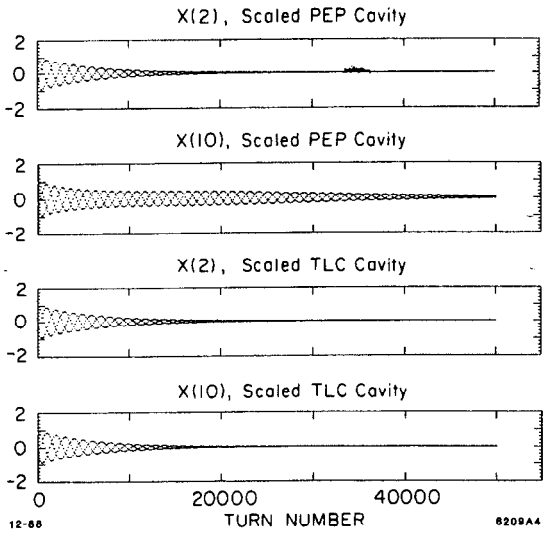

Fig. 4. Offset of second and tenth bunch as a function of turn number, for the scaled PEP and scaled TLC damping ring cavities. The value of Q for the cavity is 30 and the coherent damping parameter α_{cd} is $10^{-6}m^{-1}$.

CONCLUSIONS AND ACKNOWLEDGMENTS

Control of transverse multibunch instabilities appears to be feasible in all the subsystems of a linear collider studied here, namely the main linacs, injector linacs, preaccelerators, and damping rings. In all these subsystems, damped acceleration cavities may be a useful tool, although in the preaccelerators and injection accelerators one can probably get by without them. In the main linacs, both damped cavities and placing the bunches near wake zero crossings are essential. In the damping rings, it is highly desirable to use damped cavities to decouple the bunch trains from each other as well as to reduce the transverse wakes within each train.

We thank the members of the linear collider working group at Snowmass for useful discussion and comments.

REFERENCES

1. R. B. Palmer, SLAC–PUB–4542 (1988).
2. K. A. Thompson and R. D. Ruth, SLAC–PUB–4537, in *Proceedings of International Workshop on Linear Colliders*, Capri, Italy (1988).
3. K. A. Thompson and R. D. Ruth, SLAC–PUB–4801, to be submitted for publication (1988).
4. R. D. Ruth, SLAC–PUB–4541 (1988).